Novel geochemical fingerprints of biogenicity applied to ancient carbonates

PhD Thesis

2016

Meabh Gallagher



Trinity College Dublin
Coláiste na Tríonóide, Baile Átha Cliath
The University of Dublin

I declare that this thesis has not been submitted as an exercise for a degree at this or any other university and it is entirely my own work.

I agree to deposit this thesis in the University's open access institutional repository or allow the library to do so on my behalf, subject to Irish Copyright Legislation and Trinity College Library conditions of use and acknowledgement.

Meabh Gallagher

Novel geochemical fingerprints of biogenicity applied to ancient carbonates

Meabh Gallagher

Abstract

The oxygenation of the Earth's surface shaped our planetary environment, fundamentally altered global biogeochemical cycles, and ultimately paved the way for the rise of complex animals at the beginning of the Cambrian. The Earth's surface oxygenation was apparently achieved in two broad steps at the beginning and the end of the Proterozoic eon. However, reconstruction of the detailed redox-evolution of the Earth's surface environment remains one of the greatest scientific challenges in the geosciences. Both postulated oxidation events were apparently accompanied by global glaciations, but the causality between the apparent step increases in oxygen concentrations, and these two global glaciation events remains unclear. Marine sedimentary rocks hold great potential for the reconstruction of Precambrian atmospheric and oceanic redox evolution. However, most of the currently available information has been derived from deep-water sedimentary rocks.

This thesis presents geochemical investigations – chemical fingerprints - of microbial carbonates spanning from Palaeoarchaean to Cambrian in age. The samples have demonstrably formed in *shallow* water. Several types of geochemical proxies, including non-vital trace metals, redox sensitive vital metals, and S-isotopes were analysed to study their response to Earth's oxidation. The work has revealed the following new insights: there is a clear temporal evolution of reduced carbon and pyrite preservation; microbial carbonate-hosted pyrite chemistry mirrors that of black shale-hosted pyrite and confirms changes in fluxes to the ocean with time; S-isotopes in the Neoarchaean ocean record local signals and the S-cycle of that time can be compared to the atmospheric Pb pollution event of the 19th and 20th centuries; and microbial carbonates differ from sponge skeletons in trace element distribution.

The emerging picture is that MIF S-isotope anomalies disappeared exactly during the Huronian glaciation reflecting the initial build-up of free oxygen (and ozone) in the atmosphere, resulting in a reorganisation of the greenhouse structure, causing the icehouse. Thus, the initial oxidation of Earth's surface is not likely an expression of biological evolution, but a response to the global geological functioning of our planet. The Neoproterozoic global glaciations are currently attributed to a tectonic context. However, the findings from this thesis suggest that metazoans could have appeared in the deep Cryogenian, and that they may have contributed to the ventilation of the ocean in the Neoproterozoic oxidation event. Thus the possibility arises that the Neoproterozoic glaciations could have been caused by the rise of metazoans rather than the other way round.

Acknowledgements

I would like to express my sincere appreciation to my PhD supervisor Balz Kamber, for his unwavering support and mentorship throughout this project. Without his continuous guidance this work would not have been possible. I am also grateful to all the lecturers in the TCD Geology Department, especially Patrick Wyse Jackson and George Sevastopulo for their helpful discussions and support. I would also like to thank the geology department's technical and administrative staff; Mags Duncan, Frank Hendron, Neil Kearney, Noel McGinley and Maura Morgan, for their constant support throughout the past three and a half years. In particular, I would like to thank Cora McKenna for her support and guidance in the laboratory, and I thank Claire Kamber for beautifully drafting figures to illustrate this research. I would also like to thank my friends and colleagues in the TCD Geology department for their encouragement and moral support, which made my time as a PhD student more enjoyable.

For all my friends and extended family, I am really grateful to them for their endless encouragement and support. I would like to express deep appreciation for my parents Siofra and Frank, my brothers Darragh and Tadhg, and my sister Caoimhe, for their steadfast support. Finally, I would like to thank Dean Redmond for his unwavering support and understanding, for which I am truly grateful.

Table of Contents

Chapter 1: Introduction……1

1.1 Context of Thesis ……1

1. 2. Layout and Themes of the Thesis……5

1.3 Co-author Statement……7

Chapter 2: The rare earth element signal in Archaean microbial carbonate: information on ocean redox and biogenicity……16

Abstract……16

1. Introduction……17

1.1. Historical perspective……17

1.2. The establishment of microbial carbonates as proxies for Precambrian seawater geochemistry……18

1.3. Scope of this contribution……19

2. Methods and Sample Details……20

2.1. REE and Y analysis……20

2.2. Sample details……24

3. REE as environmental and redox proxies……28

3.1. Hydrogenous signals versus contaminants……28

3.2. Reconstruction of the depositional environment……34

3.3. The redox evolution of the Archaean ocean……39

4. REE inventories as possible biomarkers……48

4.1. Information from Phanerozoic microbial carbonates……48

4.2. New information from Neoarchaean microbial carbonates……49

4.3. Origin of the preferential REE+Y uptake into microbial carbonate….56

5. Summary……58

Acknowledgements……60

References……61

Chapter 3: In-situ trace metal analysis of Neoarchaean – Ordovician Shallow-Marine Microbial-Carbonate-Hosted Pyrites……75

Abstract……75

1. Introduction……77

1.1. The biological sulphur cycle……77

1.2. Historical perspective on ocean - atmosphere oxygenation……78

1.3. Oceanic Fe and S sources through time……81

1.4. Context of this study……84

2. Sample Selection and Analysis……86

2.1. Sample Selection – General Requirements……86

2.2. Laser Ablation Inductively Coupled Plasma Mass Spectrometry (LA-ICP-MS) ……88

3. Material……91

4. Results……96

4.1. Sulphide occurrences in shallow-marine microbial carbonates……96

4.2. Trace metal distribution in pyrite……99

4.3. Pyrite trace metal temporal patterns……101

5. Discussion……107

5.1. Pyrite occurrence……107

5.2. Pyrite trace metal substitution and temporal trends……..……..109

6. Summary……117

Acknowledgements……120

References……121

7. Supporting Information……137

Chapter 4: The Neoarchaean surficial sulphur cycle: analogies with 20th century atmospheric lead……142

Abstract……142

1. Introduction……144

2. Materials……149

3. Methods……149

4. Results……151

4.1. The 20th century atmospheric lead analogy……..……155

5. Discussion……158

5.1. The significance of the non-zero $\Delta^{33}S$ - $\delta^{34}S$ intercept……158

5.2. The significance of the wide range in Neoarchaean $\Delta^{33}S$……..162

5.3. The Neoarchaean positive $\Delta^{33}S$ bias……..……164

6. Conclusions……166

Acknowledgements……168

References……169

7. Supporting Information……179

Chapter 5: 2D Chemical Visualisations of Neoproterozoic Little Dal Group Polymud Fabrics and Spongiform Structures. ……188

1. Introduction……188

2. Materials……193

3. Methods……194

4. Results……197

4.1. Little Dal Group Samples……198

4.2. Cretaceous Sponge……210

4.3. Silurian Sponge……214

5. Discussion……219

5.1. Little Dal Group Polymud Fabrics……219

5.2. Little Dal Group Spongiform Structures vs. Cretaceous and Silurian Sponge Geochemistry……220

5.3. Origin and Significance of the Little Dal Group Spongiform Structures……222

6. Summary and Conclusions……223

References……225

Chapter 6: Synthesis……233

References……239

Chapter 1: Introduction

1.1 Context of Thesis

Life on earth is an ancient phenomenon, probably dating from at least 3.5 Ga (Allwood et al., 2006), with a recent study suggesting it may have emerged as far back as 4.1 Ga (Bell et al., 2015). The Archaean Earth was characterised by an anoxic surface environment and an anoxic ocean containing low sulphate concentrations (Walker & Brimblecombe, 1985), but by the Neoarchaean there is abundant evidence for life, including the common occurrence of well-developed stromatolites (Nisbet & Sleep, 2001). The evolution of oxygenic photosynthesis in the Neoarchaean (Grassineau et al., 2001; Farquhar et al., 2011) could essentially have provided the source of all oxygen in the atmosphere, and most bacterial biodiversity likely emerged along with the evolution of oxygenic photosynthesis (Canfield & Raiswell, 1999; Kurzweil et al., 2013). However, the Earth's atmospheric oxygenation was apparently achieved in two sharp steps; the 'Great Oxidation Event' or GOE, at the beginning of the Proterozoic eon; and the 'Neoproterozoic Oxidation Event' or NOE, towards the very end of the Proterozoic eon. Both of these events profoundly shaped the Earth, fundamentally altering global biogeochemical cycles, and ultimately paving the way for the rise of complex animals at the beginning of the Cambrian.

The GOE left clear fingerprints in the rock record; the destabilisation of O-sensitive minerals (e.g. pyrite and uraninite) at the Earth's surface (Rasmussen & Buick, 1999; England et al., 2002), the first appearance of red beds and Fe-rich paleosols (Cloud, 1968; Rye & Holland, 1998), and the first substantial accumulation of oxyanion-forming elements (e.g. S, U, Mo) in the oceans (Canfield, 1998; Collerson & Kamber, 1999; Scott et al., 2008), all converging in support of a transition from a reducing to oxidising atmosphere after ca. 2.4 Ga. The sulphur cycle also underwent a profound change after the GOE with a marked increase in seawater sulphate due to an increased flux of sulphate to the oceans from oxidatively weathered terrestrial sulphides (Canfield, 2004). The sulphur isotope record supports free oxygen in the atmosphere at ca. 2.32 Ga. The absence of an ozone screen in the pre-GOE anoxic atmosphere resulted in UV transparency and allowed for the photochemical production of mass independently fractionated (MIF) S-isotope anomalies, and their

preservation in the rock record (Farquhar et al., 2000; Farquhar et al., 2001; Pavlov & Kasting, 2002). The disappearance of MIF S-isotope anomalies at ca. 2.32 Ga (Farquhar et al., 2000; Bekker et al., 2004; Papineau et al., 2007) signifies the departure from the persistently low atmospheric oxygen levels, probably < 10^{-5} times the present atmospheric level (Pavlov & Kasting, 2002), that dominated the earlier Earth and is now cited as one of the strongest lines of evidence for the GOE (Lyons et al., 2014).

Comparatively large amounts of methane (CH_4) were produced, and persisted under the low sulphate (SO_4^{2-}) conditions of the Achaean ocean, and the low oxygen concentrations in the pre-GOE atmosphere (Pavlov et al., 2000; Habicht et al., 2002; Haqq-Misra et al., 2008; Jamieson et al., 2013). At that time, a greater amount of organic matter was available for methane production (methanogenesis) in the absence of oxygen and sulphate in the pre-GOE ocean (Lyons et al., 2014). It is possible that the post-GOE rise in atmospheric oxygen concentration eliminated the methane greenhouse, leading to the onset of global cooling (Melezhik, 2006), geologically expressed as the Huronian glaciations. However, in detail, questions remain about the causes and consequences of the Huronian glaciations, which occurred stratigraphically before the first red beds (Evans et al., 1997). Others have argued that the rise of oxygen was not the single cause of the Huronian glaciations. At ca. 2450 Ma, mantle-plume driven continental uplifts led to the emplacement of voluminous continental flood-basalts at low-latitudes (Kamber, 2010). Consumption of atmospheric CO_2 by silicate weathering of these fresh basaltic surfaces, combined with the diminished methane greenhouse, may also have contributed towards plunging the Earth into its first global glaciation (Melezhik, 2006).

Although the oxidation of the Earth's atmosphere began in earnest from ca. 2.4 Ga, the full ventilation of the ocean was a much more prolonged process (Lyons et al., 2014). Canfield championed the idea that the oxygenation of the deep ocean lagged behind the oxygenation of the atmosphere by almost two billion years (Canfield, 1998). Multiple geochemical studies point to a global oxygen deficiency in the deep-ocean, and euxinia during most, if not all, of the Proterozoic (Canfield, 1998; Raiswell & Canfield, 1998; Canfield, 2004; Lyons et al., 2009). In detail, the Mesoproterozoic and Neoproterozoic oceans may have repeatedly switched between a sulphidic and ferruginous state (Canfield et al., 2008; Poulton & Canfield, 2011), or may have had a

spatial distribution of euxinic conditions controlled by organic matter production and burial (Planavsky et al., 2011). Worldwide distribution of Neoproterozoic glacial deposits provide evidence for two episodes of long lived glaciation: the Sturtian (ca. 720 - 660 Ma) and the Marinoan (ca. 650 - 635 Ma), both showing evidence of glaciers in tropical palaeolatitudes, and are likely to have been of global extent (Halverson et al., 2005; Halverson, 2006; Fairchild & Kennedy, 2007).

Most geochemical proxies indicate that atmospheric oxygen levels remained low until a second rise in atmospheric oxygen, to concentrations comparable to modern values during the NOE at ca. 580 - 548 Ma (e.g. Fike et al., 2006; Canfield et al., 2007; Scott et al., 2008; Och & Shields-Zhou, 2012). However, current estimates for mid-Proterozoic atmospheric oxygen levels during the billion years leading up to the NOE vary widely (Planavsky et al., 2014; Zhang et al., 2016). Whereas the geological record strongly associates the second step-change in atmospheric oxygenation with the latest Neoproterozoic, geochemical proxies reveal an altogether more complicated picture suggesting a complex redox evolution through the latter half of the Mesoproterozoic and throughout the Neoproterozoic. Regardless, after the NOE, atmospheric free oxygen levels were apparently high enough to permit oxidation of deep waters and ventilation of the deep-ocean (Canfield & Raiswell, 1999; Och & Shields-Zhou, 2012) and establishment of the sediment mixed layer between the Ediacaran and base of the Cambrian (Callow & Brasier, 2009), when complex life forms started to radiate and when oxygen rose to levels significant enough to support relatively large, active, biomineralizing metazoans (Mills & Canfield, 2014).

Although the GOE and the NOE provide a rationale for the overall evolution of Earth, in detail many discrepancies remain. The geological expression of the GOE is very pronounced (Cloud, 1968; Rye & Holland, 1998; Rasmussen & Buick, 1999; England et al., 2002), and initially geochemistry seemed to support an equally sharp expression (e.g. Holland, 1994). However, as more studies were undertaken the idea of a single 'event' is no longer favoured, and discrepancies among geochemical proxies of the GOE suggest a more complex and longer pathway to oxidation (e.g. Anbar et al., 2007; Scott et al., 2008). However, before the idea of a sharp initial rise of atmospheric oxygen at the GOE is abandoned in favour of a series of 'whiffs' of oxygenation, we remind ourselves that the various geochemical proxies are

ambiguous regarding the timing of these whiffs, that MIF S-isotope data do not support a breakdown of the ozone layer before the GOE, and that oxygen is by no means the only electron acceptor that was available to drive electron transfers in the Archaean ocean. Furthermore, surprisingly, most geochemical evidence for pre-GOE oxygenation events were postulated on the basis of analysis of deep water sediments (e.g. Anbar et al., 2007; Scott et al., 2008; Konhauser et al., 2009; Large et al., 2014).

This thesis presents geochemical investigations of microbial carbonates (and microbial-carbonate-hosted pyrite) that have demonstrably formed in *shallow* water environments (typically above storm wave base), undertaken to contribute to the understanding of the Earth's oxidation in terms of the shallow marine environment. Several types of geochemical proxies, including non-vital trace metals, redox sensitive vital metals, and S-isotopes were applied and analysed to study their response to the GOE.

As far as the NOE is concerned, a troubling inconsistency lies in the timing of the emergence of metazoans (e.g. Knoll & Carroll, 1999). The Ediacaran period (Knoll et al., 2006) is defined as the time between the end of the Marinoan glaciation (635 Ma) and the base of the Cambrian (543 Ma) and preserves the appearance of conspicuously macroscopic, metazoan fossils particularly from ca. 575 Ma onwards. If they represented the first metazoans, and the NOE coincided with the end-Marinoan (e.g. Och & Shields-Zhou, 2012) the relationship between Cryogenian glaciations and biological evolution would not be obvious. However, phylogenomic studies and molecular clock estimates place the origin of the crown metazoan deep within, or even before the Cryogenian, (Dunn et al., 2008; Peterson et al., 2008; Sperling et al., 2010; Erwin et al., 2011), in the range of 833-650 Ma (dos Reis et al., 2015). Recent experiments with demosponges (Mills et al., 2014) indicate that potential relatives of these basic metazoans could have survived in an ocean under an only very mildly oxygenated atmosphere. Thus, metazoans could have predated the Cryogenian, and biological evolution may thus even have contributed to the climatic reasons for global glaciations. But evidence for Cryogenian sponge fossils is rare, poorly substantiated and widely disputed (e.g. Love et al., 2009; Neuweiler et al., 2009; Maloof et al., 2010). Thus, it remains unclear weather the appearance of animals is linked to a change in environmental oxygen levels, or whether this dramatic shift in the complexity of the biosphere reflects the timing of genetic and developmental innovation independent of

any environmental control. Detailed understanding of these cause-effect relations regarding the emergence of metazoans are lacking, largely due to the unsubstantiated nature of Cryogenian sponge fossils. For this thesis, the oldest, most controversial, pre-Sturtian putative sponge fossils (Neuweiler et al., 2009) were revisited with a novel approach to geochemical analysis in the expectation to provide a firmer idea of their origin.

1. 2. Layout and Themes of the Thesis

The principle objective of this PhD project was to produce a number of peer-reviewed publications/manuscripts while also satisfying the remit of the FP7 Career Integration Grant (to Balz Kamber), which provided the funding for my PhD. With this context in mind, a number of independent projects were defined, each forming a core chapter of the thesis. Because of the manuscript nature of these chapters, readers will find variably comprehensive introductions included in each. The conclusions of each chapter are also self-contained, and only after the last core chapter, readers are presented with a summarising conclusion and outlook. The publication status of each chapter is identified at the outset and the content is presented as available from the publisher, but formatted for the thesis.

Chapter 2 provides a comprehensive summary of the importance of microbial carbonates as proxies for aspects of Precambrian seawater chemistry. It focuses in particular on how REE can be used to reconstruct aspects of Earth's surface environment as well as the depositional environment in which stromatolites have formed in the past. The studied stromatolites range in age from 2.52 - 3.45 Ga, and are shown to record shallow-water information complementary to deep ocean proxies such as banded iron formation and black shale. The REE characterisation of ancient carbonates detailed in this chapter is an essential first step to take ahead of more sophisticated further geochemical investigations, such as redox-sensitive element analysis, stable metal isotope analysis, or multiple-S isotope analysis.

Chapter 3 presents the first comprehensive petrographic and geochemical study of pyrite hosted in microbial carbonates. Earlier recent studies (e.g. Large et al., 2014) have focussed on black-shale hosted pyrite. These papers proposed that atmospheric and oceanic redox evolutions are expressed in the inventories of redox-sensitive trace metals in marine sedimentary rocks, however, most of the previously

available information is relevant to the deep ocean and these papers only indirectly inferred element fluxes from land and redox state of the shallow marine environment. Here, the first systematic study of trace metal inventories of the shallow marine environment is presented through analysis of microbial-carbonate-hosted pyrite, from ca. 2.65 - 0.52 Ga.

In Chapter 4, I revisited microbial carbonate-hosted pyrite, but this time investigating the isotopic composition of sulphur in the near surface pre-GOE environment. In situ SIMS quadruple S-isotope data for sedimentary pyrite from the ca. 2.52 Ga Upper Campbellrand Subgroup, Transvaal South Africa are reported and a novel interpretation for the large range of Neoarchaean mass-independent S-isotope fractionation is advanced. The new hypothesis builds on a comparison with the 20th century atmospheric lead contamination event. I also propose a new explanation for non-zero intercept $\delta^{34}S_{V\text{-}CDT}$ - $\Delta^{33}S$ data arrays defined by some Neoarchaean samples, suggesting that very localised S-isotope signatures could have existed in the Neoarchaean surface environment.

The study presented in Chapter 5 is entirely devoted to enigmatic carbonate structures (Neuweiler et al., 2009) preserved in pre-Sturtian, mid-Neoproterozoic limestones of the Little Dal Group in NW Canada. Having earlier studied carbonate-hosted pyrite in Chapter 3, I realised that contrary to the common belief that the inventory of chalcophile elements would be dominated by sulphides, carbonate and carbonate-hosted reduced C are actually the dominant hosts of most of these redox-sensitive elements. This is particularly true for post-GOE carbonates, which are significantly poorer in preserved pyrite than older samples. For this reason, it appeared feasible to test whether the distribution of redox-sensitive trace metals in carbonate fabrics might shed light on the origin of the enigmatic fabrics found in the mid-Neoproterozoic samples and compare them with bona fide younger calcified sponges, with which they had been compared (Neuweiler et al., 2009). Thus, Chapter 5 presents the first detailed 2D trace element maps for such materials. The maps were obtained with the LA-ICP-MS mapping technique that has recently been refined in our laboratory (Ubide et al., 2015). Although the study did not yield conclusive results, it provides a range of new evidence that is compatible with the idea that the origin of sponges pre-dates the NOE. The proposed analytical approach will also lend

itself to the study of other Neoproterozoic putative sponges (Maloof et al., 2010; Brain et al., 2012).

Chapter 6 is a synthesis of the insight gained from the research presented in the core chapters of the thesis and the wider implications of the new findings to the study of the redox evolution of the atmosphere and hydrosphere in terms of the shallow marine environment, and to the study of life evolution on earth and the timing of the emergence of metazoans.

1.3 Co-author Statement

The four core chapters (2-5) of this thesis consist of two published papers and two submitted manuscripts, all of which are multi-authored. I am the lead author of three of these works. I wrote the lead-authored manuscripts in their entirety. The roles of the co-authors consisted of: providing samples and understanding of the geological and sedimentological context; providing expert advice and guidance on analytical work; and help with putting my interpretations into the deep time planetary context. The detailed roles are explained below.

Martin Whitehouse, Swedish Museum of Natural History, Stockholm, was involved in the S-isotope aspect of this thesis, by providing guidance throughout stages of sample preparation, analysis, data reduction at the Nordsim Laboratory, as well as editorial comments on Chapter 4.

Elizabeth Turner, Laurentian University, Sudbury, provided samples and field context of the Bylot Supergroup, Haematite Creek Group, Little Dal Group, Snake Indian Formation, Cathedral Formation, and Saint-Roch Formation samples, as well as editorial comments on chapters involving these samples (Chapters 3, and 5).

Fritz Neuweiler, University of Laval, Quebec, provided samples from the lower Cretaceous Iraneta and lower Silurian Gaspé sponge material, as well as discussion of Chapter 5.

Balz Kamber, my PhD advisor, was the main discussion partner for the interpretation of my data and provided editorial comments to the manuscripts. He is the first author of the article that constitutes Chapter 2. My contribution to this paper was to perform detailed petrography and in-situ geochemical analyses of the

Neoarchaean samples used in the study. I performed all of the LA-ICP-MS analyses, crafted figures 8, 9 and 10, provided editorial input into the manuscript and addressed some of the reviewer and editorial comments.

References

Allwood AC, Walter MR, Kamber BS, Marshall CP, Burch IW (2006) Stromatolite reef from the Early Archaean era of Australia. *Nature,* 441, 714-718.

Anbar AD, Duan Y, Lyons TW, Arnold GL, Kendall B, Creaser RA, Kaufman AJ, Gordon GW, Scott C, Garvin J (2007) A whiff of oxygen before the great oxidation event? *Science,* 317, 1903-1906.

Bekker A, Holland H, Wang P-L, Rumble D, Stein H, Hannah J, Coetzee L, Beukes N (2004) Dating the rise of atmospheric oxygen. *Nature,* 427, 117-120.

Bell EA, Boehnke P, Harrison TM, Mao WL (2015) Potentially biogenic carbon preserved in a 4.1 billion-year-old zircon. *Proceedings of the National Academy of Sciences,* 112, 14518-14521.

Brain CB, Prave AR, Hoffmann K-H, Fallick AE, Botha A, Herd DA, Sturrock C, Young I, Condon DJ, Allison SG (2012) The first animals: ca. 760-million-year-old sponge-like fossils from Namibia. *South African Journal of Science,* 108, 01-08.

Callow RHT, Brasier MD (2009) Remarkable preservation of microbial mats in Neoproterozoic siliciclastic settings: Implications for Ediacaran taphonomic models. *Earth-Science Reviews,* 96, 207-219.

Canfield D (1998) A new model for Proterozoic ocean chemistry. *Nature,* 396, 450-453.

Canfield DE (2004) The evolution of the Earth surface sulfur reservoir. *American Journal of Science,* 304, 839-861.

Canfield DE, Poulton SW, Knoll AH, Narbonne GM, Ross G, Goldberg T, Strauss H (2008) Ferruginous conditions dominated later Neoproterozoic deep-water chemistry. *Science,* 321, 949-952.

Canfield DE, Poulton SW, Narbonne GM (2007) Late-Neoproterozoic deep-ocean oxygenation and the rise of animal life. *Science,* 315, 92-95.

Canfield DE, Raiswell R (1999) The evolution of the sulfur cycle. *American Journal of Science,* 299, 697-723.

Cloud PE (1968) Atmospheric and Hydrospheric Evolution on the Primitive Earth Both secular accretion and biological and geochemical processes have affected earth's volatile envelope. *Science,* 160, 729-736.

Collerson KD, Kamber BS (1999) Evolution of the continents and the atmosphere inferred from Th-U-Nb systematics of the depleted mantle. *Science,* 283, 1519-1522.

Dos Reis M, Thawornwattana Y, Angelis K, Telford MJ, Donoghue PC, Yang Z (2015) Uncertainty in the Timing of Origin of Animals and the Limits of Precision in Molecular Timescales. *Current Biology,* 25, 2939-2950.

Dunn CW, Hejnol A, Matus DQ, Pang K, Browne WE, Smith SA, Seaver E, Rouse GW, Obst M, Edgecombe GD (2008) Broad phylogenomic sampling improves resolution of the animal tree of life. *Nature,* 452, 745-749.

England GL, Rasmussen B, Krapez B, Groves DI (2002) Palaeoenvironmental significance of rounded pyrite in siliciclastic sequences of the Late Archaean Witwatersrand Basin: oxygen-deficient atmosphere or hydrothermal alteration? *Sedimentology,* 49, 1133-1156.

Erwin DH, Laflamme M, Tweedt SM, Sperling EA, Pisani D, Peterson KJ (2011) The Cambrian conundrum: early divergence and later ecological success in the early history of animals. *Science,* 334, 1091-1097.

Evans DA, Beukes NJ, Kirschvink JL (1997) Low-latitude glaciation in the Palaeoproterozoic era. *Nature,* 386, 262-266.

Fairchild IJ, Kennedy MJ (2007) Neoproterozoic glaciation in the Earth System. *Journal of the Geological Society,* 164, 895-921.

Farquhar J, Bao H, Thiemens M (2000) Atmospheric influence of Earth's earliest sulfur cycle. *Science,* 289, 756-758.

Farquhar J, Savarino J, Airieau S, Thiemens MH (2001) Observation of wavelength‐sensitive mass‐independent sulfur isotope effects during SO2 photolysis: Implications for the early atmosphere. *Journal of Geophysical Research: Planets (1991–2012),* 106, 32829-32839.

Farquhar J, Zerkle A, Bekker A (2011) Geological constraints on the origin of oxygenic photosynthesis. *Photosynth Res,* 107, 11-36.

Fike D, Grotzinger J, Pratt L, Summons R (2006) Oxidation of the Ediacaran ocean. *Nature,* 444, 744-747.

Grassineau N, Nisbet E, Bickle M, Fowler C, Lowry D, Mattey D, Abell P, Martin A (2001) Antiquity of the biological sulphur cycle: evidence from sulphur and carbon isotopes in 2700 million–year–old rocks of the Belingwe Belt, Zimbabwe. *Proceedings of the Royal Society of London. Series B: Biological Sciences,* 268, 113-119.

Habicht KS, Gade M, Thamdrup B, Berg P, Canfield DE (2002) Calibration of Sulfate Levels in the Archean Ocean. *Science,* 298, 2372-2374.

Halverson GP (2006) A Neoproterozoic chronology. In: *Neoproterozoic geobiology and paleobiology*. Springer, pp. 231-271.

Halverson GP, Hoffman PF, Schrag DP, Maloof AC, Rice AHN (2005) Toward a Neoproterozoic composite carbon-isotope record. *Geological Society of America Bulletin,* 117, 1181-1207.

Haqq-Misra JD, Domagal-Goldman SD, Kasting PJ, Kasting JF (2008) A revised, hazy methane greenhouse for the Archean Earth. *Astrobiology,* 8, 1127-1137.

Holland H (1994) Early Proterozoic atmospheric change. *Early life on earth*, 237-244.

Jamieson JW, Wing BA, Farquhar J, Hannington MD (2013) Neoarchaean seawater sulphate concentrations from sulphur isotopes in massive sulphide ore. *Nature Geosci,* 6, 61-64.

Kamber BS (2010) Archean mafic–ultramafic volcanic landmasses and their effect on ocean–atmosphere chemistry. *Chemical Geology,* 274, 19-28.

Knoll A, Walter M, Narbonne G, Christie‐Blick N (2006) The Ediacaran Period: a new addition to the geologic time scale. *Lethaia,* 39, 13-30.

Knoll AH, Carroll SB (1999) Early animal evolution: emerging views from comparative biology and geology. *Science,* 284, 2129-2137.

Konhauser KO, Pecoits E, Lalonde SV, Papineau D, Nisbet EG, Barley ME, Arndt NT, Zahnle K, Kamber BS (2009) Oceanic nickel depletion and a methanogen famine before the Great Oxidation Event. *Nature,* 458, 750-753.

Kurzweil F, Claire M, Thomazo C, Peters M, Hannington M, Strauss H (2013) Atmospheric sulfur rearrangement 2.7 billion years ago: Evidence for oxygenic photosynthesis. *Earth and Planetary Science Letters,* 366, 17-26.

Large RR, Halpin JA, Danyushevsky LV, Maslennikov VV, Bull SW, Long JA, Gregory DD, Lounejeva E, Lyons TW, Sack PJ (2014) Trace element content of sedimentary pyrite as a new proxy for deep-time ocean–atmosphere evolution. *Earth and Planetary Science Letters,* 389, 209-220.

Love GD, Grosjean E, Stalvies C, Fike DA, Grotzinger JP, Bradley AS, Kelly AE, Bhatia M, Meredith W, Snape CE (2009) Fossil steroids record the appearance of Demospongiae during the Cryogenian period. *Nature,* 457, 718-721.

Lyons TW, Anbar AD, Severmann S, Scott C, Gill BC (2009) Tracking euxinia in the ancient ocean: a multiproxy perspective and Proterozoic case study. *Annual Review of Earth and Planetary Sciences,* 37, 507-534.

Lyons TW, Reinhard CT, Planavsky NJ (2014) The rise of oxygen in Earth/'s early ocean and atmosphere. *Nature,* 506, 307-315.

Maloof AC, Porter SM, Moore JL, Dudás FÖ, Bowring SA, Higgins JA, Fike DA, Eddy MP (2010) The earliest Cambrian record of animals and ocean geochemical change. *Geological Society of America Bulletin,* 122, 1731-1774.

Melezhik VA (2006) Multiple causes of Earth's earliest global glaciation. *Terra Nova,* 18, 130-137.

Mills DB, Canfield DE (2014) Oxygen and animal evolution: Did a rise of atmospheric oxygen "trigger" the origin of animals? *BioEssays,* 36, 1145-1155.

Mills DB, Ward LM, Jones C, Sweeten B, Forth M, Treusch AH, Canfield DE (2014) Oxygen requirements of the earliest animals. *Proceedings of the National Academy of Sciences,* 111, 4168-4172.

Neuweiler F, Turner EC, Burdige DJ (2009) Early Neoproterozoic origin of the metazoan clade recorded in carbonate rock texture. *Geology,* 37, 475-478.

Nisbet E, Sleep N (2001) The habitat and nature of early life. *Nature,* 409, 1083-1091.

Och LM, Shields-Zhou GA (2012) The Neoproterozoic oxygenation event: environmental perturbations and biogeochemical cycling. *Earth-Science Reviews,* 110, 26-57.

Papineau D, Mojzsis SJ, Schmitt AK (2007) Multiple sulfur isotopes from Paleoproterozoic Huronian interglacial sediments and the rise of atmospheric oxygen. *Earth and Planetary Science Letters,* 255, 188-212.

Pavlov A, Kasting J (2002) Mass-independent fractionation of sulfur isotopes in Archean sediments: strong evidence for an anoxic Archean atmosphere. *Astrobiology,* 2, 27-41.

Pavlov AA, Kasting JF, Brown LL, Rages KA, Freedman R (2000) Greenhouse warming by CH4 in the atmosphere of early Earth. *Journal of Geophysical Research: Planets (1991–2012),* 105, 11981-11990.

Peterson KJ, Cotton JA, Gehling JG, Pisani D (2008) The Ediacaran emergence of bilaterians: congruence between the genetic and the geological fossil records. *Philosophical Transactions of the Royal Society B: Biological Sciences,* 363, 1435-1443.

Planavsky NJ, Mcgoldrick P, Scott CT, Li C, Reinhard CT, Kelly AE, Chu X, Bekker A, Love GD, Lyons TW (2011) Widespread iron-rich conditions in the mid-Proterozoic ocean. *Nature,* 477, 448-451.

Planavsky NJ, Reinhard CT, Wang X, Thomson D, Mcgoldrick P, Rainbird RH, Johnson T, Fischer WW, Lyons TW (2014) Low Mid-Proterozoic atmospheric oxygen levels and the delayed rise of animals. *science,* 346, 635-638.

Poulton SW, Canfield DE (2011) Ferruginous conditions: a dominant feature of the ocean through Earth's history. *Elements,* 7, 107-112.

Raiswell R, Canfield DE (1998) Sources of iron for pyrite formation in marine sediments. *American Journal of Science,* 298, 219-245.

Rasmussen B, Buick R (1999) Redox state of the Archean atmosphere: evidence from detrital heavy minerals in ca. 3250–2750 Ma sandstones from the Pilbara Craton, Australia. *Geology,* 27, 115-118.

Rye R, Holland HD (1998) Paleosols and the evolution of atmospheric oxygen: a critical review. *American Journal of Science,* 298, 621-672.

Scott C, Lyons T, Bekker A, Shen Y, Poulton S, Chu X, Anbar A (2008) Tracing the stepwise oxygenation of the Proterozoic ocean. *Nature,* 452, 456-459.

Sperling E, Robinson J, Pisani D, Peterson K (2010) Where's the glass? Biomarkers, molecular clocks, and microRNAs suggest a 200‐Myr missing Precambrian fossil record of siliceous sponge spicules. *Geobiology,* 8, 24-36.

Ubide T, Mckenna CA, Chew DM, Kamber BS (2015) High-resolution LA-ICP-MS trace element mapping of igneous minerals: In search of magma histories. *Chemical Geology,* 409, 157-168.

Walker JC, Brimblecombe P (1985) Iron and sulfur in the pre-biologic ocean. *Precambrian Research,* 28, 205-222.

Zhang S, Wang X, Wang H, Bjerrum CJ, Hammarlund EU, Costa MM, Connelly JN, Zhang B, Su J, Canfield DE (2016) Sufficient oxygen for animal respiration 1,400 million years ago. *Proceedings of the National Academy of Sciences*, 201523449.

Chapter 2: The rare earth element signal in Archaean microbial carbonate: information on ocean redox and biogenicity

Published in Journal of the Geological Society, London (2014, Vol. 171, 745-763)
Authors: Balz S. Kamber, Gregory E. Webb, Meabh Gallagher

Abstract

Microbial carbonates contain valuable chemical, isotopic and molecular information regarding the Precambrian Earth. They record shallow water information complementary to deep ocean proxies, like banded iron formation and black shale. Five groups of well-preserved stromatolites illustrate how the rare earth elements (REE) are used for chemical investigation. The first task is to test whether the REE inventory of carbonate is compromised by clastic, volcanic, or diagenetic contaminants. Once the cleanliness has been verified, the shale-normalised REE pattern can be used to distinguish between marine and lacustrine settings. For marine carbonates, it is possible to distinguish between restricted basin vs. open marine settings and for thick platform limestones the relative water depth can be inferred from REE systematics. The studied shallow water stromatolites range in age from 2.52 to 3.45 Ga. They contain no evidence from the behaviour of the redox-sensitive element cerium that free oxygen levels in the shallow sea approached levels beyond a trace gas by 2.52 Ga. Compared to abiotic early diagenetic marine carbonate cements, microbial carbonate is strongly enriched in REE. This may itself not yet serve as a biomarker, but it is regarded as a necessary pre-requisite for a sample to qualify for biomarker studies.

1. Introduction

1.1. Historical perspective

Stromatolites can form spectacular structures and represent the most conspicuous type of microbial carbonate. Notwithstanding their rise to prominence in the geological literature relevant to the early Earth (e.g. Hoffman, 1967; Awramik, 1971; Walter, 1977), attempts at retrieving geochemical information from these archives lagged behind the study of the other Precambrian hydrogenous sediments (banded iron formation (BIF) and chert). Early geochemical studies focussed on the most accessible isotopic information, namely the stable C- and O-isotope composition of carbonate (and where available, co-existing reduced C) and radiogenic Sr-isotope composition. The early C-isotope studies of Archaean stromatolites (e.g. Schopf et al., 1971; Veizer and Hoefs, 1976; Hayes et al., 1983; Abell et al., 1985a&b; Beukes et al., 1990) discovered that carbonate C-isotopes clustered tightly around $\delta^{13}C$ of zero, not deviating from modern values. In their study of kerogen C in the superbly preserved Neoarchaean Bulawayan stromatolites (Zimbabwe), Schopf et al. (1971) reported a ca. $\delta^{13}C$ -33‰ for reduced C. Similarly, in the equally well-preserved Neoarchaean Cheshire Formation stromatolites (Belingwe greenstone belt, Zimbabwe), Abell et al. (1985b) confirmed very light isotope compositions ($\delta^{13}C$ -25 to -35) of kerogen. Equally light C had also been measured in Precambrian graphite extracted from clastic and chemical sediments (e.g. Oehler et al., 1972; Schoell and Wellmer, 1981). Such isotopically light C had, at the time, been interpreted by some as anomalous given the absence of a terrestrial flora (Towe, 1982) unless the CO_2 pressure in the early atmosphere was much higher. More modern studies, most notably by Nisbet and co-workers (e.g. Nisbet and Sleep, 2001; Grassineau et al., 2001, 2002, 2006) have since established that the modern C cycle was already operational during much of the Archaean.

An interesting and possibly underappreciated finding of the pioneering work of Abell et al. (1985b) on the superb stromatolites of the Cheshire Formation was that O-isotope compositions did not correlate with Sr content. This is important for two reasons. Firstly, because it argues against diagenetic overprinting with meteoric waters and implies that the stromatolite carbonate may retain original information regarding the seawater temperature and/or the O-isotope composition

of the Neoarchaean ocean. Secondly, and more relevant to the theme of the present contribution, the low Sr content of the microbial calcite (typically between 100 and 200 ppm) could be an original feature of the microbial limestone. By comparison, modern skeletal carbonates, particularly aragonitic coral, contain several thousand ppm of Sr (e.g. Corrège, 2006). Similar findings of ca. 50 to 300 ppm Sr content in Precambrian carbonate (Veizer and Compston, 1976; Veizer et al., 1982) were interpreted to imply severe diagenetic or later modification of the trace element inventory and may have contributed to the general scepticism towards using stromatolites for the purpose of extracting environmental information via carbonate geochemistry. This reservation coupled with the wider availability of BIF deposits meant that most pioneering work on the rare earth element (REE) chemistry and Nd-isotope composition of the ancient ocean was derived from studies of BIF (e.g. Fryer 1977; Miller and O'Nions, 1985; Jacobsen and Pimentel-Klose, 1988; Derry and Jacobsen, 1990; Bau and Möller, 1993).

1.2. The establishment of microbial carbonates as proxies for Precambrian seawater geochemistry

Webb and Kamber (2010) recently published an extensive review of the use and limitations of microbial carbonate geochemistry. This provides interested geochemists with essential sedimentological, structural and biochemical background reading about the formation and preservation of microbial carbonate. Here we adopt their definition (p. 129) of microbial carbonates being "structures interpreted as having formed owing to the presence of a microbial mat or biofilm". Stromatolites are a subset of microbial carbonates and are recognised as containing laminated structures of biological origin.

The possibility that microbial carbonates might contain valid geochemical information about the depositional environment and possibly regarding the metabolism of the microbial community arose not only from the O- and C-isotope data of Schopf et al. (1971) and Abell et al. (1985b) but also from the discovery that certain stromatolites appear to retain an intact Pb-Pb isotope memory. Moorbath et al. (1987) successfully dated the Mushandike stromatolites (also from Zimbabwe) to 2839±33 Ma using a Pb-Pb regression age. Many more microbial carbonates have since been subjected to Pb-isotope study and the least metamorphosed have returned

geologically meaningful if somewhat imprecise ages (e.g. Woodhead and Hergt, 1997; Folling et al., 2000; Bolhar et al., 2002). Whereas the preservation of Pb-isotope systematics is strong evidence that the mobile cation Pb has remained undisturbed since lithification in least metamorphosed samples, the age dates are too imprecise to distinguish between depositional and diagenetic stages, allowing for the possibility of element mobility prior to lithification.

In view of its importance for geochemical signal preservation, the effect of diagenetic modification of carbonate chemistry has been investigated. Webb et al. (2009) established that during the neomorphism of calcite after original aragonite in Pleistocene scleractinian coral skeletons in a vadose meteoric setting, many trace elements changed as expected in relative and absolute concentrations (e.g. Sr, Ba and U were lost whereas Mn increased). However, it was also found that the REE survived this near-worst case scenario of diagenesis (i.e. neomorphism) largely intact. For this reason, the REE have assumed a prevalent role in attempts at reconstructing aspects of the ancient environment from microbial carbonates. One of the more compelling observations for the survival of original REE is the interpretable co-variation of Fe-isotope composition with REE systematics and water depth (inferred from sedimentology) in the Neoarchaean Campbellrand microbial carbonates of South Africa (von Blanckenburg et al., 2008). An important guiding principle of successful geochemical studies is that they need to be performed on samples that have an interpretable geological and sedimentological context. Geochemical information on its own is insufficient to interpret the origin of a fully recrystallised carbonate. For example, Johannesson et al. (2006) demonstrated that terrestrial neutral to alkaline waters (typically of high salinity) can have similar REE patterns as seawater and that for this reason, it is not straightforward to infer a marine origin for carbonates on the sole basis of seawater-like REE patterns. The data discussed and presented in this contribution are from microbial carbonates with overwhelming sedimentological evidence for a marine depositional setting unless otherwise noted.

1.3. Scope of this contribution

The main aim of this paper is to review the current state of knowledge regarding the REE chemistry of Archaean microbial carbonates and for this reason, no comprehensive summary of the pertinent literature is given in this introduction. In

the broadest sense, REE studies of hydrogenous sediments serve three purposes. Firstly, they aid establishment of whether a sample classified petrographically as a hydrogenous sediment is a primary precipitate or a secondary replacement product. This is particularly useful for BIF and chert, where the distinction between original depositional structures and secondary replacements is not trivial based on petrography alone (e.g. Thurston et al., 2012). Secondly, they allow inferences about the nature of the depositional setting of genuine hydrogenous sediments. The REE pattern of a hydrogenous sediment can permit the identification of freshwater vs. marine settings (e.g. Bolhar and Van Kranendonk, 2007), it can yield information about the relative water depth (e.g. Kamber and Webb, 2001) and it can identify proximity to hydrothermal vents (e.g. Allwood et al., 2010). Thirdly, a consistent empirical observation is beginning to emerge suggesting that microbial carbonate is often significantly enriched in REE relative to co-existing skeletal carbonates or abiogenic cement (Webb and Kamber, 2000; Kamber and Webb, 2001; Nothdurft et al., 2004; Kamber and Webb, 2007). In all these cases, the microbial carbonate has a very significantly elevated REE/Ca ratio not only over the co-existing carbonate but also over that of modern seawater.

The main scope of this contribution is two-fold. In the first part, we will review existing, and present new, REE data for well-preserved Archaean microbial carbonates and discuss them in the context of depositional setting, marine redox conditions and secular change in marine REE inventory over the ca. 1 billion years represented by the samples. In the second part, we will present new data for two Neoarchaean stromatolite occurrences to discuss the potential of REE inventories as possible biomarkers.

2. Methods and Sample Details

2.1. REE and Y analysis

The study of REE in hydrogenous sediments increased significantly in scope with the application of inductively-coupled-plasma mass-spectrometry (ICP-MS), as exemplified by the landmark publications of Bau and co-workers (Bau and Dulski, 1992, 1996; Bau 1993; Bau and Möller, 1993). The chief advantages over earlier studies employing isotope dilution techniques or instrumental neutron activation analysis are that the full suite of the REE as well as other trace elements can be

analysed and that the method has very low detection limits yielding precise and accurate data for elements present at ppb concentration levels. Complete REE and Y (henceforth REE+Y) data afford inspection of the peculiar irregularities found in seawater (e.g. Zhang and Nozaki, 1996) without which erroneous conclusions can be drawn, particularly regarding the behaviour of the redox-sensitive Ce (e.g.; Bau and Dulski, 1996; Bolhar et al., 2004). The availability of other trace element data, particularly Sc, Zr, Th and U is also critical for evaluation of REE+Y patterns of hydrogenous sediments as they permit identification of detrital or volcaniclastic contaminants (e.g. Bau 1993).

One disadvantage of bulk rock analytical methods for ancient sedimentary rocks with inherently low REE content is that later veins of quartz and carbonate, infiltrated sulphides or deformation related metamorphic re-crystallisation/precipitation cannot easily be avoided and may have undue influence on the original REE+Y inventory. Micro-sampling guided by petrography helps to avoid these issues and the very low detection limits of modern ICP-MS instruments permit analysis of full REE+Y patterns from samples smaller than 100 micrograms (e.g. Allwood et al., 2010). This enables removal of minute micro-samples from areas in a portion of rock least affected by later overprint. Most recently, micro-sampling has benefited from exploratory in situ analysis by laser ablation (LA)-ICP-MS. For this purpose, preliminary REE+Y (and other trace element) data are obtained from a polished petrographic thin section *in situ* and the most suitable material is then extracted from the remaining rock slab immediately adjacent to the material represented in the thin section (e.g. Baldwin et al., 2011). The latest generation UV laser ablation systems coupled to the most sensitive ICP-MS have detection limits from 100-200 micron spots that permit direct in situ analysis of REE+Y in the more enriched components of hydrogenous sediments (chiefly the Fe-rich bands of BIF and the microbial laminae in stromatolites; e.g. Corkeron et al., 2012) and are even beginning to produce data of acceptable precision and accuracy in abiogenic cements and chert.

All literature data discussed here were obtained in the first-author's laboratories by solution ICP-MS whereas the bulk of the new data presented in this paper were obtained by LA-ICP-MS. The analytical details for the new data are

explained below. The analytical modifications relevant to earlier literature data are briefly summarised in section 2.2.

2.1.1. LA-ICP-MS analysis

Samples for LA-ICP-MS consisted of ca. 200 μm thick polished thin sections mounted with epoxy resin. They were digitally scanned at high resolution prior to analysis. Potential analytical targets were determined from petrographic context. Analysis sites were inspected after LA with a petrographic microscope equipped with a digital camera. Data were obtained on two analytical setups. At the Australian National University a custom-built 193 nm Excimer laser with a dual-volume ablation cell was coupled to a modified PQ-SE2+ ICP-MS. This is referred to as the ANU setup. At Trinity College Dublin, a Photon Machines Analyte Excite (193 nm Excimer) LA system with a dual-volume ablation cell was coupled to a Thermo Scientific iCap-Qs quadrupole ICP-MS. This will be called the TCD setup.

In both cases, analysis was performed in 99.999% pure He as line scans after pre-ablation with a 25 μm wider beam (removal of ca. 1-2 μm material) to avoid surface contamination. The analyses proceeded as a continuous profile at 50 μm sec^{-1} and resulted in ablation of <5 μm material, hence avoiding any down-hole inter-element fractionation. Due to its lower sensitivity, the ANU setup was operated with a beam diameter of 178 μm, a repetition rate of 5 Hz and a fluence of 5 J cm^{-2}. The more sensitive TCD system used a smaller beam diameter (125 μm), 5 Hz repetition rate and a lower fluence of 3.5 J cm^{-2}. On the ANU setup, a number of 137 μm spot analysis were also performed with all other laser parameters kept constant. Individual, pre-ablated sites were chosen on the basis of the profiling data. Total acquisition time per spot was 120 sec, consisting of 30 sec blank and 90 sec ablation, resulting in ca. 90 usable repeats (of 0.8 sec each) after signal stabilization.

In order to keep the quadrupole scanning time below 1 sec, the element menu on the ANU setup was limited to 21 masses for continuous profiling (one isotope each for Mg, Ca, Zn, Sr, Y, Zr, Ba & all REE). In spot analysis mode, Ca and Mg were not analysed to conserve time for the more important REE. Dwell times across the mass range were kept constant. Oxide formation was monitored and found to be negligible by measuring BaO^+ on Eu^+ in a relatively Ba-rich (158 ppm) Devonian calcite cement with less than 1 ppb Eu. Data were calibrated with analyses of NIST 614 glass

combining preferred values for this standard reported in Horn et al. (1997) and Kent et al. (2004). Data reduction was performed off-line in spreadsheets. Calcium was used as the internal standard but the difference in matrix between the silicate glass standard and the carbonate sample is likely introducing up to 20-30% uncertainty into absolute concentrations. Relative concentration errors across the REE were determined via internal errors and rarely exceeded 5%, except for the least abundant samples, for which error bars are shown on the normalised REE+Y diagrams. Raw continuous profile data were background subtracted and drift-corrected by assuming stoichiometric Ca concentration. They were first inspected by over-laying the time series of elemental concentration on the scanned petrographic images. From these times series, 'plateau'-like sections of constant microstructural context and trace element content were identified and these were then averaged to obtain representative concentration estimates. For spot analyses, the background-subtracted data were averaged without drift correction and concentrations calculated by reference to the drift-adjusted NIST 614 reference count rates. All analyses are reported in Tables 1 and 2. Reproducibility of the five analysed spots on NIST 614 in this mode was between 3 and 5.5% for all elements. On the TCD setup, 24 masses were analysed resulting in a 0.72 sec scan time. Data were calibrated relative to analyses of NIST 612 (see Kamber and Webb, 2007, for preferred values) with the "trace element" data reduction scheme in Iolite (Paton et al., 2011). The same principle of overlying raw data onto scanned petrographic images guided the definition of integration areas for which data are reported in Tables 1 and 2.

2.1.2. Solution ICP-MS analysis

The majority of the discussed literature data were obtained on sub-sampled fractions of microbial carbonate as detailed in the original papers. New solution ICP-MS data are here presented for only one of the studied samples (Rh-73-215c). The face of the ca. 7 mm thick thin section block adjacent to the studied thin section was affixed to double-sided tape. The block was then shattered in a 70 ton pneumatic press equipped with parallel steel plates. Six micro-samples ranging in mass between 3 and 0.03 mg were hand-picked from material that stuck to the tape. Samples were weighed in triplicate on a Cahn 31 microbalance calibrated in its highest resolution mode. Weighing reproducibility was better than 3% for the smallest samples and better than 1% for samples of more than 1 mg. Samples were digested overnight in

2.5 mL double sub-boiling distilled 2% nitric acid spiked with 2 ppb internal standard, in pre-cleaned 14 mL PS centrifuge tubes. Weak nitric acid was preferred for dissolution over acetic acid, because the latter increases the solution's matrix and may lead to undesired effects in the plasma. However, it is recognised that even weak nitric acid may release metals from kerogen and may therefore yield a mixed signal from carbonate and originally organic-C bound species.

Solutions were analysed at The University of Queensland on a Thermo Electron XSeries ICP-MS using a 400 µl nebuliser. Sample analyses were preceded by repeated blank analyses and followed by analyses of two 10,000 times dilutions of the calibration standard (USGS dolerite W-2; see Kamber, 2009 for preferred values). The run was followed by analyses of Ba and Nd solutions for estimates of oxide production rates. The ICP-MS was operated in high-performance mode but without shielded torch and yielded 270 MHz ppm^{-1} on In and 360 MHz ppm^{-1} on U at 1.5% CeO production rate. Backgrounds on masses 220 and 245 were determined at less than 0.3 cps. At an estimated aspiration rate of ca. 420 µl min^{-1} the 2.5 mL solutions were sufficient for 5 repeats of 18 sec each. The analysed masses were one isotope each of In, Ba, all REE, Re and U. Internal drift corrected data were reduced off-line and are listed in Table 1. Typical uncertainties for the REE are better than 2% even in the most REE-depleted samples.

2.2. Sample details

The datasets discussed represent six classic microbial carbonate occurrences, the geology of which is introduced here in chronological fashion from oldest to youngest. Interested readers are referred to the original publications for greater detail on field context, petrography and other relevant information.

The 3.45 Ga Strelley Pool stromatolites — form part of the 3490–3310 Ma Warrawoona Group, the second-oldest and thickest part of the Pilbara Supergroup of the East Pilbara Granite–Greenstone Terrain, Pilbara Craton, Western Australia. Comprehensive REE+Y data for dolomitised stromatolites, which are estimated to be 3.45 Ga old, were first published by Van Kranendonk et al. (2003) and obtained on a PQ2+ ICP-MS with the methodology described in Kamber et al. (2003). Similar shallow-water stromatolites were described in much greater morphological detail and interpreted in wider stratigraphic context by Allwood et al. (2006). More REE+Y

Table 1. *Trace element data for Huntsman quarry stromatolite (all concentrations in ppb)*

Sample name:	Rh-73-215a											Rh-73-215b							
Carbonate type:	Profile D1 mat 1	Profile D1 mat 2	Profile D2 mat 1	Profile D3 mat 1	Profile D3 mat 2	Profile D3 mat 3	Profile D1 cement 1	Profile D2 cement 1	Profile D3 cement 1	Profile D3 cement 2	Profile D3 cement 3	Mat 1 profile D1	±	Mat 2 profile D1	±	Cement 1 profile D1	±	Cement 2 profile D1	±
Method:	1	1	1	1	1	1	1	1	1	1	1	1		1		1		1	
Sample weight (mg)																			
Zn	3390	3180	1980	6600	5200	3520	3030	2570	4460	2190	4050	1090	160	3210	38	1350	32	3050	980
Sr	1166000	860000	616000	1419000	1350000	757000	1416000	618000	1657000	1853000	1432000	1060000	130000	714000	55000	1850000	91000	1960000	2E+05
Zr	116	134	204	229	134	136	141	134	136	38	229	143	35	209	25	112	27	125	31
Ba	156000	127000	42900	207000	218000	98400	228000	32800	278000	368000	209900	205000	39000	81900	7600	289000	49000	384000	70000
La	566	730	658	548	451	576	252	304	265	150	206	459	65	364	34	113	14	89	14
Ce	399	570	555	444	326	462	208	203.6	188	106	143	306	24	271	23	66	11	66	14
Pr	39.4	58	54.6	40.8	26.5	46.5	16.3	18.2	14.8	8.2	13.8	33.8	7.1	24.1	4.8	5.8	2.1	7.2	2.6
Nd	177	289	260	182	104	201	79	74.6	69	29.9	61.4	114	29	111	21	25	14	25	10
Sm	13	38	36.7	34	18	27.6	15.9	13.4	10.5	6.7	6.5	11.9	7.9	12.9	5.4	6.4	4.8	3.5	3.3
Eu	15.8	28.9	26.8	20.2	22.3	21.4	10.4	6.4	13.1	11	7.9	27	11	11.2	2.1	9.7	2.5	13.9	4.2
Gd	42	52	48	33.1	33	37	17.6	16.6	13.8	8.4	11.2	30	14	22.3	8.6	10.8	6.5	10.3	4.7
Tb	6.8	5.5	4	5.6	3.6	5.4	1.93	2.12	2.6	1.28	1.27	6.7	3.8	4.6	2.1	0.33	0.48	0.09	0.22
Dy	48	55	48.9	45.9	18.3	46.3	14.8	20.1	17.9	10.6	14.2	47	16	27.2	6.4	2.2	2	6.4	3.4
Y	1500	1810	1530	1524	860	1530	592	1025	760	472	553	1590	130	1200	120	151	23	143	24
Ho	16.2	17	14.5	12.1	6.2	13.8	3.49	6.9	5.9	3	4.26	11.4	2.5	8.1	2.1	1.24	0.78	1.24	0.66
Er	55	57	46.9	46.8	20.6	42.2	15.1	25.5	18.1	14.3	11.7	38.9	4.7	36.6	6.2	4.9	3.2	2.9	1.6
Tm	7.5	8.8	6.2	5.1	5	6.41	2.5	4.04	3.02	1.3	2	7.3	2.5	5.1	1.6	0.36	0.4	0.62	0.41
Yb	33.6	52	46.7	39.7	20.6	37.2	15.8	23	19.3	14	13.2	32.7	5.1	33.4	6.4	5.1	2.1	0.7	1.1
Lu	5.1	9.5	6.9	6.8	2.4	7.9	2.07	4.66	4.4	2.2	2.32	3.3	1.8	9.8	1.4	0.75	0.61	0.64	0.42

Sample name:	Rh-73-215b								Rh-73-215c										
Carbonate type:	Mat spot M1	Mat spot M2	Cement spot C1	Cement spot C2	Spar spot S1	Profile D3	Profile D4	Profile D5	Mat spot 1	Mat spot 2	Cement spot 1	Cement spot 2	Spar	Mat piece 1	Mat piece 2	Mat piece 3	Mat piece 4	Cement piece 1	Cement piece 2
Method:	2	2	2	2	2	1	1	1	2	2	2	2	2	3	3	3	3	3	3
Sample weight (mg):														3.64 mg	0.930 mg	0.340 mg	0.034 mg	1.12 mg	3.31 mg
Zn	491	648	75	212	-2	2540	3830	3280	1205	1149	62	294	20						
Sr	2271933	2286392	2580352	2061939	1819068	1414000	1158000	1000000	539078	495859	3570703	3108934	2164309						
Zr	107	329	35	19	48	155	258	194	237	245	12	15	3						
Ba	292507	285043	225129	171706	81381	202000	135300	120400	59505	80404	541791	435853	90788						
La	541.4	748.8	489.3	164.9	23.5	247	283	305	713.2	920.9	247.1	330.9	1.6	195.9	261.0	204.1	283.2	64.3	58.9
Ce	341.5	492.0	219.5	91.0	15.2	176	230	233	372.1	492.1	102.0	166.4	0.6	153.6	263.3	176.8	295.7	45.3	44.9
Pr	36.8	58.7	24.1	11.6	1.6	18.2	24.9	25	44.2	53.9	12.7	18.2	-0.9	15.8	31.0	18.4	30.9	4.4	4.4
Nd	146.8	270.5	116.3	40.9	15.8	77.9	108.2	97.4	195.5	244.9	31.7	62.1	-9.5	67.3	123.6	74.2	141.0	17.2	17.3
Sm	28.9	44.1	22.6	7.5	2.4	14.2	24.2	16.6	34.2	40.7	6.1	9.1	-6.8	11.4	23.8	14.1	23.0	3.7	3.1
Eu	24.3	31.5	16.0	5.5	-0.4	14	13.9	12.3	28.5	26.9	16.4	15.5	3.3	8.3	11.1	8.6	11.6	2.1	2.2
Gd	49.7	50.8	39.6	4.7	1.2	22.1	30.5	26.1	66.3	55.3	28.2	15.2	2.3	17.3	28.6	18.0	17.4	3.9	4.0
Tb	7.9	9.5	6.7	2.2	0.0	3.09	3.92	3.08	7.1	9.3	2.8	2.6	0.3	2.4	4.2	2.8	3.2	0.6	0.5
Dy	66.6	59.2	51.6	5.1	1.4	23.2	30.9	27.9	60.9	68.8	27.0	28.5	-0.8	17.6	26.9	16.5	25.6	3.9	3.5
Y	2224	2303	2232	318	50	892	1020	1029	2641	2837	1439	1384	5	697	857	791	766	226	167
Ho	18.0	18.2	15.9	2.5	-0.2	7.48	8.75	8.81	23.6	24.7	9.8	8.6	0.1	5.7	8.1	6.7	8.1	1.5	1.2
Er	72.2	73.2	46.3	8.5	2.2	27.3	31.3	31.1	80.3	74.7	34.1	31.5	-1.3	19.6	26.8	21.9	22.8	5.7	4.1
Tm	9.3	10.6	8.6	0.9	0.0	3.53	4.79	4.1	10.4	11.6	6.1	4.6	0.8	2.8	3.9	3.2	4.1	0.8	0.6
Yb	51.0	65.8	43.8	7.5	3.6	23.8	27.1	29.5	60.5	66.6	32.3	33.9	3.1	17.1	22.9	19.6	25.4	5.6	3.3
Lu	12.3	11.1	8.6	0.7	0.3	4.38	5.58	4.96	12.6	12.9	6.7	5.0	0.1	3.3	4.4	3.8	4.0	1.0	0.6

Method 1, TCD LA-ICP-MS; Method 2, ANU LA-ICP-MS; Method 3, University of Queensland solution ICP-MS.

data, including for co-existing chert and under- and overlying non-carbonate strata were published by Allwood et al. (2010). Those data were obtained using the same method as the new data reported in this paper.

The 2.93 Ga Steep Rock carbonate platform stromatolites — were deposited in the 500 m thick Mosher carbonate in the Wabigoon Subprovince, Superior Province (Ontario). The platform contains a variety of lithofacies, which could represent an ancient, drowning carbonate platform. Its age is widely quoted to be 2928 Ma (e.g. Kusky and Hudleston, 1999) but more recently, it has been suggested that the Steep Rock carbonates might be younger, possibly as young as 2.7 Ga old (Stone, 2010). A variety of stromatolites exist from a range of interpreted water depths. New REE+Y data for these lithofacies were presented by Planavsky et al. (2010) using the method described in Kamber (2009).

The 2.82 Ga Mushandike stromatolites — occur in a small undeformed block in a major development of limestone first described by Orpen and Wilson (1981). The structural setting of the ca. 200 m wide limestone band is complicated and no tight indirect age data are available. The original direct Pb-Pb regression age for the stromatolite itself is 2839±33 Ma (Moorbath et al., 1987) and has more recently been confirmed with an acetic acid leachate Pb-Pb regression age of 2817±34 Ma (Collerson et al., 2002). Within the limestone band, which has a strike length of 7 km, stromatolites are rare and where they do occur, they are highly laminated and of oblate shape. They are completely recrystallised to marble and do not preserve microscopic details of original precipitation or diagenesis. They were first subjected to isotopic analysis by Abell et al. (1985a). The only comprehensive REE+Y data (as well as Sr-isotopes) were reported by Kamber et al. (2004) with the same analytical methodology as employed by Van Kranendonk et al. (2003).

The 2.72 Ga Tumbiana Formation stromatolites — occur as horizons throughout the stratigraphic section of the 2.78-2.63 Fortescue Group. They were the subject of considerable debate regarding the possibility of having been deposited in a lacustrine setting (e.g. Buick 1992). A very detailed report on the great variety of stromatolites in the various lithofacies can be found in Awramik and Buchheim (2009), who also reported O-, C-, and Sr-isotope data for carbonate. Bolhar and Van Kranendonk (2007) published REE+Y data for a variety of carbonate facies, including stromatolites.

The 2.65 Ga Huntsman Quarry stromatolites — were discovered in 1935 and reported by MacGregor (1941). They occurred in a limestone quarry near Turk Mine in the Bulawayo greenstone belt of Zimbabwe. By 1950, quarrying had removed the spectacular stromatolites and after the limestone was exhausted the quarry pit was flooded. Later investigators sampled remnants of stromatolite from the quarry talus. The most comprehensive study on such material was conducted by Schopf et al. (1971). Those authors described a variety of stromatolite morphologies, including the remarkable microscopic preservation of the material. Of particular note is the presence of sparry calcite forming up to 1 cm wide 'birdseye' pockets interpreted to represent early diagenetic infill of what were originally gas-filled pockets in the microbial mats. These authors also reported the first C-isotope data for stromatolite and succeeded in documenting a consistent ca. 33‰ $\delta^{13}C$ contrast between reduced organic matter and carbonate. Veizer and Compston (1976) reported two Sr-isotope values for Huntsman Quarry stromatolite, yielding $^{87}Sr/^{86}Sr$ of 0.70151 to 0.70165. The present paper reports the first REE+Y data for this stromatolite. Although no direct data are available for the Bulawayo greenstone belt, the tight regional correlation of Zimbabwean greenstones (Wilson et al., 1995) and the occurrence of similar stromatolites in the Cheshire Formation of the Belingwe greenstone belt (Bolhar et al., 2002) strongly suggests a 2.65 Ga age and a maximum age of 2.72 Ga for the Huntsman Quarry limestones.

The 2.52 Ga Gamohaan Formation stromatolites — have been the subject of a large number of studies (e.g. Beukes, 1987; Klein and Beukes, 1989; Sumner, 1997a,b), most recently from cores obtained by the Agouron Drilling Project (e.g. Fischer et al., 2009). The age of the Gamohaan Formation is well-constrained. A tuff in the middle of the formation yielded a U/Pb zircon date of 2521±1 Ma (Sumner and Bowing, 1996), whereas a tuff from the upper part was U/Pb zircon dated to 2516±4 Ma (Altermann and Nelson, 1998). The Gamohaan Formation contains a variety of exceptionally well-preserved limestone lithofacies, including a large number of domal stromatolites. Extensive geochemical and isotopic datasets are available for these stromatolites (e.g. Klein and Beukes, 1989, Beukes et al., 1990; Kamber and Whitehouse, 2007; von Blanckenburg et al., 2008; Heimann et al., 2010). The REE+Y data discussed here were published by Kamber and Webb (2001) using the same method as those reported by Van Kranendonk et al. (2003). The previously published

data were obtained with compatible methods as described in Kamber (2009). Additional in situ data for one stromatolite are presented in this contribution.

3. REE as environmental and redox proxies

3.1. Hydrogenous signals versus contaminants

The first step in any analysis of REE+Y data of hydrogenous sediments is to assess the presence of contaminants that could contribute trace elements and potentially overwhelm the original hydrogenous inventory. The most likely type of contaminant is fine-grained clastic detritus. Another potential contaminant is volcanic ash, which is a well-known constituent of many BIF where it is indicated by the K-rich mineral stilpnomelane (e.g. Klein, 2005). Further possible contaminants in chert and carbonate are hydroxides of Fe and Mn that could have formed near the sediment-water interface or that could have rained from the water column. Finally, irregularly distributed diagenetic phosphates (e.g. Ulrich et al., 2009) could form during lithification, for example as a by-product of decay of organic matter, and severely influence the REE+Y inventory, particularly if phosphates scavenged REE+Y from pore waters or the overlying water column. Of all these possible complications, clastic and volcanic detritus are most easily identified on account of the very low content of high-field-strength-elements (HFSE) in clean hydrogenous sediment (Bau, 1993). The trivalent Al, Ga and Sc are also excellent monitors of detritus.

There are a number of very pure Precambrian microbial carbonates lacking siliciclastic detritus, even though the microbial mats have a capacity to trap and bind sediment. These were specifically targeted for geochemical investigation. Their existence is probably owed to a combination of two factors. Firstly, the Archaean and most of the Proterozoic clastic sediment record testifies to a paucity of clay minerals (Kennedy et al., 2006) and other products of advanced terrestrial weathering, resulting in a cleaner near-shore environment. Secondly, the typically shallow depositional environment that permitted the growth of the selected microbial mounds and reefs may itself have biased against turbid water conditions. When comparing data from such clean microbial carbonate with sediment from deeper water facies (e.g.,BIF and chert) it is necessary to recall that there is an important difference in analytical protocol. Whereas BIF and chert are digested with hot hydrofluoric acid, which will also dissolve detrital silicates, carbonate can be

dissolved much more gently (e.g. with 2 to 5% nitric acid) leaving many silicates undigested. Regardless, the Mushandike stromatolites are a good example for exposing the effects of clastic contamination on REE+Y characteristics. Figure 1a is a cross plot of Zr versus Th content in several Mushandike stromatolites. Of these, the stromatolite that was sampled by drill core (solid diamond symbols) shows variably elevated concentrations of Zr and Th, which correlate positively. The trend line extends into the data field of the much cleaner samples obtained from outcrop (dark grey circles), suggesting that uncontaminated Mushandike stromatolite incorporated ca. 100 ppb Th and ca. 250 ppb Zr. Not surprisingly, the outcrop stromatolites with their lower Zr content have higher Y/Ho ratios (this phenomenon of REE+Y dissolved in seawater is explained in the following section) and can therefore be considered better proxies for ambient seawater than the slightly contaminated drill core stromatolites whose Y/Ho ratios are lower. Successful mixing models can be constructed (e.g. Fig. 1b) between the clean stromatolites and local detritus and these indicate that most of the sampled stromatolites incorporated between 0.25 and 1% by mass of clastic sediment. In situ LA-ICP-MS data are starting to show that clastic contamination in stromatolites can be traced along individual laminae. Analytical signals from these laminae can be excluded from data integrations.

The presence of phosphate (particularly apatite) in hydrogenous sediment is typically inferred when convex middle REE (MREE) to heavy (HREE)-enriched shale-normalised patterns are encountered (e.g. Baldwin et al., 2011). In LA-ICP-MS, elevated REE contents can be linked to spikes in P counts because chert, iron oxide and carbonate are all very low in P. When the LA-ICP-MS is used to produce 2D chemical maps of sediment, it is even possible to identify individual phosphate grains (e.g. Fig 6a of Ulrich et al., 2009). Although phosphates are occasionally encountered in microbial carbonate their influence on REE+Y is readily exposed due to the characteristic convex REE pattern and the associated high U and Th contents.

The least-studied potential contaminants of hydrogenous carbonates (both microbial and cements) are hydroxides of iron and manganese. Iron as a trace element is difficult to analyse by ICP-MS and rarely reported alongside REE+Y data for carbonates. Because BIF, which often represent secondary minerals after original Fe-hydroxides, have REE+Y characteristics very similar to those of microbial carbonate, it is not trivial to exclude the possibility that a particular carbonate does

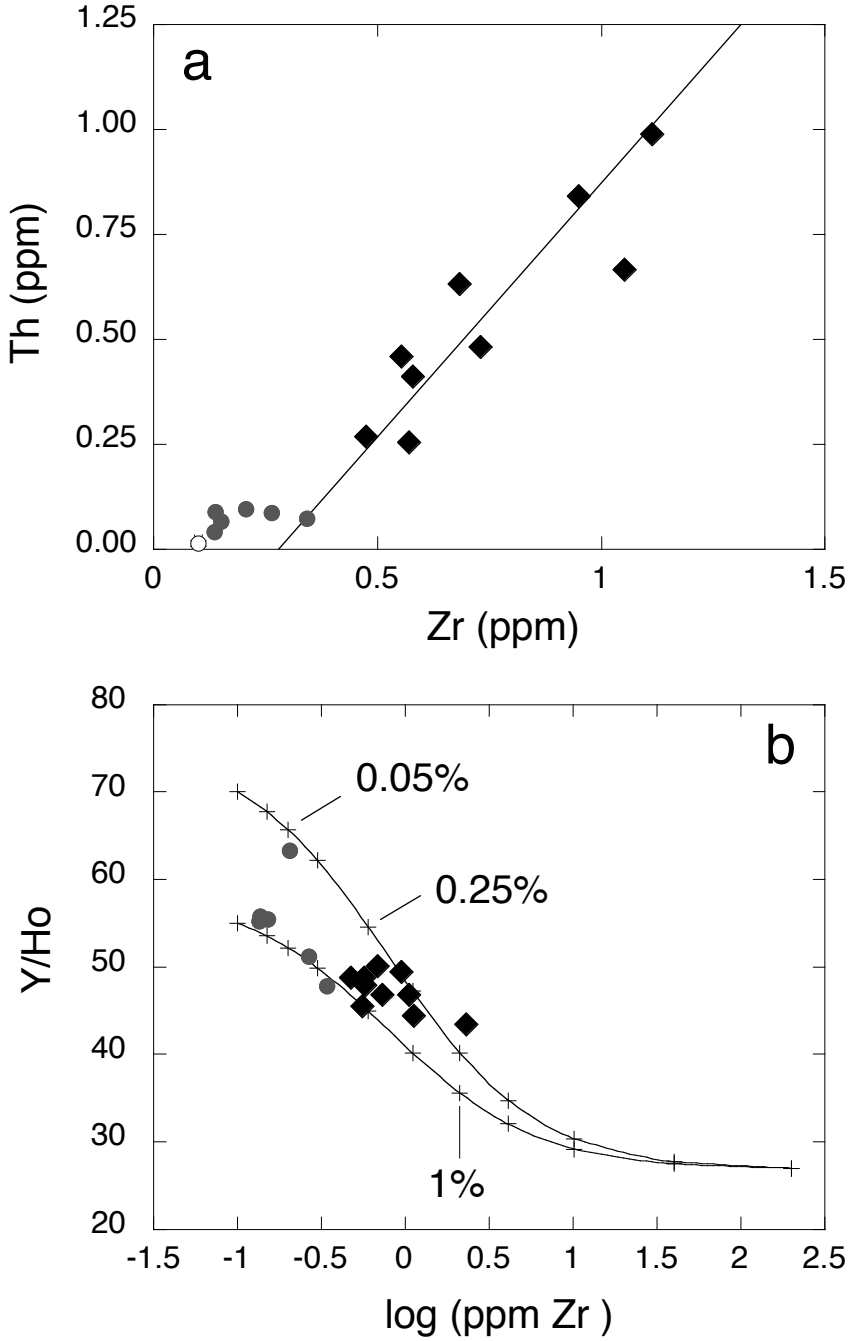


Figure 1: (a) Cross plot of Th versus Zr content in Mushandike stromatolites (data from Kamber et al., 2005). The solid diamond symbols represent subsamples of a single domal stromatolite that was drilled with a hand-held corer (Abell et al., 1985a). The dark grey circles represent individual stromatolites sampled on outcrops. The open symbol is the average of Holocene Heron Reef microbial carbonate. (b) Zr (log) content versus Y/Ho ratio shows that the outcrop stromatolites with their lower Zr content have higher Y/Ho ratios. The entire data array can be modelled by contaminating a pure hydrogenous sediment with between 0.05 and 1% detrital sediment local to the Mushandike limestone (for details of model, see Kamber et al., 2005).

not contain REE+Y from Fe-hydroxide coatings. In other words, a marine REE+Y pattern in stromatolite cannot be used to argue against the presence of Fe-hydroxides. Future low-level Fe analyses obtained in cool plasma ICP-MS mode will help to reveal whether some of the REE+Y variability within individual stromatolites could be attributed to Fe-phases. By contrast, Kamber and Webb (2007) documented with LA-ICP-MS that iron-stained late diagenetic cements surrounding Devonian stromatoporoid and the calcimicrobe *Renalcis* can readily be identified with a variety of transition metals, whose abundances are very elevated in the late (diagenetic) cement. The REE+Y data analysed in the following sections are not influenced by contaminants unless specifically stated.

3.2. Reconstruction of the depositional environment

The REE+Y, particularly in combination with radiogenic isotopes (e.g. Pb and Sr; Kamber and Webb, 2001; Bolhar et al., 2002), are useful to discriminate between stromatolites that formed in lacustrine, restricted marine and open marine depositional settings and in exceptional cases, it is also possible to infer relative water depth or proximity to hydrothermal fluid sources in a sequence of microbial carbonates. This analysis is, however, performed without knowledge of the REE+Y speciation in the Archaean ocean (see e.g. Bolhar et al., 2004; Kamber, 2010), which is widely assumed to have been dominated by carbonate complexes (e.g. Friend et al., 2008).

3.2.1. Lacustrine microbial carbonate

The vast majority of modern freshwaters sampled from rivers and lakes have quite uniform REE+Y patterns in their dissolved load. When normalised to shale, the patterns are relatively flat (Fig. 2a), reflecting the fact that the REE are not strongly fractionated during incipient and moderate stages of weathering. River waters can express Eu and Ce anomalies due to a variety of factors (e.g. the presence of plagioclase affects Eu whereas alkalinity driven pH has an effect on Ce; e.g. Xu and Han, 2009) and detailed study of release of HREE from weathering profiles reveals that Y is slightly less retained in the residuum. This is the most likely reason why many rivers have Y/Ho somewhat elevated relative to values in typical crustal rocks (25-28; Pack et al., 2007). Regardless of the irregularities in Ce, Eu and Y, typical river and lake waters have otherwise featureless and flat shale-normalised REE+Y patterns

(Fig. 2a). The most important exception to this observation are rivers that have large carbonate catchments. Xu and Han (2009) demonstrated that the dissolved load of the Xijiang river, which drains marine limestone, has a REE pattern that resembles marine carbonate. In addition to this, there are more unusual waters with irregular REE+Y patterns, some of which can look quite similar to seawater REE+Y patterns (Johannesson et al., 2006). Notwithstanding these complexities, by comparison to fresh waters, open oxygenated seawater has a uniform REE+Y pattern that is clearly identified by the following distinctive features:

i) a positive slope in shale-normalisation, quantified as a $Pr_n/Yb_n << 1$;

ii) a strongly superchondritic Y/Ho ratio, typically between ca. 40 and 80;

iii) a positive La anomaly, expressed as $La_n / (Pr_n \times (Pr_n / Nd_n)^2) > 1.1$;

iv) a moderate positive Gd anomaly, expressed as $Gd_n / (Tb^2_n \times Sm_n)^{1/3} > 1.1$;

v) a strong negative Ce anomaly, expressed as $Ce_n / (Pr_n \times (Pr_n / Nd_n)) < 0.8$.

These characteristics are shown in the examples depicted in Figure 2b and initially develop as the riverine REE+Y flux meets high ionic strength seawater in the estuary (e.g. see Lawrence and Kamber, 2006, for a review) and they become more accentuated as the REE+Y undergo continued adsorptive scavenging in the oceanic water column (de Baar et al., 1985). As a result of REE+Y cycling, there are depth dependent trends of the REE+Y features that characterise seawater. For example, the Gd anomaly becomes more positive with increasing oceanic depth, whereas the Ce anomaly becomes more negative (e.g. Zhang and Nozaki, 1998; see also Fig. 2b). Similarly, the Y/Ho ratio increases during cycling of REE+Y from surface waters to deep ocean water (Nozaki et al., 1997). Because the residence time of the REE+Y in seawater is longer than the mixing time of the modern ocean, vertical concentration profiles are also influenced by lateral advection (Piepgras and Jacobsen, 1992).

In view of these marked differences in typical freshwater and seawater dissolved load REE+Y patterns, it is not surprising that the putative lacustrine 2.72 Ga Fortescue Group stromatolites were analysed for REE+Y (Bolhar and Van Kranendonk, 2007). Their normalised REE+Y patterns are flat (Fig. 2c) and show none of the typical anomalies of seawater. In particular, they have near-chondritic

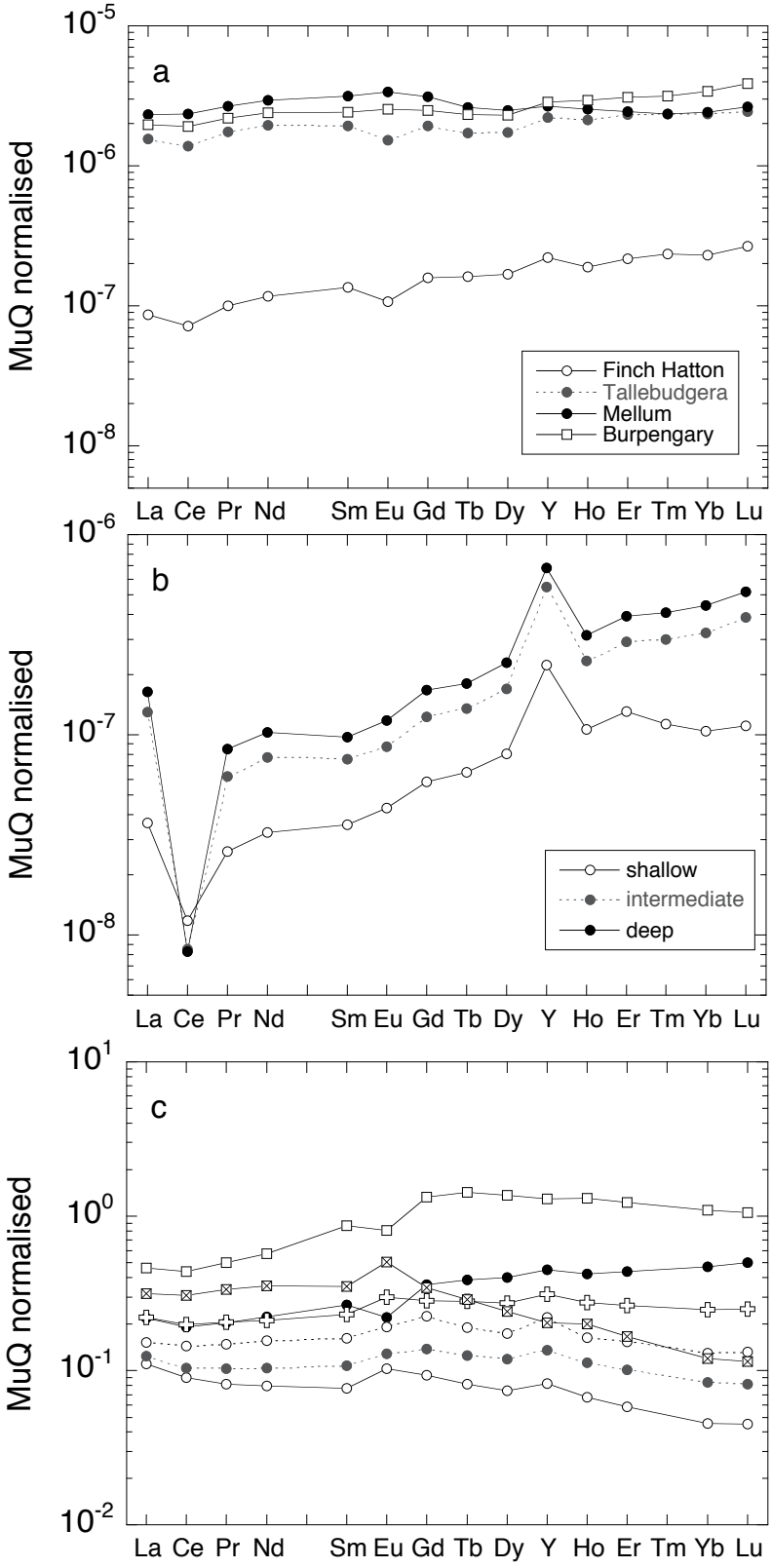


Figure 2: Upper crust normalised (MuQ alluvial sediment composite of Kamber et al., 2005) REE+Y patterns. (a) Dissolved load of selected southeast Australian rivers and creeks (data from Lawrence et al., 2006a,b). (b) Averages of shallow, intermediate and deep ocean water (for data compilation see Kamber, 2010). (c) Fortescue Group stromatolites reported by Bolhar and Van Kranendonk (2007). Note that REE-poorest sample could not be plotted due to insufficient number of reported digits.

Y/Ho and lack positive La and Gd anomalies. These features support the view that most of the carbonate formed in a giant lake system, in agreement with many other lines of evidence (e.g. Buick, 1992; Awramik and Buchheim, 2009).

3.2.2. Stromatolites from restricted ocean basins

The majority of modern ocean basins are well-connected and in terms of Sr-isotopes, seawater is very well mixed. There is a provinciality in Nd-isotope composition, which reflects the lateral transport by deep ocean currents of Nd with very distinctive isotope composition (e.g. very ancient unradiogenic Nd from the Labrador Sea is transported by North Atlantic deep water into the deep South Atlantic and beyond; Burton et al., 1997). However, the general shape of the dissolved marine REE+Y pattern appears to be uniform. By contrast to the modern terrestrial surface, the Archaean landscape had, in all likelihood, a much less developed surface roughness (e.g. Galer and Mezger, 1998; Kamber, 2010; Campbell and Squire, 2010) on which the expansion of epi-continental seas was apparently common. Epi-continental settings for greenstone belts have been advocated on the basis of multiple lines of evidence. This includes the presence of ancient, inherited zircon in mafic-ultramafic lavas (Wilson et al., 1995) and unexpectedly crustal radiogenic isotopes (Chauvel et al., 1985), both inferring that the feeder magma had passed through continental crust and assimilated significantly older, highly evolved crustal rocks. Perhaps the strongest evidence for an ensialic origin of some greenstone belts comes from direct sedimentary unconformities, some of the best of which are exposed in Zimbabwean Neoarchaean greenstone belts (e.g. Blenkinsop et al., 1993). Geochemical information from stromatolites that inhabited restricted epi-continental and possibly generally shallow water may not necessarily have significance for the global ocean. The study of REE+Y of such deposits can help to distinguish between isolated and well-connected basins. It is worth noting that the paucity or complete absence of carbonate in general, and microbial carbonate in particular, in very large juvenile greenstone belts such as the Abitibi Subprovince most likely reflects the absence of a preserved shallow water environment and a preservational bias towards deeper water sediments such as BIF. This bias compromises the scope of comparison of deep water with shallow water information in all but the most exceptional settings that expose significant transgressions, ideally over drowning platforms.

The REE+Y patterns of the 2.82 Ga Mushandike greenstone belt stromatolites (see also section 3.1) are the most extreme example of a hydrogenous sediment with a highly localised and atypical REE source. When the REE+Y are normalised with ordinary upper continental crust proxies, such as Post-Archaean-Australian Shale (PAAS: Taylor and McLennan, 1985) or MuQ (Kamber et al., 2005), the slope of the patterns is opposite (drill core sample mean = Pr_n/Yb_n = 1.84±0.25) to what is commonly observed (Figure 3). Notwithstanding the unusual slope, the REE+Y patterns still possess most of the other characteristic phenomena of the dissolved marine load (i.e. drill core sample means: Y/Ho = 47±2; La/La* = 3.1±0.6; Gd/Gd* = 1.2±0.1) arguing against a lacustrine setting and clastic contamination.

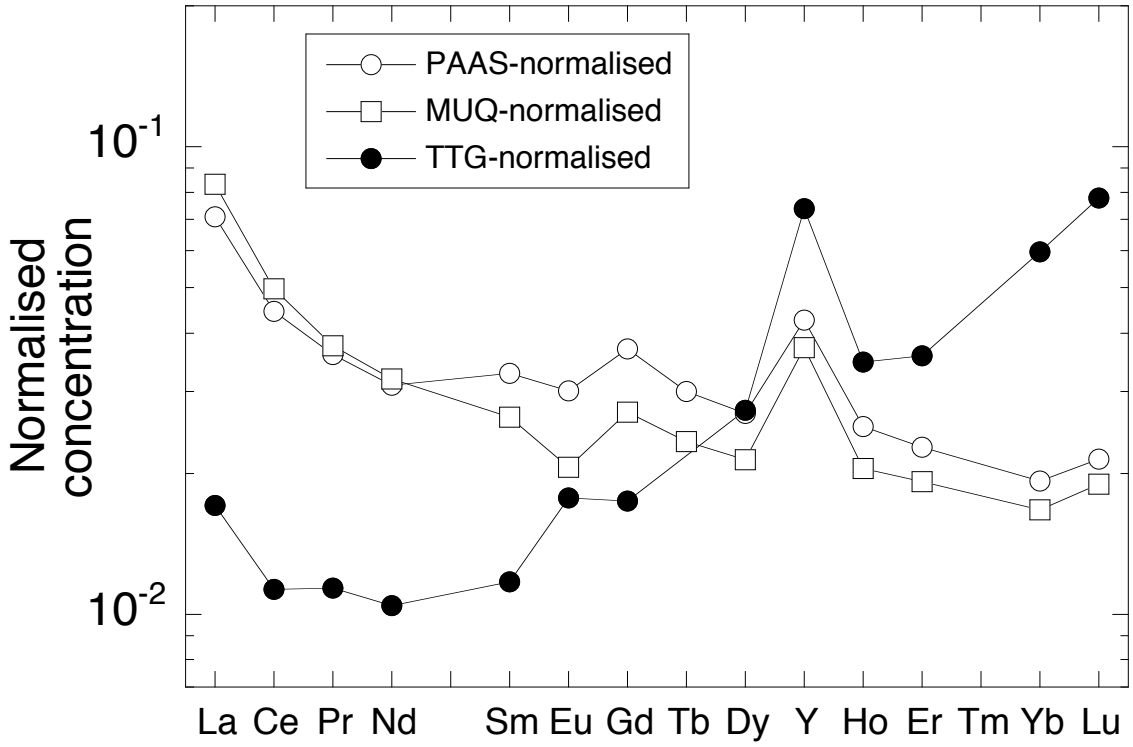


Figure 3: Normalised REE+Y pattern of average of drillcore sampled Mushandike stromatolite (data from Kamber et al., 2004). This plot highlights the effect of normalisation. Normalisation with two different upper crust composites (PAAS of Taylor and McLennan, 1985; and MuQ of Kamber et al., 2005) results in patterns with unfamiliar slopes, unfamiliar negative Eu anomalies but preserving the seawater La, Gd and Y anomalies. Normalisation with HREE-depleted local tonalite (from Berger and Rollinson, 1997), results in a REE+Y pattern with all the familiar traits of dissolved REE+Y in Archaean seawater.

Importantly, when the REE+Y are normalised with local tonalite (Berger and Rollinson, 1997), the slope is rotated and the pattern becomes familiar (Figure 3). Because the tonalites themselves have a pronounced Eu depletion, the tonalite-normalised stromatolite patterns also lose their conspicuous shale-normalised negative Eu anomaly, adding further support to the notion that the Mushandike stromatolites formed in a restricted epi-continental basin with a local REE+Y supply. This is fully compatible with the observation of unusually radiogenic Sr and initial Pb-isotopes in these stromatolites (Kamber et al., 2004) and crustal Pb and Nd-isotopes in Neoarchaean stromatolites in the nearby greenstone belts (Bolhar et al., 2002). If the REE+Y inventories of Precambrian seawater were lower (and implicitly, the elemental residence times shorter), a possibility exists that the open ocean might have had a less uniform REE+Y pattern than at present. In that case, it would be more difficult to distinguish between ancient restricted and open marine basins. However, although Nd-isotopes in Archaean BIF do show a provinciality (Alexander et al., 2009), the time-corrected relative isotopic variation is similar or slightly smaller than today's and not in favour of a substantially different Archaean REE+Y inventory.

3.2.3. Stromatolites recording water depth gradients

In the modern ocean, there are clear gradients in REE+Y phenomena of the dissolved load (e.g. de Baar et al., 1985). They form because adsorptive scavenging onto a variety of particles and re-release of the REE+Y accentuates the typical marine phenomena (e.g. the Y/Ho ratio or the negative Ce anomaly) that are first established during estuarine mixing. Off-shore studies of ocean water columns have convincingly demonstrated that there is a strong correlation between water depth and extent of REE anomalies (de Baar et al., 1985; Bau et al. 1997; Zhang and Nozaki, 1998). The most straight-forward expression of this effect is the overall steepening of the shale-normalised REE+Y pattern as expressed by the Pr_n/Yb_n ratio. A compilation of data from transects in the North and South Pacific and the Mediterranean (Fig. 4a) shows that the most rapid steepening of the pattern occurs during REE+Y cycling in the top 500 meters of the water column, and as such, the relative extent of REE+Y ratios like Pr_n/Yb_n holds potential as a palaeo-water depth proxy. The majority of preserved microbial carbonates formed in the top few tens of meters of the water column, above

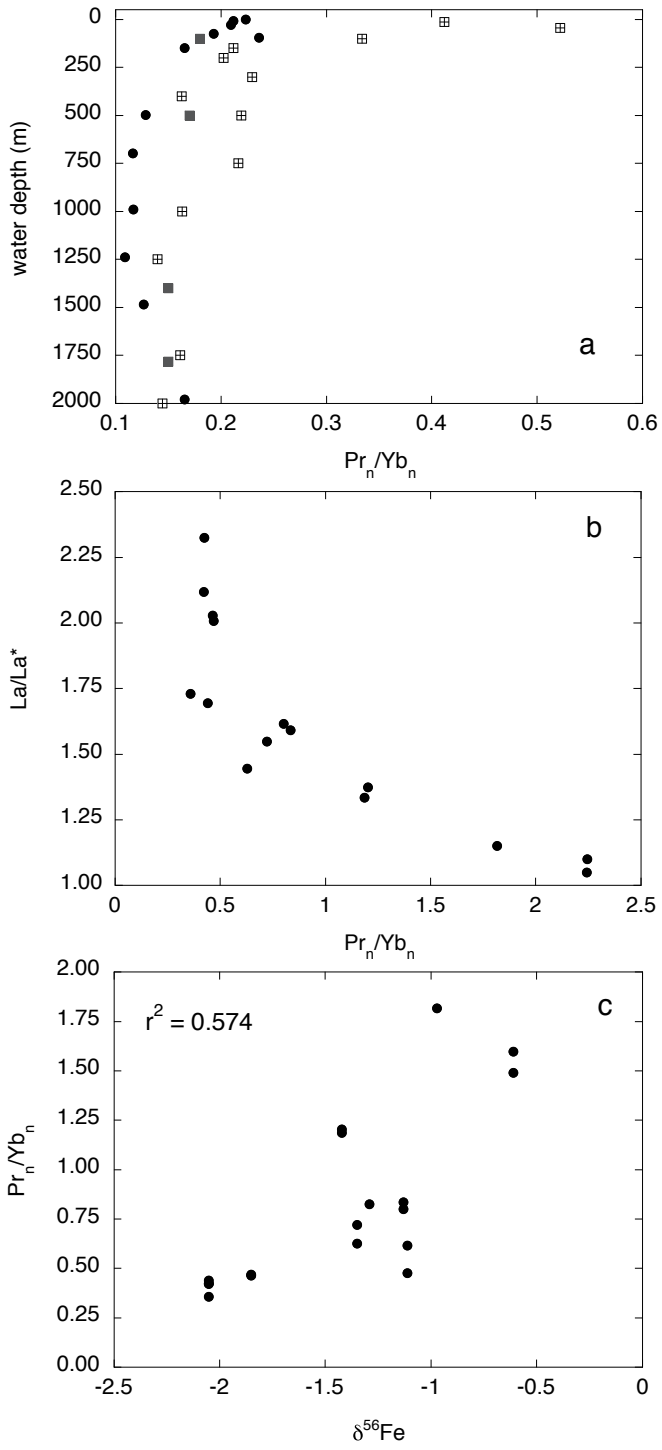


Figure 4: Panel (a): Evolution of PAAS-normalised Pr/Yb with oceanic water depth for three transects (North Pacific VERTEX II* of de Baar et al., 1985 [crossed squares]; South Pacific SA5 section of Zhang and Nozaki, 1998 [solid circles]; and East Mediterranean of Bau et al., 1997 [solid squares]). Samples are shown to a water depth of 2000 meters to avoid complexities arising form lateral advection of deep water currents. Panel (b): Inverse hyperbolical covariation between extent of positive La anomaly and MuQ-normalised Pr/Yb preserved in 2.52 Ga Campbellrand Subgroup stromatolites (data from Kamber and Webb, 2001). Panel (c): Covariation between Fe-isotope composition and MuQ-normalised Pr/Yb in 2.52 Ga Campbellrand Subgroup stromatolites implying the existence of an Fe chemocline separating isotopically light deep waters from isotopically much heavier shallow waters.

storm wave base. In the present ocean, this depth range shows the greatest depth-dependent change in marine REE+Y features.

Only a few Precambrian stromatolites occur on sufficiently thick carbonate platforms to possibly represent a variety of water depths. The best studied of these is the Neoarchaean Campbellrand Subgroup. Sumner (1997a) succeeded in a detailed reconstruction of the platformal limestones whose succession of facies reflects a transgression. Furthermore, the carbonate facies infer the existence of an (Fe) redox-chemocline. The REE+Y systematics of mixed zone stromatolites confirms these sedimentological inferences. Kamber and Webb (2001) reported data for a suite of lagoonal, shallow, and deep (sub-tidal) stromatolites whose REE+Y systematics show the relative progression of features that could be expected from modern marine ocean transects. Namely, the sedimentologically deepest samples show the best-developed marine REE+Y features. That is, the deepest samples have the strongest positive La anomaly and the steepest shale-normalised REE+Y pattern (Fig. 4b) whereas the shallow marine samples show REE+Y ratios similar to modern shallow marine waters. Whereas this agreement between two independent lines of evidence is pleasing, the real importance of this dataset is that the REE+Y ratios are useful as quantitative measures of relative water depth against which other proxies can be plotted. Most significantly, von Blanckenburg et al. (2008) discovered that the carbonate Fe-isotope composition correlated with several REE+Y ratios in Campbellrand Subgroup. The deepest samples, which have the highest Y/Ho and La-anomalies and the lowest shale-normalised Pr/Yb, have the isotopically lightest Fe (Fig. 4c), confirming the existence of the Fe redox-chemocline proposed by Sumner (1997a) on sedimentological and mineralogical grounds. In situ pyrite S-isotope data (Kamber and Whitehouse, 2007) on different lithofacies representing the transgression are also compatible with the existence of a shallow (less than storm wave base) chemocline. Although no other Archaean stromatolites have been studied in such stratigraphic detail, Planavsky et al. (2010) found similar correlated REE+Y features in the 2.93 Ga Steep Rock Group Mosher carbonates (their figure 5), which also attain considerable thickness. In summary, the best preserved Archaean limestone sequences appear to indicate that the ancient ocean already had a REE+Y cycle that was influenced by adsorptive scavenging and resulted in depth dependent dissolved REE+Y ratios.

3.3. The redox evolution of the Archaean ocean

There is a very large body of conclusive evidence that for the most part, the Archaean ocean-atmosphere system remained devoid of significant levels of free oxygen. Regardless of the wide consensus on this statement by the majority of investigators, the lack of a build-up of molecular O in the Archaean does not at all imply the lack of production of O_2. A variety of proxies have recently been put forward that promote at least episodic 'whiffs' of molecular O albeit insufficient to permit a build-up of an ozone layer that would have brought mass independent fractionation of sulphur to an end. In the light of this new evidence, it is necessary to test whether the REE+Y provide evidence for the build-up of appreciable concentrations of dissolved free O in the shallow marine realm throughout the Archaean.

3.3.1. Evidence from microbial carbonate REE+Y systematics

The REE+Y systematics in microbial carbonates can potentially offer insight into the extent of shallow water oxygenation as the stromatolites incorporate REE+Y directly from the putatively oxygenated shallow seawater. In the modern ocean, more than sufficient free O is available to oxidise a fraction of the dissolved Ce (present as Ce^{3+}) after sorption onto metal oxi-hydroxides to the more particle reactive Ce^{4+} (Bau and Koschinsky, 2009). In the process of repeated adsorptive scavenging and re-release of the REE, Ce becomes progressively more depleted relative to Pr in the dissolved load such that deep ocean water displays a very significant negative Ce anomaly (see Fig. 2b). The same process occurs in the estuary (and in certain rivers) and imparts a significant negative Ce anomaly to even the shallowest seawater. Palaeoproterozoic BIF that formed after the Great Oxygenation Event (GOE) show both negative and positive Ce anomalies, implying the presence of a sufficiently oxygenated shallow ocean to permit preferential Ce shuttling by particles below the chemocline, from where excess Ce was re-released, imparting a positive Ce anomaly onto the deep waters (e.g. Frei et al., 2008; Planavsky et al., 2010). Very similar situations are encountered in the modern ocean across chemoclines associated with restricted basins.

In view of the recent proposals for local oxygenation of at least the shallow Neoarchaean seawater, it is timely to analyse the behaviour of Ce throughout the

Archaean microbial carbonate record, represented in this study by samples spanning from 3.45 to 2.52 Ga. The most critical aspect of such an analysis is technical in nature and concerns the mathematical approach to calculating the extent of the Ce anomaly. There is very wide agreement about the fact that in seawater and its precipitates the Ce anomaly cannot be calculated in the conventional way. Namely, it is not possible to predict the expected (purely trivalent) Ce abundance by interpolating between La and Pr, due to the large excess La in seawater. This approach would result in artificial negative Ce anomalies. One convenient way to overcome this issue is to plot the apparent Ce anomaly against the apparent Pr anomaly (Bau and Dulski, 1992, 1996; Bau 1993; Bau and Möller, 1993), where the apparent Pr anomaly results from over- or under-abundance of Ce and the apparent Ce anomaly reflects over- or under-abundance of La as well as Ce (Figure 5a). This approach shows that all stromatolites studied and discussed here show positive La anomalies but none show well-developed Ce anomalies. This is unlike post-GOE BIF, which display largely positive Ce anomalies (expressed in Fig. 5a as negative apparent Pr anomalies) but also negative Ce anomalies. The prevalence of positive Ce anomalies in BIF is attributed to excess Ce scavenged from oxidised shallow seawater later released below a chemocline, where BIF precipitated. Modern seawater and Holocene microbial carbonates show consistently negative Ce anomalies, expressed in Fig. 5a as apparent positive Pr anomalies. However, this analysis of the Ce anomaly only makes use of information contained in the abundances of La, Ce, Pr and Nd (the latter used to calculate the apparent Pr anomaly).

An alternative way of directly calculating the Ce anomaly without the use of La was introduced by Lawrence and Kamber (2006; 2007). The idea behind this analysis is to project the expected Ce content from normalised Nd and Pr values as shown on figure 6, where the expected Ce abundance (Ce*) is calculated as $Ce^* = Pr_n \times (Pr_n / Nd_n)$. Although this approach eliminates artefacts introduced by the use of La, it is found commonly that the observed Ce abundance is higher by 10 to 20% than that projected from Pr and Nd. This is also evident in the plot of the apparent Ce anomaly against the apparent Pr anomaly (Bau and Dulski, 1992) as a small but consistent apparent negative Pr anomaly of ca. 0.9 (Fig. 5a).

Notwithstanding this limitation, histograms of directly calculated Ce anomalies are shown on Figures 5b and 5c. These illustrate that the post-GOE BIFs display a

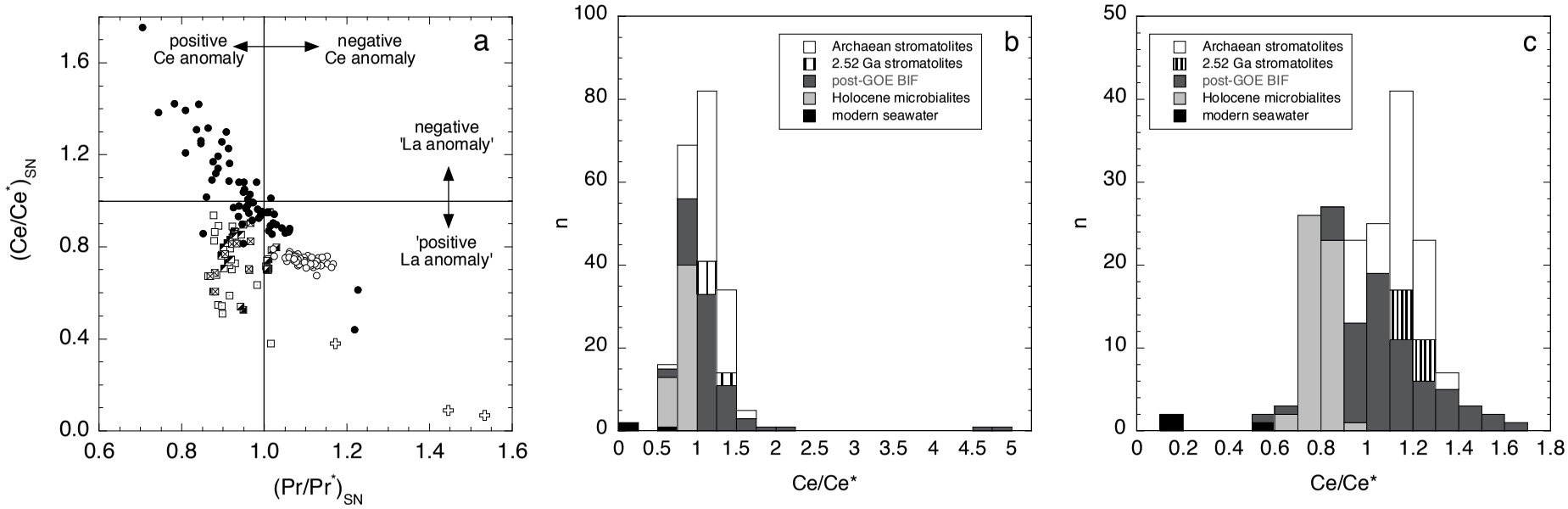


Figure 5: Panel (a): Plot of conventionally calculated Ce anomaly versus apparent Pr anomaly (normalisation with MuQ; Kamber et al., 2005). Archaean stromatolite data sources as follows: 2.52 Ga (this study), 2.65 Ga (this study: all data panel a; solution data only panels b and c), 2.82 Ga (see Fig. 3), 2.93 Ga (all data of Planavsky et al., 2010) and 3.45 Ga (all ACA samples of Allwood et al., 2010). They are shown as variably ornamented squares and all have positive La anomalies and have $(Pr/Pr^*)_{MuQN}$ of 1.0 to 0.85. By contrast, Holocene microbialites (open circles) all have $(Pr/Pr^*)_{MuQN} > 1.0$ as has modern seawater (open crosses). Post-GOE banded iron formation (data from Frei et al., 2008 and Planavsky et al., 2010) show a wide array of behaviour, ranging from large positive Ce anomalies to moderately negative anomalies. Panel (b) shows a histogram of the Ce anomaly calculated by projection from the Nd-Pr join. The range is skewed to very large positive values due to the post-GOE BIFs. Panel (c) shows a detail of panel (b) from which it becomes evident that none of the Archaean stromatolites have significant Ce anomalies, contrasting with post-GEO BIF and modern microbial carbonates (all show negative anomalies) and modern seawater (also showing negative anomalies).

very wide range of Ce anomalies, strongly supporting the view that by 2.3 Ga, there was sufficient free O to oxidise Ce that was adsorbed onto particles but also arguing for a redox chemocline below which the excess Ce was released from sinking particles. Modern seawater and Holocene microbial carbonates show clear negative Ce anomalies (see also Fig. 2b). As already mentioned, the Archaean stromatolites have an average Ce anomaly of ca. 1.1, 10% higher than a perfect neutral value. The Archaean data cluster very tightly (Figs. 5b and c) and do not approach the level of variability found in post-GOE chemical sediments.

It is likely that future discussions about the lead-up to the GOE will focus more closely on the behaviour of Ce in the shallow seawater. In this regard, the persistent apparent positive Ce anomaly (by +10%) in the calculation of Lawrence and Kamber (2006; 2007) and the equivalent ca. -10% negative Pr anomaly in the calculation of Bau and Dulski (1992) for all Archaean microbial carbonates will require an explanation. The most straight-forward solution is that many shallow seawater proxies have shale-normalised REE+Y patterns that are not simple straight lines with a positive slope in shale normalisation. Rather, there appears to be a slight upswing of the lightest REE in most Archaean marine precipitates (Fig. 6a) that may also be evident in modern seawater (e.g. Fig. 2b). Because Sm, Nd and Pr are located in the region of upswing of the REE+Y pattern, a linear projection from these elements to Ce will result in an underestimate of expected Ce (and La) abundances (Fig. 6b) and calculation of an apparent positive Ce anomaly. Since there is no non-anomalous REE lighter than La, possible solutions to this problem are restricted to making better use of the REE data heavier than Nd. One possible approach is to plot the REE+Y patterns as a function of ionic radius instead of atomic number. This permits the calculation of a function describing the normalised abundance of REE+Y. In petrological studies, this is generally referred to as an Onuma-diagram and is useful to determine the ionic radius of the cation in the ideal lattice site into which REE substitute (Onuma et al., 1968). Figure 7a shows Onuma-style REE 'patterns' for the 2.52 and 3.45 Ga average microbial carbonate data approximated by second-order polynomial fits. These fits were obtained from the non-anomalous REE only and can be used to predict the expected abundance of the REE+Y that show anomalies in seawater. The comparison of the predicted vs. observed abundances is shown in Figure 7b and demonstrates that this approach has potential to better quantify true Ce anomalies, which are 0.994 and 0.991, respectively, for the 2.52 and 3.45 Ga data. In other words, these values are

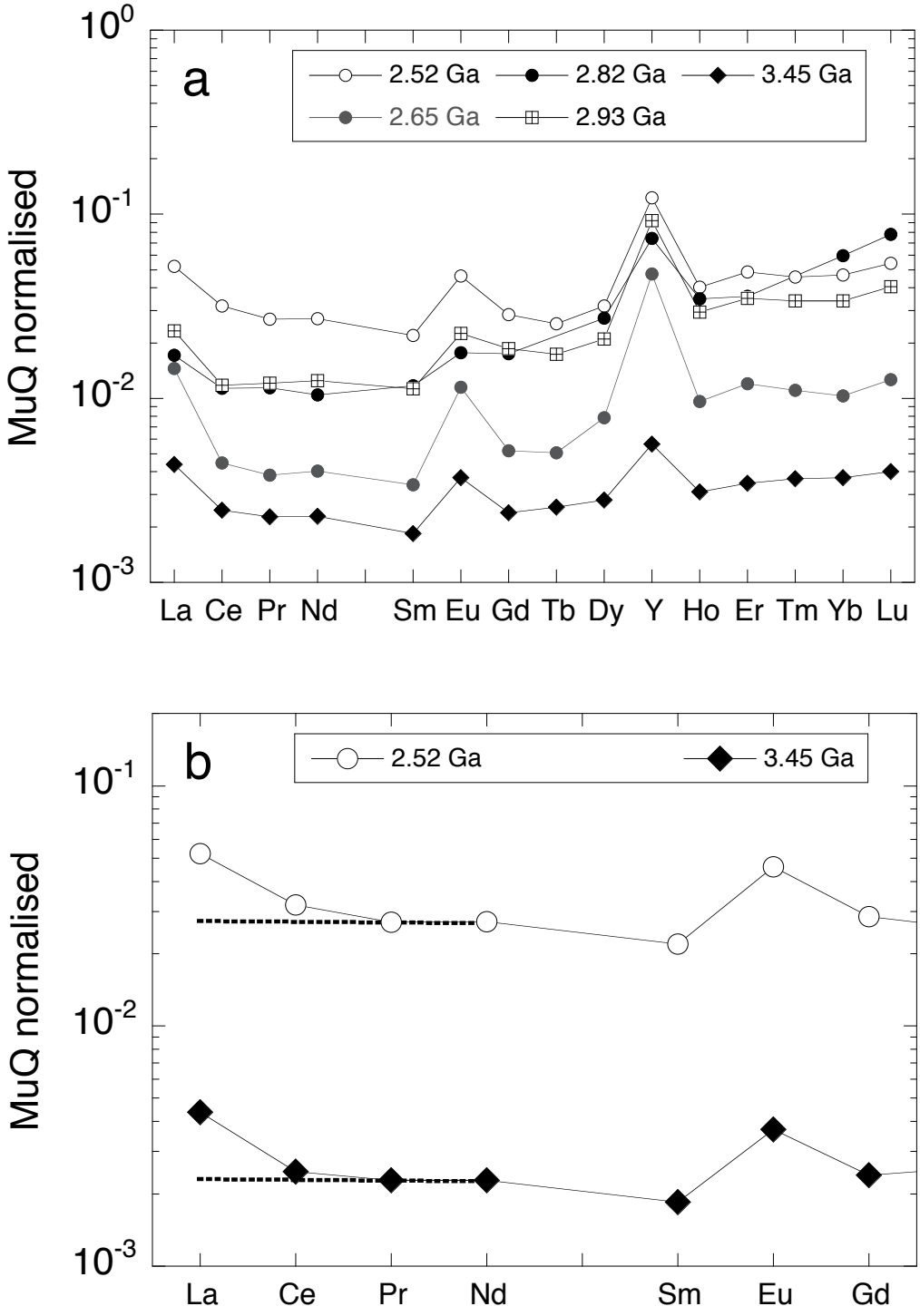


Figure 6: Panel (a): Normalised REE+Y patterns for average compositions of stromatolites studied here (note that 2.82 Ga Mushandike stromatolites are TTG normalised, as explained in Fig. 3). All sample groups show elevated La, Eu and Y, resulting in clearly discernible positive anomalies. Panel (b): Detail of lighter half of REE+Y patterns of averages of 2.52 and 3.45 Ga samples only. The heavy dotted line denotes the slope from Nd to Pr and is projected to Ce and La. The large excess in observed La over the position of the La content predicted from the Nd-Pr join permits calculation of the positive La anomaly. In a similar fashion, the Ce anomaly can be calculated. In both illustrated cases, small (ca. 10-20%) positive Ce anomalies are indicated. Same data sources as Fig. 5.

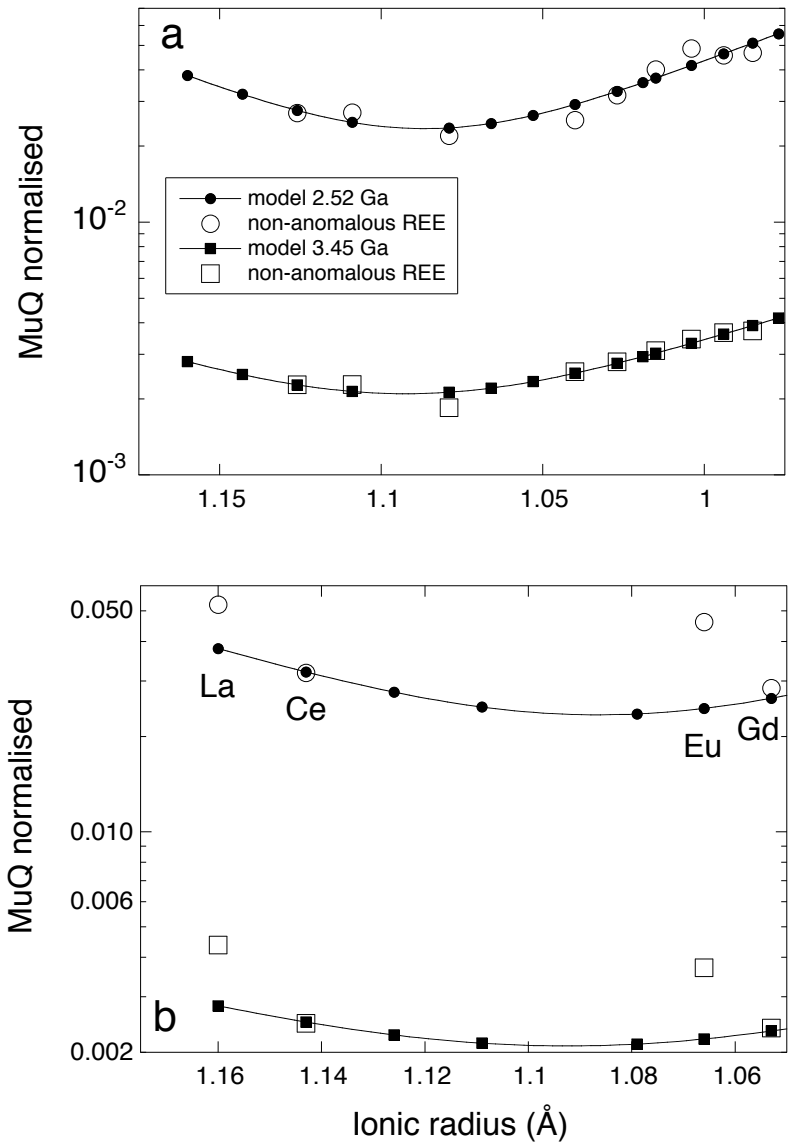


Figure 7: Panel (a): Second-order polynomial functions (normalised REE value vs. ionic radius in 8-fold coordination (note that other coordinations yield similar results), from Shannon, 1976) proximating average REE patterns of 2.52 and 3.45 Ga samples (same sources as Figs. 5 and 6). The large open symbols show the elements of non-anomalous abundance in seawater (i.e. Pr, Nd, Sm, Tb, Dy, Ho, Er, Tm and Yb), which were used to obtain the polynomial fits. Fits yielded r^2 of 0.883 and 0.955 for 2.52 Ga and 3.45 Ga average data, respectively. (b) Detail of lighter half of REE spectrum, analogous to Fig. 6b, plotting anomalous REE as open large symbols (i.e. La, Ce, Eu and Gd). As can be seen, the polynomial fits (small solid symbols connected by fine solid line) in both cases predict the observed Ce abundance very well but still result in well-resolvable La and Eu as well as small Gd anomalies.

easily within the typical 2% analytical uncertainties, and demonstrate that these samples show no appreciable deviation from strictly trivalent behaviour. A more rigorous test will have to be conducted to explore whether extrapolation with second-order polynomial fits can also lead to undesired artefacts, but the analysis presented here suggests that there is no difference in terms of redox-behaviour of Ce between 3.45 Ga and 2.52 Ga in shallow seawater as sampled by well-preserved microbial carbonates.

The final aspect of REE+Y systematics of Archaean hydrogenous sediments relevant to the redox evolution of the ocean is the persistent presence of a strong positive Eu anomaly. This phenomenon was discussed in more detail in Kamber (2010). There is wide agreement that the excess Eu enters the ocean from vents of high T hydrothermal fluids due to Cl^- complexation of the REE (Bau and Dulski, 1999; Douville et al., 1999). It is significant that strong positive Eu anomalies are found not only in deeper water hydrogenous sediment such as BIF (e.g. Jacobsen and Pimentel-Klose, 1988) but also in all shallow water microbial carbonates (Fig. 6a). This firmly indicates that the deep Archaean ocean remained anoxic because in a ventilated deep ocean, all high T hydrothermal vent-derived REE, including the excess Eu, are scavenged onto particles that form upon mixing of vent with ambient waters (Michard and Albarède, 1986).

3.3.2. Synthesis of redox information for the Neoarchaean

There is currently much research interest in the redox evolution of the Archaean ocean and an attempt to summarise and synthesise the new geochemical information together with sedimentological and geological facts would be premature. In essence, the new geochemical data can be classified into evidence that favours local oxygen 'oases' in shallow seawater versus significant build-up of free oxygen to permit oxidative weathering on land and release of redox-sensitive metals into the ocean. The key implication of the latter idea, specifically the release of Mo from weathering of terrestrial sulphides well before the GOE (e.g. Wille et al., 2007 and Anbar et al., 2007), is that oxidation of the Earth's atmosphere was not a unidirectional, irreversible process. Most claims for significant build-up of molecular O in the Neoarchaean atmosphere are based on data from deep water sediments. For example, the original proposal of a whiff of free O by Anbar et al. (2007) was made

based on redox-sensitive metal accumulation in the Neoarchaean McRae black shale. A gradual Neoarchaean increase in free O was also postulated by Wille et al. (2007) from Mo-isotope data recorded in black shales. More recently, Frei et al. (2009) used Cr-isotope evidence from deep water BIF to argue for fluctuations in Archaean atmospheric oxygenation. Godfrey and Falkowski (2009) studied N-isotope compositions in organic matter retrieved from shale to imply the presence of coupled nitrification and denitrification or anammox reactions in the surface ocean by 2.50 Ga, also requiring significant free O not only in the surface ocean but in the atmosphere. Most recently, Kendall et al. (2010) argued for pervasive oxygenation along the late Archaean ocean margins studying reactive Fe, as well as Re and U and other metal concentration profiles in the deep water sediments that are interpreted as lateral equivalents to the shallow water Campbellrand platform carbonates. The REE+Y systematics of shallow water microbial carbonates are themselves not sensitive to oxidative versus reduced weathering on land, but rather the shape of the marine REE+Y pattern is affected by the type of rock exposed to terrestrial weathering (Kamber , 2010). For this reason, it is not possible to evaluate claims for intermittent oxygenation of the Neoarchaean *atmosphere* with marine REE+Y systematics.

By contrast, it seems logical to test the local shallow seawater O oasis hypothesis with analysis of the Ce anomaly, particularly considering that stromatolite producing biota have been implied to be the source of free O. Surprisingly, there is much less sedimentological and geochemical evidence for O oases from shallow marine sedimentary rocks themselves than from deep water facies. The geochemical expression of local O build-up is not the same as that for O production. The latter has been inferred from a number of lines of evidence, including the extent of C-isotope fractionation preserved in Neoarchaean reduced C (e.g. Grassineau et al., 2002), Neoarchaean stromatolite diversity (e.g. Wilks and Nisbet, 1988, Buick, 1992), and preservation of possible cyanobacterial mats (e.g. Noffke et al., 2008). Evidence for actual build-up of dissolved free O in the shallow marine environment was presented by Zerkle et al. (2012). They provided Fe-speciation data for a variety of Transvaal sedimentary rocks, mainly from the deeper water facies, but they found that some of the shallower water microbial carbonates had low ratios of highly reactive to total Fe, which were used to argue for oxygenation of the shallow seawater. Thus, the Fe

speciation data for some of the microbial carbonates analysed by Zerkle et al. (2012) would logically predict that these very carbonates should be characterised by negative Ce anomalies. However, neither careful solution ICP-MS (Kamber and Webb, 2001), nor detailed petrographically guided LA-ICP-MS data (see next section) of microbial carbonates comparable to those analysed by Zerkle et al. (2012) yielded appreciable Ce anomalies (see also Fig. 7).

This lack of a recorded Ce anomaly in Neoarchaean stromatolites either means that shallow seawater was not oxygenated to the level required for Ce^{4+}, or that Ce^{4+} oxidation was inhibited. Bau (1999) and Bau and Koschinsky (2009) have demonstrated that Ce oxidation is ineffective for dissolved Ce^{3+} but that it proceeds readily once sorption onto Mn- or Fe-oxi-hydroxides has occurred. It could thus be argued that the absence of a negative Ce anomaly in dissolved Neoarchaean seawater proxies could be attributed to the lack of Mn- or Fe-oxi-hydroxides. However, whereas the sustained formation or preservation of Mn-oxi-hydroxides would require significant amounts of free O, the very co-existence of shallow water stromatolites with laterally equivalent BIFs across the Campbellrand platform, and in some cases the co-existence of interbedded carbonate and BIF (Sumner, 1997a), proves that Fe-oxi-hydroxides were present. Furthermore, the existence of herringbone carbonate layers that can be laterally traced along the palaeo-seafloor indicate substantial dissolved Fe concentrations in the Neoarchaean ocean. Thus, at present the limited geochemical data from shallow water Neoarchaean sedimentary rocks allow mutually incompatible interpretations.

In considering this situation, readers are reminded of the superb preservation status of the organic material in Neoarchaean stromatolites (see also the following section). Since organic matter is the main sink of molecular O, the intricate and superbly preserved kerogen mat structures in the stromatolites is, in itself, evidence against pervasive free O that would have oxygenated and destroyed the organic matter. Instead, the kerogen contains an array of molecular fossils (Waldbauer et al., 2009) indicative of the co-existence of all three domains of life. According to the latest experiments (Waldbauer et al., 2011) dissolved O_2 concentrations in these microbial mat environments may have reached only nanomolar levels and oxygen may have been rapidly cycled as a biogenic trace gas. This finding is in agreement with Sumner's (1997a) conclusion that the presence of a few $\mu mol\ l^{-1}$ dissolved Fe in the

mixed zone of the Neoarchaean ocean was not permissive of pervasive oxygenation. Taken together, the current weight of evidence supports the REE+Y observations that imply insufficient quantities of molecular O to oxidise Ce that had experienced sorption onto Fe-oxi-hydroxides.

The reconstruction of the oceanic and atmospheric redox evolution in the lead up to the GOE (and the disappearance of mass independent fractionation of S; e.g. Papineau et al., 2005) is far from complete. The indirect evidence regarding the shallow sea from deep water sedimentary rocks needs to be complemented with better study of the commonly very well-preserved but rare shallow water sedimentary rocks. All geochemical studies relying on trace elements (which may include Fe) also will need to be subjected to more critical study of the influence of overprint by diagenetic fluids (e.g. Pufahl and Hiatt, 2012) before consensus will emerge regarding the build-up of free O.

4. REE inventories as possible biomarkers

4.1. Information from Phanerozoic microbial carbonates

Coherent shale-normalised REE+Y patterns, which are indistinguishable in shape from those of ambient Coral Sea water, occur in Holocene microbial carbonates from the Great Barrier Reef (Webb and Kamber, 2000). A less widely appreciated aspect of the study by Webb and Kamber (2000) is that the absolute abundances in the microbial carbonates were significantly higher than in co-existing skeletal carbonates. The apparent partition coefficient between seawater and Holocene microbial carbonate relative to Ca concentration was found to be constant (296±30) across the REE+Y spectrum and the 1 sigma standard deviation averaged a modest 10%. Such high apparent distribution coefficients contrast with those of coral (e.g. Sholkovitz and Shen, 1995), which are between 50-250 times lower.

Nothdurft et al. (2004) obtained micro-drilled samples of the calcimicrobe *Renalcis*, interstitial *Renalcis* micrite and diagenetic clear cement from individual petrographic thick sections of Late Devonian reef limestone. Replicates of *Renalcis* concentrates yielded very similar high REE concentrations of discernible seawater origin. The surrounding micrite, which on petrographic ground was suspected to be of largely microbial origin had only marginally lower REE concentrations with

identical shale-normalised patterns, while the early marine cement proved to have much lower REE+Y concentrations. Hence, the marine carbonates in these samples shared the typical seawater REE pattern and preserved a concentration contrast on the order of 20. Kamber and Webb (2007) revisited these Devonian samples with LA-ICP-MS and found that there were discrete trace element contrasts (mainly in transition metals) between marine cement and the calcimicrobe *Renalcis* but that the contrast in La content was only ca. 20-30, unlike in modern microbial carbonate, which is 50-250 times richer in REE+Y than the co-existing skeletal carbonate. There is thus a possibility that REE+Y concentration contrasts might serve as chemical biomarkers in samples of Precambrian age.

4.2. New information from Neoarchaean microbial carbonates

In the absence of comparable skeletal carbonate, Archaean microbial carbonate REE+Y concentrations can be compared only to early diagenetic cements. Therefore, attempts at testing for REE+Y concentration contrasts are restricted to the very best preserved microbial carbonates. Even in these exceptional samples, the REE+Y concentration contrast might be reduced by incipient recrystallisation, requiring *in situ* data to make best use of petrographic information. Two exquisite stromatolite occurrences were analysed here. Both contain well-preserved fenestral carbonate available for analysis between contorted microbial carbonate and *Conophyton* structures.

The first dataset was obtained from three hand-specimens of 2.65 Ga Huntsman Quarry stromatolite (Rh-73-215A, B, C). Multiple sections were cut through all specimens and multiple thin sections were obtained from those portions with the most abundant fenestral cement. Petrographic inspection of sections from sample Rh-73-215A revealed that all clear calcite was recrystallised whereas the other samples appear to preserve >200μm domains of less recrystallised carbonate cement. The sections with the best preserved such carbonate were selected for LA analysis from both specimens.

Figure 8 shows the data for Rh-73-215A. The normalised REE+Y patterns have clear marine character and the shape of the patterns obtained from the microbial mats and the late cement are identical. The concentration contrast between the two

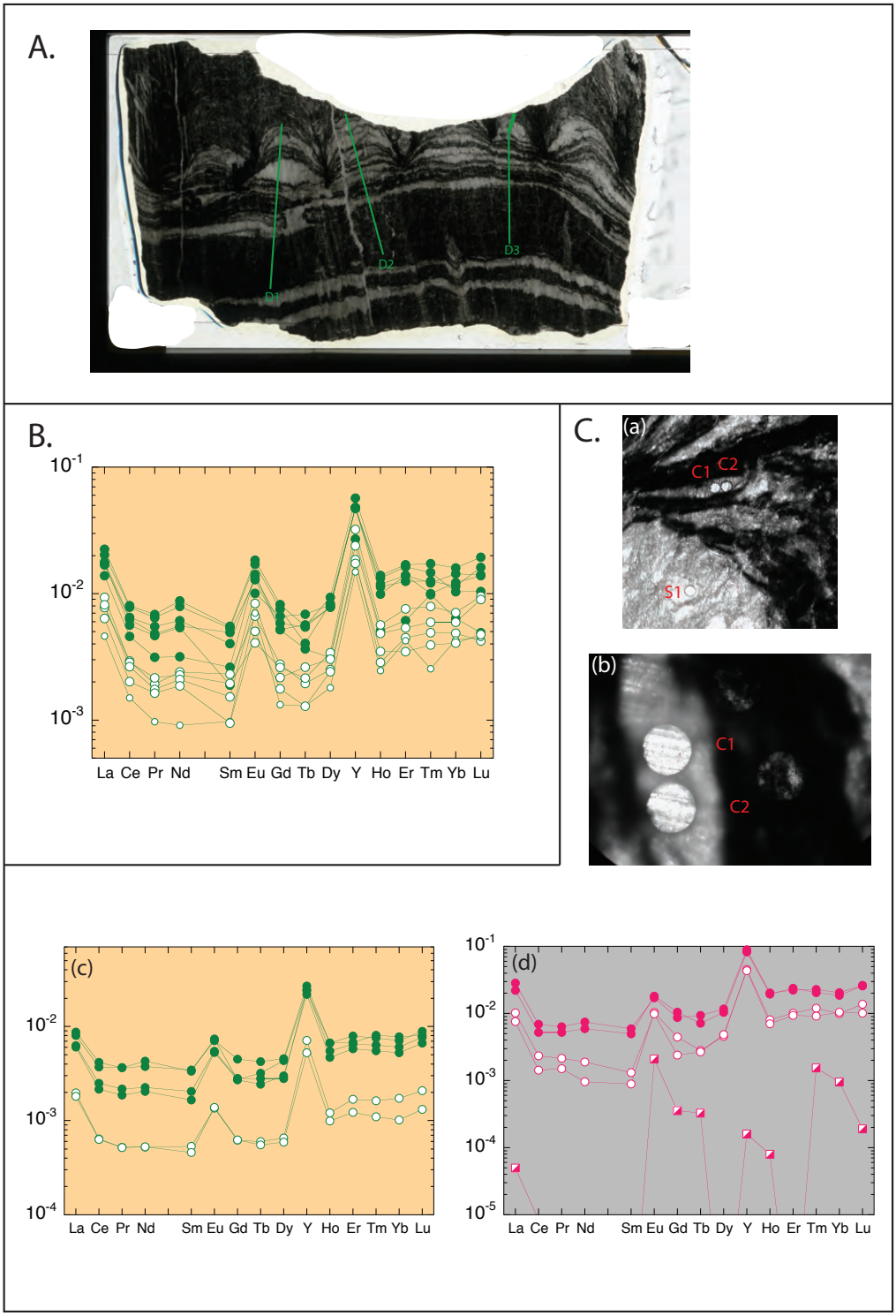


Figure 8: Photomicrographs and REE+Y patterns for samples Rh-73-215A and C. Panel (a) An overview transmitted light image (slide is 2.5 cm long) of Rh-73-215A with the Trinity College Dublin (TCD) ablation profiles shown as traces (labels identical to Table 1). Panel (c) TCD MuQ normalised REE+Y laser data for Rh-73-215A. The open circles represent the late, coarse-grained, carbonate cement segments of the ablation profiles D1, D2 and D3. The solid circles represent the dark carbonate algal mat segments of the ablation profiles D1, D2 and D3. Panels (c to f) show data relevant to sample Rh-73-215C. (c) shows an overview transmitted light image with three Australian National University (ANU) ablation spots labelled (crater diameter is 137 μm). (d) shows a close up of two ablation craters

focussed on the crater pit. These craters expose twinned coarse grained (secondary) sparry cement. (e) shows MuQ normalised REE+Y solution ICP-MS data for Rh-73-215C. The open circles represent solution data for the late, coarse-grained, carbonate cement while the green circles represent solution data for the dark carbonate algal mats. (f) displays ANU MuQ normalised REE+Y laser data for Rh-73-215C. The solid circles represent data for ablation spots M1 and M2 in the black organic, carbon rich algal mat. The open circles represent data for ablation spots C1 and C2 in the interlayered, light-coloured, early cement. The square symbols represent data for ablation spot S1 in the late, least-recrystallised carbonate cement.

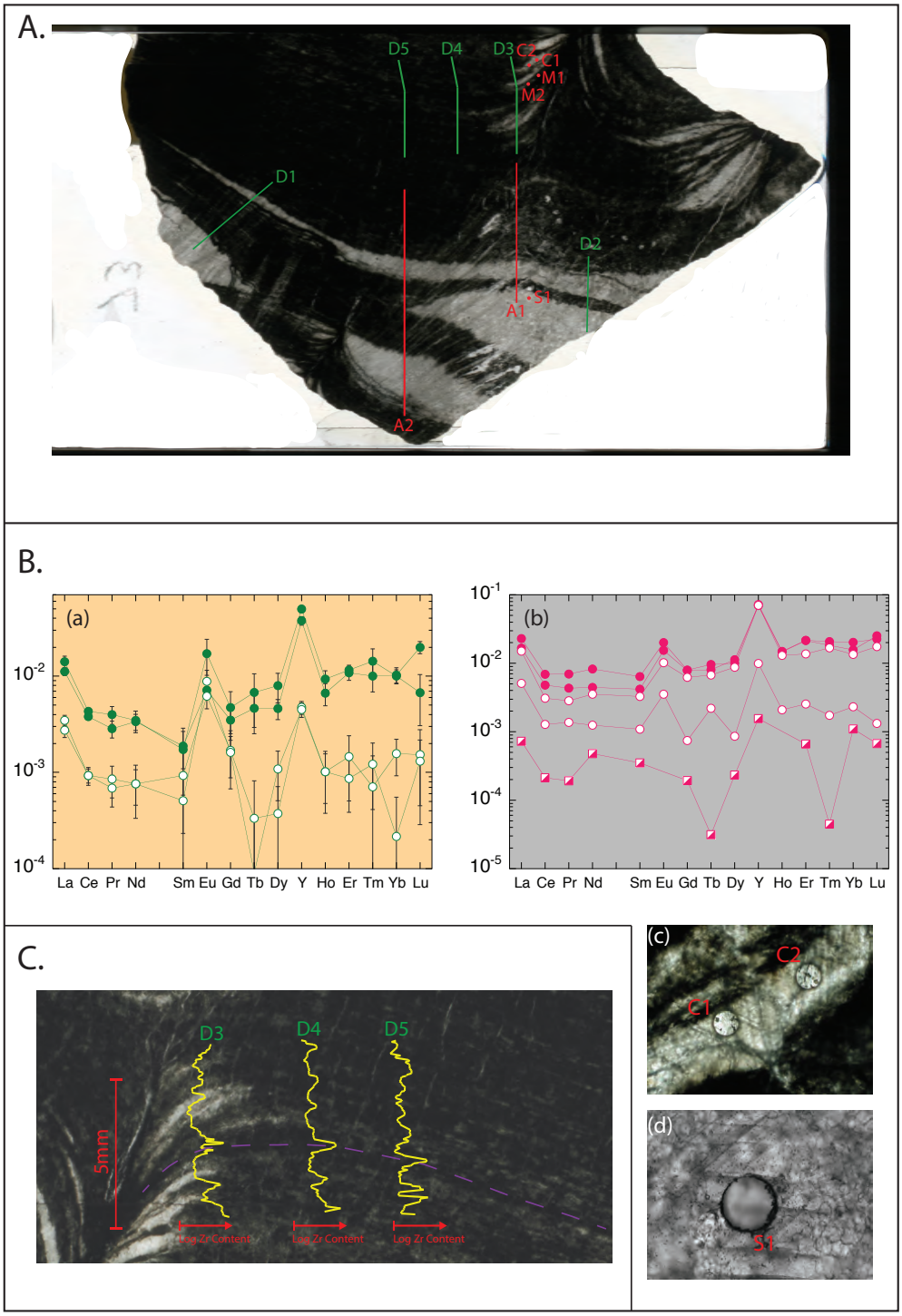


Figure 9: Panel (a): An overview transmitted light photograph of section Rh-73-215B with the Trinity College Dublin (TCD) ablation profiles labelled (D) as stippled lines (labels identical to Table 1) and the Australian National University (ANU) ablation profiles (labelled with A) as solid lines. All spot analyses performed at ANU. Panel (b) shows TCD MuQ normalised REE+Y LA-ICP-MS data with error bars. The open circles represent the late recrystallised carbonate cement segments of the ablation profile D1. The solid circles represent the dark carbonate algal mat segments of the ablation profile D1. Panel (c) ANU MuQ normalised REE+Y LA-ICP-MS data. The solid circles represent data for ablation spots M1 and M2 in the black organic, carbon rich algal mat. The open circles represent data for ablation spots C1 and C2 in the interlayered, light-coloured, early cement. The square symbols represent data for the ablation spot S1 in the latest, coarser-grained carbonate cement. Inserts (d) and (e) show petrographic inspection of Rh-73-215B focussing on the ablation sites C1, C2 and S1. C1 and C2 ablation spots are situated in the interlayered, light-coloured early cement. The S1 ablation spit is situated just inside a >200μm domain of deformed, twinned, coarser-grained carbonate cement surrounded by recrystallised finer-grained calcite. Panel (f) shows raw Zr signals (log scale) for profiles D3, D4 and D5. The Zr peaks can be traced along individual layers in otherwise indistinguishable dark coloured algal mat material.

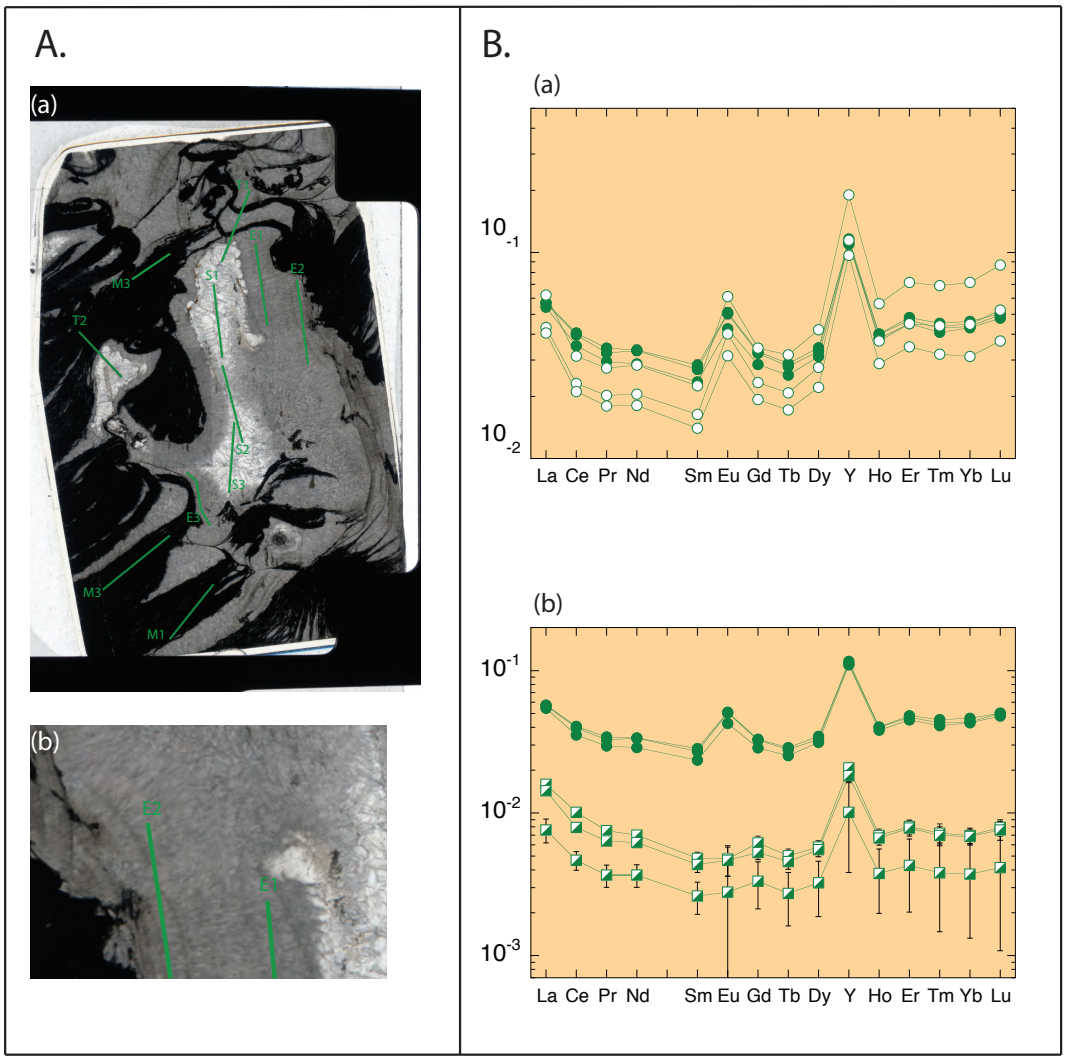


Figure 10: Petrography and REE+Y systematics in a *Conophyton* stromatolite of the 2.52 Gamohaan Formation. Panel (a) shows a transmitted light photograph of the entire thin section. This clearly illustrates the three carbonate types, consisting of black microbial structures (*Conophyton*) early directed, grey carbonate cement and later clear and coarse-grained carbonate cement. The various LA traverses are superimposed as traces and labelled identically to Table 2. Insert (b) shows an 8 mm wide detailed photograph of profiles E1 and E2 in the early carbonate cement. Panel (c) shows MuQ normalised REE+Y laser data for SrKu5. The solid circles represent data for ablation profiles M1, M2 and M3 in the dark carbonate algal mat. The white circles represent data for the ablation profiles E1, E2 and E3 in the early carbonate cement. TCD MuQ normalised REE+Y laser data for SrKu5. In insert (d) the solid circles represent data for ablation profiles M1, M2 and M3 in the dark carbonate algal mat. The square symbols represent data for the ablation profiles S1, S2 and S3 in the late clear carbonate cement.

Table 2. *Trace element concentrations (in ppb) determined by TCD LA-ICP-MS*

Sample name:	SRKU5																					
Carbonate type:	Mat 1	±	Mat 2	±	Mat 3	±	Early Cement 1	±	Early Cement 2	±	Early Cement 3	±	Spar 1	±	Spar 2	±	Spar 3	±	Traverse 1	±	Traverse 2	±
Sr	44120	380	43630	430	44750	510	53940	860	56620	610	58800	1000	40900	1500	35500	1300	42600	1600	55100	1300	69700	6700
Ba	9740	710	8550	830	13000	1000	6724	97	5746	77	5990	110	663	44	980	110	1170	200	6650	550	16300	2700
La	1764	31	1847	39	1856	57	1405	20	2016	47	1322	17	518	29	248	36	467	47	1049	85	1210	130
Ce	2506	51	2830	130	2890	130	1639	25	2228	49	1500	22	722	38	332	49	565	51	1370	110	1920	220
Pr	249.8	6.7	275.5	9.3	290	14	171.2	3.4	232.5	5.5	151.9	3.4	63.8	3	31	4.7	53.8	4.6	139	11	173	22
Nd	947	26	1099	58	1108	59	675	13	933	22	596	12	230	11	121	18	205	17	545	47	645	85
Sm	161.8	5.3	186.4	9.5	195	12	112.7	3.5	155.2	4.6	96.3	3.6	33.1	2.2	18	2.9	30	2.9	87.6	8.1	105	19
Eu	66.8	2	79.2	4.5	80.2	4.6	63.1	1.8	95.7	3.7	49.4	1.7	7.49	0.54	4.38	0.64	7.35	0.73	42.1	4.5	48.7	7.3
Gd	182	6.6	206.3	9.6	210	10	148.4	4.6	218.1	7.7	122.5	3.6	39.3	2.1	21.2	3.4	33.6	3	109	10	113	20
Tb	25.1	0.75	27.65	0.97	28.6	1.5	20.58	0.57	31.5	1.1	17.07	0.53	4.97	0.27	2.7	0.44	4.53	0.46	14.1	1.5	15.9	2.7
Dy	184.4	5	194.6	5.3	203.2	8.7	163	3.7	248.2	8	130.5	3.6	34.1	2	19.1	3	32.7	2.9	109	11	112	19
Y	3494	61	3697	64	3553	90	3642	63	6060	200	3085	51	661	60	322	53	583	77	2270	250	1870	320
Ho	46.6	1	48.9	1.4	49.1	1.8	45.4	0.94	68.7	2.2	35.27	0.9	8.49	0.6	4.61	0.7	8.16	0.81	30.3	3.1	28.5	4.8
Er	151.8	3.2	158	3.5	162.8	6.4	152.3	3.1	240.8	7.7	117.3	3.2	27.1	2	14.5	2.3	26.4	2.9	97	11	88	15
Tm	20.92	0.55	21.87	0.67	23.08	0.75	22.41	0.6	35.2	1.2	16.34	0.54	3.68	0.29	1.95	0.33	3.55	0.41	14	1.6	12.4	2.1
Yb	139.9	3.7	142.1	3.1	150.5	5	145.4	2.9	232.7	7.8	101.6	2.9	22.6	1.7	12.1	2	22.3	2.4	89	10	78	13
Lu	23.47	0.78	24.46	0.62	24.68	0.69	25.74	0.51	42.5	1.5	18.24	0.57	3.89	0.33	2.03	0.33	3.73	0.42	15.5	1.7	11.9	2.2

carbonate types ranges from ca. 2.5 to 5. In sample Rh-73-215C, an attempt was made to micro-drill small (0.034 to ca. 4 mg) aliquots from mat carbonate and clear cement. The much smoother patterns resulting from solution ICP-MS (Fig. 8C) are identical in shape to those obtained from sample Rh-73-215A and the resulting concentration contrast ranges from 3 to 7, in favour of the microbial mats. Spot analyses by LA-ICP-MS were also performed to not only target mats and cements but to distinguish between more recrystallised cement and vestiges of less recrystallised calcite. The resulting REE+Y patterns were identical to those obtained by solution ICP-MS, and the concentration contrast between mats and recrystallised cement was also comparable. However, the better preserved cement yielded much lower REE+Y contents, clearly below the LA-ICP-MS detection limit.

Figure 9 shows data for Rh-73-215B. The findings from this section are very similar to those of Rh-73-215C. The REE+Y patterns have a very similar shape to those of the other samples from the Huntsman Quarry stromatolites. In this case too, the microbial mat carbonate is between 5-10 times more enriched in the REE+Y than the cement. Although LA-ICP-MS concentrations are very low in the cements (Table 1) all element averages except Eu and Lu can be resolved outside analytical error between microbial mats and cements. Identical to Rh-73-215C, spot analyses confirm (Panel B, insert b) that the less recrystallised cement has lower concentrations in the REE+Y than the material that has either undergone annealing or shows deformation-related subgrains. An additional phenomenon that was exposed in this stromatolite is the incorporation of detrital material. For this purpose, three lines were analysed perpendicular to the inferred mat growth direction and signals of Zr, Th and Al were superimposed on the photomicrograph. This showed (Fig. 9, panel C) that individual 'events' of trapping detrital or volcanic sediment input can be identified. Because any sample period over an LA-ICP-MS scan can be integrated, it is possible to avoid undue influence of detrital REE+Y on analyses of carbonate.

The second stromatolite locality that was investigated with more detailed *in situ* analyses was a *Conophyton* from the 2.52 Ga Gamohaan Formation (Figure 10). In this sample, it is easy to distinguish between the dark microbial carbonate structures that make up the *Conophyton* and an early marine cement that grew radially away from the microbial structures. This grey cement is very fine-grained and consists of layers of epitaxial, parallel families of individual calcite crystals. This type of cement

filled the largest portion of space between the microbial mats and much coarser grained, completely clear calcite fills the final space. Extensive LA-ICP-MS work on this sample showed that all carbonate types have the same REE+Y pattern (comparable to other microbial carbonates from the Gamohaan Formation, e.g. Kamber and Webb, 2001). There is no systematic and coherent concentration contrast of REE+Y between microbial mats and early cement but a clear 6-10 fold difference between the late, less concentrated cement. This observation suggests that the early epitaxial cement still grew under the influence of microbial activity or decay and only the last clear cement is truly inorganic. A similar finding was made in the Devonian *Renalcis* bearing limestones, where early micrite likely originated from microbial activity.

4.3. Origin of the preferential REE+Y uptake into microbial carbonate

The Huntsman Quarry and Gamohaan Formation stromatolites show similar REE+Y concentration contrasts with abiogenic cements as Devonian microbial carbonate. In the Huntsman Quarry samples, the majority of cements are recrystallised and their REE+Y content is higher than least recrystallised, early cement, suggesting that the original contrast may have been higher still. The current detection limits of LA-ICP-MS do not permit precise determination of full REE+Y patterns in the most depleted cements but the possibility exists that the true concentration contrast between Huntsman Quarry microbial carbonate (as represented by the darkest, detritus-free mats) and the best preserved early marine cements is similar to that between Holocene microbial carbonate and coexisting skeletal carbonate. In the Gamohaan Formation *Conophyton* stromatolite, early epitaxial cement likely grew under the influence of microbial activity or decay but clear, coarser-grained marine cement is easily distinguished from microbial mat carbonate.

It is tempting to postulate the elevated REE+Y content in putative microbial carbonates of great antiquity as a possible biomarker. For example, Bolhar et al. (2004) noted that a carbonate-magnetite BIF from the 3.71 Ga Isua supercrustal belt had the typical REE+Y signature of Archaean seawater and also that it was substantially enriched in REE+Y over oxide facies BIF. In a later study, Friend et al. (2008) confirmed the elevated REE+Y content of further Isua supercrustal belt

carbonate BIFs, suggesting that although the rocks as they are preserved today are undoubtedly remobilised, the carbonate nonetheless likely originated as a sediment. Due to the recrystallised nature of these rocks, it is not possible to test for a concentration contrast between possibly microbial and abiotic carbonate. This is all the more a problem because the REE+Y inventory of Archaean seawater is unknown and higher absolute concentrations in carbonate could simply have resulted from a higher dissolved marine REE+Y load.

Before the preferential uptake of the REE+Y into microbial carbonate can be established as a biomarker, more experimental data on REE co-precipitation into calcite are required. Existing data (Terakado and Masuda, 1988; Zhong and Mucci, 1995; Tanaka and Kawabe; 2006) are mutually inconsistent, both in regards to absolute and relative partition coefficients. To what extent the discrepancies reflect different experimental design (e.g. constant addition vs. steady-state) or the unreasonably high REE concentrations in the experimental 'seawater' solutions remains unclear but, at present, it is not possible to experimentally predict the incorporation of dissolved marine REE into inorganic carbonate, even under known modern conditions (involving carbonate ions and humate complexes, e.g. Pourret et al., 2007). The experimental situation for biologically mediated carbonate precipiation is even less satisfactory but possibly not a first order concern. Notwithstanding the possible role of organic matter (of the microbial biofims) for REE+Y sorption, it is clear that even the surface structure of calcite strongly affects the sorption efficiency of calcite (Sawada et al., 2005). Ultimately, through the delicate processes of lithification and recrystallisation, the REE+Y that may originally have been bound onto organic matter will become incorporated into the carbonate lattice. The apparent redistribution or REE+Y between calcite of clearly microbially-induced origin into 'clear' calcite through recrystallisation shown in Neoarchaean stromatolites (e.g. Fig. 9d), for example, suggests that REE+Y may be lost in the process and that recrystallisation will tend to reduce the original concentration contrasts between inorganic and microbially induced carbonate. This could explain the pattern of diminishing contrasts found in samples of increasingly old age. At present, the authors caution against an uncritical acceptance of the REE+Y concentration contrast as a biomarker. However, it would seem prudent that the extraction of any potential biomarker from microbial carbonate should only be

attempted on samples that show the predictable REE+Y excess over coexisting abiogenic cements.

5. Summary

Ancient limestones hold great potential to help with reconstructing the Precambrian surface environment. However, their variable state of preservation demands minimum criteria that studies of such material need to satisfy:

i) The trace element budgets of the limestones must not be overwhelmed by those from associated detritus, phosphates or oxi-hydroxides;

ii) Their REE+Y patterns need to be interpretable in terms of marine versus lacustrine depositional environment;

iii) In case of marine microbial carbonates, the REE+Y should distinguish between open marine and restricted basin settings. Insight from samples from restricted basins cannot necessarily be extrapolated to the entire ocean;

iv) Claims for surface ocean oxygenation should be accompanied by supporting evidence from the redox-sensitive Ce anomaly in shallow water limestones;

v) Putative biomarkers, whether isotopic, elemental or molecular in nature, should be extracted only from microbial carbonate that shows interpretable REE+Y contrasts with co-existing abiogenic cement.

The current database for Archaean microbial carbonates spans from 3.45 Ga to 2.5 Ga and shows a very uniform behaviour of the REE+Y in the marine realm over almost 1 billion years. There is, as yet, no evidence from the redox-sensitive element Ce for detectable oxidation of the shallow seawater in the Neoarchaean. All Archaean microbial carbonates yield strong positive Eu anomalies testifying to the reduced nature of the deep sea and the transfer of hydrothermal Eu from deep vents into the shallow marine environment. In the few cases where Archaean microbial carbonates can be put into a depositional context, their REE+Y systematics are in agreement with sedimentological information regarding relative water depth, proximity to land masses and hydrothermal vents, or proposed lacustrine versus marine settings. A

consistent picture is also emerging regarding the absolute REE+Y contrast between microbial carbonate (rich in REE+Y) and abiotic carbonate (poorer in REE+Y) in samples of all ages, including Proterozoic and Phanerozoic. If the mechanism(s) for preferential REE+Y uptake can be understood, there is potential that the concentration contrast may eventually serve as a biomarker.

Acknowledgements

Malcolm McCulloch is thanked for providing access to the ANU LA-ICP-MS. Stephen Moorbath (Huntsman Quarry), and Nick Beukes (Campbellrand Formation) kindly provided stromatolite samples. Euan Nisbet, Jim Wilson and Tony Martin are thanked for discussion of Zimbabwean greenstone stratigraphy. Michael Bau is thanked for his continued interest in discussing REE in hydrogenous sediments. Two journal reviewers are thanked for their constructive suggestions for improving an earlier version of the manuscript.

References

Abell, P.I., McClory, J., Martin, A., Nisbet, E.G., Kyser, T.K., (1985a) Petrography and stable isotope ratios from Archaean stromatolites, Mushandike Formation, Zimbabwe. *Precambrian Research*, 27, 385-398.

Abell, P.I., McClory, J., Martin, A., Nisbet, E.G., (1985b) Archaean stromatolites from the Ngesi Group, Belingwe Greenstone Belt, Zimbabwe: preservation and stable isotopes - preliminary results. (Precambrian Research) 27, 357-383.

Alexander, B.W., Bau, M., Andersson, P., (2009) Neodymium isotopes in Archean seawater and implications for the marine Nd cycle in Earth's early oceans. *Earth and Planetary Science Letters*, 283, 144-155.

Allwood, A.C., Kamber, B.S., Walter, M.R., Burch, I.W., Kanik, I., (2010) Trace elements record depositional history of an Early Archean stromatolitic carbonate platform. *Chemical Geology*, 270, 148-163.

Allwood, A.C., Walter, M.R., Kamber, B.S., Marshall, C.P., Burch, I.W., (2006) Stromatolite reef from the early Archaean era of Australia. *Nature*, 441, 714-718.

Altermann, W., Nelson, D.R., (1998) Sedimentation rates, basin analysis and regional correlations of three Neoarchaean and Palaeoproterozoic sub-basins of the Kaapvaal craton as inferred from precise U-Pb zircon ages from volcaniclastic sediments. *Sedimentary Geology*, 120, 225-256.

Anbar, A.D., Duan, Y., Lyons, T.W., Arnold, G.L., Kendall, B., Creaser, R.A., Kaufman, A.J., Gordon, G.W., Scott, C., Garvin, J., Buick, R., (2007) A whiff of oxygen before the great oxidation event? *Science*, 317, 1903-1906.

Awramik, S.M., (1971) Precambrian columnar stromatolite diversity - Reflection of metazoan appearance. *Science*, 174, 825-827.

Awramik, S.M., Buchheim, H.P., (2009) A giant, Late Archean lake system: The Meentheena Member (Tumbiana Formation; Fortescue Group), Western Australia. *Precambrian Research*, 174, 215-240.

Baldwin, G.J., Thurston, P.C., Kamber, B.S., (2011) High-precision rare earth element, nickel, and chromium chemistry of chert microbands pre-screened with in-situ analysis. *Chemical Geology*, 285, 133-143.

Bau, M., (1993) Effects of syn- and post-depositional processes on the rare-earth element distribution in Precambrian iron-formations. *European Journal of Mineralogy*, 5, 257-267.

Bau, M., (1999) Scavenging of dissolved yttrium and rare earths by precipitating iron oxyhydroxide: Experimental evidence for Ce oxidation, Y-Ho fractionation, and lanthanide tetrad effect. *Geochimica Et Cosmochimica Acta*, 63, 67-77.

Bau, M., Dulski, P., (1992) Small-scale variations of the rare-earth element distribution in Precambrian iron-formations. *European Journal of Mineralogy*, 4, 1429-1433.

Bau, M., Dulski, P., (1996) Distribution of yttrium and rare-earth elements in the Penge and Kuruman iron-formations, Transvaal Supergroup, South Africa. *Precambrian Research*, 79, 37-55.

Bau, M. and Dulski, P., (1999) Comparing yttrium and rare earths in hydrothermal fluids from the Mid-Atlantic Ridge: implications for Y and REE behaviour during near-vent mixing and for the Y/Ho ratio of Proterozoic seawater. *Chemical Geology*, 155, 77-90.

Bau, M., Koschinsky, A., (2009) Oxidative scavenging of cerium on hydrous Fe oxide: Evidence from the distribution of rare earth elements and yttrium between Fe oxides and Mn oxides in hydrogenetic ferromanganese crusts. *Geochemical Journal*, 43, 37-47.

Bau, M., Möller, P., (1993) Rare earth element systematics of the chemically precipitated component in Early Precambrian iron formations and the evolution of the terrestrial atmosphere-hydrosphere-lithosphere system. *Geochimica Et Cosmochimica Acta*, 57, 2239-2249.

Bau, M., Möller, P., Dulski, P., (1997) Yttrium and lanthanides in eastern Mediterranean seawater and their fractionation during redox-cycling. *Marine Chemistry*, 56, 123-131.

Berger, M., Rollinson, H., (1997) Isotopic and geochemical evidence for crust-mantle interaction during late Archaean crustal growth. *Geochimica Et Cosmochimica Acta*, 61, 4809-4829.

Beukes, N.J., (1987) Facies relations, depositional environments and diagenesis in a major early Proterozoic stromatolitic carbonate platform to basinal sequence, Campbellrand Subgroup, Transvaal Supergroup, southern Africa. *Sedimentary Geology*, 54, 1-46.

Beukes, N.J., Klein, C., Kaufman, A.J., Hayes, J.M., (1990) Carbonate petrography, kerogen distribution, and carbon and oxygen isotope variations in an early Proterozoic transition from limestone to iron-formation deposition, Transvaal Supergroup, South Africa. *Economic Geology*, 85, 663-690.

Blenkinsop, T.G., Fedo, C.M., Eriksson, K.A., Martin, A., Nisbet, G.E., Wilson, J.F., (1993) Ensialic origin for the Ngezi Group, Belingwe greenstone belt, Zimbabwe. *Geology*, 21, 1135-1138.

Bolhar, R., Hofmann, A., Woodhead, J.D., Hergt, J.M., Dirks, P., (2002) Pb- and Nd-isotope systematics of stromatolitic limestones from the 2.7 Ga Ngezi Group of the Belingwe Greenstone Belt: constraints on timing of deposition and provenance. *Precambrian Research*, 114, 277-294.

Bolhar, R., Kamber, B.S., Moorbath, S., Fedo, C.M., Whitehouse, M.J., (2004) The characterisation of early Archaean chemical sediments by trace element signatures. *Earth Planetary Science Letters*, 222, 43-60.

Bolhar, R., Van Kranendonk, M.J., (2007) A non-marine depositional setting for the northern Fortescue Group, Pilbara Craton, inferred from trace element geochemistry of stromatolitic carbonates. *Precambrian Research*, 155, 229-250.

Buick, R., (1992) The antiquity of oxygenic photosynthesis - Evidence from stromatolites in sulfate-deficient Archean lakes. *Science*, 255, 74-77.

Burton, K.W., Ling, H.F., Onions, R.K., (1997) Closure of the Central American Isthmus and its effect on deep-water formation in the North Atlantic. *Nature*, 386, 382-385.

Campbell, I.H., Squire, R.J., (2010) The mountains that triggered the Late Neoproterozoic increase in oxygen: The Second Great Oxidation Event. *Geochimica Et Cosmochimica Acta*, 74, 4187-4206.

Chauvel, C., Dupré, B., Jenner, G.A., (1985) The Sm-Nd age of Kambalda volcanics is 500 Ma too old! *Earth and Planetary Science Letters*, 74, 315-324.

Collerson, K.D., Kamber, B.S., Schoenberg, R., (2002) Applications of accurate, high-precision Pb isotope ratio measurement by multi-collector ICP-MS. *Chemical Geology*, 188, 65-83.

Corkeron, M., Webb, G.E., Moulds, J., Grey, K., (2012) Discriminating stromatolite formation modes using rare earth element geochemistry: Trapping and binding versus in situ precipitation of stromatolites from the Neoproterozoic Bitter Springs Formation, Northern Territory, Australia. *Precambrian Research*, 212, 194-206.

Corrège, T., (2006) Sea surface temperature and salinity reconstruction from coral geochemical tracers. *Palaeogeography Palaeoclimatology Palaeoecology*, 232, 408-428.

de Baar, H.J.W., Bacon, M.P., Brewer, P.G., Bruland, K.W., (1985) Rare-earth elements in the Pacific and Atlantic oceans. *Geochimica Et Cosmochimica Acta*, 49, 1943-1959.

Derry, L.A., Jacobsen, S.B., (1990) The chemical evolution of Precambrian seawater: Evidence from REEs in banded iron formations. *Geochimica Et Cosmochimica Acta*, 54, 2965-2977.

Douville, E., Bienvenu, P., Charlou, J.L., Donval, J.P., Fouquet, Y., Appriou, P. and Gamo, T., (1999) Yttrium and rare earth elements in fluids from various deep-sea hydrothermal systems. *Geochimica Et Cosmochimica Acta*, 63, 627-643.

Fischer, W.W., Schroeder, S., Lacassie, J.P., Beukes, N.J., Goldberg, T., Strauss, H., Horstmann, U.E., Schrag, D.P., Knoll, A.H., (2009) Isotopic constraints on the Late Archean carbon cycle from the Transvaal Supergroup along the western margin of the Kaapvaal Craton, South Africa. *Precambrian Research*, 169, 15-27.

Folling, P.G., Zartman, R.E., Frimmel, H.E., (2000) A novel approach to double-spike Pb-Pb dating of carbonate rocks: examples from Neoproterozoic sequences in southern Africa. *Chemical Geology*, 171, 97-122.

Frei, R., Dahl, P.S., Duke, E.F., Frei, K.M., Hansen, T.R., Frandsson, M.M., Jensen, L.A., (2008) Trace element and isotopic characterization of Neoarchean and Paleoproterozoic iron formations in the Black Hills (South Dakota, USA): Assessment of chemical change during 2.9-1.9 Ga deposition bracketing the 2.4-2.2 Ga first rise of atmospheric oxygen. *Precambrian Research*, 162, 441-474.

Frei, R., Gaucher, C., Poulton, S.W., Canfield, D.E., (2009) Fluctuations in Precambrian atmospheric oxygenation recorded by chromium isotopes. *Nature*, 461, 250-253.

Friend, C.R.L., Nutman, A.P., Bennett, V.C., Norman, M.D., (2008) Seawater-like trace element signatures (REE+Y) of Eoarchaean chemical sedimentary rocks from southern West Greenland, and their corruption during high-grade metamorphism. *Contributions to Mineralogy and Petrology*, 155, 229-246.

Fryer, B.J., (1977). Rare-earth evidence in iron -formations for changing Precambrian oxidation-states. *Geochimica Et Cosmochimica Acta*, 41, 361-367.

Galer, S.J.G., Mezger, K., (1998) Metamorphism, denudation and sea level in the Archaean and cooling of the Earth. *Precambrian Research*, 92, 389-412.

Godfrey, L.V., Falkowski, P.G., (2009) The cycling and redox state of nitrogen in the Archaean ocean. *Nature Geoscience*, 2, 725-729.

Grassineau, N.V., Abell, P.I., Appel, P.W.U., Lowry, D., Nisbet, E.G., (2006) Early life signatures in sulfur and carbon isotopes from Isua, Barberton, Wabigoon (Steep Rock), and Belingwe Greenstone Belts (3.8 to 2.7 Ga). *Geological Society of America Memoir*, 198, 33-52.

Grassineau, N.V., Nisbet, E.G., Bickle, M.J., Fowler, C.M.R., Lowry, D., Mattey, D.P., Abell, P.I., Martin, A., (2001) Antiquity of the biological sulphur cycle: evidence from sulphur and carbon isotopes in 2700 million-year-old rocks of the Belingwe Belt, Zimbabwe. *Proceedings of the Royal Society London Biological Sciences*, 268, 113-119.

Grassineau, N.V., Nisbet, E.G., Fowler, C.M.R., Bickle, M.J., Lowry, D., Chapman, H.J., Mattey, D.P., Abell, P.I., Yong, J., Martin, A., (2002) Stable isotopes in the Archaean Belingwe belt, Zimbabwe: evidence for a diverse microbial mat ecology. In: Fowler, C.M.R., Ebinger, C.J., Hawkesworth, C.J. (Eds.), The Early Earth: Physical, Chemical and Biological Development. *Geological Society, London, Special Publications*, 199, 309-328.

Hayes, J.M., Kaplan, I.R., Wedeking, K.W., (1983) Precambrian organic geochemistry, preservation of the record. In: Schopf, J.W. (Ed), *The Earth's Earliest Biosphere: Its Origin and Evolution*. Princeton University Press, Princeton NJ, 93-134.

Heimann, A., Johnson, C.M., Beard, B.L., Valley, J.W., Roden, E.E., Spicuzza, M.J., Beukes, N.J., (2010) Fe, C, and O isotope compositions of banded iron formation carbonates demonstrate a major role for dissimilatory iron reduction in similar to 2.5 Ga marine environments. *Earth and Planetary Science Letters*, 294, 8-18.

Hoffman, P., (1967) Algal Stromatolites - Use in stratigraphic correlation and paleocurrent determination. *Science*, 157, 1043-1045.

Horn, I., Hinton, R.W., Jackson, S.E., Longerich, H.P., (1997) Ultra-trace element analysis of NIST SRM 616 and 614 using laser ablation microprobe-inductively coupled plasma-mass spectrometry (LA-ICP-MS): a comparison with secondary ion mass spectrometry (SIMS). *Geostandards Newsletter*, 21, 191-203.

Jacobsen, S.B., Pimentel-Klose, M.R., (1988) A Nd isotopic study of the Hamersley and Michipicoten banded iron formations: the source of REE and Fe in Archean oceans. *Earth and Planetary Science Letters*, 87, 29-44.

Johannesson, K.H., Hawkins, D.L., Cortes, A., (2006) Do Archean sediments record ancient seawater rare earth element patterns? *Geochimica Et Cosmochimica Acta*, 70, 871-890.

Kamber, B.S., (2009) Geochemical fingerprinting: 40 years of analytical development and real world applications. *Applied Geochemistry*, 24, 1074-1086.

Kamber, B.S., (2010) Archean mafic-ultramafic volcanic landmasses and their effect on ocean atmosphere chemistry. *Chemical Geology*, 274, 19-28.

Kamber, B.S., Bolhar, R., Webb, G.E., (2004) Geochemistry of late Archaean stromatolites from Zimbabwe: evidence for microbial life in restricted epicontinental seas. *Precambrian Research*, 132, 379-399.

Kamber, B.S., Greig, A., Collerson, K.D., (2005) A new estimate for the composition of weathered young upper continental crust from alluvial sediments, Queensland, Australia. *Geochimica Et Cosmochimica Acta*, 69, 1041-1058.

Kamber, B.S., Greig, A., Schoenberg, R., Collerson, K.D., (2003) A refined solution to Earth's hidden niobium: Implications for evolution of continental crust and depth of core formation. *Precambrian Research*, 126, 289-308.

Kamber, B.S., Webb, G.E., (2001) The geochemistry of late Archaean microbial carbonate: Implications for ocean chemistry and continental erosion history. *Geochimica Et Cosmochimica Acta*, 65, 2509-2525.

Kamber, B.S., Webb, G.E., (2007) Transition metal abundances in microbial carbonate: a pilot study based on in situ LA-ICP-MS analysis. *Geobiology*, 5, 375-389.

Kamber, B.S., Whitehouse, M.J., (2007) Micro-scale sulphur isotope evidence for sulphur cycling in the late Archean shallow ocean. *Geobiology*, 5, 5-17.

Kendall, B., Reinhard, C.T., Lyons, T., Kaufman, A.J., Poulton, S.W., Anbar, A.D., (2010) Pervasive oxygenation along late Archaean ocean margins. *Nature Geoscience*, 3, 647-652.

Kennedy, M.J., Droser, M., Mayer, L.M., Pevear, D., Mrofka, D., (2006) Late Precambrian oxygenation; inception of the clay mineral factory. *Science*, 311, 1446.

Kent, A.J.R., Jacobsen, B., Peate, D.W., Waight, T.E., Baker, J.A., (2004) Isotope dilution MC-ICP-MS rare earth element analysis of geochemical reference materials NIST

SRM 610, NIST SRM 612, NIST SRM 614, BHVO-2G, BHVO-2, BCR-2G, JB-2, WS-E, W-2, AGV-1 and AGV-2. *Geostandards and Geoanalytical Research*, 28, 417-429.

Klein, C., Beukes, N.J., (1989) Geochemistry and sedimentology of a facies transition from limestone to iron formation deposition in the early Proterozoic Transvaal supergroup, South Africa. *Economic Geology*, 84, 1731-1774.

Klein, C., (2005) Some Precambrian banded iron-formations (BIFs) from around the world: Their age, geologic setting, mineralogy, metamorphism, geochemistry, and origin. *American Mineralogist*, 90, 1473-1499.

Kusky, T.P., Hudleston, P.J., (1999) Growth and demise of an Archean carbonate platform, Steep Rock Lake, Ontario, Canada. *Canadian Journal of Earth Sciences*, 36, 565-584.

Lawrence, M.G., Greig, A., Collerson, K.D., Kamber, B.S., (2006a). Rare earth element and yttrium variability in South East Queensland waterways. *Aquatic Geochemistry*, 12, 39-72.

Lawrence, M.G., Jupiter, S.D., Kamber, B.S., (2006b) Aquatic geochemistry of the rare earth elements and yttrium in the Pioneer River catchment, Australia. *Marine and Freshwater Research*, 57, 725-736.

Lawrence, M.G., Kamber, B.S., (2006) The behaviour of the rare earth elements during estuarine mixing-revisited. *Marine Chemistry*, 100, 147-161.

Lawrence, M.G., Kamber, B.S., (2007) The behaviour of the rare earth elements during estuarine mixing - revisited (100: 147, 2006). *Marine Chemistry*, 105, 181-181.

MacGregor, A.M., (1941) A pre-Cambrian algal limestone in Southern Rhodesia. *Transactions of the Geological Society of South Africa*, 43, 9-16.

Michard, A., Albarède, F., (1986) The REE content of some hydrothermal fluids. *Chemical Geology*, 55, 51-60.

Miller, R.G., O'Nions, R.K., (1985) Source of Precambrian chemical and clastic sediments. *Nature*, 314, 325-329.

Moorbath, S., Taylor, P.N., Orpen, J.L., Treloar, P., Wilson, J.F., (1987) First direct radiometric dating of Archaean stromatolitic limestone. *Nature*, 326, 865-867.

Nisbet, E.G., Sleep, N.H., (2001) The habitat and nature of early life. *Nature*, 409, 1083-1091.

Noffke, N., Beukes, N., Bower, D., Hazen, R.M., and Swift, D.J.P., (2008) An actualistic perspective into Archean worlds — (cyano-)bacterially induced sedimentary structures in the siliciclastic Nhlazatse Section, 2.9 Pongola Supergroup, South Africa: *Geobiology*, 6, 5-20.

Nothdurft, L.D., Webb, G.E., Kamber, B.S., (2004) Rare earth element geochemistry of Late Devonian reefal carbonates, canning basin, Western Australia: Confirmation of a seawater REE proxy in ancient limestones. *Geochimica et Cosmochimica Acta*, 68, 263-283.

Nozaki, Y., Zhang, J., Amakawa, H., (1997) The fractionation between Y and Ho in the marine environment. *Earth and Planetary Science Letters*, 148, 329-340.

Oehler, D.Z., Kvenvold.Ka, Schopf, J.W., (1972) Carbon isotopic studies of organic-matter in Precambrian rocks. *Science*, 175, 1246-1248.

Onuma, N., Higuchi, H., Wakita, H., Nagasawa, H., (1968) Trace element partition between two pyroxenes and the host lava. *Earth and Planetary Science Letters*, 5, 47–51.

Orpen, J.L., Wilson, J.F., (1981) Stromatolites at ~3500 Myr and a greenstone-granite unconformity in the Zimbabwean Archaean. *Nature*, 291, 218-220.

Pack, A., Russell, S.S., Shelley, J.M.G., van Zuilen, M., (2007) Geo- and cosmochemistry of the twin elements yttrium and holmium. *Geochimica Et Cosmochimica Acta*, 71, 4592-4608.

Papineau, D., Mojzis, S.J., Coath, C.D., Karhu, J.A., McKeegan, K.D., (2005) Multiple sulfur isotopes of sulfides from sediments in the aftermath of the Paleoproterozoic glaciations. *Geochimica et Cosmochimica Acta*, 69, 5033-5060.

Paton, C., Hellstrom, J., Paul, B., Woodhead, J., Hergt, J., (2011). Iolite: Freeware for the visualisation and processing of mass spectrometric data. *Journal of Analytical Atomic Spectrometry*, 26, 2508-2518.

Piepgras, D.J., Jacobsen, S.B., (1992) The behavior of rare earth elements in seawater: Precise determination of variations in the North Pacific water column. *Geochimica et Cosmochimica Acta*, 56, 1851-1862.

Planavsky, N., Bekker, A., Rouxel, O.J., Kamber, B., Hofmann, A., Knudsen, A., Lyons, T.W., (2010) Rare Earth Element and yttrium compositions of Archean and Paleoproterozoic Fe formations revisited: New perspectives on the significance and mechanisms of deposition. *Geochimica et Cosmochimica Acta*, 74, 6387-6405.

Pourret, O., Davranche, M., Gruau, G., Dia, A., (2007) Competition between humic acid and carbonates for rare earth elements complexation. *Journal of Colloid and Interface Science*, 305, 25-31.

Pufahl, P.K., Hiatt, E.E., (2012) Oxygenation of the Earth's atmosphere-ocean system: A review of physical and chemical sedimentologic responses. *Marine and Petroleum Geology*, 32, 1-20.

Sawada, K., Abdel-Aal, K., Tan, K., Satoh, K., (2005) Adsorption of lanthanoid ions on calcite. *Dalton Transactions* 20, 3291-3296.

Schoell, M., Wellmer, F.W., (1981) Anomalous ^{13}C depletion in early Precambrian graphites from Superior Province, Canada. *Nature*, 290, 696-699.

Schopf, J.W., Oehler, D.Z., Horodyski, R.J., Kvenvold, K.A., (1971) Biogenicity and Significance of the Oldest Known Stromatolites. *Journal of Paleontology*, 45, 477-485.

Shannon, R.D., (1976) Revised effective ionic radii and systematic studies of interatomic distances in halides and chalcogenides. *Acta Crystallographica*, A 32, 751-767.

Sholkovitz, E., Shen, G.T., (1995) The Incorporation of rare-earth elements in modern coral. *Geochimica et Cosmochimica Acta*, 59, 2749-2756.

Stone, D., (2010) Precambrian geology of the central Wabigoon Subprovince area, northwestern Ontario. *Ontario Geological Survey*, Open File Report 5422, 130.

Sumner, D.Y., (1997a) Carbonate precipitation and oxygen stratification in late Archean seawater as deduced from facies and stratigraphy of the Gamohaan and Frisco Formations, Transvaal Supergroup, South Africa. *American Journal of Science*, 297, 455-487.

Sumner, D.Y., (1997b) Late Archean calcite-microbe interactions: Two morphologically distinct microbial communities that affected calcite nucleation differently. *Palaios*, 12, 302-318.

Sumner, D.Y., Bowring, S.A., (1996) U-Pb geochronologic constraints on deposition of the Campbellrand Subgroup, Transvaal Supergroup, South Africa. *Precambrian Research*, 79, 25-35.

Tanaka K. and Kawabe I., (2006) REE abundances in ancient seawater inferred from marine limestone and experimental REE partition coefficients between calcite and aqueous solution. *Geochemical Journal* 40, 425–435.

Taylor, S.R., McLennan, S.M., (1985) The continental crust: its composition and evolution. *Geoscience Texts*. Blackwell, Oxford.

Terakado Y. and Masuda A., (1988) The coprecipitation of rare-earth elements with calcite and aragonite. *Chemical Geology*, 69, 103–110.

Thurston, P.C., Kamber, B.S., Whitehouse, M., (2012). Archean cherts in banded iron formation: Insight into Neoarchean ocean chemistry and depositional processes. *Precambrian Research*, 214, 227-257.

Towe, K.M., (1982) Anomalous ^{13}C depletion in Precambrian organic-carbon. *Nature*, 295, 171-171.

Ulrich, T., Kamber, B.S., Jugo, P.J., Tinkham, D.K., (2009) Imaging element-distribution patterns in minerals by Laser Ablation - Inductively Coupled Plasma - Mass Spectrometry (LA-ICP-MS). *Canadian Mineralogist*, 47, 1001-1012.

Van Kranendonk, M.J., Webb, G.E., Kamber, B.S., (2003) Geological and trace element evidence for a marine sedimentary environment of deposition and biogenicity of 3.45 Ga stromatolitic carbonates in the Pilbara Craton, and support for a reducing Archaean ocean. *Geobiology*, 1, 91-108.

Veizer, J., Compston, W., (1976) $^{87}Sr/^{86}Sr$ in Precambrian carbonates as an index of crustal evolution. *Geochimica et Cosmochimica Acta*, 40, 905-914.

Veizer, J., Compston, W., Hoefs, J., Nelsen, H., (1982) Mantle buffering of the early oceans. *Naturwissenschaften*, 69, 173-180.

Veizer, J., Hoefs, J., (1976) Nature of ^{18}O-^{16}O and ^{13}C-^{12}C secular trends in sedimentary carbonate rocks. *Geochimica et Cosmochimica Acta*, 40, 1387-1395.

von Blanckenburg, F., Marnberti, M., Schoenberg, R., Kamber, B.S., Webb, G.E., (2008) The iron isotope composition of microbial carbonate. *Chemical Geology*, 249, 113-128.

Waldbauer, J.R., Newman, D.K., Summons, R.E., (2011) Microaerobic steroid biosynthesis and the molecular fossil record of Archean life. *Proceedings of the National Academy of Sciences of the United States of America*, 108, 13409-13414.

Waldbauer, J.R., Sherman, L.S., Sumner, D.Y., Summons, R.E., (2009) Late Archean molecular fossils from the Transvaal Supergroup record the antiquity of microbial diversity and aerobiosis. *Precambrian Research*, 169, 28-47.

Walter, M.R., (1977) Interpreting stromatolites. *American Scientist*, 65, 563-571.

Webb, G.E., Kamber, B.S., (2000) Rare earth elements in Holocene reefal microbialites: A new shallow seawater proxy. *Geochimica et Cosmochimica Acta*, 64, 1557-1565.

Webb, G.E., Kamber, B.S., (2010). Trace element geochemistry as a tool for interpreting microbialites. In: Golding, S.D., Glikson, M. (Eds.), *Earliest Life on Earth: Habitats, Environments and Methods of Detection*. Springer Science+Business Media, 127.

Webb, G.E., Nothdurft, L.D., Kamber, B.S., Kloprogge, J.T., Zhao, J.X., (2009) Rare earth element geochemistry of scleractinian coral skeleton during meteoric diagenesis: a sequence through neomorphism of aragonite to calcite. *Sedimentology*, 56, 1433-1463.

Wille, M., Kramers, J.D., Nagler, T.F., Beukes, N.J., Schroder, S., Meisel, T., Lacassie, J.P., Voegelin, A.R., (2007) Evidence for a gradual rise of oxygen between 2.6 and 2.5 Ga from Mo isotopes and Re-PGE signatures in shales. *Geochimica et Cosmochimica Acta*, 71, 2417-2435.

Wilks, M.E, Nisbet, E.G., (1988) Stratigraphy of the Steep Rock Group, northwest Ontario: a major Archaean unconformity and Archaean stromatolites. *Canadian Journal of Earth Sciences*, 25, 370-391.

Wilson, J.F., Nesbitt, R., Fanning, C.M., (1995) Zircon geochronology of Archaean felsic sequences in the Zimbabwe craton: a revision of greenstone stratigraphy and models for crustal growth. In: Coward, M.P., Ries, A.C. (Eds.), Early Precambrian Processes. *Geological Society, London, Special Publications*, 109-126.

Woodhead, J.D., Hergt, J.M., (1997) Application of the 'double spike' technique to Pb-isotope geochronology. *Chemical Geology*, 138, 311-321.

Xu, Z.F., Han, G.L., (2009) Rare earth elements (REE) of dissolved and suspended loads in the Xijiang River, South China. *Applied Geochemistry*, 24, 1803-1816.

Zerkle, A.L., Claire, M., Domagal-Goldman, S.D., Farquhar, J., Poulton, S.W., (2012) A bistable organic-rich atmosphere on the Neoarchaean Earth. *Nature Geoscience*, 5, 359-363.

Zhang, J., Nozaki, Y., (1996) Rare earth elements and yttrium in seawater: ICP-MS determinations in the East Caroline, Coral Sea, and South Fiji basins of the wetsern South Pacific Ocean. *Geochimica et Cosmochimica Acta*, 60, 4631-4644.

Zhang, J., Nozaki, Y., (1998) Behavior of rare earth elements in seawater at the ocean margin: A study along the slopes of the Sagami and Nankai throughs near Japan. *Geochimica et Cosmochimica Acta*, 62, 1307-1317.

Zhong S. and Mucci A., (1995) Partitioning of rare earth elements (REEs) between calcite and seawater solutions at 25°C and 1 atm, and high dissolved REE concentrations. *Geochimica et Cosmochimica Acta*, 59, 443–453.

Chapter 3: In-situ trace metal analysis of Neoarchaean – Ordovician Shallow-Marine Microbial-Carbonate-Hosted Pyrites

Published in Geobiology (2015, Vol 13, 316-339)
Co-authors: Elizabeth C. Turner and Balz S. Kamber

Abstract

Precambrian atmospheric and oceanic redox evolution is expressed in the inventory of redox-sensitive trace metals in marine sedimentary rocks. Most of the currently available information was derived from deep-water sedimentary rocks (black shale/banded iron formation). Many of the studied trace metals (e.g., Mo, U, Ni, and Co) are sensitive to the composition of the exposed land surface and prevailing weathering style, and their oceanic inventory ultimately depends on the terrestrial flux. The validity of claims for increased/decreased terrestrial fluxes has remained untested as far as the shallow-marine environment is concerned.

Here, the first systematic study of trace metal inventories of the shallow-marine environment by analysis of microbial-carbonate-hosted pyrite, from ca. 2.65-0.52 Ga, is presented. A petrographic survey revealed a first-order difference in preservation of early diagenetic pyrite. Microbial carbonates formed before the 2.4 Ga great oxygenation event (GOE) are much richer in pyrite, and contain pyrite grains of greater morphological variability but lesser chemical substitution than samples deposited after the GOE. This disparity in pyrite abundance and morphology is mirrored by the qualitative degree of preservation of organic matter (largely as kerogen). Thus it seems that in microbial carbonates, pyrite formation and preservation was related to presence and preservation of organic C.

Several redox-sensitive trace metals show interpretable temporal trends supporting earlier proposals derived from deep-water sedimentary rocks. Most notably, the shallow-water pyrite confirms a rise in the oceanic Mo inventory across the

Precambrian-Cambrian boundary, implying the establishment of efficient deep-ocean ventilation. The carbonate-hosted pyrite also confirms the Neoarchaean and early Palaeoproterozoic ocean had higher Ni concentration, which can now more firmly be attributed to a greater proportion of magnesian volcanic rock on land rather than a stronger hydrothermal flux of Ni. Additionally, systematic trends are reported for Co, As, and Zn, relating to terrestrial flux and oceanic productivity.

1. Introduction

For readers unfamiliar with the early Earth's surface evolution, particularly from a pyrite, Fe and S perspective, this introduction first provides a summary of pertinent observations and data. For specialist readers, the final section of this introduction provides the context of this study.

1.1. The biological sulphur cycle

The evolution of oxygenic photosynthesis in the Neoarchaean (Grassineau et al., 2001; Farquhar et al., 2011) resulted in the opening of a large range of new habitats providing for diverse metabolic possibilities that included, among others, nitrification, methanotrophy and non-photosynthetic sulphide oxidation. Thus, the global production of organic carbon likely increased due to the evolution of oxygenic photosynthesis, and most bacterial biodiversity may have emerged along with the evolution of oxygenic photosynthesis (Canfield & Raiswell, 1999). Sulphides depleted in ^{34}S, and of probable biological origin, are encountered at 2.7 Ga (Kurzweil et al., 2013) with the first highly ^{34}S-depleted sulphides, at 2.3 Ga, demonstrating a degree of fractionation that is comparable to that known from sulphate-reducing bacteria (Canfield & Raiswell, 1999).

Pyrite is a ubiquitous by-product of sulphate reduction. The sulphate-reducing bacterial community obtains energy by oxidising organic matter to CO_2 while reducing dissolved interstitial sulphate to sulphide (Berner et al., 1985; Canfield et al., 2005). The hydrogen sulphide produced by this reaction migrates upward to oxygenated parts of the sediment where it is either oxidised back to sulphate or reacts with detrital iron minerals in the sediment or dissolved Fe^{2+} in the water column to form various iron sulphides, with the chief product being pyrite. This reaction of H_2S with iron to form pyrite occurs by way of an iron monosulphide precursor: mackinawite or greigite (Raiswell et al., 1994). Trace elements can be incorporated into the iron monosulphide precursor at an early stage (Berner, 1972). These iron monosulphide precursors are subsequently converted to pyrite by reactions with a zero-valent sulphur species (Goldhaber & Kaplan, 1974; Morse et al., 1987).

The extent of pyrite formation is limited either by seawater sulphide availability or the availability of reactive iron minerals and dissolved Fe^{2+} in the water column (Canfield & Raiswell, 1999). The degree of trace metal pyritisation is controlled by the amount of pyrite production and the presence of trace metals in the water column and pore waters (Huerta-Diaz & Morse, 1992). However, variables such as atmospheric-oceanic redox conditions, hydrothermal activity, and secular changes in the composition of rocks exposed on land to weathering also determine which trace elements are available for co-precipitation with pyrite. Here, pyrite occurrences in shallow-marine microbial carbonate rocks through Earth history (Fig. 1) are discussed. The abundance and morphological diversity of early diagenetic pyrite are examined and trace metal substitution in microbial-carbonate-hosted pyrites through time are analysed.

1.2. Historical perspective on ocean - atmosphere oxygenation

The early Archaean Earth was generally characterised by an anoxic surface-environment and an anoxic ocean containing low sulphate concentrations. Numerous geochemical proxies indicate a significant increase in atmospheric oxygen concentration at ca. 2.4 Ga (e.g., Karhu & Holland, 1996; Farquhar & Wing, 2003; Bekker et al., 2004; Rouxel et al., 2005), during what is known as the Great Oxidation Event (GOE). The sulphur cycle underwent a profound change at this time, and the sulphur isotope record indicates free oxygen in the atmosphere at ca. 2.4 Ga (Farquhar et al., 2000; Farquhar et al., 2001; Farquhar & Wing, 2003). Non-mass-dependant sulphur isotope fractionations were preserved in the rock record up until ca. 2.4 Ga. Extremely low oxygen levels, probably $< 10^{-5}$ times the present atmospheric level, are required for these sulphur isotope anomalies to be generated and preserved in the rock record (Pavlov & Kasting, 2002). The disappearance of non-mass-dependant anomalies from the rock record ca. 2.32 Ga is thought to signify a departure from persistently low atmospheric oxygen levels that dominated the earliest Earth history. Although the oxidation of Earth's atmosphere began in earnest ca. 2.4 Ga, full ventilation of the ocean was a more prolonged process, and the oceanic response to the GOE is not nearly as well constrained as the oxidation of Earth's atmosphere (Lyons et al., 2014).

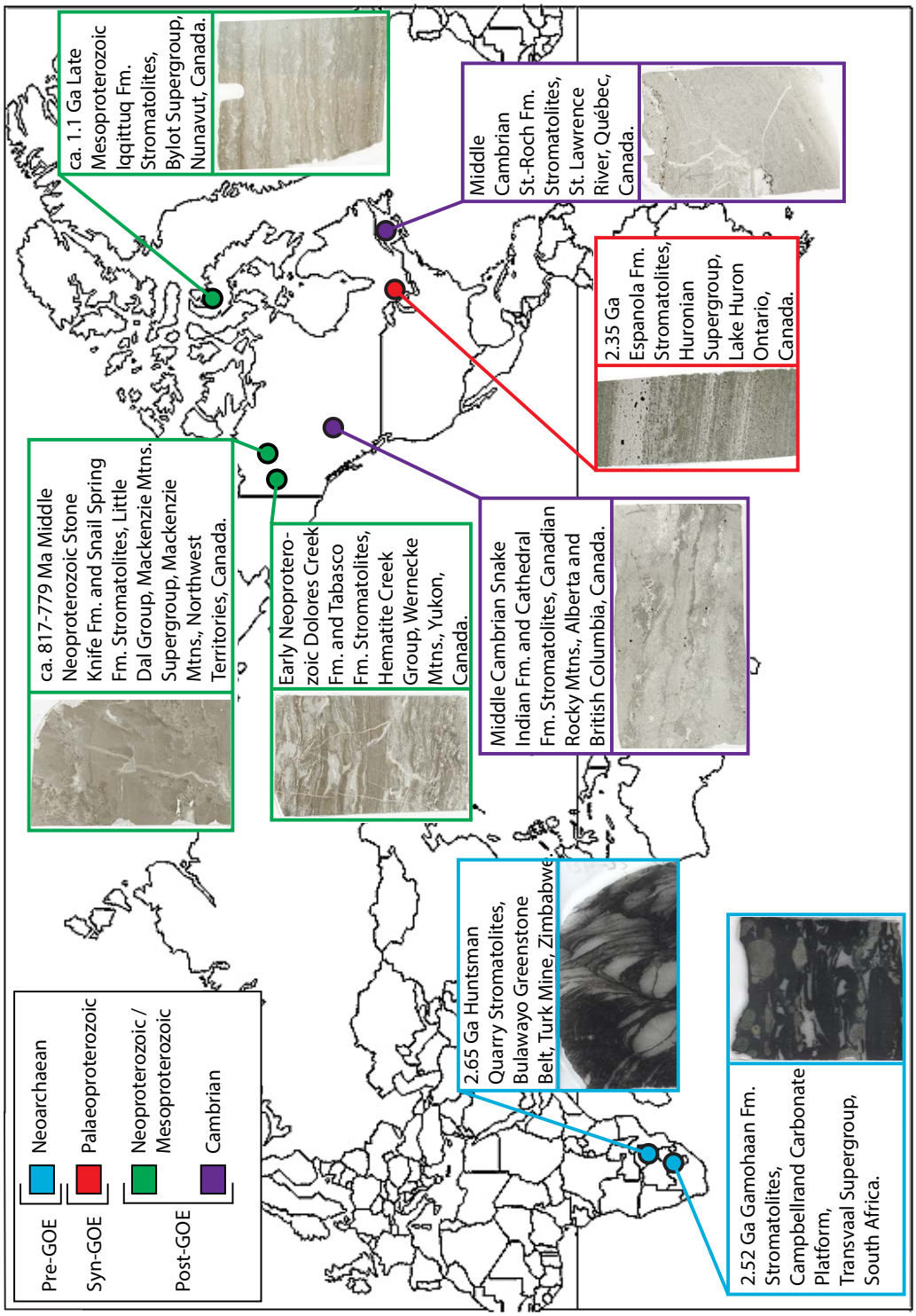


Figure 1: The materials for this study are from Neoarchaean to Palaeozoic microbial carbonate rocks. The age and geographical location of each sample group is provided on this figure along with a high-resolution scanned image of a representative thin section.

Banded iron formation (BIF) deposition is generally an expression of deep-water anoxia. Substantial deposition of BIFs in the early Proterozoic indicates anoxic and Fe-rich deep water, from which hydrothermal sulphur would have immediately been precipitated as iron sulphide minerals on the ocean floor. A number of recent studies (Scott et al., 2008; Planavsky et al., 2012; Partin et al., 2013; Lyons et al., 2014; Scott et al., 2014) detailed the early Palaeoproterozoic, ca. 1.85 – 2.4 Ga, as distinct from the rest of the Proterozoic, characterised by a dramatic rise and fall of O_2 levels in the ocean atmosphere system and a resultant rapid expansion and contraction of the early Palaeoproterozoic seawater sulfate and trace metal reservoir. Early workers invoked deep-ocean oxygenation to explain the disappearance of BIFs ca. 1.8 Ga (Holland, 1984). However, Canfield (1998) proposed instead that increasing ocean sulphate concentrations overwhelmed iron delivery rates to the oceans by 1.8 Ga. Accordingly, the expansion of sulphidic environments, in response to greater oxidative continental weathering of sulphide and resultant delivery of sulphate to the ocean, led to a Proterozoic oxidised surface ocean and a euxinic deep ocean. Multiple geochemical studies point to global oxygen-deficiency in the deep ocean and perhaps euxinia during most, if not all, of the Proterozoic (Canfield, 1998; Raiswell & Canfield, 1998; 2004; Lyons et al., 2009). Although in detail, the Mesoproterozoic and Neoproterozoic oceans may have repeatedly switched between a sulphidic and ferruginous state (Canfield et al., 2008; Poulton & Canfield, 2011), or may have had a spatial distribution of euxinic conditions controlled by organic matter production and burial (Planavsky et al., 2011).

Geochemical data suggest that the oxygenation of Earth's atmosphere proceeded further, with a second step-up in atmospheric oxygen concentration near the end of the Proterozoic Eon ca. 0.58-0.548 Ga (Fike et al., 2006; Canfield et al., 2007), when oxygen rose to levels significant enough to support the rise of animal diversity. This further rise in atmospheric oxygen levels has been termed the Neoproterozoic Oxygenation Event (NOE; e.g., Och & Shields-Zhou, 2012), and it led to the oxidation of deep waters and full ventilation of the ocean (Canfield & Raiswell, 1999). The Phanerozoic oceans also experienced a number of anoxic events, evident for example from the chemistry of black shale (Jenkyns, 2010), but was dominantly in a fully ventilated state. The NOE increase in atmospheric oxygen concentration promoted extensive weathering of terrestrial sulphide, further increasing oceanic sulphate levels and possibly supplying larger fluxes of terrestrial metals to the ocean.

Because the present study is a first order reconstruction from a data set with limited temporal resolution, we discuss new data in the context of only three time periods; pre-GOE, post-GOE and post-NOE. Pre-GOE denotes the time period up until the GOE at ca. 2.35 Ga, post-GOE refers to the time period between the GOE and the NOE ca. 2.35 – 0.58 Ga, and post-NOE refers to the time period after the NOE.

1.3. Oceanic Fe and S sources through time

Oceanic sulphur and iron sources differed in their relative importance at different points in Earth history (pre-GOE vs. post-GOE vs. post-NOE). The primary pre-GOE oceanic S-source was the mantle, via outgassing of SO_2, with subordinate H_2S, from subaerial and shallow-submarine volcanoes (Holland, 1984; Farquhar et al., 2000) and deep-water hydrothermal and volcanic vents. However, much of the H_2S that was hydrothermally vented to the deep water column as a result of subaqueous volcanism (Kump & Seyfried Jr, 2005) would immediately have precipitated as sulphide minerals in the pre-GOE anoxic ocean and thus, hydrothermal sulphur could not contribute significantly to the build-up of a pre-GOE marine dissolved sulphate pool. In the absence of a large source of sulphate provided by post-GOE oxidative weathering of the continents, the concentration of sulphate in seawater was much lower than that of the present day (Walker & Brimblecombe, 1985).

The increase of free oxygen in the atmosphere in the early Proterozoic marked a turning point for the flux of sulphate to the ocean (Walker & Brimblecombe, 1985). The primary post-GOE oceanic S-source consisted of oxidatively weathered terrestrial sulphide materials (Canfield, 2004). Sulphur, in its principal form as pyrite and other sulphides (or subordinate sulphate minerals), were weathered from the continents and delivered to the oceans as sulphate, where bacteria reduced sulphate to sulphide, which then could go on to precipitate as pyrite in the sediment. Seawater sulphate could also evaporatively precipitate as gypsum in isolated basins, which over time became uplifted and exposed to weathering and erosion. The influence of the NOE on terrestrial sulphide weathering is less well understood. Increased post-NOE metal fluxes to the ocean might not have been a direct result of higher atmospheric free O content on sulphide weathering *per se,* but rather an indirect consequence of overall increase of continental erosion and weathering rates (e.g. Campbell & Squire, 2010).

By contrast to constraints on the pre-GOE oceanic S-source, which have benefitted from discovery of mass-independent S-isotope studies, the pre-GOE oceanic Fe-sources are less well understood. The two major sources considered are Fe^{2+} derived from silicate weathering on land (Zbinden et al., 1988; Holland et al., 1989; Holland & Beukes, 1990), and hydrothermal venting of Fe into the deep anoxic ocean. Because hydrothermal venting releases more Fe^{2+} than H_2S (Canfield, 2004; Kump & Seyfried Jr, 2005), vent fluids would certainly have contributed to the total pre-GOE dissolved Fe pool. Equally, pre-GOE paleosols show upward Fe depletion, the result of Fe^{2+} loss during anoxic weathering (Macfarlane et al., 1994; Yang et al., 2002), substantiating the possibility of land-derived Fe delivery. However, neither of these observations permit an assessment of relative importance of Fe delivery.

A significant role of vent fluids for Fe-delivery has traditionally been inferred from the positive Eu anomalies in Archaean precipitated sediments, and from the generally primitive Sr isotope composition of Archaean sedimentary carbonate (Derry & Jacobsen, 1988). However, the Eu anomaly preserved in deep- and shallow-water precipitates is not nearly large enough to resemble actual hydrothermal vent fluids (e.g. Derry & Jacobsen, 1990), and their marine REE features require a substantial flux from land as well as REE removal in estuaries (Kamber, 2010). This is also evident from the Nd isotope composition of BIF (Alexander et al., 2008; Alexander et al., 2009) and the decoupling of marine dissolved Nd- and Hf-isotopes (Viehmann et al., 2014). The combined Archaean REE, Sr-, Nd-, and Hf-isotope evidence thus favours substantial Fe delivery from terrestrial weathering (Kamber, 2010) in addition to hydrothermal venting. In this context, it is worth noting that the conventional idea of enhanced hydrothermal flux was qualitatively linked to the hotter Archaean 'mantle' but a more differentiated picture of Archaean mantle temperature distribution is beginning to emerge (e.g. Bickle, 1986; Davies, 2008; Kamber, 2015), that does not require higher spreading rates. Regardless of the unresolved Fe mass balance for the pre-GOE ocean, the important observation from existing REE and Nd-isotope studies is that there was substantial communication between the deep and shallow ocean. For example, crustally-derived Nd is found in deep water BIF (Alexander et al., 2008) yet even shallow water carbonates show positive Eu anomalies of similar magnitude as deeper water BIF (e.g. Kamber & Webb, 2001). Therefore, the study of transition metals from shallow marine settings is an independent test of deep-water proxies.

Post-GOE riverine delivery of Fe was no longer in dissolved Fe^{2+} form, but consisted of particulate Fe^{3+} from continental corrosion under an oxic atmosphere (Holland, 1984). Any Fe^{2+} released from weathering of iron-bearing minerals under an oxic atmosphere was oxidised and precipitated as particulate Fe^{3+} oxides and hydroxides, and subsequently delivered to the shallow-marine environment as particles (Holland, 1978; Isley, 1995). Post-GOE clastic sedimentary rocks define a range in $\delta^{56}Fe$ only slightly more variable than the range of Fe-isotope compositions measured in terrestrial igneous rocks (Beard et al., 2003), indicating that chemical weathering, sedimentary transport and diagenesis play only a minor role in producing Fe isotope variations in oxic environments. This suggests that continental weathering under an oxic atmosphere played only a minor role as a source of dissolved Fe in the post-GOE ocean. Instead, the main post-GOE dissolved Fe flux was from hydrothermal vents in deep anoxic basins. This is evident from the persistence of the positive Eu anomaly preserved in post-GOE BIF and carbonates (Planavsky et al., 2010). This indicates that the deep ocean remained anoxic post-GOE and that after the shutdown of Fe delivery from continental weathering, high temperature, reducing, hydrothermal fluids became the main flux of dissolved Fe into sea water.

The redox evolution of the deep Proterozoic ocean was complex. By late Neoproterozoic time, there was an absence of a recorded positive Eu anomaly in Sturtian BIF (Baldwin et al., 2012), suggesting that hydrothermally sourced Fe was no longer a major source of Fe. Certainly, after the NOE deep-water ventilation, ca. 600 Ma (Lyons et al., 2014), much of the hydrothermal Fe^{2+} would have become oxidised upon venting into the deep-ocean and precipitated. Thus, the concentration of dissolved iron in the Phanerozoic ocean was very low, perhaps approaching the very low levels of the modern ocean, <1nM in the open ocean (Johnson et al., 1997), largely because oxidised iron is insoluble. Today, dust particulate iron transported by the atmosphere plays a significant role in the flux of iron to the ocean (Duce & Tindale, 1991; Jickells et al., 2005). Because the weathering products of sulphides and volcanic glass, together with hydrothermal vent fluids are the most important sources of trace metals in the ocean, it is evident that their oceanic inventories are closely tied to the history of Fe and S delivery to the ocean.

1.4. Context of this study

Whole-rock redox-sensitive trace metal concentrations of deep-marine sedimentary rock have been successfully used for reconstructing the ancient ocean-atmosphere system. For example, the magnitude of whole-rock Mo enrichment in marine sediment as a tracer of Earth's oxygenation has been of particular interest in a number of recent studies. The scope of Mo as a redox tracer in the Archaean was initially shown with unexpected variations in a sample suite of a specific age. Anbar et al. (2007) proposed that an episode of Mo enrichment in a Neoarchaean deep-water pyritic carbonaceous shale implied an early episode of atmospheric oxygenation. Subsequently, more comprehensive studies reported first order changes through time, from analysis of deep time compilations. Scott et al. (2008) recorded authigenic accumulation of Mo in deep-water sulphidic black shale and discovered extreme Mo enrichment in Phanerozoic samples. These authors interpreted this Mo enrichment as resulting from a greatly expanded Phanerozoic oceanic Mo reservoir requiring deep-ocean oxygenation and greatly reduced areal extent of euxinic marine environments. Och and Shields-Zhou (2012) analysed a number of deep-water black shales through Earth history, further substantiating earlier studies of Mo enrichment and also presenting new compilations of V and U concentrations that confirm a rise in atmospheric oxygen, in further support of the NOE. Partin et al. (2013) published a compilation of shale analyses characterised by an increase in U concentration at both the GOE and NOE, reflective of increased oxidative continental weathering and subsequent delivery of U to the ocean. Similarly, Scott et al. (2013) and Swanner et al. (2014) found temporal changes in Zn and Co concentrations respectively, in black shale compilations interpreted to have arisen from long-term evolution of oceanic euxinia.

The other type of sedimentary rock commonly employed in palaeo-redox studies is BIF. For example, Konhauser et al. (2009) analysed and compiled a deep time BIF database, revealing a decline in the molar nickel to iron ratio between 2.6 and 2.7 Ga, which they attributed to a reduced flux of Ni to the ocean. These authors inferred that the decline in deep-water BIF Ni concentration was a direct consequence of decreased eruption and exposure of Ni-rich ultramafic volcanic rock on land in the Neoarchaean. Subsequently, Konhauser et al. (2011) took a similar approach to Cr concentrations in BIF and discovered an increase between 2.48 - 2.32

Ga, which they interpreted as increased Cr^{3+} input to seawater generated by oxidative weathering. More recently, Swanner et al. (2014) and Robbins et al. (2013) presented temporal Co and Zn concentration trends from analysis of iron formations through time that are consistent with the shale record (Scott et al., 2013). Whereas reconstruction of whole rock trace metal concentrations in deep-marine sedimentary rocks has been successful for interpretation of marine palaeo-redox conditions and changes in the flux of trace metals to the ocean, most redox-sensitive trace elements in black shale are known to be concentrated in early pyrite (Huerta-Diaz & Morse, 1992; Large et al., 2007; 2009). In a move away from whole-rock trace metal analysis, Large et al. (2014) took a different approach; analysing a single species (pyrite), thereby avoiding problems inherent to metamorphically or hydrothermally altered black shale or BIF whole-rocks. The deep time compilation of trace metal concentrations in black-shale-hosted pyrite by Large et al. (2014), corroborated the findings of the earlier whole-rock studies. In-situ pyrite trace metal analysis can provide an advantage over whole-rock trace metal analysis because it allows for targeted sample selection in order to limit the overprinting effects of diagenesis, hydrothermal activity, and metamorphism. The present study also used in-situ pyrite trace metal analysis rather than whole-rock trace metal analysis, largely to ensure that only pyrite exhibiting syngenetic to earliest diagenetic textures were analysed, whereas pyrite of known post-depositional origin, such as hydrothermal pyrite overgrowths and pyrite in late, cross-cutting veins could be excluded from analysis.

One underlying assumption of any compiled temporal trend is that the analysed samples are from roughly comparable depositional settings. In this study, sample selection was guided by the desire to probe the shallow-marine realm, in basins well connected to the open-ocean. Trace elements with long residence times in the ocean are well mixed, including into the shallowest seawater. This is, for example, evident in the positive Eu anomalies of shallow-marine Neoarchaean sediments and the crustal Nd-isotope composition of some BIF. However, for metals with short residence times, the principal input sources (hydrothermal vents and run off from land) may not be well-mixed, and temporal trends could alternatively reflect local signals. All of the aforementioned studies, regardless of whether they involved whole-rock analysis or in-situ pyrite analysis, exclusively analysed deep-water sedimentary rocks from basins of unknown connectivity. This study provides a complement to the existing deep-water sediment studies. It is focussed solely on analysis of shallow-

marine microbial carbonate lithofacies that could, for example, be more sensitive to fluctuation in changes to the terrestrial run-off flux than black shale, even for elements with a short oceanic residence time. Importantly, an open-ocean signal can be verified for carbonates using REE+Y data (e.g. Kamber et al., 2014), and the microbial carbonates chosen for this study have been demonstrated to sample shallow but open ocean. The extent of connectivity to the open-ocean for black shale basins is far more difficult to establish than for carbonates. Thus, for black shales deposited under euxinic conditions in silled, restricted basins, the extent of increases in concentration of redox sensitive metals could also be local phenomena (e.g. Turner and Kamber, 2012).

2. Sample Selection and Analysis

2.1. Sample Selection – General Requirements

Webb and Kamber (2011) published an extensive review of the use and limitations of microbial carbonate geochemistry, providing essential information about the formation and preservation of microbial carbonate. Here, we adopt the Webb and Kamber (2011) definition of microbial carbonates as being 'structures interpreted as having formed owing to the presence of a microbial mat or biofilm'. Microbial carbonates were selected as material for this study owing to their widespread preservation in the geologic record, their ability to thrive in shallow-water environments near the sediment water interface, and their possession of internal fabrics which provide a prime source of evidence concerning their origins (Riding, 2000). Individual microbial carbonate samples were selected for analysis because they showed remarkably little evidence for diagenetic or metamorphic recrystallization. The selected samples represent some of the best-preserved examples of microbial carbonate known to date, resulting in a much smaller dataset than comparable black shale or BIF compilations.

Pyrite has been reported to be stable up to metamorphic conditions of greenschist facies (Cook et al., 2009; Large et al., 2009; Thomas et al., 2011) but pyrite recrystallisation can occur relatively soon after deposition (Large et al., 2009). Pyrite affected by metamorphism or hydrothermal activity commonly has a modified trace element signature, and does not retain its primary trace element composition. Syngenetic and early diagenetic pyrite textures are present in pyrite metamorphosed

at grades up to mid-upper greenschist facies, and textures preserved include bedding-parallel pyrite alignment, porous sub-rounded zoned nodules, and disseminated fine microcrystals (Huerta-Diaz & Morse, 1992; Large et al., 2007; 2009; 2014). By contrast, at higher temperatures, textures indicative of metamorphism and/or hydrothermal alteration are present: pyrite grains with euhedral overgrowths, inclusion-free pyrite crystals, pyrite cutting across bedding, and pyrite in later, cross-cutting veins (McClay & Ellis, 1983; Ulrich et al., 2011). This marked morphological contrast allows for post-depositional processes, such as metamorphic and hydrothermal overprints, to be easily petrographically distinguished from primary features.

Most of these conclusions were drawn from observations of shale or siliciclastic-hosted pyrite. It should be noted that no systematic studies of pyrite occurrence in microbial carbonate have yet been performed, although it has been known that at least in Neoarchaean samples, morphologically interesting pyrite is associated with organic C-rich microbial mat carbonate (Kamber and Whitehouse, 2007). Indeed, surprisingly little is known about the temporal preservation potential of the reduced C itself in microbial carbonate. Therefore we applied the same morphological criteria for authigenic origin to carbonate-hosted pyrite. Regardless, careful petrographic selection was critical and only microbial carbonate samples of mid-greenschist facies or lower, containing pyrite with syngenetic or early diagenetic textures were chosen for analysis, and all other pyrite morphologies were excluded.

The spot position for LA-ICP-MS analysis on each pyrite grain was selected with great care to be at the centre of each pyrite grain, in order to avoid analysis of post-depositional overprints and overgrowths. A recent study of post-depositional modification and trace metal mobility in pyrite-bearing conglomerate (Ulrich et al., 2011) documented limited geochemical variation and homogeneous S-isotope signatures of pyrite grains indicating that, although small-scale transport and re-precipitation occurred during hydrothermal alteration and dissolution of pyrite grains, the cores of larger pyrite grains were left relatively undisturbed. Early pyrite varieties exhibited generally enriched trace metal concentrations, whereas later recrystallised and post-depositional pyrite exhibited depleted trace metal concentrations. It appears that although the early pyrite formed in a relatively open system in communication with seawater, the late, post-depositional pyrite formed in

a reasonably closed system in communication with pore waters only, mostly by in-situ dissolution and re-precipitation of the early detrital pyrite into separate sulphide crystals (Ulrich et al., 2011). As a result, inadvertent sampling of recrystallised post-depositional pyrite can yield false lows, as opposed to falsely high trace metal concentrations.

As mentioned earlier, a marine origin with an open ocean signal was established for all the analysed pyritiferous microbial carbonate samples using their shale-normalised REE+Y signatures. The data also allowed to establish a lack of proximity to a local riverine source. Only the depositional setting of the Espanola Formation could not be firmly established. It may represent a "cap carbonate" associated with flooding of continental margins during the retreat of Huronian ice sheets (Bekker et al., 2005). Other authors have interpreted the Espanola Formation to have formed in a lacustrine environment (Bernstein & Young, 1990; Veizer et al., 1992). New REE+Y data with stratigraphic context are reported here. The REE patterns of the stratigraphically lowest samples show no typical marine features (Fig. 2) but farther up in the formation, begin to flatten and develop the typical, elevated Y/Ho ratio of marine carbonates. Thus, the REE+Y data support initial deposition under low-salinity water during glacial retreat, and a gradual increase in salinity through time. Pyrite is present only in the lowermost Espanola Formation and its trace element inventory probably records post-glacial terrestrial influx rather than shallow seawater. Despite the limited constraint on the depositional setting of the Espanola Formation, it was included for analysis due to its age of deposition, right at the GOE transition.

2.2. Laser Ablation Inductively Coupled Plasma Mass Spectrometry (LA-ICP-MS)

Of the numerous microbial carbonate samples initially inspected for pyrite, 28 Neoarchaean to Ordovician samples were selected for pyrite trace metal analysis (Fig. 1) using in-situ LA-ICP-MS. This method has a number of advantages over other analysis techniques. A full suite of trace metals can be analysed very rapidly, later quartz or carbonate veins or deformation-related metamorphic recrystallization/precipitation can be easily avoided, and the method has very low

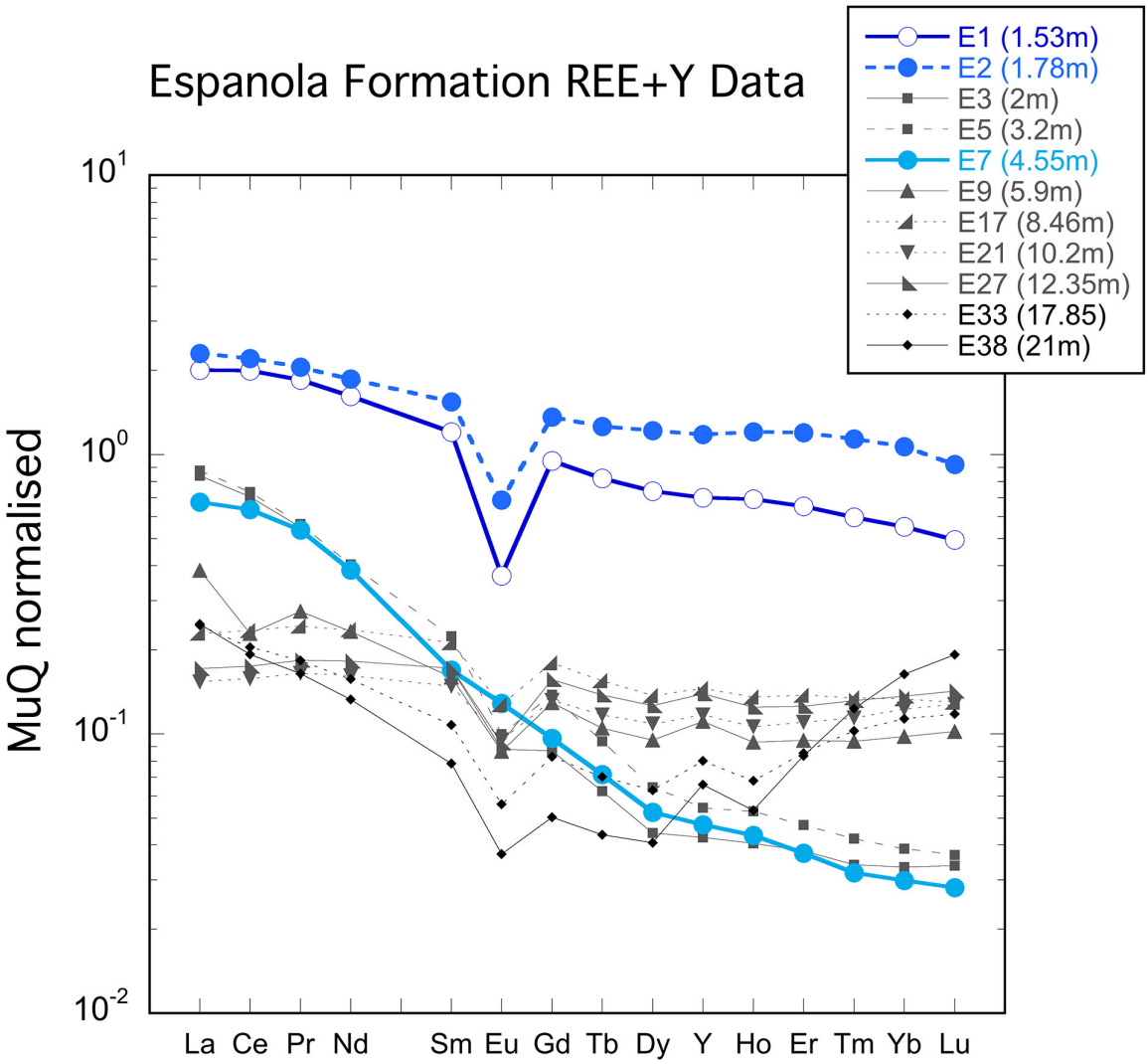


Figure 2: Upper continental crust-normalised REE+Y data for the three pyritiferous samples analysed from the Espanola Formation, E1, E2 and E7, along with eight other Espanola Formation samples representing the full chemostratigraphy of the lower limestone member (numbers in legend refer to meters above base of Espanola Formation). The REE patterns of the stratigraphically lowest samples show none of the typical marine features but further up in the Formation, begin to flatten and develop the elevated Y/Ho ratio of marine carbonates. The sample suite shows gradation up section from a light REE enriched clastic, detritus rich calcareous siltstone to a more REE depleted carbonate exhibiting a more open seawater signature. Thus, the REE+Y data are supportive of a start of deposition in low salinity waters during glacial retreat with a gradual increase in salinity. Pyrite is only found in the lowermost Espanola Formation and its trace element inventory is more likely to reflect that of post-glacial terrestrial influx than shallow seawater.

detection limits, yielding precise and accurate data for elements present at ppm concentrations (e.g. Kamber et al., 2014; Large et al., 2014).

All data were obtained at Trinity College Dublin on a Photon Machines Analyte Excel (193 nm Excimer) LA system with a dual-volume ablation cell that is coupled to a Thermo Scientific iCap-Qs quadrupole ICP-MS. Samples for LA-ICP-MS consisted of polished thin sections mounted with epoxy resin along with a number of polished rock fragments mounted in an epoxy resin puck. All materials were digitally scanned in reflected light at high resolution prior to analysis, and possible analytical targets were determined from petrographic context. Analytical targets were then inspected with a petrographic microscope equipped with a digital camera before laser ablation.

Analysis was performed as spot analyses in 99.9995 % pure He, using a beam diameter of 30 µm, a shot count of 180, a fluence of 3.2 J/cm^2, and a 4 Hz repetition rate. A number of line scans were ablated with an 80 µm beam proceeding as a continuous profile at 50 µm sec^{-1} and with a repetition rate of 10 Hz. All other parameters were the same as in spot analysis. The element menu for spot analysis was limited to 13 masses for continuous profiling with dwell times across the mass range kept constant (one isotope each for S, V, Mn, Fe, Co, Ni, Cu, Zn, As, Mo, Cd, Pb and Bi). The element menu for the line-scan analysis was limited to 19 masses for continuous profiling, with dwell times across the mass range varying according to expected abundance (one isotope each for Ca, Sr, Y, Ba, La, Ce, Pr, Nd, Sm, Eu, Gd, Tb, Dy, Ho, Er, Tm, Yb, Lu and Th).

Data reduction was performed with the “trace elements” data reduction scheme of Iolite (Paton et al., 2011) using the semi-quantitative approach. The background-subtracted data were drift-corrected and calibrated by reference to NIST 612 glass. Iolite was also used to stitch some of the line scan data into a two-dimensional map (Paul et al., 2012). In total, LA-ICP-MS analyses of 313 pyrites from 28 microbial carbonate samples were performed. Of these 313 analyses, 98 data points were rejected, owing to their low S and / or Fe counts or their non-FeS_2 empirical stoichiometry, leaving 215 individual pyrite spot analyses. These data are reported in the supplementary information.

3. Material

The datasets discussed below are from microbial carbonate rocks of various ages (Fig. 1), the geology of which is introduced in chronological order. All the analysed material comes from hand samples, excluding the Gamohaan Formation (section 3.2.) drill core samples. The overriding selection criterion was the preservation quality of samples; only sites of exceptional preservation with samples preserving kerogen and fine morphological structures, free from recrystallisation and post depositional alteration were selected for analysis. The only exception being the Espanola Formation. Interested readers are referred to the original publications for greater contextual detail.

3.1. Neoarchean, 2.65 Ga, Huntsman Quarry Stromatolites, Bulawayo Greenstone Belt, Zimbabwe.

The 2.65 Ga Huntsman Quarry stromatolites were first reported by Macgregor (1941) in a limestone quarry near Turk Mine in the Bulawayo greenstone belt, Zimbabwe, but later investigators were able to sample only stromatolitic quarry waste rock. The most comprehensive study (Schopf et al., 1971) described remarkable microscopic preservation of symmetrical, regularly alternating carbonaceous and calcareous laminae, considered to be characteristic of stromatolitic microbial mats. Of particular note is the presence of sparry calcite, forming 'birdseye' pockets up to 1 cm wide, which are interpreted as early diagenetic fill of what were originally gas-filled pockets in the microbial mats. Although no direct date is available for the Bulawayo greenstone belt, tight regional correlation of Zimbabwean greenstones (Wilson et al., 1995) and the occurrence of similar stromatolites in the Cheshire Formation of the Belingwe greenstone belt strongly suggest a 2.65 Ga depositional age and a maximum depositional age of 2.72 Ga for the Huntsman Quarry limestone (Bolhar et al., 2002). Kamber et al. (2014) recently published REE+Y data for these carbonate rocks, confirming their open marine character.

3.2. Neoarchean, 2.52 Ga, Gamohaan Formation Stromatolites, Campbellrand Carbonate Platform, Transvaal Supergroup, South Africa.

The Transvaal Supergroup, exposed over an area of 200,000 km^2, probably covered the entire 600,000 km^2 surface of the Kaapvaal Craton (Beukes, 1987). The

succession sits disconformably on volcanic rocks of the Ventersdorp Supergroup. Thermal subsidence after heating and thinning of the Kaapvaal Craton during the deposition of the Ventersdorp Supergroup is thought to have produced the accommodation space necessary for the deposition of the Transvaal Supergroup (Sumner & Beukes, 2006).

The Campbellrand Subgroup is an extensive, ~ 2 km-thick carbonate succession that rests conformably on siliciclastic and carbonate strata of the Schmidtsdrif Subgroup. Eventually the Campbellrand carbonate "platform" was drowned during a major transgression recorded by deposition of the Kuruman iron formation (Fischer et al., 2009). Today the Campbellrand-Kuruman succession is essentially undeformed and metamorphism is below greenschist facies (Miyano & Beukes, 1984).

The 2.52 Ga Gamohaan Formation stromatolites, from the uppermost Campbellrand Subgroup, have been the subject of numerous studies (e.g., Beukes, 1987; Klein & Beukes, 1989; Sumner, 1997a; 1997b), most recently from cores (e.g., Fischer et al., 2009). The Gamohaan Formation is characterised by deep subtidal fenestral microbialites and shales that ultimately grade into overlying Kuruman Formation iron formation (Fischer et al., 2009). The age of the Gamohaan Formation is well constrained: a tuff in the middle of the formation yielded a U/Pb zircon date of 2.521±0.001 Ga (Sumner & Bowring, 1996), whereas tuff from the upper part was U/Pb zircon dated to 2.516±0.004 Ga (Altermann & Nelson, 1998).

3.3. Palaeoproterozoic, ca. 2.35 Ga, Espanola Formation, Huronian Supergroup, Ontario, Canada.

The Espanola Formation, part of the Palaeoproterozoic Huronian Supergroup, was first described by Coleman (1908) from the north shore of Lake Huron in Ontario, Canada. The Huronian Supergroup was deposited between 2.5 and 2.1 Ga (Krogh et al., 1984; Andrews et al., 1986) and comprises a southward-thickening succession of predominantly terrigenous clastic rocks derived from the Archean Superior Province to the north (Young, 1973). The Huronian Supergroup contains three groups, each exhibiting a basal glaciogenic unit overlain by siltstone-argillite unit and thick cross-bedded quartzite (Young, 1973).

The Espanola Formation, in the middle of the Huronian Supergroup, is unique in the Huronian succession, and is one of the oldest extensive, sedimentary carbonate formations in the world. The Espanola Formation overlies glaciogenic diamictite of the Bruce Formation and is overlain by cross-bedded fluvial sandstone of the Serpent Formation (Parviainen, 1973; Long, 1976). The Espanola Formation comprises a lower limestone member, a middle siltstone member and an upper heterolithic member (Bernstein & Young, 1990).

The Espanola Formation has been the subject of numerous studies because it represents a possible Palaeoproterozoic analogue for the Neoproterozoic "cap carbonate" conditions (Hoffman et al., 1998) that mark the transition from "snowball Earth" to greenhouse atmospheric conditions (Hoffman, 1980). The Espanola Formation has been interpreted as the product of diachronous deposition during marine transgression following withdrawal of the glaciers responsible for deposition of underlying glaciogenic diamictite of the Bruce Formation (Young, 1973; Bekker et al., 2005).

Samples used in this study are from a dense stratigraphic profile (40 samples over 22.7 metres) from the lower limestone member of the formation, near Elliot Lake, Ontario. The pyrite samples analysed from the post-GOE Espanola Formation differ markedly in their appearance, size (Fig. 3 g-h) and isotopic composition from pyrite in the underlying, pre-GOE Archaean Mississagi Formation (Ulrich et al., 2011) such that a detrital origin can be ruled out. The occurrence of pyrite in the measured section is strictly controlled by stratigraphy and not by proximity to thin dykes and sills of Nipissing diabase. A baked limestone sample taken 2 cm away from a 1 m thick sill was devoid of pyrite and its chemistry indistinguishable from samples several m away. Furthermore, the pyrite from the underlying Mississagi Formation, also affected by the Nipissing diabase, analysed for in-situ trace metals and S-isotopes by Ulrich et al. (2011) preserved plenty of detrital pyrite. These authors could clearly identify later recrystallised pyrite by its shape. Finally, Ulrich et al. (2011) found the recrystallised pyrite to be very pure. Therefore, any undetected recrystallised pyrite in our samples would likely return false low trace metal concentrations as opposed to erroneously elevated concentrations (Ulrich et al., 2011).

3.4. Late Mesoproterozoic Iqqittuq Formation, Bylot Supergroup, Nunavut, Canada.

The Iqqittuq Formation is part of the Bylot Supergroup in the Borden Basin, one of a group of late Mesoproterozoic epicratonic basins in Canada's Arctic archipelago collectively known as the Bylot basins (Fahrig et al., 1981). The depositional age of the Bylot Supergroup is at least in part ≤1.1 Ga, and its origin is probably related to far-field tectonic stress associated with the assembly of Rodinia (Long & Turner, 2012; Turner & Kamber, 2012). The Borden Basin consists of three "troughs" (Jackson & Iannelli, 1981), the largest of which is the Milne Inlet Graben (MIG). The Iqqittuq Formation is a NW-deepening carbonate ramp in the shallower, southeastern part of the MIG (Turner, 2009); it passes northwestward to a coeval black shale basin (Arctic Bay Formation; Turner & Kamber, 2012). The Iqqittuq Formation consists of southeastern shallow-water zone characterised by subtidal microbial laminite and peritidal dolomudstone, and a western region of deeper-water lithofacies passing into thinly bedded slope limestone interbedded with shale (Turner, 2009). Material used in this study is from subtidal microbial dololaminite in the southeastern area.

3.5. Early Neoproterozoic Dolores Creek Formation and Tabasco Formation, Hematite Creek Group, Wernecke Mountains, Yukon and Northwest Territories, Canada.

The Hematite Creek Group (Thorkelson, 2000; Turner, 2011) consists of shallow-water clastic and carbonate units at the base of the Mackenzie Mountains Supergroup. The Hematite Creek Group is a diverse succession of shallow-water carbonate and terrigenous clastic rocks approximately 1 km thick (Thorkelson, 2000; Turner, 2011). Material used in this study is from columnar-stromatolitic dolostone interlayered with bituminous shallow-water black siltstone in the rift-like Dolores Creek Formation and from large cuspate stromatolites in dolostone of the Tabasco Formation (Turner & Long, 2012).

3.6. Middle Neoproterozoic Stone Knife Formation and Snail Spring Formation , Little Dal Group, Mackenzie Mountains Supergroup, Northwest Territories, Canada

The Neoproterozoic Little Dal Group, exposed in the Mackenzie Mountains, Northwest Territories, Canada, is a succession of shallow-water carbonate, siliciclastic and evaporite rocks (Aitken, 1981). Material used in this study is from microbial reefs of the Stone Knife Formation and columnar-stromatolitic dolostone of the middle Snail Spring Formation (Turner & Long, 2012).

Calcimicrobial reefs of the Stone Knife Formation ("Little Dal reefs"), hectometres thick and kilometres in diameter, are enclosed by deep-water limestone and shale that accumulated in an epicratonic basin at low latitude (Turner et al., 1997; 2000). The reef framework consists of mm- to dm-scale filamentous-calcimicrobial stromatolites that vary in external morphology depending on the stage of reef growth and position on the reef edifice (Turner et al., 2000). Stromatolites of the Snail Spring Formation, in contrast, have muddy lamination more typical of Proterozoic shallow-water stromatoites. The age of the Little Dal Group is bracketed between ca. 0.817 Ga (Ar-Ar detrital muscovite; Powell & Schneider, 2013)and 0.779 Ga (U-Pb on cross-cutting igneous rocks; Jefferson & Parrish, 1989; Heaman et al., 1992).

3.7. Mid-Cambrian Snake Indian Formation and Cathedral Formation, Western Canada Sedimentary Basin, Canada

Cambrian to lower Ordovician strata of western Canada record accumulation of terrigenous and carbonate material on a passive margin that followed late Neoproterozoic rifting and early Palaeozoic sea-level rise of the Sauk sequence. Among the middle Cambrian units exposed in southwestern Canada (Alberta and British Columbia) are the Snake Indian and (partly) laterally equivalent Cathedral Formations. The Cathedral Formation is an areally extensive, massive, shallow-water carbonate unit. The southwest-facing and -thickening lithofacies of the Cathedral Formation are geographically complex (Aitken, 1997; Pratt, 2002). The most seaward lithofacies represent peritidal and ooid shoal environments at and near a tectonic escarpment that defined the abrupt southwestward transition into deeper-water environments of the Stephen Formation (which contains the "Burgess Shale"). The

Cathedral Formation passes northward into carbonate and shale of part of the Snake Indian Formation (Aitken, 1997). Samples used in this study are peritidal microbialite (Cathedral Formation) and microbial (*Girvanella*) cortoids (Snake Indian Formation).

3.8. Middle Cambrian Saint-Roch Formation, southern Québec, Canada

The lower Palaeozoic geology of eastern Laurentia was controlled by segmented promontories and embayments that appeared in the continental margin during late Neoproterozoic rifting (Allen et al., 2009); shallow-water carbonate and associated slope environments developed along this young passive margin. Material used in this study consists of a mid-Cambrian upper-slope or outer-ramp microbialite that was re-sedimented into slope strata of the St.-Roch Formation in the Quebec re-entrant of Laurentia's eastern margin (Lavoie et al., 2003).

4. Results

4.1. Sulphide occurrences in shallow-marine microbial carbonates

Petrographic inspection of 90 thin sections revealed striking differences between the preservation of both reduced C and S. In terms of C, a first order observation was that many of the microbial structures in the pre-GOE carbonates are black or dark in colour and very rich in kerogen (the portion of organic matter in sedimentary rocks that is insoluble in organic solvents (Dow, 1977)), while the post-GOE microbial carbonate samples were much paler in colour and poorer in if not devoid of kerogen. In terms of sulphide content, most notably, the pre-GOE, black, kerogen-rich microbialites are rich in pyrite (Fig. 3a-f), whereas the post-GOE microbial carbonates are considerably paler and poorer in pyrite content (Fig. 3g-l).

Morphological diversity of pyrite is greater in the pre-GOE Archaean samples, where five different types are present: pyrite sphaeroids (Fig. 3b and f), pyrite disseminated in microbial mats (Fig. 3e), later pyrite in fenestral fill (Figure 3c), randomly dispersed matrix pyrite (Fig. 3d) and individual euhedral pyrite crystals (Fig. 3a). Post-GOE pyrite tends to be more difficult to classify, and largely consists of xenomorphic, porous, subrounded nodules (Fig. 3g-i) and disseminated, fine microcrystals commonly with euhedral overgrowths (Fig. 3j-l). It is also apparent that

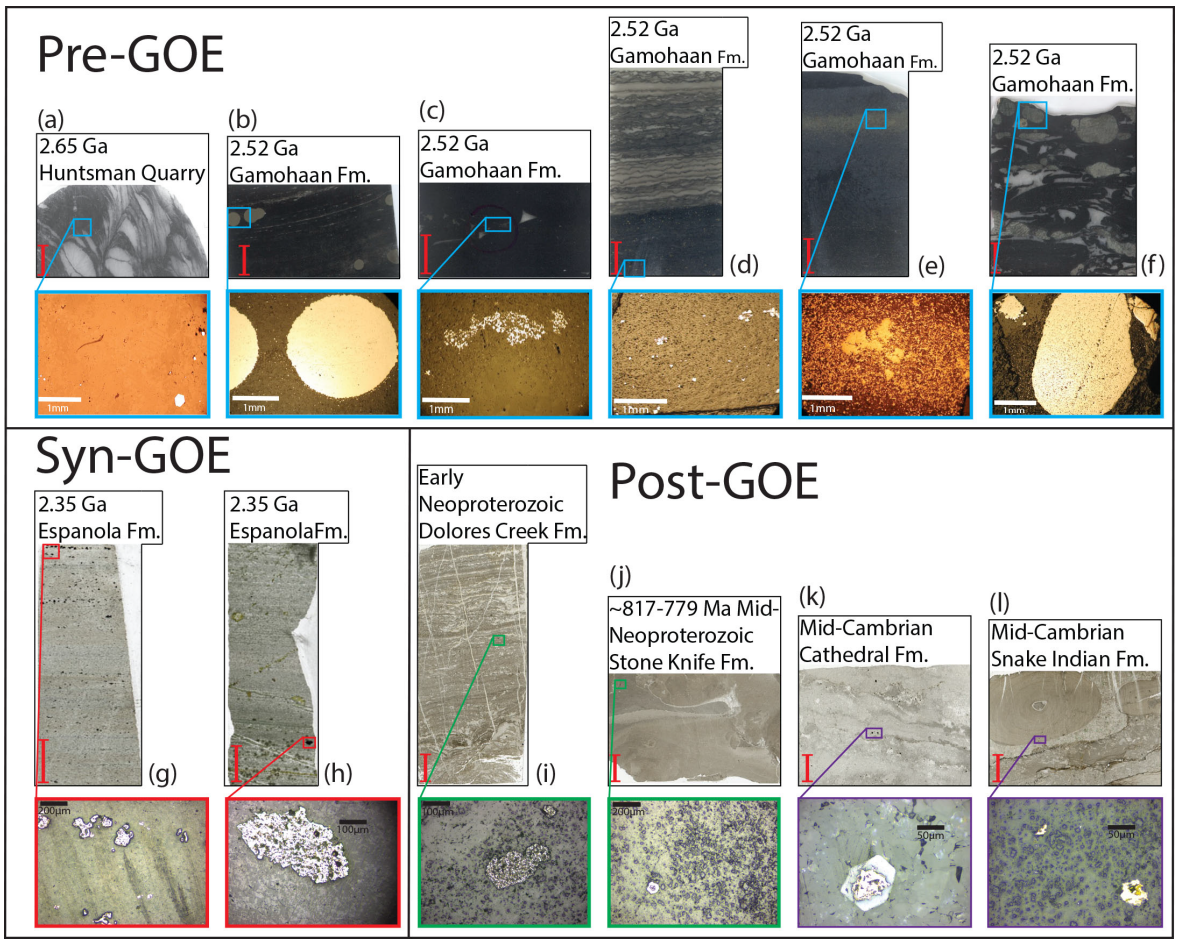


Figure 3: Scanned images of typical microbial carbonate samples pre-GOE (a-f), syn-GOE (g-h) and post-GOE in age (i-l) are provided, along with a red 5 mm bar for scale. In each case the inset provides a detailed reflected light petrographic image of typical pyrite morphology and its thin section location. The insets are colour coded according to the key in Figure 1; blue for Neoarchaean, red for Palaeoproterozoic, green for Neoproterozoic and Mesoproterozoic, and purple for Cambrian samples. It is clear that the pre-GOE Archaean (a-f), black, kerogen-rich microbial carbonates are very rich in pyrite content. By contrast, the syn-GOE Palaeoproterozoic (g-h) and post-GOE Neoproterozoic (i-j) and Palaeozoic (k-l) microbial carbonates are considerably paler and poorer in pyrite content. Equally the morphological diversity of pyrite is much greater in the pre-GOE samples where a number of distinct pyrite morphologies can be identified; large rounded sphaeroidal pyrites (b+f), pyrite forming in later fenestral fill (c), pyrite disseminated in the microbial mat (e), randomly dispersed matrix pyrite (d), and individual euhedral pyrite grains (a). Syn-GOE and post-GOE pyrite tends to be much more difficult to classify, largely consisting of xenomorphic, porous, subrounded nodules (g-i) with later euhedral pyrite overgrowths common in the younger samples (j-l).

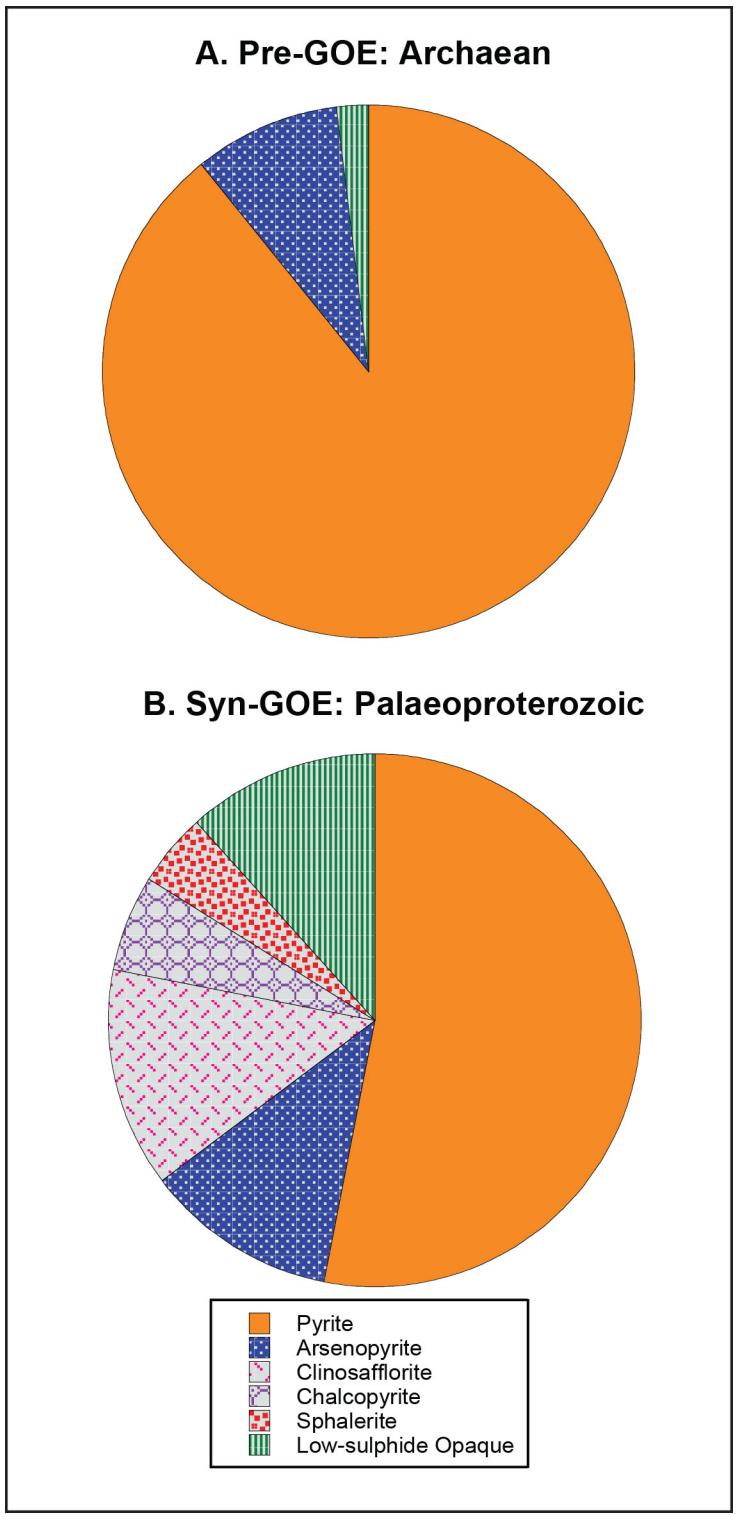


Figure 4: Illustration of pyrite chemical variation and substitution. Almost all of the pre-GOE Archaean sulphides consist of pure pyrite (a), whereas only slightly more than half of the syn-GOE Palaeoproterozoic sulphides consist of pure, FeS_2, pyrite (b). The syn-GOE Palaeoproterozoic sulphides exhibit much greater chemical diversity and substitution with Cu, Zn, As, Co and Ni commonly substituting for Fe.

the post-GOE pyrite is restricted to few laminae in the microbial carbonate, whereas abundant pyrite is present in the pre-GOE microbial carbonate samples.

Sulphide chemical variation and substitution is significantly greater in post-GOE material than in pre-GOE material. Almost all of the Archaean pre-GOE samples contain only simple FeS_2 pyrite, and only a small number contain arsenopyrite (Fig. 4a). Conversely, the syn-GOE Palaeoproterozoic sulphides show much greater chemical variation, with variable Cu, Zn, As, Co and Ni substitution for Fe (Fig. 4b).

4.2. Trace metal distribution in pyrite

Large et al. (2014) produced two-dimensional LA-ICP-MS images of trace element (Se, Mo, Zn, Cu, As and V) distribution in a pyrite nodule and its surrounding matrix to obtain an understanding of which trace metals most strongly partition into pyrite. In the present study, trace element maps (Fig. 5) of a pyrite sphaeroid (Fig. 3b, Fig. 5c) corroborate findings from Large et al. (2014) regarding the distribution of Cu, As and V, and provide new data about the distribution of Ni, Au and Bi. Certain elements (V, Au) are clearly excluded from the sphaeroid, and are preferentially concentrated in the carbonate material and/or kerogen immediately surrounding the sphaeroid. Other elements (Cu, Bi, Ni, As) show inverted-bell-shaped, possibly diffusional, patterns with elevated concentrations at both the rim and the centre of the sphaeroid (Fig. 5). Sulphur isotope data for this very sphaeroidal pyrite reveal negatively mass-independently-fractionated sulphur with $\Delta^{33}S$ values of ca. -1 (Kamber & Whitehouse, 2007). This indicates that the S was of sulphate-reducing bacteria origin (SRBO), but it is not known whether the sphaeroid formed in close proximity to the sulphate-reducing bacteria. The S-isotope data also reveal a gradient from $\delta^{34}S_{CDT}$ values as low as -8.27 at the centre of the sphaeroid, to values as high as -0.21 towards the rim of the sphaeroid (Kamber & Whitehouse, 2007). This provides strong evidence for limited sulfate availability in the Neoarchaean, and that towards the end of pyrite formation sulphate concentration dropped and bacteria were forced instead to metabolise isotopically heavier S. Other pyrite from this study that were analysed for S-isotopes, did not reveal negative mass independent fractionation and thus did not reveal a sulphate reducing bacteria origin. The fact that this SRBO pyrite actively excluded several elements from the sphaeroid, but preferentially enriched others, is an intriguing feature chemically distinguishing these pyrites from non-

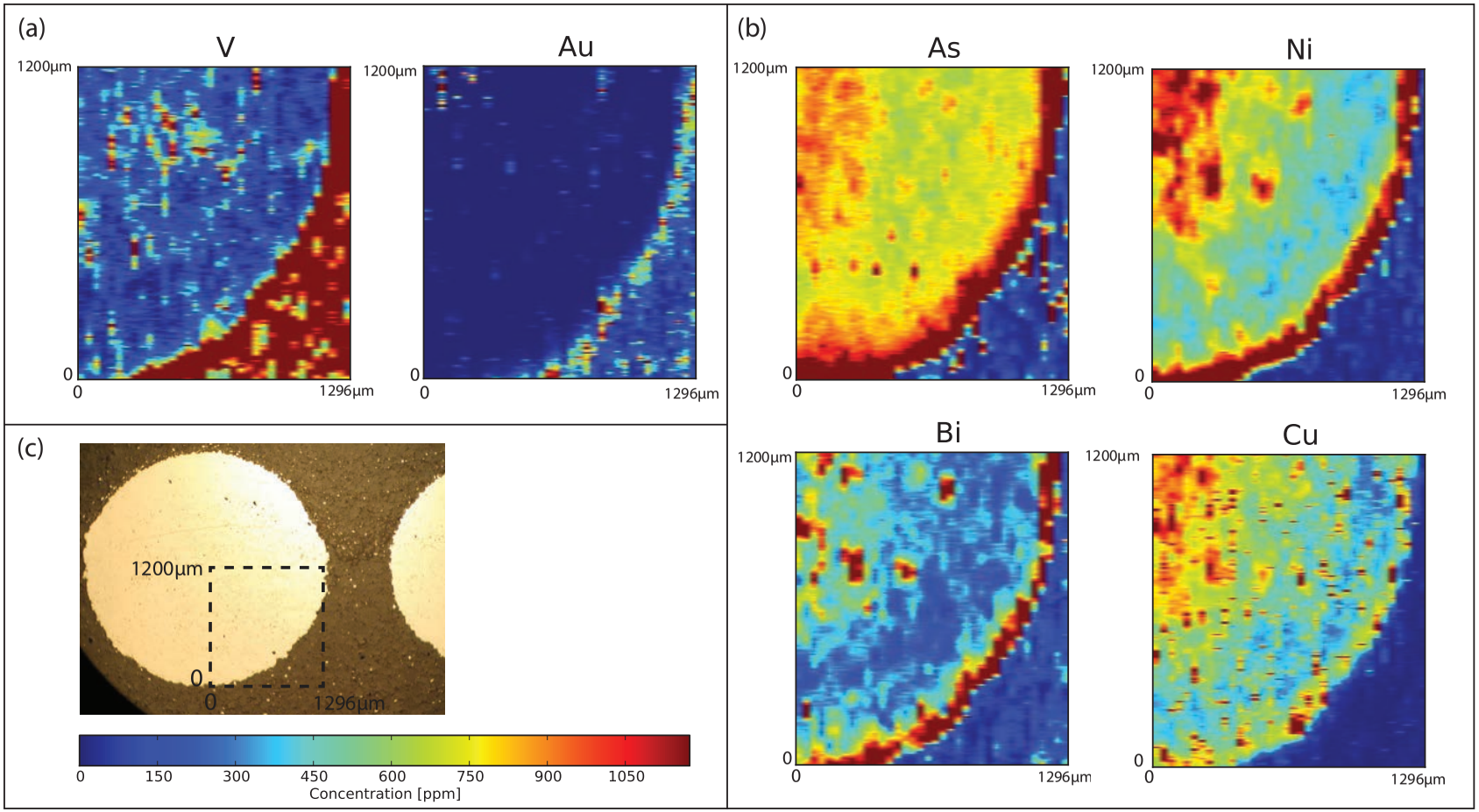


Figure 5: Trace-metal maps for a quadrant of a sphaeroidal pyrite (Fig. 3b), for which a detailed reflected-light petrographic image is provided along with a scale bar indicating concentration levels in ppm. The map was produced by LA-ICP-MS similar to the protocol outlined in Ulrich et al. (2009). The sulphur in these sphaeroids is known to have been processed by sulphate-reducing bacteria (Kamber & Whitehouse, 2007) and the pyrite reveals a complex spatial distribution of trace metals. Certain metals, (a) V and Au, were clearly excluded from the spheroid itself and thus very concentrated in the immediately surrounding carbonate material. Other metals, (b) As, Ni, Bi and Cu, show bell shaped possibly diffusional patterns with elevated concentrations at both the rim and the centre of the spheroid.

SRBO pyrite. Further work is required to explore whether this distribution pattern, a combination of exclusion and inclusion of certain trace metals, could have biomarker potential for sulphate-reducing bacteria, although this was not the aim of this study. Selective uptake and exclusion of certain trace elements into pyrite of microbial origin could confound the main effort of this study, namely the temporal analysis of metal concentration in pyrite, as these processes likely lead to variable content of trace metals. As a result, selective uptake of trace elements into these sphaeroidal pyrites of microbial origin was taken into account when collecting data for temporal trace metal patterns. Because the laser spot size was ca. 60 times smaller than the exposed sphaeroid grain diameters, the average trace metal content was obtained from line averages traversing the entire sphaeroid as opposed to individual spot analysis. However, the majority of analysed pyrites were the same size as or smaller than the diameter of the laser spot, so that laser ablation encompassed the entire pyrite grain and thus the entire metal inventory of the pyrite grain was analysed.

It is worth noting that complexity of trace metal incorporation into all pyrite, not only of microbial origin, and the resultant variability of metals in pyrite, is a natural limitation of the approach employed here. However, other proxies for ancient ocean redox also suffer from limitations. For example, the molar Ni/Fe ratios of BIF and Mo content of black shales from a single time period show variabilities of several orders of magnitude, reflecting complex pathways of metal incorporation.

4.3. Pyrite trace metal temporal patterns

Several of the analysed transition metals yielded clear temporal patterns. The most striking result is that pyrite from the Middle Cambrian St.-Roch Formation is notably enriched in Mo as compared to older material. The Middle Cambrian pyrite contain Mo concentration of ~20-70 ppm, whereas the Neoarchaean to Neoproterozoic samples exhibit Mo concentrations of ~ 0-30 ppm (Fig. 6), with many samples showing Mo concentrations below 10 ppm.

The pyrite data also reveal a significant drop in nickel concentration in post Palaeoproterozoic samples. The pre-GOE Neoarchaean and syn-GOE Palaeoproterozoic samples exhibit a much wider Ni concentration range of 0-8,000 ppm, whereas the majority of Neoproterozoic and Palaeozoic samples (excluding only two samples) contain Ni concentration of 0-2,500 ppm (Fig. 7).

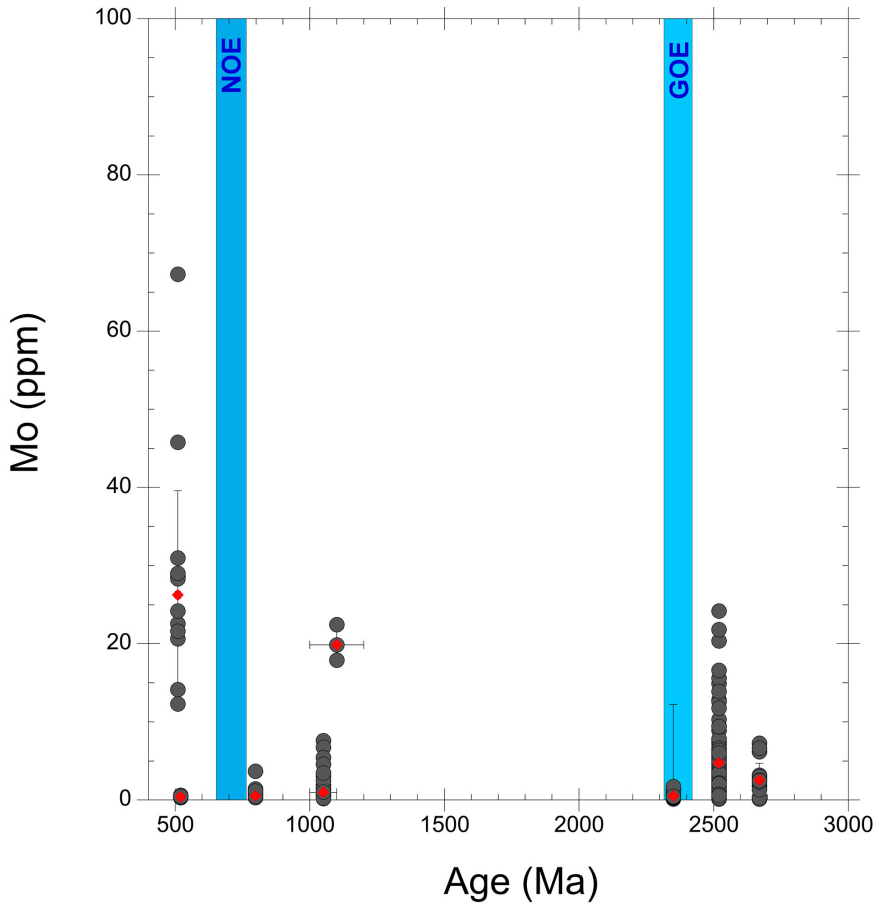


Figure 6: Plot of pyrite Mo content versus sample age. The post-NOE mid-Cambrian pyrites are markedly enriched in Mo concentration. Middle Cambrian pyrites contain a Mo range of ~20-70 ppm whereas the Neoarchaean to Neoproterozoic samples contain Mo concentrations of ~0-30 ppm. Also shown in Figures 6-10 is the timing of the GOE and NOE as vertical bars, and a red symbol illustrating the median concentration value for each sample set.

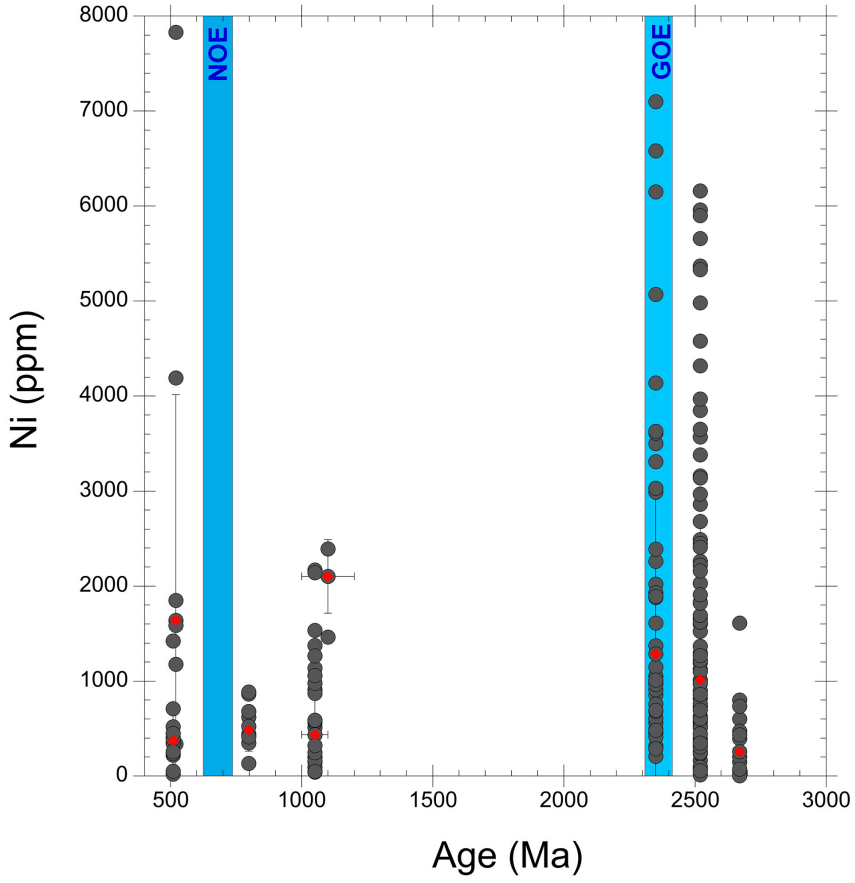


Figure 7: Plot of pyrite Ni content versus sample age. The pre-GOE Neoarchaean and syn-GOE Palaeoproterozoic samples exhibit a much wider concentration range (0-8,000 ppm) and higher maxima as compared to Neoproterozoic and Palaeozoic samples, of which the vast majority (excluding only two samples) contain Ni concentrations of 0-2,500 ppm.

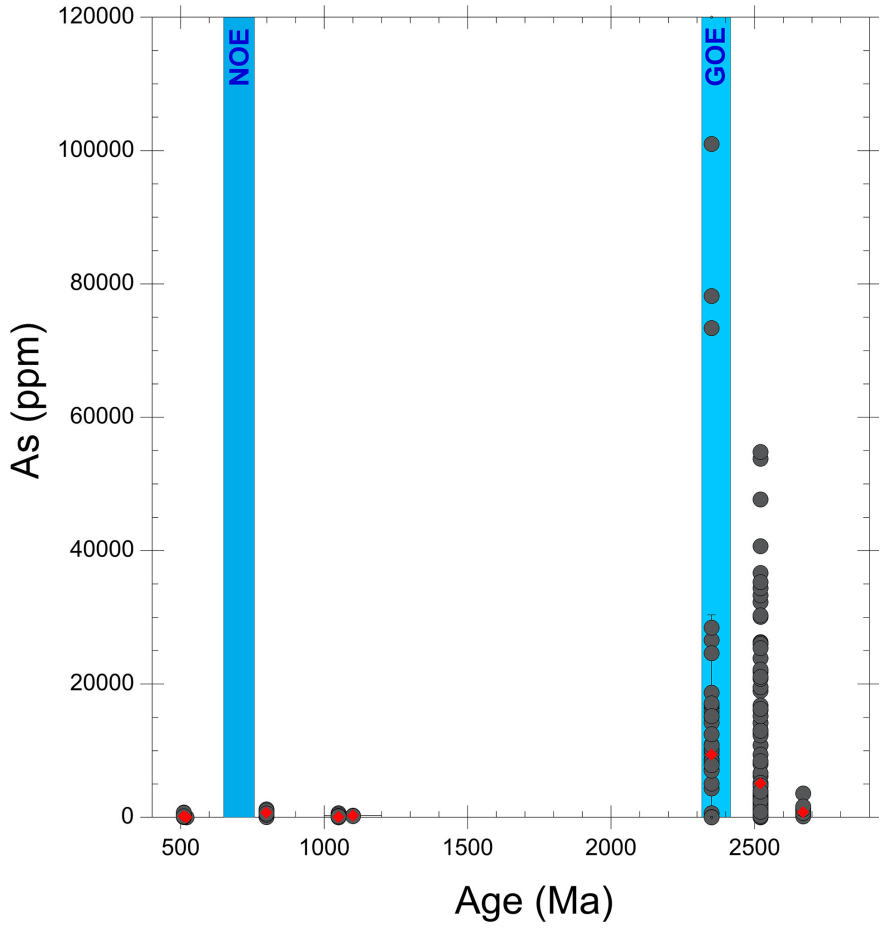


Figure 8: Plot of pyrite As content versus sample age. The Palaeoproterozoic and pre-GOE Neoarchaean samples are enriched in As by an order of magnitude over the younger Neoproterozoic and Palaeozoic samples. Palaeoproterozoic and Neoarchaean samples record maximum As concentrations of ~100,000 ppm whereas maximum As concentrations in the younger samples are ~1,000 ppm.

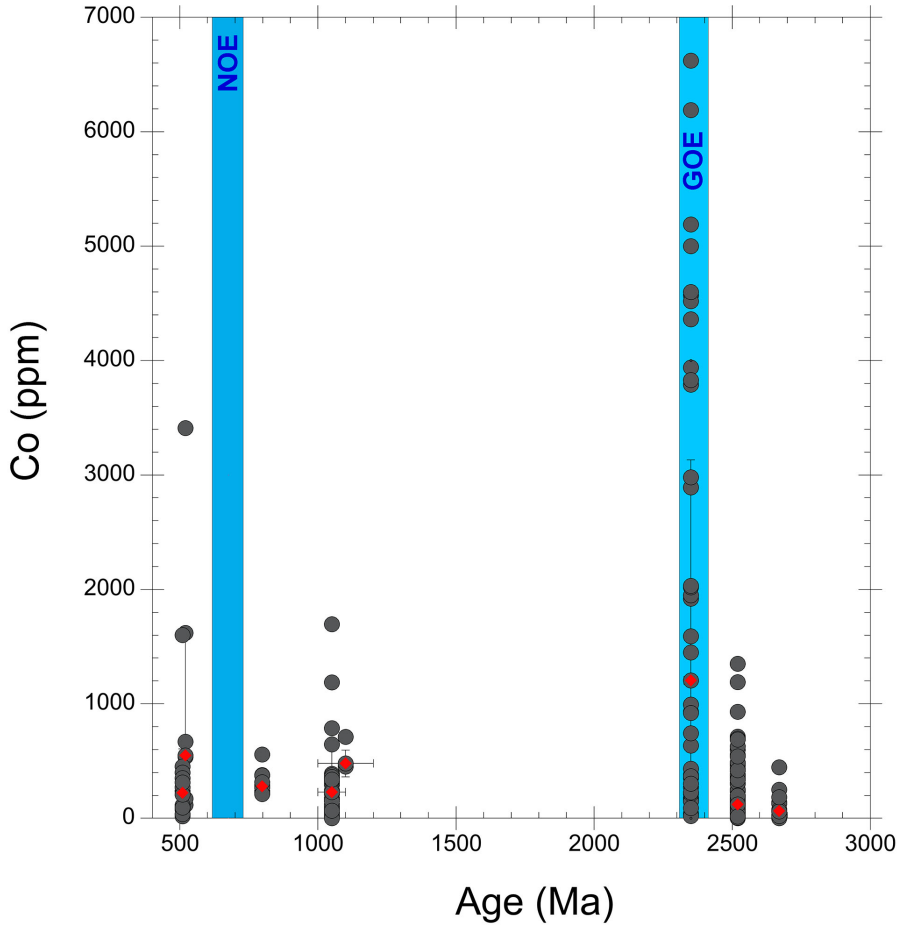


Figure 9: Plot of pyrite Co content versus sample age. Cobalt concentration is significantly elevated, up to 7,000 ppm, in syn-GOE Palaeoproterozoic samples, while all of the older samples and all but one of the younger samples contain concentrations well below 2,000 ppm. A number of other metals V, Bi, and Pb all show a similar pattern although to a lesser extent than Co.

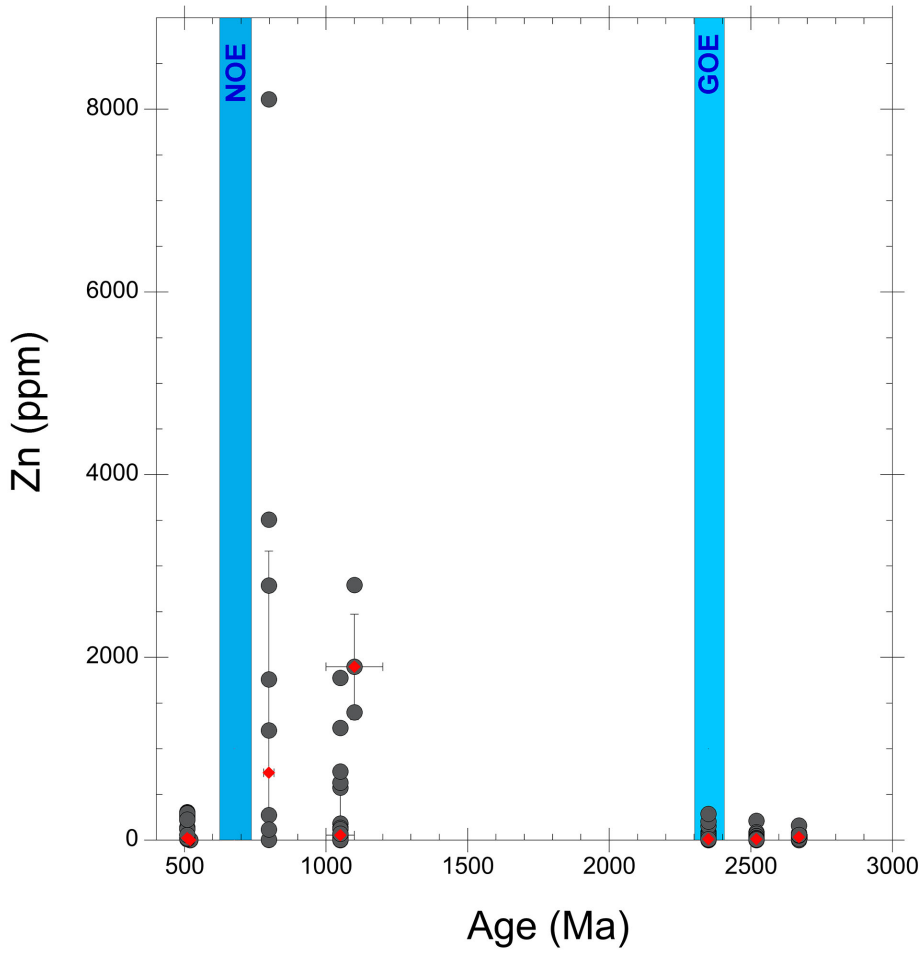


Figure 10: Plot of pyrite Zn content versus sample age. The Mesoproterozoic and Neoproterozoic pyrites are enriched in Zn concentration by an order of magnitude over the Palaeozoic and the Palaeoproterozoic and Neoarchaean pyrite samples. The Mesoproterozoic and Neoproterozoic pyrite samples record concentrations of up to 10,000 ppm whereas the Palaeozoic and Neoarchaean and Palaeoproterozoic samples record concentrations of ~100 ppm.

Arsenic reveals a significant temporal pattern. The pre-GOE Neoarchaean and syn-GOE Palaeoproterozoic pyrite samples are enriched in As by an order of magnitude over the Neoproterozoic and Palaeozoic samples. Many of the Neoarchaean and Palaeoproterozoic pyrite samples record As concentrations of up to 100,000 ppm, whereas the maximum As concentrations in the Neoproterozoic and Palaeozoic samples are less than 1,000 ppm (Fig. 8).

Cobalt exhibits very significantly elevated concentrations in syn-GOE Palaeoproterozoic samples from the Espanola Formation, from a few ppm up to 7,000 ppm, whereas all of the older pre-GOE, and all but one of the Neoproterozoic and Palaeozoic pyrite samples contained Co concentrations of well below 2,000 ppm (Fig. 9). Other transition metals (V, Bi, and Pb) show a similar pattern, although to a lesser extent than Co, of elevated concentrations in the syn-GOE Palaeoproterozoic samples when compared with the older pre-GOE Archaean and Neoproterozoic and Palaeozoic samples.

Finally, a clear temporal trend is apparent in zinc concentration of the pyrite samples. The Mesoproterozoic and Neoproterozoic pyrite samples are enriched in Zn by an order of magnitude over the Palaeozoic and Palaeoproterozoic and Archaean pyrite samples. The Mesoproterozoic and Neoproterozoic pyrite samples record Zn concentrations of up to 10,000 ppm, whereas the Palaeozoic and the Neoarchaean and Palaeoproterozoic pyrite samples record concentrations of ~100 ppm (Fig. 10).

5. Discussion

5.1. Pyrite occurrence

Pyrite is especially abundant in the black, kerogen-rich pre-GOE carbonate samples (Fig. 3a-f), whereas the paler, kerogen-poor post-GOE carbonate samples contain far less pyrite (Fig. 3g-l). Thus, although marine sulphate availability grew substantially after the GOE (Canfield & Raiswell, 1999; Lyons et al., 2009; Planavsky et al., 2014; Scott et al., 2014) the abundance of *preserved* pyrite in microbial carbonates did not. By contrast to sulphate, the flux of Fe to the ocean progressively declined after both the GOE and NOE. This is evident from Fe concentrations in Archaean carbonates at an order of magnitude higher than their Phanerozoic counterparts (Veizer et al., 1989). Whereas the reduced Fe flux may have contributed

to the reduction in pyrite preservation, at least in the shallow post-GOE oceanic environment, our observations suggest that organic C preservation may have been the more important factor.

Sulphate-reducing bacteria obtain energy by oxidising organic matter while the accompanying reduction reaction reduces sulphate to H_2S, which goes on to react with iron in the water column to produce pyrite (Berner et al., 1985). Thus, availability of organic matter is an absolute requirement for bacterial sulphate reduction, and the subsequent pyrite formation. Abundant pyrite in the black, kerogen-rich, pre-GOE carbonate samples, is empirically associated with preservation of organic matter (see also: Klein & Beukes, 1989; Kamber & Whitehouse, 2007). For example, reduced C in the Huntsman Quarry stromatolites is so abundant that it was successfully analysed for isotope composition as early as in 1971 (Schopf et al., 1971). Klein and Beukes (1989) analysed comparable stromatolites of the Campbellrand Supergroup to our study and obtained reduced C contents between 0.59 and 2.79 wt%. By contrast, the Palaeoproterozoic limestones of the Espanola Formation consistently contain less than 0.1 mg g^{-1} of reduced C, i.e., less than 0.01 wt% (Bekker et al., 2005).

Post-GOE oxidation of organic matter in shallow-marine sediment would likely have led to a reduction in the activity of sulphate-reducing bacteria and H_2S produced by sulphate-reducing bacteria could also have been oxidised back to sulphate instead of going on to react with detrital iron minerals or dissolved Fe^{2+} to form iron sulphides. Both these factors leading in turn a diminution of pyrite formation in the sediment (Fig. 3g-l). Finally, the increase in oxygen levels in post-GOE shallow-marine environments could also have promoted diagenetic loss of pyrite.

The morphological diversity of pre-GOE Archaean microbial-carbonate-hosted pyrite (Fig. 3a-f) is much greater than that of the syn- and post-GOE microbial-carbonate-hosted pyrite (Fig. 3g-l). The instability of pyrite in oxic post-GOE shallow-marine environments not only resulted in a dramatic reduction in pyrite preservation, but was also likely responsible for this lack of preserved morphological diversity in post-GOE pyrites. Post-GOE pyrite consists largely of xenomorphic, porous, subrounded nodules and disseminated fine microcrystals, commonly with euhedral overgrowths. By contrast, the Archaean pre-GOE pyrites preserve a number

of distinct morphological types, including pyrite sphaeroids, pyrite disseminated in microbial mats, and later-pyrite in fenestral fill.

5.2. Pyrite trace metal substitution and temporal trends

The new trace metal data for the Neoarchaean to Ordovician microbial-carbonate-hosted pyrites reveals obvious temporal trends for several of the transition metals analysed. At any given time there is a substantial spread in the data, similar to the wide range in Ni/Fe ratio in BIF or Mo content in black shale. In the case of pyrite trace metal content two factors likely contributed to the concentration range. Firstly, in instances of rapid pyrite formation, the local sediment may have become depleted in metals. Secondly, different pyrite formation paths may be associated with unique trace metal incorporation, affecting overall concentrations. Regardless, Large et al. (2014) presented a number of lines of evidence supporting the contention that the trace metal content of early-formed sedimentary pyrite is a valid first-order proxy for trace metal variations in the ocean through time and that the temporal trends have geological significance.

The following temporal trends are discussed with reference to three stages in shallow marine trace metal and S inventories. Figure 11 summarises a few of the key geological, atmospheric and oceanic features that may have influenced the inventories and thus the temporal concentration trends in pyrite from shallow marine carbonates.

Pyrite formed in pre-GOE Archean microbial carbonates would have likely derived Fe predominantly from weathering of silicates (Zbinden et al., 1988; Holland et al., 1989; Holland & Beukes, 1990) along with substantial input of Fe^{2+} from hydrothermal venting, and derived S predominantly from volcanic degassing. The atmospheric origin of S is implied from the strongly mass independent fractionation of Archaean sedimentary sulphides (Walker & Brimblecombe, 1985; Farquhar et al., 2000) (Fig. 11a). However, on the post-GOE land surface, the chemical stability of minerals was very different with profound implications for Fe and S cycles. Because of the conversion of Fe^{2+} to insoluble Fe^{3+}, iron was almost quantitatively retained in weathering products (Fig. 11b), whereas the anoxic deep ocean still permitted the flux of hydrothermally sourced Fe into the oceanic inventory. On the post-GOE surface environment sulphides became unstable in the critical zone, and when

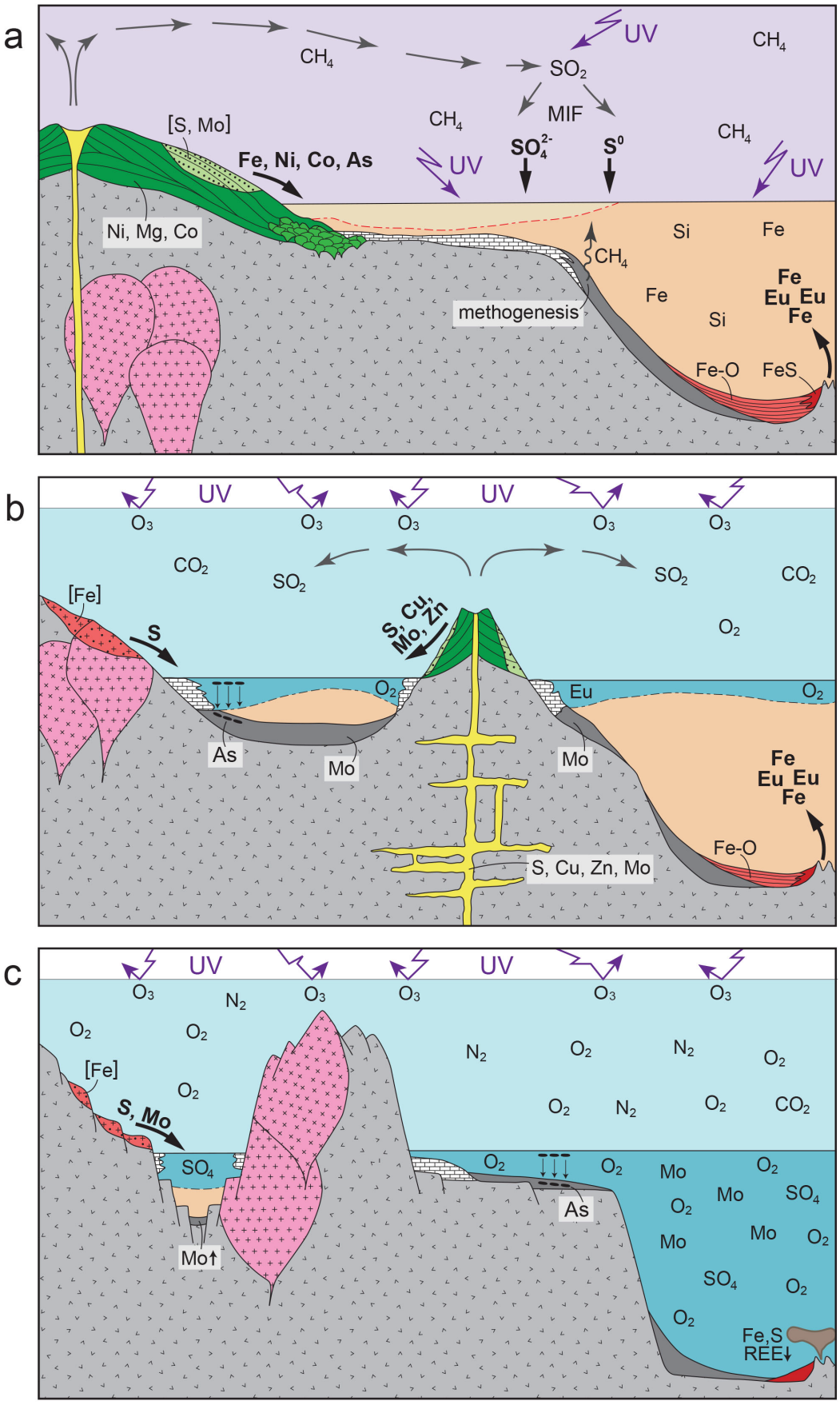

a
UV
CH4
SO2
MIF
CH4
[S, Mo]
Fe, Ni, Co, As
UV
SO4 2-
S0
CH4
UV
Ni, Mg, Co
Si
Fe
CH4
Fe
Fe
Eu Eu
Fe
Si
methogenesis
Fe-O
FeS
b
UV
UV
O3
O3
O3
O3
O3
CO2
SO2
SO2
CO2
[Fe]
S
S, Cu,
Mo, Zn
O2
O2
Eu
O2
As
Mo
Mo
Fe
Eu Eu
Fe
Fe-O
S, Cu, Zn, Mo
c
UV
UV
O3
N2
O3
O3
O3
O3
O2
O2
N2
O2
N2
O2
[Fe]
O2
O2
N2
O2
CO2
S, Mo
SO4
O2
O2
Mo
O2
Mo
SO4
As
O2
Mo
Mo
O2
SO4
O2
O2
Mo↑
Fe,S
REE↓

Figure 11: Schematic illustration of geological, atmospheric and oceanic factors influencing the Fe, S and trace metal cycles. Panel (a) shows Archaean situation, panel (b) refers to Palaeoproterozoic Earth after the GOE and panel (c) depicts the Earth close to the Cambrian/Precambrian boundary, The defining features are briefly explained but for a full explanation, readers are referred to the text. In the Archaean, the exposed land surface was dominated by volcanic rocks of mainly mafic composition (i.e. basaltic resurfacing). The only source of dissolved sulphur was volcanic degassing and all sulphur was mass independently fractionated. High UV load inhibited very shallow water planktonic productivity. Dissolved iron was sourced both from land and from hydrothermal vents. Methanogens thrived due to the high flux of dissolved Ni from land. The ocean was anoxic but an Fe and O chemocline existed (red broken line) possibly in response to biological activity on shallow shelves (e.g., Sumner, 1997a). Microbial carbonate factories shown with limestone symbol. In post-GOE Palaeoproterozoic times, the dominant exposed lithologies had changed to arc-type volcanoes and mixed plutonic, metamorphic and sedimentary rocks, providing a greater flux of Zn, Mo and Cu and much reduced Ni flux to the ocean. Weathering under the now slightly oxidised atmosphere converted silicate Fe^{2+} to insoluble Fe^{3+}, effectively shutting down the terrestrial dissolved Fe supply. The shallow ocean was oxygenated but at depth anoxic and variably euxinic conditions prevailed, drawing down the oceanic Mo inventory. Greater planktonic productivity, now shielded from harmful UV rays, may have drawn down the As inventory. Iron was mainly delivered from high-T hydrothermal vents resulting in detectable excesses of Eu in deep sea sediments (e.g., Planavsky et al., 2010). After the NOE, the ocean became fully ventilated, terminating hydrothermal Fe supply, resulting also in the loss of a detectable Eu excess (e.g., Baldwin et al., 2012). The extent of euxinic basins was restricted with concomitant loss of Mo draw-down potential and build-up of the oceanic Mo reservoir. This may have additionally been increased by the greater extent of sulphide weathering aided by the higher free O content of the atmosphere.

exposed to air and/or water decomposed, thereby releasing a much greater flux of sulphate into the ocean (Fig. 11b). Thus, Fe and S sources in post-GOE pyrite would have changed dramatically. Post-GOE pyrite Fe was more likely sourced from deep hydrothermal vents while post-GOE pyrite S was largely sourced from oxidative weathering of terrestrial sulphides (Fig. 11b). By post-NOE times, the deep ocean became ventilated inhibiting a significant contribution of hydrothermal Fe, and the overall oceanic Fe inventory dropped, such that marine dissolved Fe was sourced from a variety of minor sources, similar to the present day.

The post-GOE oxidative weathering of terrestrial sulphides and landmasses not only caused a transition in pyrite iron and sulphur sources, but also greatly affected the flux of sulphide-hosted trace metals (e.g., Mo, Co, Cu, Zn, As) to the ocean (Fig. 11b). This change greatly increased the oceanic transition metal inventory, providing greater opportunity for trace metal substitution into pyrite. To a first order, this evolution seems to be reflected in the composition of analysed sulphides, with the younger syn-GOE microbial-carbonate-hosted sulphides exhibiting much greater chemical variation and substitution (Fig. 4.B) than the pre-GOE microbial-carbonate-hosted sulphides (Fig. 4.A). However, only analyses of pyrite revealing FeS_2 chemistry were utilised for the reconstruction of oceanic trace metal temporal trends reported here.

5.2.1. Pyrite Mo temporal trend

A striking outcome of this study is that Mo concentrations in pyrite deposited after the Neoproterozoic icehouse (Hoffman et al., 1998) (Middle Cambrian St.-Roch Formation) are notably higher than those of all other material analysed (Fig. 6). Molybdenum is a robust redox proxy owing to its pronounced redox sensitivity, minimal detrital influence and uniquely bimodal geochemical features (Och & Shields-Zhou, 2012). Molybdenum in oxic water is mainly present as molybdate, (MoO_4^{2-}) and primarily delivered to the ocean through riverine influx when Mo is liberated during oxidative weathering of continental crust (Broecker et al., 1982). Under oxic oceanic conditions, Mo is removed from the water column by co-precipitation and burial with Mn-oxyhydroxides (Bertine & Turekian, 1973), a slowly occurring process. Although oxygenated environments overlie most of the sea floor today, removal of molybdate in association with Mn-oxyhydroxides consumes only 35% of the annual riverine flux (Scott et al., 2008). The remainder of the riverine flux

is removed in spatially limited sulphidic settings where molybdate is converted to particle-reactive thiomolybdates, and Mo removal by organic matter and other reduced substances far outpaces that of oxygenated environments. Importantly, under sub-oxic to anoxic, non-euxinic conditions where Mn oxides and sulphide (the principal consumers of Mo) are absent no significant enrichment of Mo is achieved. The finding here is that throughout the Precambrian, the oceanic Mo inventory has remained very low. In pre-GOE times, this was mainly because little Mo was released into the ocean. After the GOE, much greater amounts of Mo and sulphate entered the ocean. Because most of the deeper ocean remained anoxic and possibly temporally or at least locally euxinic, Mo was sequestered into oceanic sediments (Fig. 11b), thereby preventing the build-up of a large dissolved Mo pool. This study suggests, albeit through a limited data set with a large gap in data between ca. 2.35 and 1.1 Ga, that at least by middle Cambrian times, shallow water pyrites had became notably enriched in Mo, implying that the marine Mo inventory had significantly increased because of the reduction of euxinic basins (Fig. 11c) in response to global deep ocean ventilation.

To a first order, this finding is consistent with results from a number of recent studies on diverse deep-water black shales. Scott et al. (2008) reported extreme Mo enrichment in Phanerozoic black shales, thought to reflect deep-ocean oxygenation and very limited Mo-removing sulphidic environments. Och and Shields-Zhou (2012) implied that enhanced oxidative weathering on the continents and/or bioturbation may have contributed more significantly than the retreat of euxinic environments to the growth of the oceanic trace metal, Mo and possibly V and U, reservoirs. Large et al. (2014) also reported strongly elevated maximum Mo concentrations in Phanerozoic black shale-hosted pyrite. By comparison, the onset of the Mo enrichment in this dataset occurs some 0.05-0.1 Ga later. However, it is noted that both Scott et al. (2008) and Large et al. (2014), also reported low Mo concentrations for some early Cambrian samples. It is likely that the slight discrepancy in the onset of the enrichment is a statistical artefact, caused by the much less dense sampling of shallow-water pyrites and the resulting limited dataset of the present study.

Previous studies of the evolution of the oceanic Mo reservoir sampled deep-marine (rift?) basins from which inferences regarding the global (open) oceanic Mo inventory were made. Since the inventory is strongly dependent on the terrestrial Mo

flux (e.g., Och & Shields-Zhou, 2012) it is significant that the Phanerozoic Mo enrichment is now also found in shallow-marine microbial-carbonate-hosted pyrites reported here.

5.2.2. Pyrite Ni temporal trend

Konhauser et al. (2009) analysed the Ni/Fe ratios preserved in deep-water BIFs over time, recording a significant, irreversible decline in oceanic Ni concentration at the end of the Archaean, which they attributed to a reduced flux of Ni to the ocean. The reduced flux of Ni to the ocean ca. 2.7 Ga was interpreted to reflect cooling Archaean mantle temperatures and a concomitant end of very high-Mg volcanism (Konhauser et al., 2009). Because the Ni content of mafic magma increases strongly with increasing Mg-content, Archaean komatiite and high-Mg basalts on land (Fig. 11a) are the most plausible reason for the high molar Ni/Fe ratio of Archaean BIF (Kamber, 2010).

The shallow-marine microbial-carbonate-hosted pyrites analysed here show an overall decrease in Ni concentration through the Precambrian (Fig. 7), although high Ni concentrations in pyrite apparently persisted until the GOE. Two factors qualify this finding. Firstly, the 2.35 Ga Espanola Formation pyrite formed immediately after an inferred influx of glacial outwash, and is not necessarily representative of metal incorporation from open seawater. Secondly, the glaciated continental interior associated with this part of the Huronian Supergroup consisted of reworked upper crust of the southernmost Superior Province that was dominated by bimodal classic granite-greenstone terrains from which all detrital zircon is Neoarchaean (Long et al., 2011). The 2.35 Ga data from this study therefore probably reflects a locally elevated Ni-source rather than a global condition. The decrease in shallow-marine Ni concentration reported here for all the younger samples is significant because it confirms that the Ni concentration of all seawater decreased, not just deep basinal waters as previously described (Konhauser et al., 2009; Large et al., 2014). This phenomenon reported here is attributed to a change in lithological make-up of the exposed land surface which is also evident in the secular change in clastic sediment composition (Condie, 1993). The Proterozoic data in our study are too widely spaced to substantiate whether a further drop in oceanic Ni inventory occurred after the NOE. However, because terrestrial Ni is primarily released from Fe- or Mg-silicates and not from sulphides, the redox evolution of the atmosphere has

less influence on the oceanic Ni inventory than on strongly chalcophile metals. Instead, it appears as though there may have been a slight increase in Ni concentration in the Palaeozoic, similarly to findings from Large et al. (2014).

5.2.3. Pyrite As temporal trend

Arsenic is common in sulphide minerals and for this reason one might expect a post-GOE increase in oceanic As concentration owing to the onset of terrestrial sulphide weathering after the GOE. However this is not the case, the As temporal trend reported here reveals a drop in concentration similar to the post-Palaeoproterozoic drop in Ni concentration, although to an even greater extent (Fig. 8). Similarly, an overall declining As trend through the Precambrian was discovered by Large et al. (2014).

Although it is not possible to pinpoint exactly what caused the prominent drop in As, two main factors can be considered. Firstly, the nature of the As source material remains uncertain. The most common sources of As in the natural environment are volcanic rocks, specifically ash and volcanic weathering products, marine sedimentary rocks, and hydrothermal ore deposits and associated geothermal waters (Wang & Mulligan, 2006b). The Archaean rock record from greenstone belts shows abundant evidence for prolific volcanic resurfacing and for deposition of easily weathered volcanic deposits (e.g., Ross et al., 2011). The post-Palaeoproterozoic drop in As concentration reported here could, therefore, relate to a change in the composition of the post-Palaeoproterozoic land surface source material - namely, a transition from a volcanic surface (e.g., Condie, 1993) to reworked plutonic and metamorphic upper crustal material that may have been less susceptible to release of As. It is important to recall that although the presently exposed level of Archaean continental crust is rich in granitoids, the make-up of Archaean clastic sedimentary rocks shows that at the time, the main exposed rock sources were mafic and volcanic. Only by Palaeoproterozoic times did the Archaean granitoids get exposed (Fig. 11b).

Second, As in natural waters has been attributed to several geochemical processes, including oxidation of arsenic-bearing sulphides, desorption of arsenic from (hydro)oxides, reductive dissolution of As-bearing iron (hydro)oxides, release of arsenic from geothermal water, and leaching of arsenic from sulphides by carbonates (Kim et al., 1999; Bennett & Dudas, 2003; Wang & Mulligan, 2006a;

2006b), but many studies have also underlined the importance of sorption of As onto organic material (e.g., Bugueño et al., 2014). The post-Palaeoproterozoic drop in As concentration reported here must also relate at least in part to these processes. Adsorption of dissolved As onto organic molecules or a change in fluvial As speciation after the GOE may also have contributed to the reduced As inventory of the ocean.

Finally, Large et al. (2014) proposed that the declining As trend could be related to the higher level of volatile elements, in the context of a progressively less degassing Earth in the Archaean. This may have contributed to stabilise the arsenic polysulfide complexes which declined in concentration through the early Proterozoic as euxinia dropped.

5.2.4. Pyrite Co temporal trend

Cobalt exhibits significantly elevated concentrations in the syn-GOE Palaeoproterozoic samples only (Fig. 9). Vanadium, Bi and Pb all show a similar pattern of elevated concentrations in syn-GOE Palaeoproterozoic samples (Supplementary Information). These trends are less well-developed than that of Co are not separately discussed here.

A moderately well-developed pattern of elevated, albeit variably, Co seawater concentrations from ca. 2.8 - 1.84 Ga has recently been reported from studies of iron formation and authigenic pyrite (Large et al., 2014; Swanner et al., 2014). Swanner et al. (2014) attributed this trend to a combination of factors. Firstly, the large volume of hydrothermal fluids circulating through submarine ultramafic rocks could have resulted in an increased hydrothermal flux. Secondly, increased terrestrial Co delivery to the ocean governed by the preponderance of mafic rocks at the exposed surface, i.e., olivine and pyroxene in ultramafic rocks tend to be enriched in Co (e.g., Carr & Turekian, 1961). Thirdly, a predominately anoxic ocean with a low capacity for Co burial also contributed to the large dissolved marine Co inventory from ca. 2.8 - 1.84 Ga.

The very high Co contents of the syn-GOE Palaeoproterozoic Espanola Formation pyrite are relevant to this debate. As can be seen from the REE patterns of these rocks, the (local) waterbody lacks the positive Eu anomaly, which is seen as the hallmark of enhanced high-temperature hydrothermal input into the ocean (Figure 11 (a) and (b)). Yet, despite a clear lack for hydrothermal vent fluid flux, the pyrite is

strongly enriched in Co. The Co trend established by Large et al. (2014) resembles that of Ni. These authors founds particularly elevated concentrations coinciding with large igneous province (LIP) eruption of mafic lavas (Prokoph et al., 2004). Archaean komatiitic LIPs are enriched in Ni and Co thus contributing to high levels of Ni and Co in the ocean (Large et al., 2014). The absence of an elevated Eu anomaly in the elevated Co samples reported here, together with the equally elevated Ni content reported by Large et al. (2014), suggests that the terrestrial Co flux may have been the more important factor governing the elevated 2.8 - 1.84 Ga marine Co pool.

5.2.5. Pyrite Zn temporal trend

The Mesoproterozoic and Neoproterozoic pyrite samples are notably enriched in Zn over both the younger and older pyrites (Fig. 10). This contrasts with the findings of Robbins et al. (2013), Scott et al. (2013) and Large et al. (2014), where the marine zinc abundance appears relatively constant throughout Earth history. This disparity may point to a different Zn abundance in the shallow sea or may be an artefact of the very limited sampling density of the present study. In the former case, increased local supply of Zn could have arisen from the newly established arc-dominated volcanic systems (e.g., DeWolfe & Gibson, 2013) or from preferential weathering of Proterozoic zinc deposits under oxic atmospheric conditions.

Scott et al. (2013) proposed that Zn-enriched material may represent sediment influenced by a local hydrothermal source containing iron. Hydrothermal fluids are strongly enriched in Zn (German & Von Damm, 2006), but in oxic or euxinic deep water, little zinc will leave the proximal hydrothermal setting owing to oxide and sulphide mineral formation (Fig. 11c; Edmonds & German, 2004). Furthermore, the samples analysed in the present study do not contain positive Eu anomalies, indicating that the seawater from which the carbonates formed was not influenced by hydrothermal fluids.

6. Summary

Marine sedimentary rocks hold great potential for the reconstruction of Precambrian atmospheric and oceanic redox evolution, which can be expressed in their inventory of redox-sensitive trace metals. The oceanic inventory of many redox sensitive trace metals ultimately depends on their terrestrial flux. However, most of

the currently available information has been derived from deep-water sedimentary rocks and the validity of claims for increased or decreased terrestrial fluxes has remained untested as far as the shallow-marine environment is concerned. Here, the first systematic study of trace metal inventories of the shallow-marine environment by analysis of microbial-carbonate-hosted pyrite is presented.

A petrographic survey of microbial carbonates, from ca. 2.65-0.52 Ga, revealed a first-order difference in preservation of early diagenetic pyrite and reduced C. Microbial carbonates formed before the 2.4 Ga GOE are much richer in kerogen, preserve more pyrite, and contain pyrite grains of greater morphological variability than samples deposited after the GOE. This disparity is probably a function of better pyrite preservation in the pre-GOE sedimentary environment, which was starved of free O_2.

Post-GOE oxidative weathering of terrestrial sulphides and landmasses caused major transitions in oceanic iron and sulphur sources (Fig. 11), but also greatly affected the flux of sulphide-hosted transition metals to the ocean providing greater opportunity for trace metal substitution into pyrite. This evolution seems to be reflected in the composition of pyrite, with the younger post-GOE microbial-carbonate-hosted sulphides exhibiting much greater chemical variation and substitution than the pre-GOE microbial-carbonate-hosted sulphides (Fig. 4).

Trace metal analysis of the Neoarchaean to Ordovician microbial-carbonate-hosted pyrites reveals obvious temporal trends for several of the transition metals analysed, supporting earlier proposals derived from deep-water sedimentary rocks:

1. The shallow-marine microbial-carbonate-hosted pyrite confirms a rise in the oceanic Mo inventory across the Precambrian-Cambrian boundary, implying the establishment of efficient deep-ocean ventilation;

2. The carbonate-hosted pyrite confirms that the Neoarchaean ocean had higher Ni concentration, attributed to a greater proportion of magnesian volcanic rock on land;

3. The carbonate-hosted pyrite record a post-Palaeoproterozoic drop in As concentration which could relate to a change in the composition of

the land surface source material that may have been less susceptible to release of As, and must also relate at least in part to adsorption of dissolved As onto organic material and may additionally have been influenced by mantle degassing;

4. Increased terrestrial Co delivery to the ocean governed by the preponderance of mafic rocks at the exposed surface and a predominately anoxic ocean with a low capacity for Co burial also contributed to the large dissolved marine Co inventory from ca. 2.8 - 1.84 Ga;

5. Mesoproterozoic and Neoproterozoic pyrite Zn enrichment reported here may reflect increased local supply of Zn arisen from newly established arc-dominated volcanic systems or from oxic weathering of Proterozoic zinc deposits.

Acknowledgements

This research was supported by an EU FP7 Marie Curie Actions – Career Integration Grant awarded to B.S.K. which supported the analytical work and provided financial support to M.G. Joe Petrus is thanked for analytical support. Claire Kamber drafted figure 11. Stephen Moorbath (Huntsman Quarry), and Nick Beukes (Campbellrand Formation) kindly provided stromatolite samples. Three journal reviewers provided very helpful comments on an earlier draft.

References

Aitken JD (1997) *Stratigraphy of the Middle Cambrian platformal succession, southern Rocky Mountains,* Geological Survey of Canada.

Aitken J (1981) Stratigraphy and sedimentology of the Upper Proterozoic Little Dal Group, Mackenzie Mountains, Northwest Territories. *Proterozoic basins of Canada. Edited by FHA Campbell. Geological Survey of Canada, Paper,* 8, 1-10.

Aitken JD (1997) *Stratigraphy of the Middle Cambrian platformal succession, southern Rocky Mountains,* Geological Survey of Canada.

Alexander BW, Bau M, Andersson P (2009) Neodymium isotopes in Archean seawater and implications for the marine Nd cycle in Earth's early oceans. *Earth and Planetary Science Letters,* 283, 144-155.

Alexander BW, Bau M, Andersson P, Dulski P (2008) Continentally-derived solutes in shallow Archean seawater: rare earth element and Nd isotope evidence in iron formation from the 2.9 Ga Pongola Supergroup, South Africa. *Geochimica et Cosmochimica Acta,* 72, 378-394.

Allen JS, Thomas WA, Lavoie D (2009) Stratigraphy and structure of the Laurentian rifted margin in the northern Appalachians: A low-angle detachment rift system. *Geology,* 37, 335-338.

Altermann W, Nelson DR (1998) Sedimentation rates, basin analysis and regional correlations of three Neoarchaean and Palaeoproterozoic sub-basins of the Kaapvaal craton as inferred from precise U–Pb zircon ages from volcaniclastic sediments. *Sedimentary Geology,* 120, 225-256.

Anbar AD, Duan Y, Lyons TW, Arnold GL, Kendall B, Creaser RA, Kaufman AJ, Gordon GW, Scott C, Garvin J (2007) A whiff of oxygen before the great oxidation event? *Science,* 317, 1903-1906.

Andrews A, Masliwec A, Morris W, Owsiacki L, York D (1986) The silver deposits at Cobalt and Gowganda, Ontario. II: An experiment in age determinations

employing radiometric and paleomagnetic measurements. *Canadian Journal of Earth Sciences,* 23, 1507-1518.

Baldwin GJ, Turner EC, Kamber BS, Colpron M (2012) A new depositional model for glaciogenic Neoproterozoic iron formation: insights from the chemostratigraphy and basin configuration of the Rapitan iron formation 1 1 Northwest Territories Geoscience Office Contribution 0052. *Canadian Journal of Earth Sciences,* 49, 455-476.

Beard BL, Johnson CM, Von Damm KL, Poulson RL (2003) Iron isotope constraints on Fe cycling and mass balance in oxygenated Earth oceans. *Geology,* 31, 629-632.

Bekker A, Holland H, Wang P-L, Rumble D, Stein H, Hannah J, Coetzee L, Beukes N (2004) Dating the rise of atmospheric oxygen. *Nature,* 427, 117-120.

Bekker A, Kaufman A, Karhu J, Eriksson K (2005) Evidence for Paleoproterozoic cap carbonates in North America. *Precambrian Research,* 137, 167-206.

Bennett B, Dudas MJ (2003) Release of arsenic and molybdenum by reductive dissolution of iron oxides in a soil with enriched levels of native arsenic. *Journal of Environmental Engineering and Science,* 2, 265-272.

Berner R, De Leeuw J, Spiro B, Murchison D, Eglinton G (1985) Sulphate reduction, organic matter decomposition and pyrite formation [and discussion]. *Philosophical Transactions of the Royal Society of London. Series A, Mathematical and Physical Sciences,* 315, 25-38.

Berner RA (1972) Sulfate reduction, pyrite formation, and the oceanic sulfur budget. *In The Changing Chemistry of the Oceans: Nobel Symposium 20*, 347–361.

Bernstein L, Young GM (1990) Depositional environments of the Early Proterozoic Espanola Formation, Ontario, Canada. *Canadian Journal of Earth Sciences,* 27, 539-551.

Bertine KK, Turekian KK (1973) Molybdenum in marine deposits. *Geochimica et Cosmochimica Acta,* 37, 1415-1434.

Beukes NJ (1987) Facies relations, depositional environments and diagenesis in a major early Proterozoic stromatolitic carbonate platform to basinal sequence, Campbellrand Subgroup, Transvaal Supergroup, southern Africa. *Sedimentary Geology,* 54, 1-46.

Bickle MJ (1986) Implications of melting for stabilisation of the lithosphere and heat loss in the Archaean. *Earth and Planetary Science Letters,* 80, 314-324.

Bolhar R, Hofmann A, Woodhead J, Hergt J, Dirks P (2002) Pb-and Nd-isotope systematics of stromatolitic limestones from the 2.7 Ga Ngezi Group of the Belingwe Greenstone Belt: constraints on timing of deposition and provenance. *Precambrian Research,* 114, 277-294.

Broecker WS, Peng T-H, Beng Z (1982) *Tracers in the Sea,* Lamont-Doherty Geological Observatory, Columbia University.

Bugueño MP, Acevedo SE, Bonilla CA, Pizarro GE, Pasten PA (2014) Differential arsenic binding in the sediments of two sites in Chile's lower Loa River basin. *Science of The Total Environment,* 466, 387-396.

Campbell IH, Squire RJ (2010) The mountains that triggered the Late Neoproterozoic increase in oxygen: the Second Great Oxidation Event. *Geochimica et Cosmochimica Acta,* 74, 4187-4206.

Canfield D (1998) A new model for Proterozoic ocean chemistry. *Nature,* 396, 450-453.

Canfield DE (2004) The evolution of the Earth surface sulfur reservoir. *American Journal of Science,* 304, 839-861.

Canfield DE, Kristensen E, Thamdrup B (2005) *Aquatic geomicrobiology,* Gulf Professional Publishing.

Canfield DE, Poulton SW, Knoll AH, Narbonne GM, Ross G, Goldberg T, Strauss H (2008) Ferruginous conditions dominated later Neoproterozoic deep-water chemistry. *Science,* 321, 949-952.

Canfield DE, Poulton SW, Narbonne GM (2007) Late-Neoproterozoic deep-ocean oxygenation and the rise of animal life. *Science,* 315, 92-95.

Canfield DE, Raiswell R (1999) The evolution of the sulfur cycle. *American Journal of Science,* 299, 697-723.

Carr MH, Turekian K (1961) The geochemistry of cobalt. *Geochimica et Cosmochimica Acta,* 23, 9-60.

Coleman AP (1908) The lower Huronian ice age. *The Journal of Geology,* 16, 149-158.

Condie KC (1993) Chemical composition and evolution of the upper continental crust: contrasting results from surface samples and shales. *Chemical Geology,* 104, 1-37.

Cook NJ, Ciobanu CL, Mao J (2009) Textural control on gold distribution in As-free pyrite from the Dongping, Huangtuliang and Hougou gold deposits, North China Craton (Hebei Province, China). *Chemical Geology,* 264, 101-121.

Davies GF (2008) Episodic layering of the early mantle by the 'basalt barrier'mechanism. *Earth and Planetary Science Letters,* 275, 382-392.

Derry LA, Jacobsen SB (1988) The Nd and Sr isotopic evolution of Proterozoic seawater. *Geophysical Research Letters,* 15, 397-400.

Derry LA, Jacobsen SB (1990) The chemical evolution of Precambrian seawater: Evidence from REEs in banded iron formations. *Geochimica et Cosmochimica Acta,* 54, 2965-2977.

Dewolfe Y, Gibson H (2013) The facies architecture of a paleoproterozoic basaltic andesite synvolcanic intrusion, Flin Flon, Manitoba, Canada. *Bulletin of volcanology,* 75, 1-14.

Dow WG (1977) Kerogen studies and geological interpretations. *Journal of Geochemical Exploration,* 7, 79-99.

Duce RA, Tindale NW (1991) Atmospheric transport of iron and its deposition in the ocean.

Edmonds HN, German CR (2004) Particle geochemistry in the Rainbow hydrothermal plume, Mid-Atlantic Ridge. *Geochimica et Cosmochimica Acta,* 68, 759-772.

Fahrig W, Christie K, Jones D (1981) Paleomagnetism of the Bylot basins: evidence for Mackenzie continental tensional tectonics. *Proterozoic basins of Canada. Edited by FHA Campbell. Geological Survey of Canada, Paper*, 81-10.

Farquhar J, Bao H, Thiemens M (2000) Atmospheric influence of Earth's earliest sulfur cycle. *Science,* 289, 756-758.

Farquhar J, Savarino J, Airieau S, Thiemens MH (2001) Observation of wavelength‐sensitive mass‐independent sulfur isotope effects during SO2 photolysis: Implications for the early atmosphere. *Journal of Geophysical Research: Planets (1991–2012),* 106, 32829-32839.

Farquhar J, Wing BA (2003) Multiple sulfur isotopes and the evolution of the atmosphere. *Earth and Planetary Science Letters,* 213, 1-13.

Farquhar J, Zerkle A, Bekker A (2011) Geological constraints on the origin of oxygenic photosynthesis. *Photosynth Res,* 107, 11-36.

Fike D, Grotzinger J, Pratt L, Summons R (2006) Oxidation of the Ediacaran ocean. *Nature,* 444, 744-747.

Fischer W, Schroeder S, Lacassie J, Beukes N, Goldberg T, Strauss H, Horstmann U, Schrag D, Knoll A (2009) Isotopic constraints on the Late Archean carbon cycle from the Transvaal Supergroup along the western margin of the Kaapvaal Craton, South Africa. *Precambrian Research,* 169, 15-27.

German C, Von Damm K (2006) Hydrothermal processes. *The oceans & marine geochemistry (Treatise on geochemistry series, Vol. 6), Elsevier*, 181-222.

Goldhaber MB, Kaplan IR (1974) *The Sulfur Cycle,* Wiley Interscience

, New York.

Grassineau N, Nisbet E, Bickle M, Fowler C, Lowry D, Mattey D, Abell P, Martin A (2001) Antiquity of the biological sulphur cycle: evidence from sulphur and carbon isotopes in 2700 million–year–old rocks of the Belingwe Belt, Zimbabwe. *Proceedings of the Royal Society of London. Series B: Biological Sciences,* 268, 113-119.

Heaman L, Lecheminant A, Rainbird R (1992) Nature and timing of Franklin igneous events, Canada: implications for a Late Proterozoic mantle plume and the break-up of Laurentia. *Earth and Planetary Science Letters,* 109, 117-131.

Hoffman PF (1980) Wopmay Orogen: a Wilson Cycle of early Proterozoic age in the northwest of the Canadian Shield. *The continental crust and its mineral deposits. Proc. symposium held for J.Tuzo Wilson, Toronto, May 1979*, 523-549.

Hoffman PF, Kaufman AJ, Halverson GP, Schrag DP (1998) A Neoproterozoic snowball earth. *science,* 281, 1342-1346.

Holland H, Feakes C, Zbinden E (1989) The Flin Flon paleosol and the composition of the atmosphere 1.8 BYBP. *American Journal of Science,* 289, 362-389.

Holland HD (1978) The chemistry of the atmosphere and oceans. 351.

Holland HD (1984) *The chemical evolution of the atmosphere and oceans,* Princeton University Press.

Holland HD, Beukes NJ (1990) A paleoweathering profile from Griqualand West, South Africa: evidence for a dramatic rise in atmospheric oxygen between 2.2 and 1.9 bybp. *Am. J. Sci,* 290, 1-34.

Huerta-Diaz MA, Morse JW (1992) Pyritization of trace metals in anoxic marine sediments. *Geochimica et Cosmochimica Acta,* 56, 2681-2702.

Isley AE (1995) Hydrothermal plumes and the delivery of iron to banded iron formation. *The Journal of Geology*, 169-185.

Jackson G, Iannelli T (1981) Rift-related cyclic sedimentation in the Neohelikian Borden Basin, northern Baffin Island. *Geological Survey of Canada, Paper*, 81-10.

Jefferson CW, Parrish RR (1989) Late Proterozoic stratigraphy, U-Pb zircon ages, and rift tectonics, Mackenzie Mountains, northwestern Canada. *Canadian Journal of Earth Sciences,* 26, 1784-1801.

Jenkyns HC (2010) Geochemistry of oceanic anoxic events. *Geochemistry, Geophysics, Geosystems,* 11.

Jickells T, An Z, Andersen KK, Baker A, Bergametti G, Brooks N, Cao J, Boyd P, Duce R, Hunter K (2005) Global iron connections between desert dust, ocean biogeochemistry, and climate. *science,* 308, 67-71.

Johnson KS, Gordon RM, Coale KH (1997) What controls dissolved iron concentrations in the world ocean? *Marine Chemistry,* 57, 137-161.

Kamber B, Whitehouse M (2007) Micro‐scale sulphur isotope evidence for sulphur cycling in the late Archean shallow ocean. *Geobiology,* 5, 5-17.

Kamber BS (2010) Archean mafic–ultramafic volcanic landmasses and their effect on ocean–atmosphere chemistry. *Chemical Geology,* 274, 19-28.

Kamber BS (2015) The evolving nature of terrestrial crust from the Hadean, through the Archaean, into the Proterozoic. *Precambrian Research,* 258, 48-82.

Kamber BS, Webb GE (2001) The geochemistry of late Archaean microbial carbonate: implications for ocean chemistry and continental erosion history. *Geochimica et Cosmochimica Acta,* 65, 2509-2525.

Kamber BS, Webb GE, Gallagher M (2014) The rare earth element signal in Archaean microbial carbonate: information on ocean redox and biogenicity. *Journal of the Geological Society,* 171, 745-763.

Karhu JA, Holland HD (1996) Carbon isotopes and the rise of atmospheric oxygen. *Geology,* 24, 867-870.

Kim M, Nriagu J, Haack S (1999) Carbonate ion and dissolution of arsenic by groundwater. *Environ. Sci. Technol,* 34, 3094-3100.

Klein C, Beukes NJ (1989) Geochemistry and sedimentology of a facies transition from limestone to iron-formation deposition in the early Proterozoic Transvaal Supergroup, South Africa. *Economic Geology,* 84, 1733-1774.

Konhauser KO, Lalonde SV, Planavsky NJ, Pecoits E, Lyons TW, Mojzsis SJ, Rouxel O, Barley ME, Rosìere C, Fralick PW, Kump LR, Bekker A (2011) Aerobic bacterial pyrite oxidation and acid rock drainage during the Great Oxidation Event. *Nature,* 478, 369-373.

Konhauser KO, Pecoits E, Lalonde SV, Papineau D, Nisbet EG, Barley ME, Arndt NT, Zahnle K, Kamber BS (2009) Oceanic nickel depletion and a methanogen famine before the Great Oxidation Event. *Nature,* 458, 750-753.

Krogh T, Davis D, Corfu F (1984) Precise U-Pb zircon and baddeleyite ages for the Sudbury area. *The geology and ore deposits of the Sudbury structure,* 1, 431-446.

Kump LR, Seyfried Jr WE (2005) Hydrothermal Fe fluxes during the Precambrian: Effect of low oceanic sulfate concentrations and low hydrostatic pressure on the composition of black smokers. *Earth and Planetary Science Letters,* 235, 654-662.

Kurzweil F, Claire M, Thomazo C, Peters M, Hannington M, Strauss H (2013) Atmospheric sulfur rearrangement 2.7 billion years ago: Evidence for oxygenic photosynthesis. *Earth and Planetary Science Letters,* 366, 17-26.

Large RR, Danyushevsky L, Hollit C, Maslennikov V, Meffre S, Gilbert S, Bull S, Scott R, Emsbo P, Thomas H (2009) Gold and trace element zonation in pyrite using a laser imaging technique: implications for the timing of gold in orogenic and Carlin-style sediment-hosted deposits. *Economic Geology,* 104, 635-668.

Large RR, Halpin JA, Danyushevsky LV, Maslennikov VV, Bull SW, Long JA, Gregory DD, Lounejeva E, Lyons TW, Sack PJ (2014) Trace element content of sedimentary pyrite as a new proxy for deep-time ocean–atmosphere evolution. *Earth and Planetary Science Letters,* 389, 209-220.

Large RR, Maslennikov VV, Robert F, Danyushevsky LV, Chang Z (2007) Multistage sedimentary and metamorphic origin of pyrite and gold in the giant Sukhoi Log deposit, Lena gold province, Russia. *Economic Geology,* 102, 1233-1267.

Lavoie D, Burden E, Lebel D (2003) Stratigraphic framework for the Cambrian Ordovician rift and passive margin successions from southern Quebec to western Newfoundland. *Canadian Journal of Earth Sciences,* 40, 177-205.

Long DG (1976) The Stratigraphy and sedimentology of the Huronian (Lower Aphebian) Mississagi and Serpernt Formation. University of Western Ontario, London, Ontario, Canada, Unpublished*,* pp. 291.

Long DG, Turner EC (2012) Tectonic, sedimentary and metallogenic re-evaluation of basal strata in the Mesoproterozoic Bylot basins, Nunavut, Canada: Are unconformity-type uranium concentrations a realistic expectation? *Precambrian Research,* 214, 192-209.

Long DGF, Ulrich T, Kamber BS (2011) Laterally extensive modified placer gold deposits in the paleoproterozoic Mississagi formation, clement and Pardo Townships, Ontario. *Canadian Journal of Earth Sciences,* 48, 779-792.

Lyons TW, Anbar AD, Severmann S, Scott C, Gill BC (2009) Tracking euxinia in the ancient ocean: a multiproxy perspective and Proterozoic case study. *Annual Review of Earth and Planetary Sciences,* 37, 507-534.

Lyons TW, Reinhard CT, Planavsky NJ (2014) The rise of oxygen in Earth/'s early ocean and atmosphere. *Nature,* 506, 307-315.

Macfarlane AW, Danielson A, Holland HD (1994) Geology and major and trace element chemistry of late Archean weathering profiles in the Fortescue Group,

Western Australia: implications for atmospheric O_2. *Precambrian research,* 65, 297-317.

Macgregor AM (1941) A Precambrian algal limestone in Southern Rhodesia. *Transactions of the Geological Society of South Africa,* 43, 9-16.

Mcclay K, Ellis P (1983) Deformation and recrystallization of pyrite. *Mineralogical Magazine,* 47, 527-538.

Miyano T, Beukes N (1984) Phase relations of stilpnomelane, ferri-annite, and riebeckite in very low-grade metamorphosed iron-formations. *South African Journal of Geology,* 87, 111-124.

Morse JW, Millero FJ, Cornwell JC, Rickard D (1987) The chemistry of the hydrogen sulfide and iron sulfide systems in natural waters. *Earth-Science Reviews,* 24, 1-42.

Och LM, Shields-Zhou GA (2012) The Neoproterozoic oxygenation event: environmental perturbations and biogeochemical cycling. *Earth-Science Reviews,* 110, 26-57.

Partin C, Bekker A, Planavsky N, Scott C, Gill B, Li C, Podkovyrov V, Maslov A, Konhauser K, Lalonde S (2013) Large-scale fluctuations in Precambrian atmospheric and oceanic oxygen levels from the record of U in shales. *Earth and Planetary Science Letters,* 369, 284-293.

Parviainen EaU (1973) The sedimentology of the Huronian Ramsay Lake and Bruce Formations, north shore of Lake Huron, Ontario. University of Western Ontario, London, Ontario, Canada, unpublished, pp. 426.

Paton C, Hellstrom J, Paul B, Woodhead J, Hergt J (2011) Iolite: Freeware for the visualisation and processing of mass spectrometric data. *Journal of Analytical Atomic Spectrometry,* 26, 2508-2518.

Paul B, Paton C, Norris A, Woodhead J, Hellstrom J, Hergt J, Greig A (2012) CellSpace: A module for creating spatially registered laser ablation images within the

Iolite freeware environment. *Journal of Analytical Atomic Spectrometry,* 27, 700-706.

Pavlov A, Kasting J (2002) Mass-independent fractionation of sulfur isotopes in Archean sediments: strong evidence for an anoxic Archean atmosphere. *Astrobiology,* 2, 27-41.

Planavsky N, Bekker A, Rouxel OJ, Kamber B, Hofmann A, Knudsen A, Lyons TW (2010) Rare earth element and yttrium compositions of Archean and Paleoproterozoic Fe formations revisited: new perspectives on the significance and mechanisms of deposition. *Geochimica et Cosmochimica Acta,* 74, 6387-6405.

Planavsky NJ, Asael D, Hofmann A, Reinhard CT, Lalonde SV, Knudsen A, Wang X, Ossa Ossa F, Pecoits E, Smith AJB, Beukes NJ, Bekker A, Johnson TM, Konhauser KO, Lyons TW, Rouxel OJ (2014) Evidence for oxygenic photosynthesis half a billion years before the Great Oxidation Event. *Nature Geosci,* 7, 283-286.

Planavsky NJ, Bekker A, Hofmann A, Owens JD, Lyons TW (2012) Sulfur record of rising and falling marine oxygen and sulfate levels during the Lomagundi event. *Proceedings of the National Academy of Sciences,* 109, 18300-18305.

Planavsky NJ, Mcgoldrick P, Scott CT, Li C, Reinhard CT, Kelly AE, Chu X, Bekker A, Love GD, Lyons TW (2011) Widespread iron-rich conditions in the mid-Proterozoic ocean. *Nature,* 477, 448-451.

Poulton SW, Canfield DE (2011) Ferruginous conditions: a dominant feature of the ocean through Earth's history. *Elements,* 7, 107-112.

Powell J, Schneider D (2013) *Preliminary Results of Detrital Muscovite 40Ar/39Ar Geochronology from the Eastern Mackenzie Mountains and Mackenzie Plain, Northwest Territories*.

Pratt BR (2002) Tepees in peritidal carbonates: origin via earthquake-induced deformation, with example from the Middle Cambrian of western Canada. *Sedimentary Geology,* 153, 57-64.

Prokoph A, Ernst RE, Buchan KL (2004) Time‐series analysis of large igneous provinces: 3500 Ma to present. *The Journal of geology,* 112, 1-22.

Raiswell R, Canfield D, Berner R (1994) A comparison of iron extraction methods for the determination of degree of pyritisation and the recognition of iron-limited pyrite formation. *Chemical Geology,* 111, 101-110.

Raiswell R, Canfield DE (1998) Sources of iron for pyrite formation in marine sediments. *American Journal of Science,* 298, 219-245.

Riding R (2000) Microbial carbonates: the geological record of calcified bacterial–algal mats and biofilms. *Sedimentology,* 47, 179-214.

Robbins LJ, Lalonde SV, Saito MA, Planavsky NJ, Mloszewska AM, Pecoits E, Scott C, Dupont CL, Kappler A, Konhauser KO (2013) Authigenic iron oxide proxies for marine zinc over geological time and implications for eukaryotic metallome evolution. *Geobiology,* 11, 295-306.

Ross P-S, Goutier J, Mercier-Langevin P, Dubé B, Polat A (2011) Basaltic to andesitic volcaniclastic rocks in the Blake River Group, Abitibi Greenstone Belt: 1. Mode of emplacement in three areas 1 This article is a companion paper to Ross et al. 2011. Basaltic to andesitic volcaniclastic rocks in the Blake River Group, Abitibi Greenstone Belt: 2. Origin, geochemistry, and geochronology. Canadian Journal of Earth Sciences, 48: this issue. 2 MRNF Contribution BEGQ 8439-2010/2011-1. Natural Resources Canada, Earth Science Sector Contribution 20100253. *Canadian Journal of Earth Sciences,* 48, 728-756.

Rouxel OJ, Bekker A, Edwards KJ (2005) Iron isotope constraints on the Archean and Paleoproterozoic ocean redox state. *Science,* 307, 1088-1091.

Schopf JW, Oehler DZ, Horodyski RJ, Kvenvolden KA (1971) Biogenicity and significance of the oldest known stromatolites. *Journal of Paleontology,* 45, 477-485.

Scott C, Lyons T, Bekker A, Shen Y, Poulton S, Chu X, Anbar A (2008) Tracing the stepwise oxygenation of the Proterozoic ocean. *Nature,* 452, 456-459.

Scott C, Planavsky NJ, Dupont CL, Kendall B, Gill BC, Robbins LJ, Husband KF, Arnold GL, Wing BA, Poulton SW (2013) Bioavailability of zinc in marine systems through time. *Nature Geoscience,* 6, 125-128.

Scott C, Wing BA, Bekker A, Planavsky NJ, Medvedev P, Bates SM, Yun M, Lyons TW (2014) Pyrite multiple-sulfur isotope evidence for rapid expansion and contraction of the early Paleoproterozoic seawater sulfate reservoir. *Earth and Planetary Science Letters,* 389, 95-104.

Sumner DY (1997a) Carbonate precipitation and oxygen stratification in late Archean seawater as deduced from facies and stratigraphy of the Gamohaan and Frisco formations, Transvaal Supergroup, South Africa. *American Journal of Science,* 297, 455-487.

Sumner DY (1997b) Late Archean calcite-microbe interactions; two morphologically distinct microbial communities that affected calcite nucleation differently. *Palaios,* 12, 302-318.

Sumner DY, Beukes NJ (2006) Sequence stratigraphic development of the Neoarchean Transvaal carbonate platform, Kaapvaal Craton, South Africa. *South African Journal of Geology,* 109, 11-22.

Sumner DY, Bowring SA (1996) U−Pb geochronologic constraints on deposition of the Campbellrand Subgroup, Transvaal Supergroup, South Africa. *Precambrian Research,* 79, 25-35.

Swanner ED, Planavsky NJ, Lalonde SV, Robbins LJ, Bekker A, Rouxel OJ, Saito MA, Kappler A, Mojzsis SJ, Konhauser KO (2014) Cobalt and marine redox evolution. *Earth and Planetary Science Letters,* 390, 253-263.

Thomas HV, Large RR, Bull SW, Maslennikov V, Berry RF, Fraser R, Froud S, Moye R (2011) Pyrite and pyrrhotite textures and composition in sediments,

laminated quartz veins, and reefs at Bendigo gold mine, Australia: insights for ore genesis. *Economic Geology,* 106, 1-31.

Thorkelson DJ (2000) Geology and mineral occurrences of the Slats Creek, Fairchild Lake and "Dolores Creek" areas, Wernecke Mountains (106D/16, 106C/13, 106C/14), Yukon Territory. Exploration and Geological Services Division, Yukon, Indian and Northern Affairs Canada. *Bulletin,* 10, 73.

Turner E, Long D (2012) Formal definition of the Neoproterozoic Mackenzie Mountains Supergroup (NWT), and formal stratigraphic nomenclature for its carbonate and evaporite formations: Geological Survey of Canada. *Open File,* 7112, 57.

Turner EC (2009) Mesoproterozoic carbonate systems in the Borden Basin, Nunavut. *Canadian Journal of Earth Sciences,* 46, 915-938.

Turner EC (2011) Structural and stratigraphic controls on carbonate-hosted base metal mineralization in the mesoproterozoic Borden basin (Nanisivik district), Nunavut. *Economic Geology,* 106, 1197-1223.

Turner EC, James NP, Narbonne GM (1997) Growth dynamics of neoproterozoic calcimicrobial reefs, Mackenzie Mountains, Northwest Canada. *Journal of Sedimentary Research,* 67, 437-450.

Turner EC, James NP, Narbonne GM (2000) Taphonomic control on microstructure in Early Neoproterozoic reefal stromatolites and thrombolites. *Palaios,* 15, 87-111.

Turner EC, Kamber BS (2012) Arctic Bay Formation, Borden Basin, Nunavut (Canada): Basin evolution, black shale, and dissolved metal systematics in the Mesoproterozoic ocean. *Precambrian Research,* 208, 1-18.

Ulrich T, Kamber BS, Jugo PJ, Tinkham DK (2009) Imaging element-distribution patterns in minerals by laser ablation–inductively coupled plasma–mass spectrometry (LA–ICP–MS). *The Canadian Mineralogist,* 47, 1001-1012.

Ulrich T, Long D, Kamber B, Whitehouse M (2011) In situ trace element and sulfur isotope analysis of pyrite in a paleoproterozoic gold placer deposit, Pardo and Clement Townships, Ontario, Canada. *Economic Geology,* 106, 667-686.

Veizer J, Clayton R, Hinton R (1992) Geochemistry of precambrian carbonates: IV. Early paleoproterozoic (2.25±0.25 Ga) seawater. *Geochimica et Cosmochimica Acta,* 56, 875-885.

Veizer J, Hoefs J, Lowe DR, Thurston PC (1989) Geochemistry of Precambrian carbonates: II. Archean greenstone belts and Archean sea water. *Geochimica et Cosmochimica Acta,* 53, 859-871.

Viehmann S, Hoffmann JE, Münker C, Bau M (2014) Decoupled Hf-Nd isotopes in Neoarchean seawater reveal weathering of emerged continents. *Geology,* 42, 115-118.

Walker JC, Brimblecombe P (1985) Iron and sulfur in the pre-biologic ocean. *Precambrian Research,* 28, 205-222.

Wang S, Mulligan CN (2006a) Effect of natural organic matter on arsenic release from soils and sediments into groundwater. *Environmental Geochemistry and Health,* 28, 197-214.

Wang S, Mulligan CN (2006b) Occurrence of arsenic contamination in Canada: Sources, behavior and distribution. *Science of The Total Environment,* 366, 701-721.

Webb GE, Kamber BS (2011) Trace element Geochemistry as a tool for interpreting microbialites. In: *Earliest Life on Earth: Habitats, Environments and Methods of Detection*. Springer, pp. 127-170.

Wilson JF, Nesbitt RW, Fanning CM (1995) Zircon geochronology of Archaean felsic sequences in the Zimbabwe craton: a revision of greenstone stratigraphy and a model for crustal growth. *Geological Society, London, Special Publications,* 95, 109-126.

Yang W, Holland HD, Rye R (2002) Evidence for low or no oxygen in the late Archean atmosphere from the~ 2.76 Ga Mt. Roe# 2 paleosol, Western Australia: Part 3†† Part 1 is listed under References as Macfarlane et al.(1994a), Part 2 as Macfarlane et al.(1994b). *Geochimica et cosmochimica acta,* 66, 3707-3718.

Young GM (1973) Tillites and aluminous quartzites as possible time markers for middle Precambrian (Aphebian) rocks of North America. *Huronian stratigraphy and sedimentation,* 12, 97-125.

Zbinden E, Holland H, Feakes C, Dobos S (1988) The Sturgeon Falls paleosol and the composition of the atmosphere 1.1 Ga BP. *Precambrian research,* 42, 141-163.

7. Supporting Information

Supplementary Table 1: Pyrite trace metal concentrations (ppm)

Age (Ma)	ge error (Ma)	Sample	Sample No.	V	Mn	Co	Ni	Cu	Zn	As	Mo	Ag	Cd	Au	Pb	Bi
2670	25	Huntsman Q	Rh A 1	6.68	8.8	139	147.9	93.3	34	601	2.6	0.392	3.3		14.7	0.353
2670	25	Huntsman Q	Rh A 2	BDL	1.1	2.94	56.7	19.1	30	247	7.27	0.163	0.58		25.8	0.412
2670	25	Huntsman Q	Rh A 3	6.44	527	250	393	129	50	962	3.18	2.16	5.37		279	9.24
2670	25	Huntsman Q	Rh A 4	0.73	1991	445	600	26.3	76	562	1.79	0.35	1.05		34.3	2.1
2670	25	Huntsman Q	Rh A 5	2.27	436	30.4	201	35.5	55	326	2.8	0.52	1.06		65.5	2
2670	25	Huntsman Q	Rh Suff 1 1	0.28	970	0.66	10.5	23.9	3.1	720	0.13	0.044	0.16		25.5	0.118
2670	25	Huntsman Q	Rh Suff 1 2	0.12	BDL	1.37	3.6	19.7	1.4	164	0.35	0.051	0.36		7.78	0.027
2670	25	Huntsman Q	Rh Suff 1 3	BDL	1.3	64.8	473	8.9	0.62	3590	0.313	0.09	-0.26		8.73	0.191
2670	25	Huntsman Q	Rh Suff 2 1	0.33	28.2	76.2	801	162	19	1526	3.05	1.79	7.67		247.9	11.13
2670	25	Huntsman Q	Rh Suff 2 2	0.03	44	128	1610	71.9	2.7	1057	2.55	0.94	1.35		85.9	3.94
2670	25	Huntsman Q	BSK 4 1	0.04	94	19.9	255	42.1	15.1	780	1.33	0.19	1.91	0.76	49.8	1.98
2670	25	Huntsman Q	BSK 4 2	0.17	296	19.8	73	47.8	71	649	2.33	1	0.61	34.1	45.2	0.56
2670	25	Huntsman Q	BSK 4 3	1.17	264	74.9	433	117.9	51.7	1231	2.47	1.89	2.51	260	216	7.09
2670	25	Huntsman Q	BSK 4 4	0.91	557	59.8	257	436	160	1230	6.2	5.5	3.5	4860	392	11.3
2670	25	Huntsman Q	BSK 4 5	0.05	1742	184	735	111.9	59.6	1660	6.63	3.2	1.87	6.5	258	8.67
2520	5	Gamohaan F 31	T-1	0.99	29.5	31.3	262	171	48.6	1025	20.4	0.13	2.1		36.5	1.49
2520	5	Gamohaan F 31	A-1_1	38.6	5080	1350	741	233	74.9	19020	14.9	0.39	1.1		345	7.11
2520	5	Gamohaan F 31	T-2	11.2	100	107	759	342	85	2710	24.2	0.48	-0.1		278	12.02
2520	5	Gamohaan F 31	A-2	1.6	26.4	57.1	568	272.6	40.2	1805	12.8	0.43	0.64		254	10.9
2520	5	Gamohaan F 31	T-3	33.8	210	48.6	355	236	213	891	21.8	2.01	-0.32		35	0.85
2520	5	Gamohaan F 31	A-3a	86.9	7050	25.7	90	60	88	1010	12.6	-0.03	-0.49		60.8	1.04
2520	5	Gamohaan F 31	A-3b	81.6	142.8	42.8	100	34.6	14.8	3030	15.6	0.08	0.5		59.7	1.36
2520	5	Gamohaan F 33	T-1	24.6	302	555	5370	1730	70.5	8010	9.5	3.29	1.5		1038	38.4
2520	5	Gamohaan F 33	A-1a_1	0.3	7720	346	527	24.6	11.8	473	0.13	2.9	0.5		150	2.78
2520	5	Gamohaan F 33	A-1b	1.04	4173	600	1600	460	12	4690	3	0.51	1.6		233	5.99
2520	5	Gamohaan F 33	T-2	0.24	14.8	113.5	1830	2190	35.5	1327	4.47	2.13	0.44		55	3.26
2520	5	Gamohaan F 33	A-2a	4.5	2050	930	5330	419	23.2	3990	1.38	0.66	0.06		169	4.4
2520	5	Gamohaan F 33	T-3	2.02	27.6	360	2490	488	5.9	4.07E+04	1.97	0.76	0.7		420	6.69
2520	5	Gamohaan F 33	A-3a	8.4	3190	435	2860	943	6.7	5.38E+04	3.14	0.73	1.4		280	3.94
2520	5	Gamohaan F 33	A-3b	37	1420	337	2260	1290	31.5	3.35E+04	8.9	0.68	-0.8		454	12.4
2520	5	Gamohaan F 33	F-1	1.7	33	181	1660	1780	7.3	3.23E+04	5.6	1.5	2.5		449	8.66
2520	5	Gamohaan F 33	F-2	1	1270	465	2220	890	13.3	10820	6.6	2.02	2.4		1091	37.1
2520	5	Gamohaan F 33	F-3	3.8	89	628	3380	620	14.8	2.09E+04	9.4	7.4	2.7		925	32
2520	5	Gamohaan F 36	Fa-1	1.89	8.4	146	1523	4820	20.5	9.40E+03	2.21	1.42	0.3		234	6.7
2520	5	Gamohaan F 36	Fa-2	4.76	16.1	714	3570	2010	17.4	19510	7.7	1.71	2.3		1711	72.3
2520	5	Gamohaan F 36	Fa-3_1	7.95	38.2	697	5660	1180	28.2	2.63E+04	5.83	1.11	1.9		881	44.5
2520	5	Gamohaan F 36	Fa-4	4.78	490	688	4980	2520	25.2	2.08E+04	4.15	1.51	4.1		1247	58.2
2520	5	Gamohaan F 36	Fb-1	9	4790	247	3650	550	14.2	2.18E+04	6.3	0.34	0.42		760	16.7
2520	5	Gamohaan F 36	Fb-2	0.34	21.2	188	2970	1084	10.9	2.62E+04	4.05	1.08	0.92		611	18.9
2520	5	Gamohaan F 36	Fb-3	0.06	36.5	162	2410	1380	24.8	5.48E+04	4.61	0.7	3.2		740	20
2520	5	Gamohaan F 36	Fb-4	0.25	40	95	985	420	6.4	12630	1.54	0.58	0.26		266	7.72
2520	5	Gamohaan F 26	M-1	0.96	20	6.6	100.8	214	6.2	88	7.39	1.07	0.33		775	0.62
2520	5	Gamohaan F 26	M2	1.1	570	28.7	55.8	50.2	8	105	10.33	2.44	1.14		1552	0.554
2520	5	Gamohaan F 26	M-3	10.7	3760	93.8	258	178	1.2	890	3.64	0.89	0.3		1109	1.53
2520	5	Gamohaan F 26	M-4	0.89	162	89.4	321	94.3	4.1	201	4.2	0.87	0.16		909	1.36
2520	5	Gamohaan F 26	M-5	3.04	990	131	972	1100	BDL	3.33E+04	7.1	2.92	0.03		1800	0.95
2520	5	Gamohaan F 31	L	1.756	6.03	39.82	588.8	337.7	9.55	722.3	2.935	2.875	0.331		22.91	0.213
2520	5	Gamohaan F 31	S	1.94	3.49	26.32	398	238.8	8.45	598.8	2.562	2.397	0.277		16.5	0.243
2520	5	Gamohaan F 33	H	2.4	4.58	33.9	506	700	9.2	431.5	1.569	12.3	0.361		183	2.99

| | | |

| | | |

| | | |

510	10	Lisi 1 5	5.04	1890	93.2	236	571	301	45.4	12.3	0.32	0.94	294	2.14
510	10	Lisi 1 6	5.91	2070	271	393	547	144	97	24.2	0.66	0.6	472	0.75
510	10	Lisi 1 7	17.2	1850	208	257	316	293	126.4	31	0.62	0.3	375	0.477
510	10	Lisi 1 8	81.1	2220	351	520	490	121	122.8	28.3	0.82	0.22	346	1.02
510	10	Lisi 1 9	21.01	194.6	1602	1423	1190	59.7	659	29	1.15	0.61	2917	0.464
510	10	Lisi 1 10	3.9	1574	314	449	699	224.3	154.4	21.62	1	0.96	796	3.84

Chapter 4: The Neoarchaean surficial sulphur cycle: analogies with 20th century atmospheric lead

Submitted to Geobiology
Co-Authors: Martin Whitehouse, Balz Kamber

Abstract

We report in situ SIMS quadruple S-isotope data for sedimentary pyrite from the ca. 2.52 Ga Upper Campbellrand Subgroup, Transvaal, South Africa. The analysed rock is a shaly limestone from the Gamohaan Formation interpreted to have been deposited in a water depth of ca. 50-100 m, in a restricted basin. A previous study discovered that the pyrites define a non-zero intercept $\delta^{34}S_{V\text{-}CDT}$ - $\Delta^{33}S$ data array. The present study revisited the sample, carrying out further analyses of pyrite. The new data confirm and expand this linear array, which does not pass through the origin representing bulk Earth sulphur, instead intersecting $\delta^{34}S$ of 0 at $\Delta^{33}S$ of ca. +5. This was previously interpreted to indicate mixing of unrelated S-sources in the sediment environment, involving a combination of recycled sulphur from sulphides that had originally formed by sulphate reducing bacteria, along with elemental sulphur.

However, recent studies have highlighted the very low Archaean seawater sulfate concentration, which imply the Archaean ocean was poorly mixed with respect to sulphur. Thus, modern oceanic sulphur systematics provide limited insight into the Archaean sulphur cycle. Instead, we propose that the 20th century atmospheric lead event provides a better analogue. Similar to industrial lead, the main oceanic input of Archaean sulphur was through atmospheric raindown, with individual giant point sources capeable of temporally dominating atmospheric input. This leaves little doubt that local S-isotope signals are not all global phenomena representing whole Earth processes. Thus, the non-zero intercept $\delta^{34}S_{V\text{-}CDT}$ - $\Delta^{33}S$ data array may alternatively represent a very localised S-isotope signature in the Neoarchaean surface environment. Fallout from local volcanic eruptions could imprint recycled MIF-S signals into pyrite of restricted basins, thereby avoiding attenuation of the signal in

the subdued, averaged global open ocean sulphur pool. Thus, the superposition of extreme local S-isotope signals offers an alternative explanation for the large Neoarchaean MIF-S excursions and asymmetry of the $\Delta^{33}S$ rock record.

1. Introduction

A major breakthrough in understanding the long-term evolution of the atmosphere was the discovery that mass independently fractionated sulphur (MIF-S) is preserved in sedimentary rocks older than ca. 2.4 Ga, but absent in younger strata (Farquhar et al., 2000). In the context of experimental UV photolysis of SO_2 and atmospheric chemistry models (Farquhar et al., 2000; Farquhar et al., 2001; Pavlov & Kasting, 2002), this discovery implied that extremely low free oxygen levels, less than 0.001 % of the present atmospheric concentration (Pavlov & Kasting, 2002), characterised the atmosphere before 2.4 Ga. At such low oxygen levels, the effective absence of ozone allowed for photochemical production of MIF-S in the atmosphere and its delivery to the Earth's surface. Since the discovery of MIF-S in the pre-great oxygenation event (GOE) sedimentary rock record, the combined data from many studies reveal an apparent temporal trend in the magnitude of observed $\Delta^{33}S$ anomalies (e.g. Hofmann et al., 2009; Halevy et al., 2010; Thurston et al., 2012). Somewhat counter-intuitively, the largest anomalies are not found in the oldest terrestrial sediments but occur in sedimentary rocks of Neoarchaean age (2.5 to 2.8 Ga), deposited only ca. 100 Ma prior to the putative GOE (e.g. Farquhar & Wing, 2003; Bekker et al., 2004; Rouxel et al., 2005). It is worth noting that widely contrasting ranges of $\Delta^{33}S$ have been reported from time equivalent ca. 2.5 Ga old, but geographically and spatially discrete samples; the Batatal Formation in Brazil (Cheney, 1996) and the South African Campbellrand Carbonate Platform (Paris et al., 2014; Zhelezinskaia et al., 2014). In addition, an asymmetry in the $\Delta^{33}S$ record has emerged, with mean data skewed in favour of positive $\Delta^{33}S$ values during the ca. 2.5-2.7 Ga age window (Reinhard et al., 2013). The significance of the topology and reason for the asymmetry of the Neoarchaean MIF-S record are subject of active research (e.g. Ohmoto et al., 2006; Ono et al., 2006; Hofmann et al., 2009; Halevy et al., 2010; Halevy, 2013) but remain to be fully established.

Preservation of the ancient atmospheric MIF-S signal in the sedimentary environment was aided by the inability of the O-depleted, pre-GOE atmosphere to oxidatively weather sulphides from land. Therefore, oceanic sulphur was not sourced from riverine run-off (Ono et al., 2003; Canfield, 2004) but instead almost exclusively derived from the atmosphere. The discovery of MIF-S significantly strengthened earlier arguments for low oceanic sulphate levels that were based on the observation

that the range in $\delta^{34}S$ is much lower in Archaean sedimentary pyrite than in Phanerozoic equivalents (e.g. Canfield, 2004; Fike et al., 2013). Thus, the Archaean oceanic sulphur was almost exclusively derived from volcanic emissions (Holland, 1984; Walker & Brimblecombe, 1985). In this respect, it is important to recall that the style of magmatism may have evolved throughout the Precambrian. Agreement exists that the Archaean witnessed abundant emplacement of plume-derived basalt, driven by very high temperature plumes (e.g. Kamber, 2015). However, a significant irreversible decline in oceanic Ni concentration at ca. 2.6 Ga is observed (Konhauser et al., 2009), likely reflecting the disappearance of komatiite and high-Mg basalts on land (Kamber, 2010), a direct consequence of cooling mantle plume temperatures and a concomitant end of very high-Mg volcanism (Konhauser et al., 2009). Once plume magmas became less magnesian, the crust too was being reorganised in terms of radioactive heat production, and the geology started to resume a more familiar look to that of the Phanerozoic (Kamber, 2015). The onset of Wilson style plate tectonics has most recently been proposed to have occurred at ca. 3 Ga (Shirey & Richardson, 2011). For these reasons, there is a possibility that throughout the Archaean, the relative contributions of sulphur species from plume-related versus subduction volcanoes may have changed and influenced the evolution of the Neoarchaean sulphur cycle.

Here we develop a new working model for the interpretation of the Neoarchaean S-cycle. It is based on an analogy with the 20th century anthropogenic atmospheric Pb emission 'experiment'. It posits that Neoarchaean S-cycling was far more dynamic than previously thought, and that seawater isotopic compositions could have fluctuated on much shorter timescales than they do today (Crowe et al., 2014), facilitating the preservation of local S-isotope signatures. This model is applied to new quadruple S-isotope data and compiled triple S-isotope MIF-S data for Neoarchaean sulphides, addressing the magnitude of MIF-S, the apparent asymmetry of Neoarchaean MIF values, and linear data arrays from a single Neoarchaean sample (Figure 1a), that do not pass through the origin of the $\delta^{34}S_{V\text{-}CDT}$ - $\Delta^{33}S$ plot (e.g. Kamber & Whitehouse, 2007; Whitehouse, 2013).

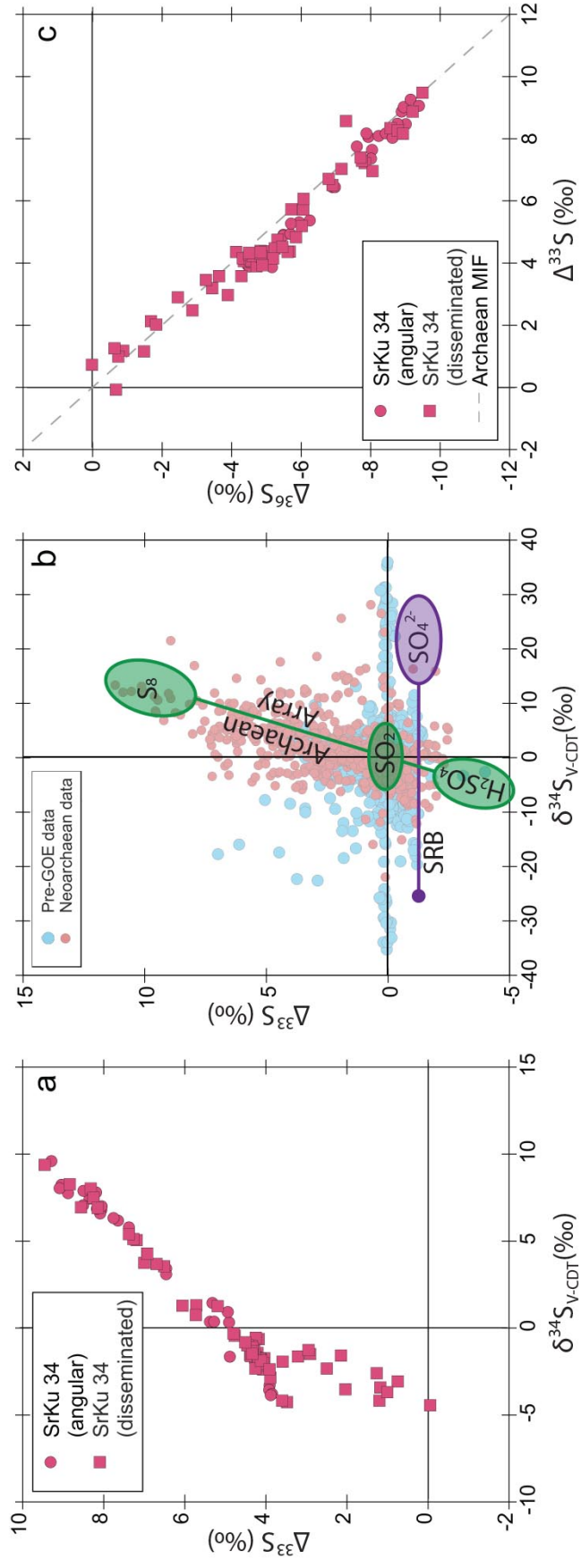


Figure 1: Panels a, and c illustrate new quadruple S-isotope data from analysis of the shaley limestone SrKu 34. Panel a shows a $\delta^{34}S_{V\text{-}CDT}$ - $\Delta^{33}S$ plot of the new data, exhibiting two well-defined linear arrays. These arrays do not pass through the origin of the $\delta^{34}S_{V\text{-}CDT}$ - $\Delta^{33}S$ plot, instead intercepting $\Delta^{33}S$ at a value of ca. + 5 ‰ and + 4 ‰ (see Figure 2b). The major, shallowly sloping trend (Figure 2b, m = 0.444) is picked out by both angular and disseminated pyrite morphologies while the minor, more steeply sloping trend (Figure 2b, m = 0.848) is picked out only by a small portion of the disseminated pyrite. Panel b shows compiled Neoarchaean and other pre-GOE MIF-S data, with the Neoarchaean data depicting the Archaean array. Many data points fall on an empirical linear trend in $\delta^{34}S$ - $\Delta^{33}S$ ($\Delta^{33}S = 0.9 \times \delta^{34}S$; Ono et al. 2003), termed the Archaean array. This is widely interpreted to reflect formation of sulphides formed by mixing sulphur from two primary atmospheric sources carrying opposite S-MIF signals; reduced sulphur e.g. S_8 ($\Delta^{33}S > 0$) and residual oxidised sulphur e.g. SO_2 and/or H_2SO_4 ($\Delta^{33}S < 0$), both of which are rained out to the hydrosphere and subsequently delivered to the ocean and sediments (Ono et al. 2003 ; Farquhar et al. 2001). Additionally, S-species may be subject to MDF and exhibit fractionation in $\delta^{34}S$, along the SRB trend parallel to the $\delta^{34}S$ axis. Panel c shows a $\Delta^{33}S$ - $\Delta^{36}S$ plot of the new Gamohaan Fm. data from SrKu 34. Both the angular and disseminated SrKu 34 pyrite data clearly exhibit the characteristic negative $\Delta^{33}S$ - $\Delta^{36}S$ correlation with a slope of ca. -1, reported from Archaean sulphides. The pale grey dashed line represents the Archaean MIF array (e.g. Shen et al., 2009).

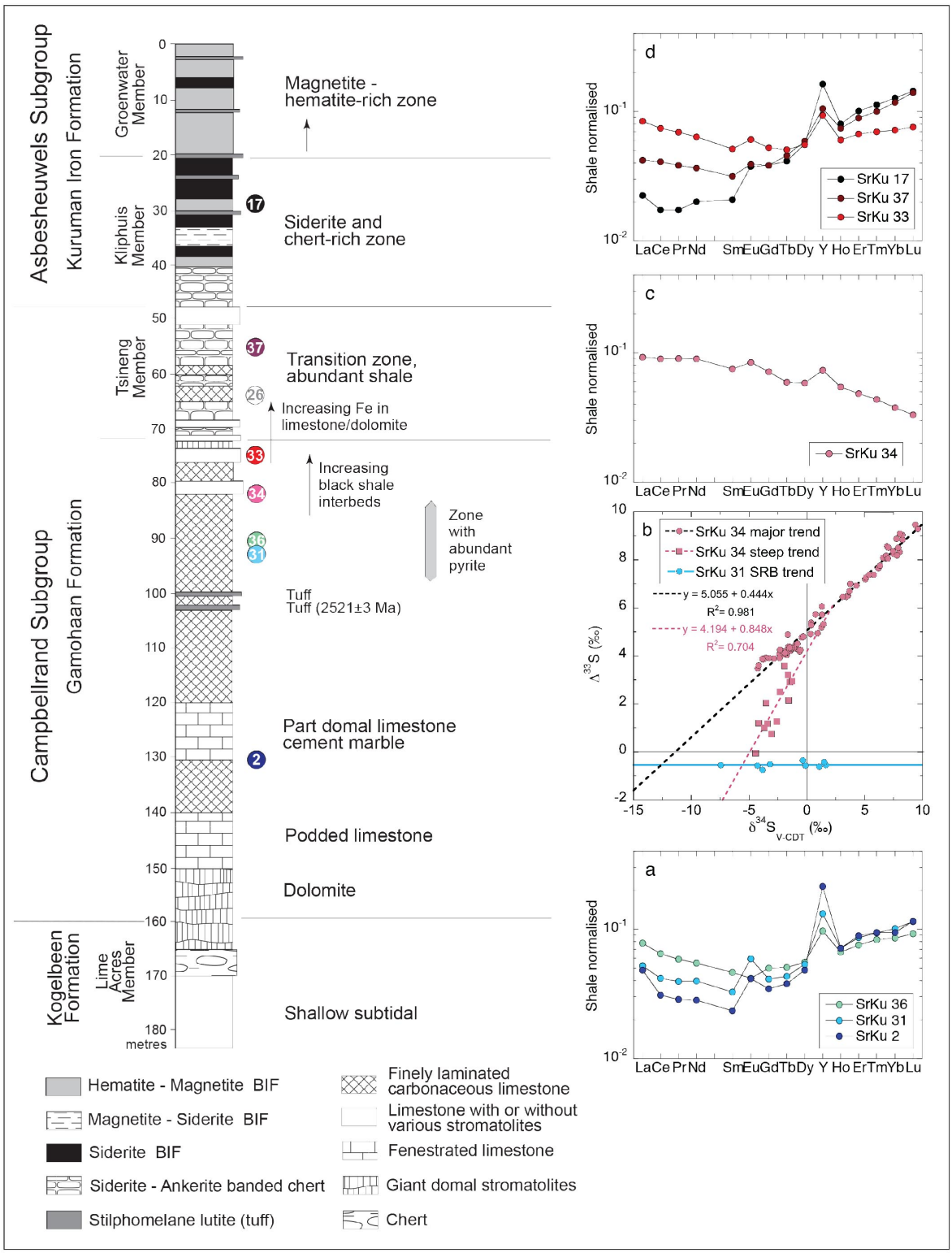

Asbesheuwels Subgroup
Kuruman Iron Formation
Groenwater Member
Kliphuis Member
Campbellrand Subgroup
Gamohaan Formation
Tsineng Member
Kogelbeen Formation
Lime Acres Member
metres
Magnetite - hematite-rich zone
Siderite and chert-rich zone
Transition zone, abundant shale
Increasing Fe in limestone/dolomite
Increasing black shale interbeds
Zone with abundant pyrite
Tuff
Tuff (2521±3 Ma)
Part domal limestone cement marble
Podded limestone
Dolomite
Shallow subtidal
Hematite - Magnetite BIF
Magnetite - Siderite BIF
Siderite BIF
Siderite - Ankerite banded chert
Stilphomelane lutite (tuff)
Finely laminated carbonaceous limestone
Limestone with or without various stromatolites
Fenestrated limestone
Giant domal stromatolites
Chert
d
Shale normalised
SrKu 17
SrKu 37
SrKu 33
LaCe PrNd SmEuGdTbDy Y Ho ErTmYbLu
c
SrKu 34
b
SrKu 34 major trend
SrKu 34 steep trend
SrKu 31 SRB trend
y = 5.055 + 0.444x
R2= 0.981
y = 4.194 + 0.848x
R2= 0.704
Δ33S (‰)
δ34SV-CDT (‰)
a
SrKu 36
SrKu 31
SrKu 2

Figure 2: Schematic lithostratigraphic context of the studied samples, including representative REE+Y patterns of carbonates and selected S-isotope plots. The positions of all samples discussed in text are shown relative to stratigraphic depth in the drill core. The tuff bed at 103 m depth was dated to 2521±3 Ma by Sumner and Bowring (1996). Insets a, b, and d show representative REE+Y diagrams (see Table S1 in the supporting information for data). The symbols are colour-coded from dark blue (deepest in core) grading to pink (middle) and further to dark red and black (shallowest in core). The shape of the patterns shows a coherent trend, starting with steeply positive slopes and typical marine features (e.g. SrKu 2). Up core, the LREE start to increase in abundance and the patterns flatten out (inset a), exemplified by calcareous shale sample SrKu34 (inset c). Further up the core, the trend is reversed and patterns become steeper again with more prominent marine features, as shown, for example, by sample SrKu 17 (inset d). The data were first normalised with local shale SrKu 32 (see supporting information Table S1) followed by vertical transposition to a constant sum of normalised values of 1 to aid visual comparison. Inset b shows a $\delta^{34}S_{V\text{-}CDT}$ - $\Delta^{33}S$ plot of the newly reported SrKu 34 S-isotope data, along with previously reported (Kamber & Whitehouse, 2007) data for SrKu 31. The sphaeroidal pyrites of SrKu 31 exhibit consistently negative MIF-S, with $\Delta^{33}S$ values of ca. -0.54 ‰, indicative of a sulphate reducing bacterial origin (SRBO).

2. Materials

In terms of new data, this study revisits the 2.521±3 Ga (Sumner & Bowring, 1996) shallow water sedimentary rocks of the Gamohaan Formation of the Campbellrand Carbonate platform, Transvaal Supergroup, South Africa (Beukes, 1987; Sumner & Bowring, 1996). Rocks from this Formation were first investigated for their MIF-S composition by Papineau et al. (2005) and have since been the subject of further, more comprehensive, studies (Kamber & Whitehouse, 2007; Whitehouse, 2013). The Gamohaan Formation is characterised by platformal subtidal fenestral microbialites and shales that ultimately grade into the overlying deeper water Kuruman Formation iron formation (Figure 2), and has been interpreted to have formed in a progressively deepening depositional environment (Fischer et al., 2009). Sample SrKu 31 is a contorted microbial mat limestone containing spheroidal pyrite grains (typically > ca. 2 mm) of a sulphate reducing bacterial origin (SRBO) (Kamber & Whitehouse, 2007), interpreted to have formed above the storm wave base in a shallow marine environment.

Further up the section sample SrKu34 is located. This is a shaley limestone interbedded with microbial limestones and abiotic calcite precipitates. It is interpreted to have formed in deeper water than SrKu31, at a depth of 50-100 m, during a brief episode of drowning. Pyrite in SrKu34 is present in a range of grain sizes from massive (ca. 1 mm) concretionary solid angular aggregates, to fine-grained (typically < ca. 20 μm) and disseminated (Figure 5: Kamber & Whitehouse, 2007). Importantly, previous studies (Kamber & Whitehouse, 2007; Whitehouse 2013) reported a range of 7.5 ‰ $\Delta^{33}S$ within a 15 x 5 mm cutting from a single 76 x 26 mm thin section of this sample. In addition, data from this single sample define a strong linear array that clearly does not pass through the origin of the $\delta^{34}S_{V\text{-}CDT}$ - $\Delta^{33}S$ plot (Kamber & Whitehouse, 2007), thus strongly deviating from the 'Archaean' array (Ono et al., 2003).

3. Methods

Sulphur isotopes (^{32}S, ^{33}S, ^{34}S, and ^{36}S) were analysed using a CAMECA IMS1280 ion microprobe at NordSIM, Swedish Museum of Natural History,

Stockholm. Analytical settings are described briefly below, and closely follow those reported in Kamber and Whitehouse (2007) and Whitehouse (2013). Sulphur was sputtered using a $^{133}Cs^+$ primary beam with 20 kV incident energy (10 kV primary, -10 kV secondary) and a primary beam current of ~1.5 nA, producing secondary ions from a slightly elliptical area ~10 μm in diameter (long axis). A normal-incidence low-energy electron gun was used for charge compensation. Analyses were performed in automated sequences, with each analysis comprising a 70-s pre-sputter to remove the gold coating of the sample mount over a rastered 15 x 15 μm area, the secondary beam being centred in the field aperture to correct for small variations in surface relief, and data acquisition in 24 4 s integration cycles. The magnetic field was locked at the beginning of the session using an NMR field sensor. Secondary ion signals of all four S isotopes were detected simultaneously using three Faraday detectors (for ^{32}S, ^{33}S and ^{34}S) and an ion counting electron multiplier (^{36}S), with a mass resolution appropriate to resolve ^{33}S from $^{32}S^1H$ (ca. 4860 M/ΔM).

Data were normalised for instrumental mass fractionation using matrix-matched standards mounted together with the sample mount and analysed after every seventh sample. The standards were Ruttan pyrite and Balmat pyrite, with conventionally determined values of +1.2 ‰ and + 15.1 ‰, respectively (Crowe & Vaughan, 1996). However, recent detailed re-evaluation (Whitehouse, 2013) of the pyrite standards has resulted in slightly higher recommended values (+ 1.408 ‰ for Ruttan and + 16.515 ‰ for Balmat, reported in Cabral et al., 2013), which were used for normalisation in this study. The typical precision of $\delta^{34}S$, $\Delta^{33}S$, and $\Delta^{36}S$ values, after propagating the within-run and external uncertainties from standard measurements, were ± 0.09 ‰, ± 0.041 ‰, and ± 0.255 ‰ respectively. All results are reported with respect to the Vienna-Canyon Diablo troilite (V-CDT) meteorite standard (Ding et al., 2001). In addition to these standards, a MIF-positive pyrite from the early Archaean banded iron formation (BIF) in the Isua Greenstone Belt, which previously yielded $\Delta^{33}S$ of + 3.18 ± 0.05 ‰, and $\Delta^{36}S$ of - 2.20 ± 0.21 ‰ (95 % confidence interval) by SIMS (Whitehouse, 2013), was analysed seven times during this study. The seven analyses yielded an average $\Delta^{33}S$ of + 3.12 ± 0.11 ‰ (± 1 σ), and $\Delta^{36}S$ of - 2.44 ± 0.25 ‰ (± 1 σ), confirming the accuracy of the SIMS method.

New rare earth element (REE) data are reported for a few samples bracketing the pyrite-bearing limestones and the shaley limestone. These were obtained with

routine solution quadrupole ICP-MS method after preferential digestion of the carbonate fraction in 5 % triple-distilled HNO_3 (Kamber et al., 2014).

In order to verify the possibility that the recorded Neoarchaean MIF-S might not average the canonical terrestrial value of V-CDT, statistical analysis of compiled, previously published Neoarchaean and other pre-GOE MIF-S data was performed (Figure 3). Neoarchaean data were defined as those having been obtained from Neoarchaean rocks i.e. aged between 2500 – 2800 Ma. Pre-GOE data were defined as those having been obtained from rocks aged between 2320 – 4000 Ma, excluding all Neoarchaean data. Separate analysis of three distinct lithological subdivisions was also undertaken. The supporting information gives further detail on how the lithological subdivisions were defined. The compiled data are from references assembled in Reinhard et al. (2013), see supporting information for a full list of references. For each subset of data, the sample size (n), the range of values i.e. the maximum and minimum, the mean, the first quartile, the median, and the third quartiles of the data are provided.

4. Results

The new REE+Y data are reported in Table S1 of the supporting information, and illustrated in stratigraphic context (Figure 2a, c, and d). The shale normalised REE+Y patterns display a coherent trend with respect to stratigraphic depth. A marine origin with an open ocean signal is indicated for the stratigraphically lowest samples (SrKu 2, SrKu 31, and SrKu 36) (Figure 2a). These samples show the well-established marine REE features, such as a positive slope ($Pr/Yb < 1$), a positive La anomaly, and a superchondritic Y/Ho ratio (see Kamber et al., 2014 for a full discussion) that were originally reported for the Gamohaan Formation by Kamber and Webb (2001). By contrast, up section, SrKu34 exhibits a relatively flat shale normalised REE+Y pattern (Figure 2c) indicative of deposition in a more restricted basin, while further up the section, the REE+Y patterns of samples from the top of the formation (SrKu 33, SrKu 37, and SrKu 17) (Figure 2d) return to those typical of more open marine conditions (Kamber et al., 2014).

In situ secondary ion mass spectrometer quadruple S-isotope data for SrKu 34 are reported in Table S2 of the supporting information, and photomicrographs of analytical sites are given in Figure S1 of the supporting information. The new data

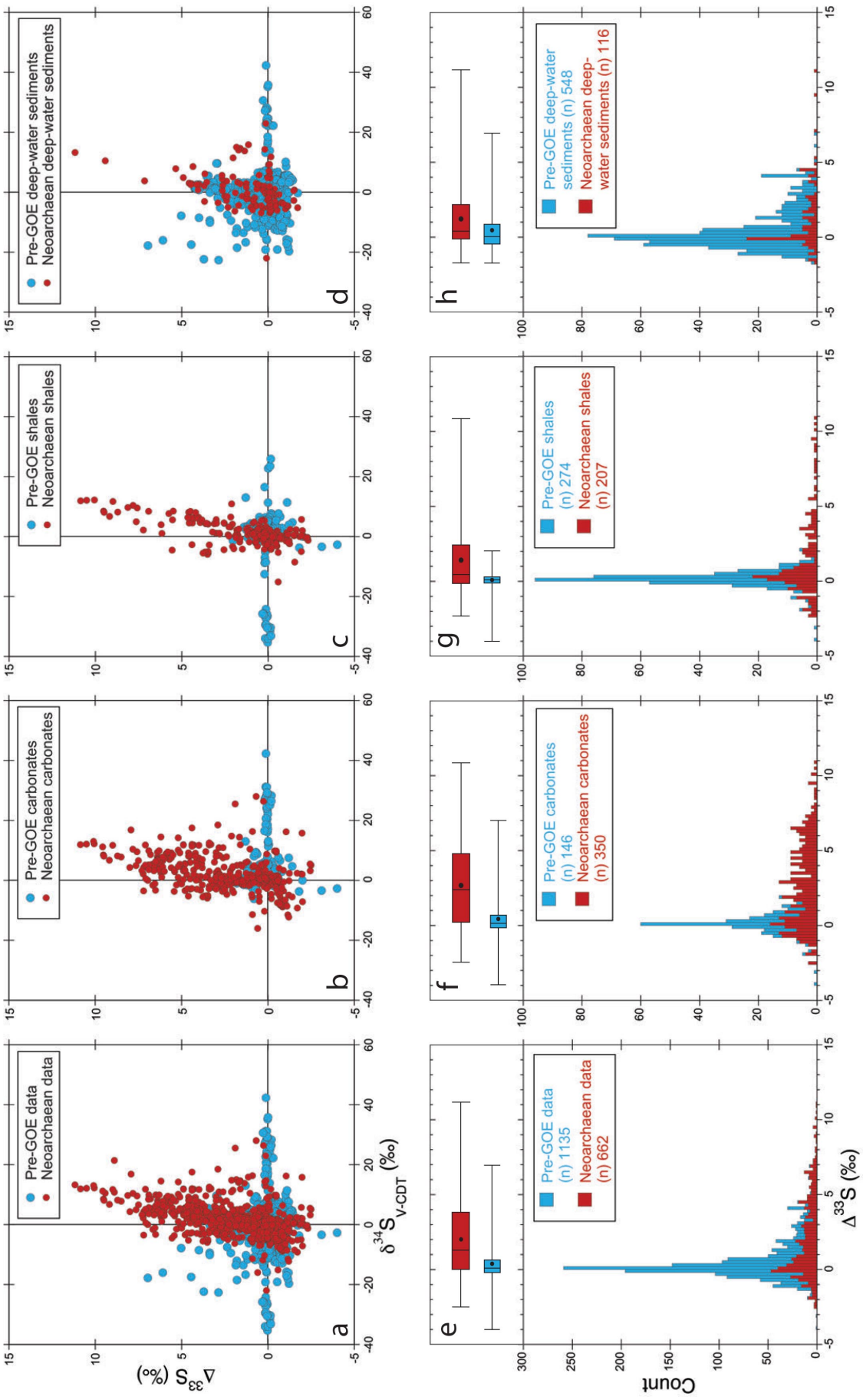

a
b
c
d
e
f
g
h
Pre-GOE data
Neoarchaean data
Pre-GOE carbonates
Neoarchaean carbonates
Pre-GOE shales
Neoarchaean shales
Pre-GOE deep-water sediments
Neoarchaean deep-water sediments
Pre-GOE data (n) 1135
Neoarchaean data (n) 662
Pre-GOE carbonates (n) 146
Neoarchaean carbonates (n) 350
Pre-GOE shales (n) 274
Neoarchaean shales (n) 207
Pre-GOE deep-water sediments (n) 548
Neoarchaean deep-water sediments (n) 116
Δ33S (‰)
δ34SV-CDT (‰)
Count

Figure 3: Four $\delta^{34}S_{V\text{-}CDT}$ - $\Delta^{33}S$ plots of compiled, previously published MIF-S data (a), along with the data subdivided into three distinct lithological types; carbonates (b), shales (c), and deep-water sediments (d, including chert, BIF and barite). Compiled, previously published, Neoarchean MIF-S data are shown in red, while all other pre-GOE data, excluding the Neoarchaean data, are shown in blue. Panels e to h show corresponding histograms and box and whisker plots identically colour coded. The range in magnitude of analysed $\Delta^{33}S$ values is illustrated with histograms. The histogram bin size represents 0.2 ‰ $\Delta^{33}S$, within the range of 0.06 ± 0.16 ‰ (average ± 2 s.d.) of all mass dependently fractionated data from the past 2.2 Ga (Reinhard et al. 2013). In each case, the number of analyses (n) for both Neoarchaean and other pre-GOE data is noted. In box and whisker plots, the whisker ends illustrate maximum and minimum values, the box illustrates the inter quartile range with the median at the centre, and the mean value in each case is superimposed on the box and whisker plot as a black filled circle.

confirm and extend the extreme range in MIF-S recorded in this relatively small, single sample, ranging from $\Delta^{33}S$ of 0 to + 9.5 ‰ (Figure 1a). The new data also confirm and expand the previously established linear arrays and non-zero intercept in the $\delta^{34}S_{V\text{-}CDT}$ - $\Delta^{33}S$ plot. There is a dominant, shallow trend (m = 0.44) and a secondary, steeper trend (m = 0.85), neither of which intersect the origin, instead intercepting $\Delta^{33}S$ at ca. + 5.06 ‰ and ca. + 4.19 ‰ respectively (Figure 2b). In detail, both the solid angular pyrite and the fine-grained disseminated pyrite from SrKu 34 define the dominant, non-zero intercept linear trend, while only a small portion of the fine-grained disseminated pyrite from SrKu 34 define the minor, more steeply sloping, non-zero intercept linear trend (Figure 1a). Both the angular and disseminated SrKu 34 pyrite data clearly exhibit the characteristic negative $\Delta^{33}S$ - $\Delta^{36}S$ correlation with a slope of -1 (e.g. Shen et al., 2009), reported for many Archaean sulphides (Figure 1c). For the purpose of discussion, the newly reported S-isotope data for SrKu 34 are shown along with compiled MIF-S data for Neoarchaean and other pre-GOE sulphides (Figure 1b), and previously reported (Kamber & Whitehouse, 2007) S-isotope data for Srku 31 (Figure 2b).

Neoarchaean and other pre-GOE MIF-S data are shown as $\delta^{34}S_{V\text{-}CDT}$ - $\Delta^{33}S$ plots (Figure 3a-d), along with corresponding statistical analysis (Figure 3e-h). In all cases the Neoarchaean data are seen to form an overall trend from positive $\delta^{34}S$ and $\Delta^{33}S$ towards slightly negative $\delta^{34}S$ and $\Delta^{33}S$ (Figure 3a-d), broadly delineating Ono et al.'s (2003) Archaean atmospheric array (Figure 1b). In contrast, the other pre-GOE data, excluding all Neoarchaean data, appear to cluster more tightly around the origin of the $\delta^{34}S_{V\text{-}CDT}$ - $\Delta^{33}S$ plot and exhibit greater fractionation in $\delta^{34}S$ values (Figure 3a-d). In each case, the corresponding histograms with box and whisker plots illustrate the range in magnitude of data, the maximum and minimum values, the interquartile range, the mean and the median of the compiled data (Figure 3e-h). The most important result of this analysis is that the mean $\Delta^{33}S$ value of all compiled Neoarchaean data is significantly higher than a neutral, 0 ‰ $\Delta^{33}S_{V\text{-}CDT}$ mantle composition (Figure 3e). This holds true for each of the Neoarchaean lithological subdivisions, with none of the lithologies showing an average 0 ‰ $\Delta^{33}S_{V\text{-}CDT}$ mantle composition (Figure 3f-h). The mean $\Delta^{33}S$ value of Neoarchaean carbonate data is furthest from a mantle composition, at a $\Delta^{33}S$ value of + 2.7 ‰ (Figure 3f), while the mean $\Delta^{33}S$ value of Neoarchaean deep-water sediments is closest to a mantle composition, albeit still well above 0 ‰ at 1.2 ‰ (Figure 3d). The findings for

statistical analysis of the compiled Neoarchaean data contrast significantly with findings for the compiled pre-GEO database, excluding Neoarchaean data. For all lithological subdivisions, the mean $\Delta^{33}S$ value of those data is much closer to a MIF-neutral mantle composition (Figure 3e-h). The pre-GOE carbonates, excluding Neoarchaean data, have a mean $\Delta^{33}S$ value approaching 0 ‰ $\Delta^{33}S_{V\text{-}CDT}$, at 0.09 ‰ (Figure 3f). The pre-GOE deep-water sediments have a mean furthest from a MIF-neutral mantle composition, at 0.467 ‰ (Figure 3d). The magnitude of $\Delta^{33}S$ excursions for all compiled Neoarchaean data encompass a wider range of values ($\Delta^{33}S$ from - 2.49 ‰ to 11.177 ‰) than the rest of the pre-GOE data ($\Delta^{33}S$ from - 4 ‰ to 6.96 ‰) (Figure 3e). Furthermore, in all cases the compiled, previously published Neoarchaean data are asymmetrical about 0 ‰, with a clear bias towards positive $\Delta^{33}S$ values (Figure 3e-h).

4.1. The 20th century atmospheric lead analogy

Before discussing the new data and the statistical analysis, we draw attention to the Archaean seawater sulphur concentrations, and the limitations of using modern oceanic sulphur systematics as a key to the past. Instead we propose that the 20th century atmospheric lead event may be a better analogue for the Archaean sulphur cycle.

In the absence of oxidative weathering of terrestrial sulphides, the global pre-GOE sulphur cycle was radically different from the present situation (Fike et al., 2013). To appreciate the magnitude of the difference, readers are reminded that sulphate is the second most abundant anion after chloride in the modern ocean at concentrations of 28,000 μM (Ueno, 2014), whereas pre-GOE seawater sulphate concentration was very low. Available estimates range from < 1 % (Zhelezinskaia et al., 2014) to < 0.01 % (Crowe et al., 2014) of that of modern seawater. Such low sulphate concentrations translate into a very short oceanic sulphur residence time, estimated at 10^3 to 10^4 years (Crowe et al., 2014). These residence times are shorter than the ocean mixing time, implying that the Archaean ocean was poorly mixed with respect to sulphur.

In a situation where the ocean harbours a very large dissolved non-MIF sulphate inventory, it becomes impossible to transmit an atmospheric MIF-S signal into the sedimentary record. This can be illustrated with data from sulphur retrieved

from modern ice caps. Unlike the ocean, present-day polar ice caps have very low sulphur concentrations (Minikin et al., 1998; Wagenbach et al., 1998) and, akin to the pre-GOE ocean, do not obtain sulphur from sulphide weathering on land. This allows for preservation of MIF-S anomalies associated with large, low latitude, stratospheric volcanic eruptions in polar ice even under the modern oxic atmosphere (e.g. Mt. Pinatubo, June 15, 1991: Savarino et al., 2003; Baroni et al., 2007). Naturally, the extent of MIF-S measured in polar ice cores ($\Delta^{33}S$: - 0.5 to + 0.7 ‰ ; Ono et al., 2003) is much smaller than that observed in pre-GOE sediments ($\Delta^{33}S$: - 2.5 to + 12.5 ‰ ; Reinhard et al., 2013), because stratospheric MIF-S that may actually have reached the extreme values recorded in Archaean rocks (Baroni et al., 2007), is heavily diluted with atmospheric sulphur that shows only mass-dependent fractionation (MDF-S). The polar ice cap data thus show the limitations of using the modern oceanic sulphur systematics as a key to the past. Rather, a much more useful modern analogue for the ancient sulphur cycle can come from an element that has a very short residence time in the ocean and whose main pathway to the ocean is via the atmosphere and not through the dissolved load of rivers or hydrothermal venting. Here we argue that a well-studied example of this situation is the anthropogenically dominated lead cycle of the19th and 20th centuries.

Lead has a very low natural concentration in seawater, due in part to its high particle reactivity (Schaule & Patterson, 1981), resulting in very short oceanic residence time (2-100 years: Chow & Patterson, 1962; Bacon et al., 1976; Nozaki et al., 1976; Nozaki & Tsunogai, 1976). Before industrialisation, the various ocean basins had their individual, unique Pb-isotope signatures. These can, for example, be reconstructed from analysis of pre-anthropogenic hydrogenous sediments, such as ferromanganese deposits (e.g. Abouchami & Goldstein, 1995). From the distribution of the isotope values and their temporal evolution, it is possible to reconstruct aspects of the ocean circulation over the past 100 Ma or so (e.g. Ling et al., 1997) and riverine as well as volcanic aerosol input into the ocean basins (e.g. van de Flierdt et al., 2003; Chen et al., 2013). Thus, prior to industrial pollution, local riverine and atmospheric isotope signals were transmitted to sediments on the ocean floor, yielding provincial patterns (Von Blanckenburg et al., 1996).

With the advent of industrialisation and particularly with the use of tetraethyl lead as an anti-knock agent in petrol, the natural atmospheric-oceanic lead cycle

became completely transformed. In the early 19th century, local industrial lead signals developed in response to coal burning (e.g. Arnaud et al., 2004) before large-scale mining and lead smelting and refining resulted in dominant point sources of atmospheric lead. For example, release of lead from the giant Pb-Zn-Ag deposit of Broken Hill (New South Wales) can be quantitatively reconstructed thousands of km down-wind in peat and lake sediment cores (e.g. Marx et al., 2010). The addition of tetraethyl lead to petrol increased from the early 20th century to a peak in 1970, after which international bans led to the near-complete phasing out towards the end of the 20th century. Due to the fact that tetraethyl lead was largely sourced from only a few very large mines and widely distributed, hemispheric differences in the atmospheric Pb-isotope compositions were created and transposed into the oceans and eventually into coeval sediments (e.g. Patterson, 1965; Wu & Boyle, 1997). These industrial signals completely overwhelmed the pre-anthropogenic Pb-isotope provinciality but since the phase-out, more regional atmospheric pollution patterns have again become apparent (e.g. Bollhöfer & Rosman, 2002). There are thus many similarities between the industrial lead cycle and the Archaean sulphur cycles:

i) the oceanic inventories of both elements are/were low;

ii) both elements have/had short oceanic residence times;

iii) the main oceanic input was atmospheric rain down;

iv) individual giant point sources (explosive large-scale volcanic eruptions in the case of sulphur, and giant smelters in the case of lead) could at least temporally dominate atmospheric input and be transported thousands of km down-wind.

By analogy with the findings from the inadvertent industrial lead experiment, it can thus be hypothesised that in the Neoarchaean, the above factors combined permitted the effective transmission and preservation of localised MIF-S signals and that seawater sulphate and its isotopic composition were extremely sensitive to perturbations in the global sulphur cycle, particularly to large volcanic eruptions that released high quantities of sulphur.

5. Discussion

We initially address the significance and possible origin of the observed non-zero intercept $\delta^{34}S_{V\text{-}CDT}$ - $\Delta^{33}S$ data array. Next we discuss the apparent temporal variation in the extent of MIF-S throughout the Archaean before concluding on the origin of the Neoarchaean bias towards positive $\Delta^{33}S$.

5.1. The significance of the non-zero $\Delta^{33}S$ - $\delta^{34}S$ intercept

Kamber and Whitehouse (2007) proposed that the main non-zero intercept $\delta^{34}S_{V\text{-}CDT}$ - $\Delta^{33}S$ data array shown by sample SrKu34 could indicate diagenetic mixing of unrelated sulphur sources in the sediment environment. More specifically, recycled sulphur from basinal brines (e.g. from stratigraphically lower samples similar to SrKu31, which contained SRBO sphaeroidal pyrite) could have mixed with elemental sulphur from the water column. The geological context for this idea, from REE+Y data (Figure 2) and petrographic analysis (Kamber & Whitehouse, 2007), is that SrKu31was deposited in open-ocean, shallow-water (Figure 2a) incorporating SRBO pyrite largely plotting in the bottom left quadrant of the $\delta^{34}S_{V\text{-}CDT}$ - $\Delta^{33}S$ plot, with consistently negative $\Delta^{33}S$ values, ca. - 0.54 ‰, and an isotopic gradient in $\delta^{34}S$ from ca. - 8 to + 2 ‰ (Figure 2b). Subsequently, the basin became restricted and the carbonate platform was slightly drowned as SrKu34 was deposited in deeper water in a temporarily restricted basin (Figure 2c), while simultaneously burying the sediment below, i.e. strata like the host of SrKu31. Basinal fluids then potentially dissolved pyrites from sediment such as SrKu31, transporting its S-isotope signature to the sediment water interface where it was mixed with S_8 in the water column. Here SrKu34 pyrite grew by incorporating sulphur from these two distinct sulphur sources. The non-zero intercept array obtained from SrKu34 may thus imply a hybrid sulphur source, leading to a mixing line between sulphur with an isotopic signal similar to SrKu31 SRBO sulfate from the bottom left quadrant of the $\delta^{34}S_{V\text{-}CDT}$ - $\Delta^{33}S$ plot, and water column S_8 from the top right quadrant of the $\delta^{34}S_{V\text{-}CDT}$ - $\Delta^{33}S$ plot (Figure 2b). With this interpretation, the non-zero intercept of the array has no atmospheric significance. This explanation requires basinal fluids to have been sufficiently oxidised to dissolve the pyrite and transfer its S-isotope signature upwards. This requirement is in contrast with the lack of petrographic evidence for oxidation and dissolution of sulphides. Namely, very delicate microbial kerogen is

preserved in exquisite detail in the limestones below the host of SrKu34 (e.g. Sumner, 1997; Kamber et al., 2014) and many of these limestones contain intricately distributed micron-scale pyrite grains with no evidence for dissolution. Furthermore, the pyrite chemistry itself (Gallagher et al., 2015) as well as the REE systematics of the hosting limestones (e.g. Kamber et al., 2014) argue strongly in favour of reducing conditions during the Gamohaan Fm.'s deposition and diagenesis.

The alternative explanation for the non-zero intercept $\delta^{34}S_{V\text{-}CDT}$ - $\Delta^{33}S$ main data array (Figure 1a) proposed here, is that it represents the atmospheric signal from local rainout of aerosol from a proximal arc volcano eruption. The volcano is envisaged to have emitted sulphur that did not have the canonical V-CDT bulk Earth isotope composition, but rather, recycled subducted sedimentary sulphur that had a positive mean $\Delta^{33}S$ signal (Figure 3e-h, and Figure 4). Thus, UV photolysis proceeded to fractionate the already positive $\Delta^{33}S$ of the volcanic aerosol to even higher values (+ 9.46 ‰ Δ^{33}) in the S_8 phase, and lower the sulphate phase towards lower, but still positive values (ca. + 3.5 ‰ $\Delta^{33}S$). Thus, with respect to the original volcanic aerosol, the sulphate phase was MIF-negative, even if, with respect to V-CDT, it remained positive. The original volcanic aerosol composition cannot be accurately established because the $\delta^{34}S$ value of the aerosol is not known. If $\delta^{34}S$ was 0, then the aerosol $\Delta^{33}S$ was + 5.06 ‰ (Figure 2b), and UV photolysis fractionated this signal by ca. + 4.5 and - 1.5 $\Delta^{33}S$ units (Figure 2b). The slope of the main non-zero intercept array (m = 0.44, Figure 2b) is less steep than that of the 'Archaean array' (m = 0.89, Figure 1b) proposed by (Ono et al., 2003), but is much more similar than the negative slope of data reported by Philippot et al. (2012). Since our model envisages a local volcanic emission, it is possible that the recorded slope is characteristic of UV photolysis operating at specific atmospheric height, unlike the global background sulphur whose UV photolysis reflected reactions across the entire stratospheric and atmospheric cross section. In our explanation, the secondary steeper array (m = 0.85, Figure 2b) that is recorded only by some of the disseminated pyrite could indicate resumption of background sulphate delivery from the wider basin, with the more normal lower $\Delta^{33}S$ composition.

We appreciate that the idea of emitting volcanic aerosols with non-V-CDT S-isotope composition is a significant departure from the current paradigm. However, we stress here again that the stratigraphic context (Figure 2) informs us that the most

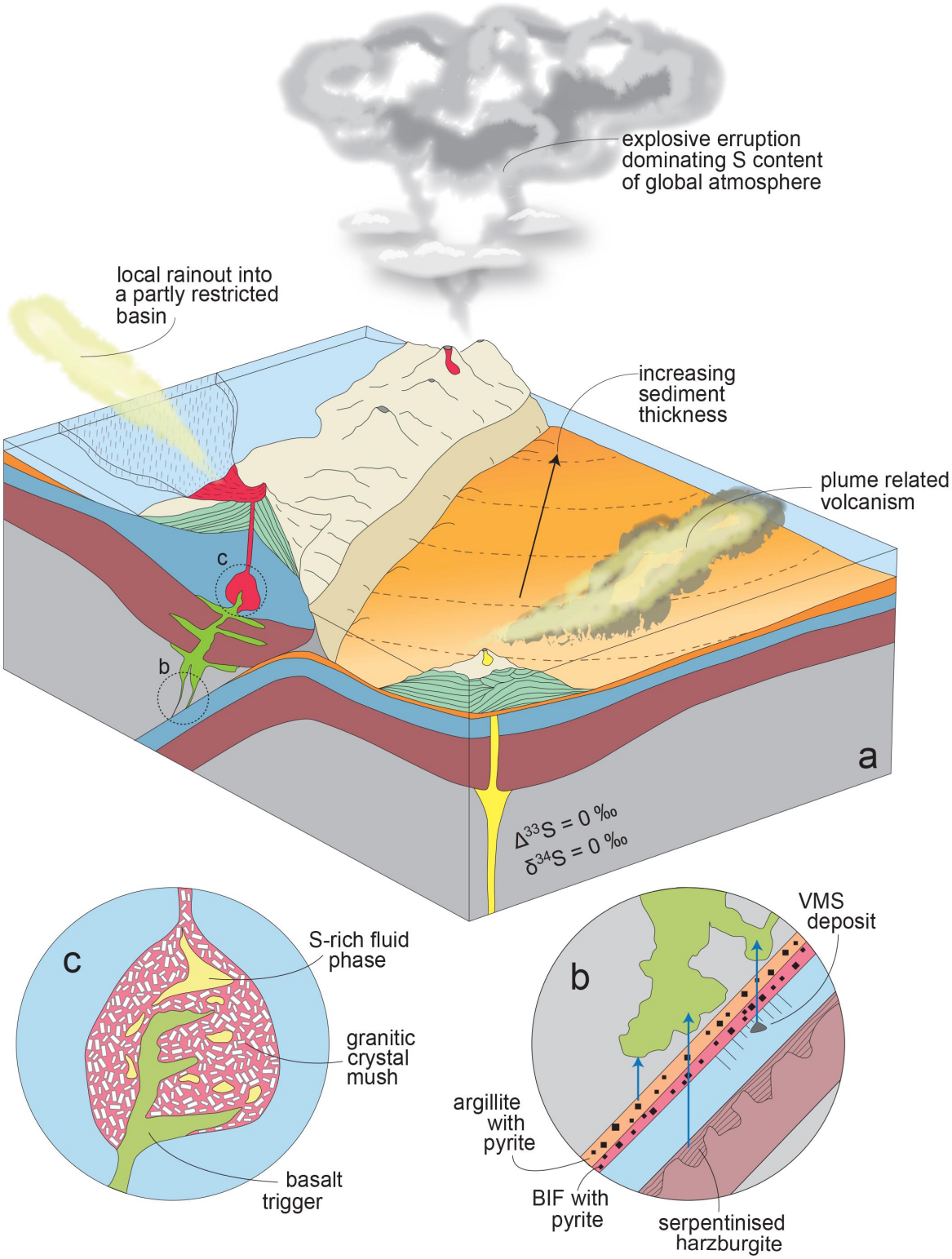

explosive erruption
dominating S content
of global atmosphere
local rainout into
a partly restricted
basin
increasing
sediment
thickness
plume related
volcanism
c
b
a
$\Delta^{33}S = 0$ ‰
$\delta^{34}S = 0$ ‰
c
S-rich fluid
phase
granitic
crystal
mush
basalt
trigger
b
VMS
deposit
argillite
with
pyrite
BIF with
pyrite
serpentinised
harzburgite

Figure 4: Schematic illustration of terrestrial magmatism at play during the Neoarchaean, depicting three distinct volcanogenic sources of atmospheric sulphur. The block diagram (a) depicts a newly-formed, Neoarchaean subduction zone and resultant volcanic arc, in addition to a hotspot volcano, more typical of the plume related volcanism prevalent throughout the early Archaean. The hotspot volcano quiescently degasses 0 ‰ $\Delta^{33}S_{CDT}$ mantle sulphur to the atmosphere. Subsequent atmospheric UV interaction with this mantle CDT type S imparted a MIF-S signal before incorporation into sedimentary sulphides of the oceanic crust. Once effective subduction was underway, sedimentary sulphides may have been recycled from the subducting oceanic plate into the melt source of the arc volcano, and released as anomalous non-zero $\Delta^{33}S$ MIF-S. The oceanic sediments depicted in the block diagram show a colour gradient and contours representative of thickness illustrating that oceanic crust with thicker sediment was more successful in transferring MIF-S into the subduction zone. Additionally, the transfer of sulphur is highly dependent on rock type (insert b). Potential S-sources in the subducted Archaean oceanic crust include argillite, BIFs, VMS deposits, and serpentinised harzburgite (insert b). Sulphur from VMS deposits is difficult to mobilise (Ulrich et al., 2011) and not likely a significant contributor to the subduction zone melt source, while the subduction of lithospheric mantle, i.e. serpentinised hartzbergite, is a potential source when undergoing devolatisation and expulsion of sulphur (Evans, 2012). Only 10% of sedimentary sulphur from mud is estimated to make it to the subduction zone melt source (Evans et al., 2014), analogous to Archaean argillite. Liberation of sulphur from BIF sulphides (Thurston et al., 2012), BIF may have had the largest potential for preferential release of S in the subduction zone. The diagram also highlights how explosivity of eruptions determine the potential for production of a global S-signal. Basaltic recharge into an evolved magma reservoir (Pallister et al., 1992; Pallister et al., 1996), can separate a SO_2 rich fluid phase and trigger an eruption (insert c) releasing several million tonnes of SO_2 into the atmosphere (e.g. Bluth et al., 1992; Daag et al., 1996). Also shown is local rainout from a lesser eruptions into a restricted basin that may have facilitated preservation of a localised S-signal.

pyritiferous sample, exhibiting the most extreme S-fractionation with a non-zero intercept $\delta^{34}S_{V\text{-}CDT}$ - $\Delta^{33}S$ data array, was deposited during temporary basin restriction (Hälbich et al., 1992). Thus, we do not envisage the entire atmospheric inventory to have had a non-V-CDT S-isotope composition. Rather, a local volcanic aerosol experienced UV photolysis at a specific atmospheric height and was transmitted into a local, partly restricted basin. For reference, we draw attention to the June 15th 1991 eruption of Pinatubo, whose plume travelled west south-west, forming a layer of aerosol at heights approximately 20-25 km above sea level, with main rainout occurring across the South China Sea (Oppenheimer et al., 2011).

It is noteworthy that distinctive volcanic ash layers occur throughout the Gamohaan Formation. The resulting tuffs are present above and below SrKu34 (Figure 2) and these have been used for U/Pb zircon geochronology (e.g. Sumner & Bowring, 1996), providing strong evidence for proximal, explosive volcanism from evolved magmas (that permitted crystallisation of zircon). Finally, there is evidence that the Gamohaan basin was sulphate limited; not only is the range in $\delta^{34}S$ limited (Papineau et al., 2005; Domagal-Goldman et al., 2008; Guo et al., 2009; Whitehouse, 2013) but several Gamohaan Formation sphaeroidal pyrites also preserve $\delta^{34}S$ isotopic gradients as a function of their spherical segment radius, indicative of a limit on sulphate availability during BSR (Kamber & Whitehouse, 2007; Gallagher et al., 2015). Thus, sulphur fallout could easily overwhelm the ambient isotopic signal.

5.2. The significance of the wide range in Neoarchaean $\Delta^{33}S$

The implicit assumption from global compilations of the $\Delta^{33}S$ MIF record is that the maxima and minima recorded correspond to the least hybridised and thus purest end-member isotope compositions of sulphur species formed by prevailing UV photolysis. Consequently, the very large Neoarchaean spread in $\Delta^{33}S$ has global atmospheric significance, and is seen as a global phenomenon that persisted for some 150-200 Ma. According to this interpretation, the sulphur cycle can be modeled with a mass conservation approach. Here we propose to consider the implications of the possibility that the sedimentary record preserves local signals, and that maxima and minima do not represent global end members.

In this alternative explanation, the extent of UV photolysis-induced MIF-S fractionation could have remained relatively unchanged throughout the Archaean.

The greater extent of Neoarchaean observed $\Delta^{33}S$ was instead caused by two evolutions. Firstly, as discussed in greater detail in the final section, the onset of Wilson-type plate tectonics (at ca. 3 Ga; Shirey & Richardson, 2011) and associated subduction of sediment, from which sulphur with pre-existing MIF signals was recycled into arc magmas and eventually released as volcanic aerosols into the atmosphere (Figure 4). Thus, at least in local volcanic aerosol plumes of non-V-CDT average composition, both higher and lower $\Delta^{33}S$ compositions could be produced than before 3 Ga. Volcanic arc magmas occur in the same subduction zone tectonic setting as porphyry-copper systems (Imai et al., 1993), when an aqueous sulphur-rich gas phase develops. Thus, arc volcanoes emitting high quantities of sulphur can be viewed as failed potential porphyry-copper deposits (Pasteris, 1996).

Secondly, the establishment of the first platformal carbonate factories occurred at ca. 2.6 Ga (Eriksson and Fedo, 1995). Evidence for such carbonate factories are found both on the Kaapvaal craton (i.e. the Gamohaan Fm.) and on the Pilbara Craton (i.e the Carawine dolomite) and also on the São Francisco Craton (i.e. the Batatal Fm.). These sedimentary environments were characterised by a proliferation of microbial life, preserved as an unprecedented diversity of stromatolites (e.g. Summons et al., 1999). On these shallow, high organic productivity platforms, sulphate concentrations may have been very low. They also provided an environment in which local sub-basins evidently formed (e.g. Hälbich et al., 1992). Local aerosol signals could quickly be transmitted into the sediment of such sub-basins, as exemplified by sample SrKu34. These settings thus provided an ideal environment to rapidly transfer local aerosol signals without dilution with the more global marine background signal. It may be significant that when omitting samples from the Kaapvaal and Pilbara cratons, the remaining Neoarchaean data show much less extreme $\Delta^{33}S$ values ($\Delta^{33}S$: - 3 ‰ to + 2.12 ‰). Because at the time of sediment deposition, these two cratons were likely adjacent parts of an originally larger craton (i.e. Vaalbara; Zegers et al., 1998; Nelson et al., 1999), the evidence for global extreme $\Delta^{33}S$ actually only comes from one large platform and its sub-basins.

A corollary of our new hypothesis is that atmospheric sulphate could have had variable $\Delta^{33}S$ signals with reference to V-CDT. We note that three broadly contemporary carbonate-hosted Neoarchaean datasets show distinctive negative $\Delta^{33}S$ values. The most negative $\Delta^{33}S$ values are found in the Batatal Fm. which preserves

$\Delta^{33}S$ values as low as - 3 ‰ (Zhelezinskaia et al., 2014). By contrast, the Carawine dolomite preserves negative $\Delta^{33}S$ extremes of - 2.5 ‰ (Ono et al., 2003), while the contemporaneous Gamohaan Fm. preserves negative $\Delta^{33}S$ extremes of - 0.9 ‰ (Kamber & Whitehouse, 2007). The discussion of the extent of MIF-S has previously been focused on the positive MIF-S range. However, our hypotheses provides an explanation for why different magnitudes of negative MIF-S were preserved, namely if the atmosphere was at least locally slightly MIF-positive, the resulting negative MIF after UV-photolysis would vary in turn. In summary, the large MIF-S excursions in global Neoarchaean $\Delta^{33}S$ compilations could be superpositions of local signals, which reflect atmospheric processing of individual volcanic eruptions.

5.3. The Neoarchaean positive $\Delta^{33}S$ bias

Because the predominant source of seawater sulphate in the Archaean was volcanogenic, the evolving nature of terrestrial magmatism may have strongly influenced the quantity, species and isotope composition of sulphur emitted into the Archaean atmosphere. The possibility of recycling of sedimentary sulphides at subduction zones is of paramount importance. In this regard, it is important that anomalous $\Delta^{33}S$ sulfide inclusions in 2.9 Ga diamonds have been interpreted as direct evidence for recycling of sedimentary sulphur (Farquhar et al., 2002). Diamond sulphide inclusions exhibit a major compositional change at 3 Ga, when eclogite inclusions resembling metamorphosed basaltic crust become more prevalent. This has been interpreted as the capture of eclogite via subduction (Shirey & Richardson, 2011) and that Wilson cycle plate tectonics were in operation from 2.9 to 3.0 Ga onwards (Dhuime et al., 2012)

The subduction of sediment to sufficient depth for capture by arc magmas alone is not sufficient to support the notion that individual arc eruptions could have emitted sulphur of non-V-CDT composition. Modern subduction zone studies offer some insight but like the modern marine analogue, the major issue is that modern subduction zones contain a lot more sulphide than would have been possible in the Archaean, because of the much lower sulphate content of Archaean seawater. Nonetheless, modern studies show that arc magmas have $\delta^{34}S$ heavier than mantle, implying that slab derived sediments are significant contributors to the sulphur flux in subduction zone volcanoes (Métrich et al., 1999; De Hoog et al., 2001). An

important insight is that only a small proportion of the total subducted sulphur is actually recycled at arc volcanoes. For example, Evans (2012) estimated that < 20% of sulphur subducted in sediments, altered oceanic crust and serpentinised lithospheric mantle is recycled. Jégo and Dasgupta (2013) estimated that 15 – 30 % of the subducted sulphur is returned to surface reservoirs by arc processes, whereas the remaining, larger portion of subducted sulphur is apparently transported to the mantle at depths of >150 km (Evans & Powell, 2015). This evidence for non-quantitative recycling of sulphur opens the possibility for preferential transfer of sulphur with particular isotope compositions to arc magmas. Thus, the recycled sulphur may not have had 'average sedimentary' isotope composition.

In modern subduction zones, the transfer of sulphur from the slab with fluids is dependent on metamorphic grade. The most efficient transfer of sulphur from sulphides apparently occurs at eclogite facies (Giacometti et al., 2014). Although no agreement exists about the thermal structure of Archaean subduction zones, melting of eclogite facies metabasalt is widely discussed in the literature as a means of producing tonalite-trondhjemite-granodiorite magmas that show evidence of arc-type geochemistry (e.g. Kamber et al., 2003). Thus, transfer of sulphur from slabs may have been different in the Archaean, just as different as the arc-style magmas are. In addition to metamorphic grade, the transfer of sedimentary sulphur is also regulated by rock type (Figure 4b). In this regard, it is important to recall that the Archaean seafloor was covered with unique sediments, including BIF. Given the strong evidence for secondary mobility of BIF sulphides (Thurston et al., 2012) and the ease of pyrite recrystallization (Ulrich et al., 2011), BIFs may hold potential for preferential sulphur release in subduction zones.

If it is accepted that preferential transfer of non-V-CDT sulphur into Archaean arc magmas was at least theoretically feasible, the behaviour of sulphur in the evolving magma then determined whether the signal became local or hemispheric. Only highly explosive volcanic eruptions, where a separate sulphur fluid phase developed in the magma (Figure 4c) and was released as a steam plume of SO_2 into the stratosphere (e.g. Mount Pinatubo 1991 ; Pasteris, 1996), had the potential to dominate the sulphur content of the global atmosphere, at least for several years, producing a hemispheric sulphur signal. By contrast fast rainout from lesser eruptions into a restricted basin could have facilitated preservation of the isotopic

composition of a localised volcanic source (Figure 4a). In addition, variability in the location of arc volcanoes contributes to the preservation of localised S-isotope signatures because atmospheric circulation limits the dispersion of high latitude eruptions. Thus, very little aerosol of a high latitude eruption will reach the opposing hemisphere (Oppenheimer et al., 2011). The MDF S-isotope composition of volcanically emitted sulphur can also vary with eruption style. For example, the gas phase during early open system degassing is often $\delta^{34}S$-depleted whereas during later large eruptions there is a correspondingly $\delta^{34}S$-enriched gas phase (Mandeville et al., 2009). Subsequent UV photolysis MIF of initially $\delta^{34}S$ depleted sulphur could further shift the isotope composition of the resultant MIF array in the $\delta^{34}S_{V\text{-}CDT}$ - $\Delta^{33}S$ plot. Furthermore, the sulphur concentration of volcanic gas emitted from individual modern arc volcanoes is also highly variable (Oppenheimer et al., 2011).

In summary, there are several processes that undoubtedly influenced the S-isotope composition of volcanic emissions as the Earth transitioned from a plume-dominated planet towards Wilson-style tectonics. In this context of the evolution of Archaean magmatism, the mean +2 ‰ $\Delta^{33}S$ value of pyrite from all Neoarchaean sedimentary rocks (Figure 3a-d) may imply preferential recycling of $\Delta^{33}S$ positive sulphur in subduction zones, rather than a change in photochemical reactions or evolving atmospheric composition. The absence of this bias towards positive $\Delta^{33}S$ in older sedimentary rocks would then be a tectonic consequence, namely only after initiation of Wilson-style subduction, did transfer of sulphur from slabs to arc magmas become feasible. The extent of the MIF-S signal rapidly diminished after 2.5 Ga, some 150 Ma before evidence for the GOE. There are currently too few data to accurately reconstruct the post-Archaean MIF evolution but there is wide agreement that a major change in magmatic evolution occurred at that point (Keller & Schoene, 2012). This manifests in the geochemistry of the emplaced < 2.5 Ga igneous rocks and may have strongly affected volcanic degasing.

6. Conclusions

Previous studies modelling the sulphur cycle (e.g. Canfield & Raiswell, 1999) worked from the implicit assumption that sulphur was globally mixed in the Archaean atmosphere and hydrosphere. Here we have used the 20th century lead analogue to argue that the low concentration and short residence time of oceanic

sulphur combined with its near exclusive volcanogenic source meant that the Archaean atmosphere and ocean were more likely poorly mixed with respect to sulphur. Thus, although preservation of MIF-S in Archaean sediments continues to have implications for the Archaean redox state of the global atmosphere, Archaean sedimentary rocks likely preserve local MIF-S signals. Very large explosive volcanic eruptions had potential to inject large amounts of SO_2 into the stratosphere, where it persisted for years and could dominate the atmospheric sulphur budget. In the sedimentary record, however, even such global events will only represent a miniscule layer, found in a rock as a few microns of pyrite growth. Thus, the variability of MIF-S signals in individual Archaean pyrites is not surprising. Furthermore, regional rainout from lesser volcanic eruptions had the potential to impart very local sulphur signals, particularly if they occurred over restricted basins. These volcanic perturbations are not as visible in today's ocean due to masking of the signal by the high oceanic sulphate pool. Non-zero intercept $\Delta^{33}S$ - $\delta^{34}S$ data arrays could form in basins near arc volcanoes that emitted recycled sedimentary sulphur that was not MIF-neutral. The transfer of as such sedimentary sulphur from subduction zones to the atmosphere via arc volcanoes, after initiation of Wilson-style plate tectonics ca. 3 Ga, could explain the deviation of Neoarchaean sedimentary sulphur from the 0 ‰ $\Delta^{33}S_{V\text{-}CDT}$ mantle composition. At least temporally and locally, the sampled atmospheric sulphur could have had a different composition from average bulk Earth, and the large Neoarchaean excursions and asymmetry could be explained by superposition of local signals.

Acknowledgements

The Nordsim facility is operated under an agreement between the research funding agencies of Denmark, Norway and Sweden, the Geological Survey of Finland, and the Swedish Museum of Natural History. This analytical work was supported by a SYNTHESYS grant, SE-TAF-3395, funded by the European Community – Research Infrastructure Action under the FP7 "Capacities" Specific Programme. This research was supported by an EU FP7 Marie Curie Actions – Career Integration Grant awarded to B.S.K. which provided financial support to M.G. We thank Nick Beukes for providing samples and Claire Kamber for kindly drafting figure 4.

References

Abouchami W, Goldstein SL (1995) A lead isotopic study of Circum-Antarctic manganese nodules. *Geochimica et cosmochimica acta,* 59, 1809-1820.

Arnaud F, Revel-Rolland M, Bosch D, Winiarski T, Desmet M, Tribovillard N, Givelet N (2004) A 300 year history of lead contamination in northern French Alps reconstructed from distant lake sediment records. *Journal of Environmental Monitoring,* 6, 448-456.

Bacon M, Spencer D, Brewer P (1976) 210 Pb/226 Ra and 210 Po/210 Pb disequilibria in seawater and suspended particulate matter. *Earth and Planetary Science Letters,* 32, 277-296.

Baroni M, Thiemens MH, Delmas RJ, Savarino J (2007) Mass-Independent Sulfur Isotopic Compositions in Stratospheric Volcanic Eruptions. *Science,* 315, 84-87.

Bekker A, Holland H, Wang P-L, Rumble D, Stein H, Hannah J, Coetzee L, Beukes N (2004) Dating the rise of atmospheric oxygen. *Nature,* 427, 117-120.

Beukes NJ (1987) Facies relations, depositional environments and diagenesis in a major early Proterozoic stromatolitic carbonate platform to basinal sequence, Campbellrand Subgroup, Transvaal Supergroup, southern Africa. *Sedimentary Geology,* 54, 1-46.

Bluth GJS, Doiron SD, Schnetzler CC, Krueger AJ, Walter LS (1992) Global tracking of the SO2 clouds from the June, 1991 Mount Pinatubo eruptions. *Geophysical Research Letters,* 19, 151-154.

Bollhöfer A, Rosman K (2002) The temporal stability in lead isotopic signatures at selected sites in the Southern and Northern Hemispheres. *Geochimica et Cosmochimica Acta,* 66, 1375-1386.

Cabral RA, Jackson MG, Rose-Koga EF, Koga KT, Whitehouse MJ, Antonelli MA, Farquhar J, Day JM, Hauri EH (2013) Anomalous sulphur isotopes in plume lavas reveal deep mantle storage of Archaean crust. *Nature,* 496, 490-493.

Canfield DE (2004) The evolution of the Earth surface sulfur reservoir. *American Journal of Science,* 304, 839-861.

Canfield DE, Raiswell R (1999) The evolution of the sulfur cycle. *American Journal of Science,* 299, 697-723.

Chen TY, Ling HF, Hu R, Frank M, Jiang SY (2013) Lead isotope provinciality of central North Pacific Deep Water over the Cenozoic. *Geochemistry, Geophysics, Geosystems,* 14, 1523-1537.

Cheney E (1996) Sequence stratigraphy and plate tectonic significance of the Transvaal succession of southern Africa and its equivalent in Western Australia. *Precambrian Research,* 79, 3-24.

Chow TJ, Patterson C (1962) The occurrence and significance of lead isotopes in pelagic sediments. *Geochimica et Cosmochimica Acta,* 26, 263-308.

Crowe D, Vaughan R (1996) Characterization and use of isotopically homogeneous standards for in situ laser microprobe analysis of 34S/32S ratios. *American Mineralogist,* 81, 187-193.

Crowe SA, Paris G, Katsev S, Jones C, Kim S-T, Zerkle AL, Nomosatryo S, Fowle DA, Adkins JF, Sessions AL, Farquhar J, Canfield DE (2014) Sulfate was a trace constituent of Archean seawater. *Science,* 346, 735-739.

Daag A, Tubianosa B, Newhall C, Tungol N, Javier D, Dolan M, Delos Reyes P, Arboleda R, Martinez M, Regalado T (1996) Monitoring sulfur dioxide emission at Mount Pinatubo. *Fire and Mud: eruptions and lahars of Mount Pinatubo, Philippines*, 409-414.

De Hoog J, Taylor B, Van Bergen M (2001) Sulfur isotope systematics of basaltic lavas from Indonesia: implications for the sulfur cycle in subduction zones. *Earth and Planetary Science Letters,* 189, 237-252.

Dhuime B, Hawkesworth CJ, Cawood PA, Storey CD (2012) A change in the geodynamics of continental growth 3 billion years ago. *Science,* 335, 1334-1336.

Ding T, Valkiers S, Kipphardt H, De Bievre P, Taylor P, Gonfiantini R, Krouse R (2001) Calibrated sulfur isotope abundance ratios of three IAEA sulfur isotope reference materials and V-CDT with a reassessment of the atomic weight of sulfur. *Geochimica et Cosmochimica Acta,* 65, 2433-2437.

Domagal-Goldman SD, Kasting JF, Johnston DT, Farquhar J (2008) Organic haze, glaciations and multiple sulfur isotopes in the Mid-Archean Era. *Earth and Planetary Science Letters,* 269, 29-40.

Evans K (2012) The redox budget of subduction zones. *Earth-Science Reviews,* 113, 11-32.

Evans K, Powell R (2015) The effect of subduction on the sulfur, carbon, and redox budget of lithospheric mantle. *Journal of Metamorphic Geology*.

Evans K, Tomkins A, Cliff J, Fiorentini M (2014) Insights into subduction zone sulfur recycling from isotopic analysis of eclogite-hosted sulfides. *Chemical Geology,* 365, 1-19.

Farquhar J, Bao H, Thiemens M (2000) Atmospheric influence of Earth's earliest sulfur cycle. *Science,* 289, 756-758.

Farquhar J, Savarino J, Airieau S, Thiemens MH (2001) Observation of wavelength‐sensitive mass‐independent sulfur isotope effects during SO2 photolysis: Implications for the early atmosphere. *Journal of Geophysical Research: Planets (1991–2012),* 106, 32829-32839.

Farquhar J, Wing B, Mckeegan K, Harris J, Cartigny P, Thiemens M (2002) Mass-independent sulfur of inclusions in diamond and sulfur recycling on early Earth. *Science,* 298, 2369-2372.

Farquhar J, Wing BA (2003) Multiple sulfur isotopes and the evolution of the atmosphere. *Earth and Planetary Science Letters,* 213, 1-13.

Fike DA, Bradley AS, Rose CV (2013) Rethinking the Ancient Sulfur Cycle. *Annual Review of Earth and Planetary Sciences*.

Fischer W, Schroeder S, Lacassie J, Beukes N, Goldberg T, Strauss H, Horstmann U, Schrag D, Knoll A (2009) Isotopic constraints on the Late Archean carbon cycle from the Transvaal Supergroup along the western margin of the Kaapvaal Craton, South Africa. *Precambrian Research,* 169, 15-27.

Gallagher M, Turner EC, Kamber BS (2015) In situ trace metal analysis of Neoarchaean – Ordovician shallow-marine microbial-carbonate-hosted pyrites. *Geobiology,* 13, 316-339.

Giacometti F, Evans KA, Rebay G, Cliff J, Tomkins AG, Rossetti P, Vaggelli G, Adams DT (2014) Sulfur isotope evolution in sulfide ores from Western Alps: Assessing the influence of subduction‐related metamorphism. *Geochemistry, Geophysics, Geosystems,* 15, 3808-3829.

Guo Q, Strauss H, Kaufman AJ, Schröder S, Gutzmer J, Wing B, Baker MA, Bekker A, Jin Q, Kim S-T (2009) Reconstructing Earth's surface oxidation across the Archean-Proterozoic transition. *Geology,* 37, 399-402.

Hälbich IW, Lamprecht D, Altermann W, Horstmann U (1992) A carbonate-banded iron formation transition in the Early Protorezoicum of South Africa. *Journal of African Earth Sciences (and the Middle East),* 15, 217-236.

Halevy I (2013) Production, preservation, and biological processing of mass-independent sulfur isotope fractionation in the Archean surface environment. *Proceedings of the National Academy of Sciences,* 110, 17644-17649.

Halevy I, Johnston DT, Schrag DP (2010) Explaining the structure of the Archean mass-independent sulfur isotope record. *Science,* 329, 204-207.

Hofmann A, Bekker A, Rouxel O, Rumble D, Master S (2009) Multiple sulphur and iron isotope composition of detrital pyrite in Archaean sedimentary rocks: a new tool for provenance analysis. *Earth and Planetary Science Letters,* 286, 436-445.

Holland HD (1984) *The chemical evolution of the atmosphere and oceans,* Princeton University Press.

Imai A, Listanco E, Fujii T (1993) Petrologic and sulfur isotopic significance of highly oxidized and sulfur-rich magma of Mt. Pinatubo, Philippines. *Geology,* 21, 699-702.

Jégo S, Dasgupta R (2013) Fluid-present melting of sulfide-bearing ocean-crust: Experimental constraints on the transport of sulfur from subducting slab to mantle wedge. *Geochimica et Cosmochimica Acta,* 110, 106-134.

Kamber B, Whitehouse M (2007) Micro‐scale sulphur isotope evidence for sulphur cycling in the late Archean shallow ocean. *Geobiology,* 5, 5-17.

Kamber BS (2010) Archean mafic–ultramafic volcanic landmasses and their effect on ocean–atmosphere chemistry. *Chemical Geology,* 274, 19-28.

Kamber BS (2015) The evolving nature of terrestrial crust from the Hadean, through the Archaean, into the Proterozoic. *Precambrian Research,* 258, 48-82.

Kamber BS, Collerson KD, Moorbath S, Whitehouse MJ (2003) Inheritance of early Archaean Pb-isotope variability from long-lived Hadean protocrust. *Contributions to Mineralogy and Petrology,* 145, 25-46.

Kamber BS, Webb GE (2001) The geochemistry of late Archaean microbial carbonate: implications for ocean chemistry and continental erosion history. *Geochimica et Cosmochimica Acta,* 65, 2509-2525.

Kamber BS, Webb GE, Gallagher M (2014) The rare earth element signal in Archaean microbial carbonate: information on ocean redox and biogenicity. *Journal of the Geological Society,* 171, 745-763.

Keller CB, Schoene B (2012) Statistical geochemistry reveals disruption in secular lithospheric evolution about 2.5 [thinsp] Gyr ago. *Nature,* 485, 490-493.

Konhauser KO, Pecoits E, Lalonde SV, Papineau D, Nisbet EG, Barley ME, Arndt NT, Zahnle K, Kamber BS (2009) Oceanic nickel depletion and a methanogen famine before the Great Oxidation Event. *Nature,* 458, 750-753.

Ling H, Burton K, O'nions R, Kamber B, Von Blanckenburg F, Gibb A, Hein J (1997) Evolution of Nd and Pb isotopes in Central Pacific seawater from ferromanganese crusts. *Earth and Planetary Science Letters,* 146, 1-12.

Mandeville CW, Webster JD, Tappen C, Taylor BE, Timbal A, Sasaki A, Hauri E, Bacon CR (2009) Stable isotope and petrologic evidence for open-system degassing during the climactic and pre-climactic eruptions of Mt. Mazama, Crater Lake, Oregon. *Geochimica et Cosmochimica Acta,* 73, 2978-3012.

Marx SK, Kamber BS, Mcgowan HA, Zawadzki A (2010) Atmospheric pollutants in alpine peat bogs record a detailed chronology of industrial and agricultural development on the Australian continent. *Environmental Pollution,* 158, 1615-1628.

Métrich N, Schiano P, Clocchiatti R, Maury RC (1999) Transfer of sulfur in subduction settings: an example from Batan Island (Luzon volcanic arc, Philippines). *Earth and Planetary Science Letters,* 167, 1-14.

Minikin A, Legrand M, Hall J, Wagenbach D, Kleefeld C, Wolff E, Pasteur EC, Ducroz F (1998) Sulfur-containing species (sulfate and methanesulfonate) in coastal Antarctic aerosol and precipitation. *Journal of Geophysical Research: Atmospheres,* 103, 10975-10990.

Nelson D, Trendall A, Altermann W (1999) Chronological correlations between the Pilbara and Kaapvaal cratons. *Precambrian Research,* 97, 165-189.

Nozaki Y, Thomson J, Turekian K (1976) The distribution of 210 Pb and 210 Po in the surface waters of the Pacific Ocean. *Earth and Planetary Science Letters,* 32, 304-312.

Nozaki Y, Tsunogai S (1976) 226Ra, 210Pb and 210Po disequilibria in the Western North Pacific. *Earth and Planetary Science Letters,* 32, 313-321.

Ohmoto H, Watanabe Y, Ikemi H, Poulson SR, Taylor BE (2006) Sulphur isotope evidence for an oxic Archaean atmosphere. *Nature,* 442, 908-911.

Ono S, Beukes NJ, Rumble D, Fogel ML (2006) Early evolution of atmospheric oxygen from multiple-sulfur and carbon isotope records of the 2.9 Ga Mozaan Group of the Pongola Supergroup, Southern Africa. *South African Journal of Geology,* 109, 97-108.

Ono S, Eigenbrode JL, Pavlov AA, Kharecha P, Rumble Iii D, Kasting JF, Freeman KH (2003) New insights into Archean sulfur cycle from mass-independent sulfur isotope records from the Hamersley Basin, Australia. *Earth and Planetary Science Letters,* 213, 15-30.

Oppenheimer C, Scaillet B, Martin RS (2011) Sulfur degassing from volcanoes: source conditions, surveillance, plume chemistry and earth system impacts. *Reviews in mineralogy and geochemistry,* 73, 363-421.

Pallister JS, Hoblitt RP, Meeker GP, Knight RJ, Siems DF (1996) Magma mixing at Mount Pinatubo: petrographic and chemical evidence from the 1991 deposits. *Fire and mud: eruptions and lahars of Mount Pinatubo, Philippines*, 687-731.

Pallister JS, Hoblitt RP, Reyes AG (1992) A basalt trigger for the 1991 eruptions of Pinatubo volcano? *Nature,* 356, 426-428.

Papineau D, Mojzsis S, Coath C, Karhu J, Mckeegan K (2005) Multiple sulfur isotopes of sulfides from sediments in the aftermath of Paleoproterozoic glaciations. *Geochimica et Cosmochimica Acta,* 69, 5033-5060.

Paris G, Adkins JF, Sessions AL, Webb SM, Fischer WW (2014) Neoarchean carbonate-associated sulfate records positive $\Delta^{33}S$ anomalies. *Science,* 346, 739-741.

Pasteris JD (1996) Mount Pinatubo volcano and “negative” porphyry copper deposits. *Geology,* 24, 1075-1078.

Patterson CC (1965) Contaminated and natural lead environments of man. *Archives of Environmental Health: An International Journal,* 11, 344-360.

Pavlov A, Kasting J (2002) Mass-independent fractionation of sulfur isotopes in Archean sediments: strong evidence for an anoxic Archean atmosphere. *Astrobiology,* 2, 27-41.

Philippot P, Van Zuilen M, Rollion-Bard C (2012) Variations in atmospheric sulphur chemistry on early Earth linked to volcanic activity. *Nature Geoscience,* 5, 668-674.

Reinhard CT, Planavsky NJ, Lyons TW (2013) Long-term sedimentary recycling of rare sulphur isotope anomalies. *Nature,* 497, 100-103.

Rouxel OJ, Bekker A, Edwards KJ (2005) Iron isotope constraints on the Archean and Paleoproterozoic ocean redox state. *Science,* 307, 1088-1091.

Savarino J, Romero A, Cole‐Dai J, Bekki S, Thiemens M (2003) UV induced mass‐independent sulfur isotope fractionation in stratospheric volcanic sulfate. *Geophysical Research Letters,* 30.

Schaule BK, Patterson CC (1981) Lead concentrations in the northeast Pacific: evidence for global anthropogenic perturbations. *Earth and Planetary Science Letters,* 54, 97-116.

Shen Y, Farquhar J, Masterson A, Kaufman AJ, Buick R (2009) Evaluating the role of microbial sulfate reduction in the early Archean using quadruple isotope systematics. *Earth and Planetary Science Letters,* 279, 383-391.

Shirey SB, Richardson SH (2011) Start of the Wilson cycle at 3 Ga shown by diamonds from subcontinental mantle. *Science,* 333, 434-436.

Summons RE, Jahnke LL, Hope JM, Logan GA (1999) 2-Methylhopanoids as biomarkers for cyanobacterial oxygenic photosynthesis. *Nature,* 400, 554-557.

Sumner DY (1997) Late Archean calcite-microbe interactions; two morphologically distinct microbial communities that affected calcite nucleation differently. *PALAIOS,* 12, 302-318.

Sumner DY, Bowring SA (1996) U □ Pb geochronologic constraints on deposition of the Campbellrand Subgroup, Transvaal Supergroup, South Africa. *Precambrian Research,* 79, 25-35.

Thurston P, Kamber B, Whitehouse M (2012) Archean cherts in banded iron formation: Insight into Neoarchean ocean chemistry and depositional processes. *Precambrian Research,* 214, 227-257.

Ueno Y (2014) Coping with low ocean sulfate. *Science,* 346, 703-704.

Ulrich T, Long D, Kamber B, Whitehouse M (2011) In situ trace element and sulfur isotope analysis of pyrite in a paleoproterozoic gold placer deposit, Pardo and Clement Townships, Ontario, Canada. *Economic Geology,* 106, 667-686.

Van De Flierdt T, Frank M, Halliday AN, Hein JR, Hattendorf B, Günther D, Kubik PW (2003) Lead isotopes in North Pacific deep water–implications for past changes in input sources and circulation patterns. *Earth and Planetary Science Letters,* 209, 149-164.

Von Blanckenburg F, O'nions R, Heinz J (1996) Distribution and sources of pre-anthropogenic lead isotopes in deep ocean water from Fe Mn crusts. *Geochimica et cosmochimica acta,* 60, 4957-4963.

Wagenbach D, Ducroz F, Mulvaney R, Keck L, Minikin A, Legrand M, Hall JS, Wolff EW (1998) Sea-salt aerosol in coastal Antarctic regions. *Journal of Geophysical Research: Atmospheres,* 103, 10961-10974.

Walker JC, Brimblecombe P (1985) Iron and sulfur in the pre-biologic ocean. *Precambrian Research,* 28, 205-222.

Whitehouse MJ (2013) Multiple Sulfur Isotope Determination by SIMS: Evaluation of Reference Sulfides for Δ33S with Observations and a Case Study on the Determination of Δ36S. *Geostandards and Geoanalytical Research,* 37, 19-33.

Wu J, Boyle EA (1997) Lead in the western North Atlantic Ocean: Completed response to leaded gasoline phaseout. *Geochimica et Cosmochimica Acta,* 61, 3279-3283.

Zegers T, De Wit M, Dann J, White S (1998) Vaalbara, Earth's oldest assembled continent? A combined structural, geochronological, and palaeomagnetic test. *Terra Nova,* 10, 250-259.

Zhelezinskaia I, Kaufman AJ, Farquhar J, Cliff J (2014) Large sulfur isotope fractionations associated with Neoarchean microbial sulfate reduction. *Science,* 346, 742-744.

7. Supporting Information

Supporting Information Table S1: Trace element concentrations (in ppm)

Sample ID	SrKu 2	SrKu 17	SrKu 31	SrKu 32	SrKu 33	SrKu 34	SrKu 36	SrKu 37
Sample type	stromatolite	micro-banded siderite/ankerite chert	Contorted microbial mat limestone	shale	Contorted microbial mat limestone	shaley limestone	Contorted microbial mat limestone	micro-banded siderite/ankerite chert
Sr	37.7	46.7	38.3	26.2	67.8	5.90	48.5	5.00
Zr	0.65	0.19	1.89	15.4	1.35	5.92	0.56	0.19
Y	2.42	7.29	11.5	10.6	2.57	2.39	1.90	1.57
Ba	3.62	5.43	7.46	34.5	9.37	6.16	5.24	1.02
La	0.85	1.56	7.08	16.5	3.623	4.70	2.38	0.972
Ce	1.06	2.35	11.1	32.2	6.21	8.90	3.86	1.85
Pr	0.118	0.283	1.26	3.87	0.698	1.08	0.421	0.208
Nd	0.421	1.18	4.60	14.0	2.33	3.88	1.42	0.720
Sm	0.071	0.249	0.767	2.84	0.38	0.654	0.243	0.126
Eu	0.028	0.100	0.309	0.635	0.100	0.165	0.049	0.035
Gd	0.096	0.421	0.888	2.61	0.355	0.575	0.241	0.141
Tb	0.015	0.065	0.133	0.373	0.049	0.068	0.035	0.024
Dy	0.104	0.476	0.892	2.02	0.291	0.364	0.208	0.168
Ho	0.029	0.129	0.225	0.382	0.06	0.064	0.047	0.04
Er	0.101	0.449	0.751	1.06	0.185	0.158	0.148	0.133
Tm	0.015	0.071	0.115	0.149	0.027	0.02	0.023	0.021
Yb	0.095	0.507	0.789	0.946	0.177	0.11	0.15	0.156
Lu	0.018	0.089	0.139	0.147	0.029	0.015	0.025	0.029
Th	0.016	0.027	0.344	7.74	0.813	2.35	0.225	0.028
U	0.062	0.017	0.531	1.23	0.39	0.236	0.173	0.014

Supporting Information Table S2: Quadruple S-isotope data (in ‰)

Sample ID	Sample type	$\delta^{34}S_{V\text{-}CDT}$ (‰)	$\delta^{33}S_{V\text{-}CDT}$ (‰)	$\Delta^{33}S$ (‰)	$\delta^{36}S_{V\text{-}CDT}$ (‰)	$\Delta^{36}S$ (‰)
34d_(MSK4)_@1	disseminated pyrite	-3.34 ± 0.09	-0.55 ± 0.07	1.16 ± 0.07	-7.78 ± 0.23	-1.48 ± 0.24
34d_(MSK4)_@02	disseminated pyrite	-4.36 ± 0.08	-2.31 ± 0.08	-0.07 ± 0.08	-8.90 ± 0.21	-0.67 ± 0.21
34d_(MSK4)_@03	disseminated pyrite	-2.25 ± 0.10	1.33 ± 0.09	2.48 ± 0.09	-7.12 ± 0.27	-2.87 ± 0.27
34d_(MSK4)_@04	disseminated pyrite	-1.55 ± 0.10	2.39 ± 0.06	3.19 ± 0.07	-6.37 ± 0.20	-3.44 ± 0.20
34d_(MSK4)_@05	disseminated pyrite	-3.00 ± 0.11	-0.82 ± 0.09	0.73 ± 0.10	-5.65 ± 0.21	0.02 ± 0.22
34d_(MSK4)_@06	disseminated pyrite	-4.11 ± 0.14	-0.93 ± 0.09	1.18 ± 0.11	-8.63 ± 0.31	-0.88 ± 0.32
34d_(MSK4)_@07	disseminated pyrite	-0.38 ± 0.11	4.56 ± 0.08	4.75 ± 0.09	-6.03 ± 0.25	-5.32 ± 0.26
34d_(MSK4)_@08	disseminated pyrite	-1.53 ± 0.09	1.35 ± 0.07	2.13 ± 0.07	-4.57 ± 0.22	-1.68 ± 0.22
34d_(MSK4)_@09	disseminated pyrite	-1.89 ± 0.13	2.61 ± 0.09	3.58 ± 0.10	-7.84 ± 0.38	-4.28 ± 0.38
34d_(MSK4)_@10	disseminated pyrite	-4.22 ± 0.18	1.30 ± 0.10	3.46 ± 0.13	-11.22 ± 0.37	-3.26 ± 0.37
34d_(MSK4)_@11	disseminated pyrite	-3.66 ± 0.08	-0.89 ± 0.07	0.99 ± 0.07	-7.64 ± 0.21	-0.74 ± 0.21
34d_(MSK4)_@12	disseminated pyrite	-3.49 ± 0.12	0.23 ± 0.10	2.02 ± 0.11	-8.41 ± 0.24	-1.83 ± 0.24
34d_(MSK4)_@13	disseminated pyrite	-2.57 ± 0.08	-0.06 ± 0.06	1.26 ± 0.06	-5.48 ± 0.22	-0.63 ± 0.23
34d_(MSK4)_@14	disseminated pyrite	-0.61 ± 0.08	3.85 ± 0.07	4.17 ± 0.06	-5.65 ± 0.25	-4.51 ± 0.25
34d_(MSK4)_@15	disseminated pyrite	-1.49 ± 0.08	2.14 ± 0.07	2.90 ± 0.07	-5.26 ± 0.19	-2.45 ± 0.20
34d_(MSK4)_@16	disseminated pyrite	3.56 ± 0.08	8.34 ± 0.07	6.51 ± 0.07	-0.16 ± 0.23	-6.90 ± 0.24
34d_(MSK4)_@17	disseminated pyrite	-0.93 ± 0.07	3.83 ± 0.07	4.30 ± 0.07	-6.37 ± 0.20	-4.62 ± 0.20
34d_(MSK4)_@18	disseminated pyrite	-1.44 ± 0.11	3.47 ± 0.08	4.20 ± 0.08	-7.20 ± 0.30	-4.49 ± 0.30
34d_(MSK4)_@19	disseminated pyrite	-1.75 ± 0.09	3.13 ± 0.07	4.03 ± 0.07	-7.90 ± 0.23	-4.60 ± 0.23
34d_(MSK4)_@20	disseminated pyrite	-4.18 ± 0.11	1.44 ± 0.09	3.58 ± 0.10	-11.54 ± 0.26	-3.64 ± 0.27
34d_(MSK4)_@21	disseminated pyrite	1.30 ± 0.09	6.38 ± 0.07	5.72 ± 0.07	-3.60 ± 0.23	-6.06 ± 0.23
34d_(MSK4)_@22	disseminated pyrite	1.23 ± 0.07	5.82 ± 0.07	5.19 ± 0.06	-3.70 ± 0.20	-6.02 ± 0.20
34d_(MSK4)_@23	disseminated pyrite	0.71 ± 0.14	6.10 ± 0.10	5.73 ± 0.11	-4.38 ± 0.29	-5.72 ± 0.30
34d_(MSK4)_@24	disseminated pyrite	-0.60 ± 0.08	3.94 ± 0.07	4.25 ± 0.07	-5.94 ± 0.20	-4.80 ± 0.20
34d_(MSK4)_@25	disseminated pyrite	-1.59 ± 0.08	3.57 ± 0.06	4.39 ± 0.06	-7.84 ± 0.20	-4.83 ± 0.20
34d_(MSK4)_@26	disseminated pyrite	-1.73 ± 0.08	3.36 ± 0.06	4.24 ± 0.06	-7.94 ± 0.23	-4.67 ± 0.23
34d_(MSK4)_@27	disseminated pyrite	7.97 ± 0.06	12.42 ± 0.07	8.34 ± 0.06	6.55 ± 0.20	-8.57 ± 0.20
34d_(MSK4)_@28	disseminated pyrite	3.62 ± 0.08	8.56 ± 0.07	6.71 ± 0.06	0.06 ± 0.26	-6.79 ± 0.26
34d_(MSK4)_@29	disseminated pyrite	6.87 ± 0.16	12.09 ± 0.12	8.57 ± 0.14	5.74 ± 0.31	-7.29 ± 0.32
34d_(MSK4)_@30	disseminated pyrite	-2.09 ± 0.10	2.98 ± 0.08	4.06 ± 0.08	-8.31 ± 0.24	-4.35 ± 0.24
34d_(MSK4)_@31	disseminated pyrite	-1.11 ± 0.07	3.79 ± 0.07	4.36 ± 0.06	-6.22 ± 0.21	-4.13 ± 0.21
34d_(MSK4)_@32	disseminated pyrite	-1.81 ± 0.08	3.22 ± 0.07	4.15 ± 0.07	-7.73 ± 0.20	-4.32 ± 0.20
34d_(MSK4)_@33	disseminated pyrite	-2.06 ± 0.07	3.08 ± 0.07	4.13 ± 0.06	-8.41 ± 0.22	-4.52 ± 0.22
34d_(MSK4)_@34	disseminated pyrite	-1.87 ± 0.07	3.20 ± 0.06	4.15 ± 0.06	-8.18 ± 0.22	-4.66 ± 0.22
34d_(MSK4)_@35	disseminated pyrite	1.18 ± 0.10	6.67 ± 0.11	6.07 ± 0.11	-3.84 ± 0.20	-6.07 ± 0.21
34d_(MSK4)_@36	disseminated pyrite	-2.49 ± 0.08	2.79 ± 0.07	4.07 ± 0.07	-9.27 ± 0.20	-4.57 ± 0.20
34d_(MSK4)_@37	disseminated pyrite	-1.81 ± 0.08	3.35 ± 0.07	4.28 ± 0.06	-7.93 ± 0.21	-4.51 ± 0.21
34d_(MSK4)_@38	disseminated pyrite	-1.72 ± 0.08	3.50 ± 0.07	4.38 ± 0.07	-8.22 ± 0.24	-4.96 ± 0.24
34d_(MSK4)_@39	disseminated pyrite	-1.11 ± 0.06	3.90 ± 0.06	4.47 ± 0.05	-7.34 ± 0.21	-5.24 ± 0.21
34d_(MSK4)_@40	disseminated pyrite	-2.98 ± 0.07	2.37 ± 0.06	3.90 ± 0.06	-10.34 ± 0.24	-4.72 ± 0.24
34d_(MSK4)_@41	disseminated pyrite	-2.28 ± 0.09	3.04 ± 0.07	4.21 ± 0.07	-9.18 ± 0.22	-4.87 ± 0.22
34d_(MSK4)_@42	disseminated pyrite	-2.09 ± 0.13	3.15 ± 0.09	4.23 ± 0.06	-8.52 ± 0.22	-4.61 ± 0.22
34d_(MSK4)_@43	disseminated pyrite	3.71 ± 0.14	8.95 ± 0.10	7.03 ± 0.08	-0.22 ± 0.23	-7.16 ± 0.24
34d_(MSK4)_@44	disseminated pyrite	-1.35 ± 0.13	3.64 ± 0.09	4.33 ± 0.06	-7.02 ± 0.21	-4.50 ± 0.21
34d_(MSK4)_@45	disseminated pyrite	5.01 ± 0.13	9.81 ± 0.09	7.22 ± 0.06	1.56 ± 0.23	-7.83 ± 0.24
34d_(MSK4)_@46	disseminated pyrite	-1.17 ± 0.14	3.77 ± 0.09	4.37 ± 0.07	-7.85 ± 0.24	-5.67 ± 0.24
34d_(MSK4)_@47	disseminated pyrite	4.24 ± 0.14	9.14 ± 0.10	6.96 ± 0.08	-0.12 ± 0.22	-8.05 ± 0.22
34d_(MSK4)_@48	disseminated pyrite	8.23 ± 0.14	13.10 ± 0.09	8.87 ± 0.07	6.23 ± 0.22	-9.21 ± 0.22
34d_(MSK4)_@49	disseminated pyrite	-2.36 ± 0.13	3.08 ± 0.09	4.30 ± 0.06	-9.24 ± 0.22	-4.83 ± 0.22
34d_(MSK4)_@50	disseminated pyrite	9.35 ± 0.13	14.29 ± 0.09	9.48 ± 0.07	8.06 ± 0.24	-9.49 ± 0.25
34d_(MSK4)_@51	disseminated pyrite	7.46 ± 0.13	12.11 ± 0.09	8.27 ± 0.06	5.22 ± 0.21	-8.78 ± 0.22
34d_(MSK4)_@52	disseminated pyrite	-0.33 ± 0.13	4.66 ± 0.09	4.83 ± 0.05	-6.47 ± 0.21	-5.85 ± 0.22
34d_(MSK4)_@53	disseminated pyrite	-1.35 ± 0.13	3.66 ± 0.09	4.36 ± 0.06	-7.35 ± 0.25	-4.83 ± 0.25
34d_(MSK4)_@54	disseminated pyrite	-1.92 ± 0.13	3.16 ± 0.09	4.15 ± 0.06	-8.78 ± 0.21	-5.19 ± 0.22
34d_(MSK4)_@55	disseminated pyrite	5.10 ± 0.13	9.91 ± 0.09	7.29 ± 0.06	1.81 ± 0.25	-7.75 ± 0.25
34d_(MSK4)_@56	disseminated pyrite	5.38 ± 0.13	10.17 ± 0.10	7.40 ± 0.07	2.38 ± 0.22	-7.71 ± 0.23
34d_(MSK4)_@57	disseminated pyrite	-1.49 ± 0.15	3.59 ± 0.10	4.36 ± 0.08	-8.39 ± 0.33	-5.61 ± 0.33
34d_(MSK4)_@58	disseminated pyrite	-2.39 ± 0.15	2.70 ± 0.10	3.93 ± 0.08	-9.34 ± 0.26	-4.89 ± 0.26
34d_(MSK4)_@59	disseminated pyrite	6.88 ± 0.13	11.71 ± 0.09	8.16 ± 0.07	3.98 ± 0.22	-8.93 ± 0.22
34d_(MSK4)_@60	disseminated pyrite	-1.28 ± 0.13	2.31 ± 0.09	2.97 ± 0.06	-6.28 ± 0.24	-3.89 ± 0.24
34d_(MSK4)_@61	disseminated pyrite	-0.83 ± 0.13	4.10 ± 0.09	4.52 ± 0.06	-7.01 ± 0.23	-5.46 ± 0.23
34a_(MSK4)_@1	angular pyrite	-3.29 ± 0.13	2.23 ± 0.10	3.93 ± 0.07	-10.60 ± 0.21	-4.46 ± 0.21
34a_(MSK4)_@02	angular pyrite	-3.55 ± 0.13	2.09 ± 0.10	3.93 ± 0.07	-11.41 ± 0.21	-4.77 ± 0.21
34a_(MSK4)_@03	angular pyrite	-3.78 ± 0.13	1.92 ± 0.09	3.87 ± 0.06	-12.22 ± 0.22	-5.16 ± 0.22
34a_(MSK4)_@04	angular pyrite	-3.86 ± 0.13	1.90 ± 0.09	3.89 ± 0.06	-11.71 ± 0.22	-4.51 ± 0.22
34a_(MSK4)_@05	angular pyrite	0.32 ± 0.13	5.08 ± 0.10	4.91 ± 0.07	-4.89 ± 0.22	-5.49 ± 0.22
34a_(MSK4)_@06	angular pyrite	6.79 ± 0.13	11.56 ± 0.09	8.06 ± 0.06	4.81 ± 0.23	-7.93 ± 0.24
34a_(MSK4)_@07	angular pyrite	6.60 ± 0.13	11.48 ± 0.09	8.09 ± 0.06	4.14 ± 0.23	-8.23 ± 0.24
34a_(MSK4)_@08	angular pyrite	7.76 ± 0.14	12.86 ± 0.10	8.87 ± 0.08	5.67 ± 0.24	-8.89 ± 0.24
34a_(MSK4)_@09	angular pyrite	6.87 ± 0.13	11.70 ± 0.09	8.17 ± 0.06	4.45 ± 0.22	-8.44 ± 0.22
34a_(MSK4)_@10	angular pyrite	7.47 ± 0.13	12.19 ± 0.09	8.34 ± 0.06	5.39 ± 0.26	-8.62 ± 0.27

34a_(MSK4)_@11	angular pyrite	-1.63 ± 0.13	4.05 ± 0.09	4.89 ± 0.06	-8.54 ± 0.22	-5.49 ± 0.22
34a_(MSK4)_@12	angular pyrite	6.19 ± 0.13	10.83 ± 0.09	7.64 ± 0.06	3.57 ± 0.21	-8.04 ± 0.22
34a_(MSK4)_@13	angular pyrite	0.94 ± 0.13	5.42 ± 0.09	4.94 ± 0.06	-3.93 ± 0.22	-5.69 ± 0.22
34a_(MSK4)_@14	angular pyrite	0.38 ± 0.17	5.57 ± 0.11	5.37 ± 0.10	-5.55 ± 0.28	-6.25 ± 0.28
34a_(MSK4)_@15	angular pyrite	1.46 ± 0.14	6.06 ± 0.10	5.31 ± 0.08	-3.20 ± 0.22	-5.94 ± 0.22
34a_(MSK4)_@16	angular pyrite	6.36 ± 0.13	11.02 ± 0.10	7.75 ± 0.08	4.33 ± 0.22	-7.60 ± 0.22
34a_(MSK4)_@17	angular pyrite	3.45 ± 0.13	8.22 ± 0.09	6.44 ± 0.06	-0.44 ± 0.22	-6.90 ± 0.22
34a_(MSK4)_@18	angular pyrite	0.40 ± 0.15	5.48 ± 0.11	5.27 ± 0.09	-4.96 ± 0.24	-5.71 ± 0.24
34a_(MSK4)_@19	angular pyrite	7.03 ± 0.13	11.65 ± 0.09	8.03 ± 0.07	4.55 ± 0.25	-8.63 ± 0.25
34a_(MSK4)_@20	angular pyrite	8.27 ± 0.13	13.27 ± 0.09	9.02 ± 0.06	6.57 ± 0.22	-8.95 ± 0.22
34a_(MSK4)_@21	angular pyrite	7.83 ± 0.13	12.20 ± 0.10	8.17 ± 0.07	6.82 ± 0.22	-7.88 ± 0.22
34a_(MSK4)_@22	angular pyrite	7.92 ± 0.13	12.55 ± 0.10	8.47 ± 0.07	5.86 ± 0.22	-9.01 ± 0.22
34a_(MSK4)_@23	angular pyrite	5.82 ± 0.13	10.36 ± 0.10	7.36 ± 0.07	2.91 ± 0.22	-8.01 ± 0.22
34a_(MSK4)_@24	angular pyrite	3.14 ± 0.13	8.06 ± 0.09	6.44 ± 0.06	-1.10 ± 0.22	-6.97 ± 0.22
34a_(MSK4)_@25	angular pyrite	9.64 ± 0.14	14.22 ± 0.10	9.26 ± 0.07	8.96 ± 0.27	-9.15 ± 0.27
34a_(MSK4)_@26	angular pyrite	7.10 ± 0.13	12.13 ± 0.09	8.48 ± 0.06	4.55 ± 0.22	-8.77 ± 0.22
34a_(MSK4)_@27	angular pyrite	8.09 ± 0.13	13.22 ± 0.09	9.06 ± 0.07	5.79 ± 0.22	-9.39 ± 0.22

Previously published Neoarchaean and other pre-GOE S-isotope data were compiled and used for statistical analysis in this study, presented in Figure 3. Data are from the references as compiled by Reinhard et al. (2013), with references listed below. However, all data from Williford et al. (2011), and all data from felsic ash from Philippot et al. (2012) were excluded from analysis. Data from Williford et al. (2011) were excluded due to difficulty in accessing corresponding $\delta^{34}S$ data, while the felsic ash data from Philippot et al. (2012) were excluded due to their atypical $\delta^{34}S$ - $\Delta^{33}S$ relationship, which defines a linear trend with negative slope termed the felsic volcanic array, deviating substantially from nearly all other S-isotope records.

The compiled data were separately analysed by three distinct lithological types; carbonates, shales, and deep-water sediments. Criteria for the three lithological subdivisions were as follows. 'Carbonate' lithologies were defined as those specified as carbonate, limestone, dolomite, marl or wackestone, including carbonate lithological variations e.g. stromatolitic limestone and oolitic dolomite, in addition to carbonate-bearing lithologies e.g. carbonaceous shale or calcareous sandstone. 'Shale' lithologies were defined as those specified as shale or argillite, including shale lithological variations e.g. pyritic shale or black shale, in addition to shale-bearing lithologies e.g. intercalacted shales and sandstones, and carbonaceous shales. 'Deep Water" lithologies were defined as those specified as banded iron formation, chert or barite, including lithological variations e.g. jaspilitic chert or siderite bearing iron formation.

References

Bao H, Rumble Iii D, Lowe DR (2007) The five stable isotope compositions of Fig Tree barites: Implications on sulfur cycle in ca. 3.2 Ga oceans. *Geochimica et Cosmochimica Acta,* 71, 4868-4879.

Bekker A, Holland H, Wang P-L, Rumble D, Stein H, Hannah J, Coetzee L, Beukes N (2004) Dating the rise of atmospheric oxygen. *Nature,* 427, 117-120.

Cates NL, Mojzsis SJ (2006) Chemical and isotopic evidence for widespread Eoarchean metasedimentary enclaves in southern West Greenland. *Geochimica et Cosmochimica Acta,* 70, 4229-4257.

Domagal-Goldman SD, Kasting JF, Johnston DT, Farquhar J (2008) Organic haze, glaciations and multiple sulfur isotopes in the Mid-Archean Era. *Earth and Planetary Science Letters,* 269, 29-40.

Farquhar J, Bao H, Thiemens M (2000) Atmospheric influence of Earth's earliest sulfur cycle. *Science,* 289, 756-758.

Farquhar J, Peters M, Johnston DT, Strauss H, Masterson A, Wiechert U, Kaufman AJ (2007) Isotopic evidence for Mesoarchaean anoxia and changing atmospheric sulphur chemistry. *Nature,* 449, 706-709.

Farquhar J, Wing B, Mckeegan K, Harris J, Cartigny P, Thiemens M (2002) Mass-independent sulfur of inclusions in diamond and sulfur recycling on early Earth. *Science,* 298, 2369-2372.

Guo Q, Strauss H, Kaufman AJ, Schröder S, Gutzmer J, Wing B, Baker MA, Bekker A, Jin Q, Kim S-T (2009) Reconstructing Earth's surface oxidation across the Archean-Proterozoic transition. *Geology,* 37, 399-402.

Guy B, Ono S, Gutzmer J, Kaufman A, Lin Y, Fogel M, Beukes N (2012) A multiple sulfur and organic carbon isotope record from non-conglomeratic sedimentary rocks of the Mesoarchean Witwatersrand Supergroup, South Africa. *Precambrian Research,* 216, 208-231.

Hou K, Li Y, Wan D (2007) Constraints on the Archean atmospheric oxygen and sulfur cycle from mass-independent sulfur records from Anshan-Benxi BIFs, Liaoning Province, China. *Science in China Series D: Earth Sciences,* 50, 1471-1478.

Hu G, Rumble D, Wang P-L (2003) An ultraviolet laser microprobe for the in situ analysis of multisulfur isotopes and its use in measuring Archean sulfur isotope mass-independent anomalies. *Geochimica et Cosmochimica Acta,* 67, 3101-3118.

Johnston DT, Farquhar J, Habicht KS, Canfield DE (2008a) Sulphur isotopes and the search for life: strategies for identifying sulphur metabolisms in the rock record and beyond. *Geobiology,* 6, 425-435.

Johnston DT, Farquhar J, Summons RE, Shen Y, Kaufman AJ, Masterson AL, Canfield DE (2008b) Sulfur isotope biogeochemistry of the Proterozoic McArthur Basin. *Geochimica et Cosmochimica Acta,* 72, 4278-4290.

Johnston DT, Poulton SW, Fralick PW, Wing BA, Canfield DE, Farquhar J (2006) Evolution of the oceanic sulfur cycle at the end of the Paleoproterozoic. *Geochimica et Cosmochimica Acta,* 70, 5723-5739.

Johnston DT, Wing BA, Farquhar J, Kaufman AJ, Strauss H, Lyons TW, Kah LC, Canfield DE (2005) Active microbial sulfur disproportionation in the Mesoproterozoic. *Science,* 310, 1477-1479.

Kamber B, Whitehouse M (2007) Micro‐scale sulphur isotope evidence for sulphur cycling in the late Archean shallow ocean. *Geobiology,* 5, 5-17.

Kaufman AJ, Johnston DT, Farquhar J, Masterson AL, Lyons TW, Bates S, Anbar AD, Arnold GL, Garvin J, Buick R (2007) Late Archean biospheric oxygenation and atmospheric evolution. *Science,* 317, 1900-1903.

Mojzsis S, Coath C, Greenwood J, Mckeegan K, Harrison T (2003) Mass-independent isotope effects in Archean (2.5 to 3.8 Ga) sedimentary sulfides determined by ion microprobe analysis. *Geochimica et Cosmochimica Acta,* 67, 1635-1658.

Ohmoto H, Watanabe Y, Ikemi H, Poulson SR, Taylor BE (2006) Sulphur isotope evidence for an oxic Archaean atmosphere. *Nature,* 442, 908-911.

Ono S, Beukes NJ, Rumble D (2009a) Origin of two distinct multiple-sulfur isotope compositions of pyrite in the 2.5 Ga Klein Naute Formation, Griqualand West Basin, South Africa. *Precambrian Research,* 169, 48-57.

Ono S, Beukes NJ, Rumble D, Fogel ML (2006a) Early evolution of atmospheric oxygen from multiple-sulfur and carbon isotope records of the 2.9 Ga Mozaan Group of the Pongola Supergroup, Southern Africa. *South African Journal of Geology,* 109, 97-108.

Ono S, Eigenbrode JL, Pavlov AA, Kharecha P, Rumble Iii D, Kasting JF, Freeman KH (2003) New insights into Archean sulfur cycle from mass-independent sulfur isotope records from the Hamersley Basin, Australia. *Earth and Planetary Science Letters,* 213, 15-30.

Ono S, Kaufman AJ, Farquhar J, Sumner DY, Beukes NJ (2009b) Lithofacies control on multiple-sulfur isotope records and Neoarchean sulfur cycles. *Precambrian Research,* 169, 58-67.

Ono S, Shanks Iii WC, Rouxel OJ, Rumble D (2007) S-33 constraints on the seawater sulfate contribution in modern seafloor hydrothermal vent sulfides. *Geochimica et Cosmochimica Acta,* 71, 1170-1182.

Ono S, Wing B, Johnston D, Farquhar J, Rumble D (2006b) Mass-dependent fractionation of quadruple stable sulfur isotope system as a new tracer of sulfur biogeochemical cycles. *Geochimica et Cosmochimica Acta,* 70, 2238-2252.

Papineau D, Mojzsis S, Coath C, Karhu J, Mckeegan K (2005) Multiple sulfur isotopes of sulfides from sediments in the aftermath of Paleoproterozoic glaciations. *Geochimica et Cosmochimica Acta,* 69, 5033-5060.

Papineau D, Mojzsis SJ, Schmitt AK (2007) Multiple sulfur isotopes from Paleoproterozoic Huronian interglacial sediments and the rise of atmospheric oxygen. *Earth and Planetary Science Letters,* 255, 188-212.

Partridge MA, Golding SD, Baublys KA, Young E (2008) Pyrite paragenesis and multiple sulfur isotope distribution in late Archean and early Paleoproterozoic Hamersley Basin sediments. *Earth and Planetary Science Letters,* 272, 41-49.

Philippot P, Van Zuilen M, Lepot K, Thomazo C, Farquhar J, Van Kranendonk MJ (2007) Early Archaean microorganisms preferred elemental sulfur, not sulfate. *Science,* 317, 1534-1537.

Philippot P, Van Zuilen M, Rollion-Bard C (2012) Variations in atmospheric sulphur chemistry on early Earth linked to volcanic activity. *Nature Geoscience,* 5, 668-674.

Reinhard CT, Planavsky NJ, Lyons TW (2013) Long-term sedimentary recycling of rare sulphur isotope anomalies. *Nature,* 497, 100-103.

Shen Y, Farquhar J, Masterson A, Kaufman AJ, Buick R (2009) Evaluating the role of microbial sulfate reduction in the early Archean using quadruple isotope systematics. *Earth and Planetary Science Letters,* 279, 383-391.

Thomazo C, Ader M, Farquhar J, Philippot P (2009) Methanotrophs regulated atmospheric sulfur isotope anomalies during the Mesoarchean (Tumbiana Formation, Western Australia). *Earth and Planetary Science Letters,* 279, 65-75.

Ueno Y, Ono S, Rumble D, Maruyama S (2008) Quadruple sulfur isotope analysis of ca. 3.5 Ga Dresser Formation: New evidence for microbial sulfate reduction in the early Archean. *Geochimica et Cosmochimica Acta,* 72, 5675-5691.

Whitehouse MJ (2013) Multiple Sulfur Isotope Determination by SIMS: Evaluation of Reference Sulfides for Δ33S with Observations and a Case Study on the Determination of Δ36S. *Geostandards and Geoanalytical Research,* 37, 19-33.

Williford KH, Van Kranendonk MJ, Ushikubo T, Kozdon R, Valley JW (2011) Constraining atmospheric oxygen and seawater sulfate concentrations during Paleoproterozoic glaciation: In situ sulfur three-isotope microanalysis of pyrite from the Turee Creek Group, Western Australia. *Geochimica et Cosmochimica Acta,* 75, 5686-5705.

Wu J, Boyle EA (1997) Lead in the western North Atlantic Ocean: Completed response to leaded gasoline phaseout. *Geochimica et Cosmochimica Acta,* 61, 3279-3283.

Zerkle AL, Claire MW, Domagal-Goldman SD, Farquhar J, Poulton SW (2012) A bistable organic-rich atmosphere on the Neoarchaean Earth. *Nature Geoscience,* 5, 359-363.

Chapter 5: 2D Chemical Visualisations of Neoproterozoic Little Dal Group Polymud Fabrics and Spongiform Structures.

Submitted to Precambrian Research
Co-authors: Balz Kamber, Elizabeth Turner and Fritz Neuweiler

1. Introduction

The beginning of the Cambrian period, ca. 541 Ma (Bowring et al., 2007), is defined by the first appearance of the trace fossil *Treptichnus pedum* (Landing, 1994), representing the emergence of bilaterian animals in the rock record. The timing of the appearance of metazoans has troubled evolutionary biologists at least since Darwin. He regarded the lack of an animal fossil record predating the rise of organisms with hard-mineralised skeletons as a very problematic issue facing his theory of evolution. In his words: "There is another and allied difficulty, which is much graver. I allude to the manner in which numbers of species in the same group suddenly appear in the lowest known fossiliferous rocks" (Darwin, 1859, p. 306). There has since been a long history of attempts to rationalise the rapid radiation of animals marking the Cambrian explosion. The earlier Ediacaran biota (575-542 Ma) reflect the appearance of large, architecturally complex, soft-bodied organisms (Billings, 1872; Glaessner, 1959). However, their widespread appearance was apparently just as abrupt as that of the bilaterian animals in the Cambrian (Erwin et al., 2011), and the relatively sudden emergence of these advanced organisms in the geological record was very likely predated by an as yet enigmatic evolutionary event marking the origin of metazoans.

Because Porifera are basal in the Metazoan group (Halanych, 2004; Srivastava et al., 2010; Wörheide et al., 2012; dos Reis et al., 2015) the existence of sponges, morphologically, developmentally, and genetically simpler than bilaterians, has been widely anticipated in the Precambrian rock record. Ediacaran rocks of the c.a. 600 Ma Doushanto Fm. in central Guizhou, South China contain some of the oldest evidence of

metazoans in the form of conventional sponge body fossils, sponge spicules, and metazoan embryos (Li et al., 1998; Xiao et al., 1998; Du & Wang, 2012; Yin et al., 2015). However, since sponges likely had a very low preservation potential, and because neither sponge spicules nor any other form of biomineralisation are an essential character of the sponge or metazoan taxon (Ax, 1996), the Doushanto Fm. evidence provides only a minimum age for the appearance of metazoans. The crown metazoa is predicted by phylogenomic studies and molecular clock estimates to have originated between 650 – 833 Ma, deep within the Cryogenian (Dunn et al., 2008; Peterson et al., 2008; Sperling et al., 2010; Erwin et al., 2011; dos Reis et al., 2015), placing the major split in animal evolution much earlier than apparently preserved in the fossil record. However, despite this phylogenomic and molecular clock evidence for a Cryogenian sponge ancestor, there is a lack of substantial palaeontological data directly supporting this prediction. This dilemma has given rise to a major debate about the length of the implied interval of hidden evolution in the Neoproterozoic. Rather than envisaging an explosive radiation of metazoans close to the base of the Cambrian (e.g. Budd, 2008; Lee et al., 2013), recent studies proposed that there was an extensive Precambrian metazoan history extending deep into the Cryogenian, with the absence of a fossil record merely reflecting preservation, collection, and/or interpretation biases (e.g. Erwin et al., 2011; dos Reis et al., 2015).

Over the last ten years, a number of tantalising paleontological reports of sponge grade metazoan fossils from Cryogenian rocks have surfaced. Brief summaries of these reports are listed in Table 1. Regardless, Cryogenian sponge fossils are rare, poorly substantiated and controversial, and the validity of the various reports has been widely questioned. Geochemical evidence for late Cryogenian demosponge biomarkers (Love et al., 2009) is in doubt regarding reflecting the original biology and whether the used molecular character is exclusive to sponges (e.g. Antcliffe, 2013), with a subsequent study suggesting that they may in fact be of poribacterial origin (Siegl et al., 2011). Morphological evidence for Cryogenian sponge fossils (e.g. Maloof et al., 2010b) are disputed because the fossils lack morphology that is diagnostic of sponges, and alternate hypotheses such as a bacterial origin or sediment reworking have not been fully ruled out (Antcliffe et al., 2014). Because sponges do not display tissue grade anatomical characters or organs beyond a general gross, sponge-like structure, fossils displaying identifiable sponge characteristics require

Age	Location	Authors	Methods	Evidence Type
Age of the Little Dal Group is bracketed between ca. 817±0.9 Ma (Ar-Ar detrital muscovite; Powell & Schneider, 2013) and 723±4 Ma (U-Pb on cross-cutting igneous rocks; Heaman et al., 1992 ; Jefferson & Parrish, 1989).	Middle Neoproterozoic, Little Dal Group, Mackenzie Mountains Supergroup, Northwest Territories, Canada.	(Neuweiler et al., 2009)	Scanning Electron Microscopy (SEM) analysis of a modern Bahamian sponge (*Spheciospongia Vesparium*) (Neuweiler et al., 2007) detailed the exclusive selectivity for degrading collagen as the substrate for mineral precipitation in sponge soft tissue calcification. Fluorescent dissolved organic matter extraction and Excitation-emission matrix spectroscopy of the Bahamian sponge demonstrated that polymud textures develop in modern sediment through calcification of the degrading extracellular collagenous matrix (ECM) of a siliceous sponge. Similarities of the fluorescence spectra indicate that such a calcification mechanism is recorded in a Cretaceous calcified siliceous sponge, linking modern calcifying sponges to Phanerozoic polymuds. Thin Section Petrography of the Little Dal polymuds linked these microstructures to Phanerozoic polymuds (Cretaceous sponge from Spain and Silurian sponge from Canada), possibly indicating the local presence of a Metazoan-grade organism in the middle Neoproterozoic. Little Dal polymuds were interpreted as vestiges of degraditive ECM calcification in mm to cm scale sponges, but SEM did not reveal detectable structure.	Morphological evidence as discovered by optical petrography.
Ca. 760 Ma (radiometric age date for an ash bed below the Fm. Halverson et al., 2005)	Otavi Group, Northern Namibia.	(Brain et al., 2012)	SEM, Electron probe imaging, Cathode Luminescence, and X-ray microtomography: Calcareous sponges occurring as ovoid to irregularly elongate globular forms, ranging in size from 0.3 mm to 5 mm in the longest dimension, exhibited features interpreted as the ostia, oscula and paragastric chamber of an ancient calcareous sponge.	Morphological evidence as discovered by sub-microscopic methods.
635 Ma (age for the end of the Marinoan glaciation from correlation to Namibia and China Condon et al., 2005 ; Hoffmann et al., 2004) to 659.7±5.3 Ma (SHRIMP U-Pb zircon age for the underlying Wilyerpa Fm. Fanning & Link, 2006)	Trezona Fm., Upalinna Subgroup, Umbertana Group, South Australia.	(Maloof et al., 2010)	3D fossil reconstruction involving serial grinding and scanning at 50.8 µm intervals produced 3D models of a sponge fossil that is cm in scale, ellipsoidal, and contains an interconnected network of 1 mm diameter interior canals.	Morphological evidence as discovered by serial sectioning and petrography.

658 Ma (U-Pb zircon age from a tuff in the uppermost Sturtian diamictites Fanning & Link, 2006) to 635 Ma (age of the Marinoan glaciation by correlation of the Elatina Fm. with the Ghaub Fm. in Namibia Hoffmann et al., 2004)	Oodnaminta Reef, Umberatana Group, Heysen Supergroup, Northern Flinders Range, South Australia.	(Wallace & Woon, 2008)	Thin Section Petrography revealed a distinctive fossilised calcified organism that has rounded or vesicular chambers that encrust one another, and a regular arrangement of primary and secondary chambers morphologically reminiscent of some Phanerozoic chambered sphinctozoan sponges. Interconnected network of 1mm diameter canals entering and exiting the fossil through circular apertures.	Morphological evidence as discovered by petrography.
>635 Ma (U-Pb zircon age measurements of Huqf detrital zircons and ash beds Bowring et al., 2007)	Huqf Supergroup South Oman Salt Basin	(Love et al., 2009)	Gas chromatography, mass spectrometry, and multi-reaction-monitoring mass spectrometry. An abundance of C_{30} steranes with a 24-isopropyl moiety – lipid biomarkers suggestive of demospongiae.	Geochemical biomarker evidence.

preservation of recognisable cell types and unfortunately none of the currently proposed Cryogenian fossils display any evidence of particular cell types (Yin et al., 2015). Tracing the evolution of metazoans in Neoproterozoic sedimentary rocks well before the advent of animal skeletons therefore relies on ethological traces, casts, changing biomarker patterns and the recognition of vestiges of soft tissue (Neuweiler et al., 2009).

Neuweiler et al. (2009) linked polymud fabrics in Neoproterozoic Little Dal Group carbonates with a modern sponge, *Spheciospongia Vesparium* (Lamarck, 1815), from northwest of Andros Island, Great Bahama Bank (Neuweiler et al., 2007), Phanerozoic sponge material from the Cretaceous of Spain (Neuweiler et al., 2003) and the Silurian of Anticosti Island, Canada (Desrochers et al., 2007). Polymud fabrics are characterised by authigenic Ca-carbonate and irregular secondary voids containing internal sediment (Lees et al., 1985; Lees & Miller, 2009), and are shown to develop through the calcification of degrading extracellular collagenous matrix (ECM) of siliceous sponges as they decay in sediment at the ocean floor, producing a complex texture of calcareous material and voids (Neuweiler et al., 2009). As ECM is a fundamental character of the metazoan clade (Ax, 1996), Neuweiler et al. (2009) proposed the presence of a texture associated with ECM in the rocks of the Cryogenian Little Dal Group, implying the existence of metazoan grade organisms at that time. However, this study was met with criticism, largely over doubts over the exclusive sponge nature of polymud fabrics, with some authors instead proposing a possible microbial origin (e.g. Planavsky, 2009). To date, polymud fabrics have only been identified through field observations, descriptions of polished slabs, and thin section petrography (Lees & Miller, 1985; Lees & Miller, 2009), and there has not yet been a successful combination of morphological and geochemical evidence for a Cryogenian sponge fossil. Recently, in situ sub-micron scale analytical techniques invalidated the veracity of spicule like microstructures from the Ediacaran Doushantuo Formation (Muscente et al., 2015), suggesting in situ geochemical analytical techniques are one way forward in substantiating rare, controversial Precambrian sponge fossils.

Here, we revisit Little Dal Group samples analysed by Neuweiler et al. (2009). The aim of this study was to visualise the polymud fabrics as well as previously unreported spongiform structures by major and trace element mapping, in the

expectation that visualisations will provide the next step in understandiing these structures. In addition, we report 2D chemical visualisations of a Silurian and a Cretaceous sponge, and compare and contrast these results with those of the Little Dal Group samples.

2. Materials

The lower Cretaceous material is from an upper Albian mudmound near Iraneta, Navarra Province, Northern Spain (Neuweiler et al., 2003). The sample, containing calcified siliceous sponges (Neuweiler et al., 2009), was obtained from an interval of massive limestone within a sequence of argillaceous limestones and silty marls (Neuweiler et al., 2000).

The lower Silurian material is from the sponge-constructed stromatactis mud mounds of the Gaspé peninsula, Québec, Canada (Bourque & Gignac, 1983). The sample contains calcified sponge tissue (sponge automicrite) carrying autochthonous sponge spicules and incorporated bioclasts (Neuweiler et al., 2007) from a calcified hexactinellid sponge *malumispongium hartnageli* (Rigby, 1967). It displays a mummification style of sponge body preservation via the calcification of degrading connective tissue (Neuweiler et al., 2007).

The Precambrian material is from the Neoproterozoic Little Dal Group, exposed in the Mackenzie Mountains, Northwest Territories, Canada. The group represents a succession of shallow-water carbonate, siliciclastic and evaporite rocks (Aitken, 1981). Material used in this study is from calcimicrobial reefs of the Stone Knife Formation ("Little Dal reefs"). Hectometres thick and kilometres in diameter, the reefs are enclosed by deep-water limestone and shale that accumulated in an epicratonic basin at low latitude (Turner et al., 1997; 2000). The reef framework consists of mm- to dm-scale filamentous-calcimicrobial stromatolites that vary in external morphology depending on the stage of reef growth and position on the reef edifice (Turner et al., 2000). The Little Dal Group occurs stratigraphically more than 2.5 km below the Sturtian, which in the study area is represented by diamictite and banded iron formation dated at 701 ± 5 Ma (Fanning & Link, 2008). The age of the Little Dal Group is bracketed between ca. 817.8 ± 0.9 Ma (youngest Ar-Ar dated detrital muscovite; Powell & Schneider, 2013) and 723 ± 4 Ma (U-Pb on cross-cutting

igneous rocks; Jefferson & Parrish, 1989; Heaman et al., 1992), but the absolute age is presently ill-constrained.

3. Methods

Trace element mapping was performed with laser ablation inductively coupled mass spectrometry (LA-ICP-MS). It was carried out at the Geochemistry Laboratories of Trinity College Dublin, using the method described in Ubide et al. (2015). A Photon Machines Excite 193 nm excimer Ar F laser system with a Helex 2-volume ablation cell and He–Ar carrier gas (ca. 0.8 l/min He and ca. 0.7 l/min Ar) was used, in conjunction with a Thermo iCapQs quadrupole ICP-MS.

The ablation area (i.e. the mapped area) was defined with the Chromium 2.1 software (Photon Machines Inc.) as illustrated in Ubide et al. (2015). We used a square-shaped laser aperture, which generated an evenly ablated line from overlapping squares, and adjacent lines were ablated in a successive manner allowing for a small overlap of <1 μm to avoid un-ablated gaps to produce the full map. Prior to analysis, samples were carefully cleaned with semiconductor grade solvent, and the ablation area was pre-ablated using the laser parameters outlined in table 2. Ablation areas had variable sizes, with side lengths ranging from 400 μm to 6 mm depending on the size of the target. Full details of laser parameters and analyte dwell times are summarised in table 2. Although the system has a fast washout (90% signal reduction in less than 1.5 s), 30 s were allowed for washout between lines to avoid any carry-over from standards to samples and vice versa (Ubide et al., 2015). NIST610 glass reference material (Jochum et al., 2011) was used as the calibration standard, along with additional accuracy standards BHVO-2G (Gao et al., 2002) and NIST612 (Jochum et al., 2011). Standards were always ablated with the same parameters as the samples. Two NIST610, BHVO-2G and NIST612 lines were analysed at the beginning and end of each experiment, and two NIST610 lines along with 1 BHVO-2G line and 1 NIST612 line, systematically every 2 to 20 sample lines, depending on the length/scan speed of the individual sample lines.

The data acquisition on the mass spectrometer was performed with the Qtegra 2.2 software (Thermo Fisher Scientific Inc.) in time-resolved analysis mode as one single continuous experiment. The cumulative dwell times for all analytes were kept short, between 0.1 and 0.12 seconds, so as not to compromise spatial resolution of

Figure	Experiment ID	Apparent Fluence	Repetition Rate	Spot Size	Scan Speed	Analytes and Selected Dwell Times (seconds)
Figure 15 + 16	12NOV_SG5_raster1b 12NOV_SG5_raster2	4.75 J/cm^2	5 Hz	24 µm square	36 µm/s	^{25}Mg (0.005), ^{43}Ca (0.005), ^{51}V (0.02), ^{57}Fe (0.005), ^{63}Cu (0.01), ^{66}Zn (0.01), ^{89}Y (0.01), ^{90}Zr (0.01), ^{118}Sn (0.01), ^{140}Ce (0.01).
Figure 17	R3_SG5_13NOV	5.5 J/cm^2	10 Hz	24 µm square	12 µm/s	^{25}Mg (0.005), ^{43}Ca (0.005), ^{51}V (0.02), ^{57}Fe (0.005), ^{63}Cu (0.01), ^{66}Zn (0.01), ^{89}Y (0.01), ^{90}Zr (0.01), ^{118}Sn (0.01), ^{140}Ce (0.01).
Figure 3, 10, +15	R1b_SG5_13NOV R1_07-KEC-21Ai_13NOV R1_07-KEC-20i_13NOV15	5.5 J/cm^2	10 Hz	24 µm square	36 µm/s	^{25}Mg (0.005), ^{43}Ca (0.005), ^{51}V (0.02), ^{57}Fe (0.005), ^{63}Cu (0.01), ^{66}Zn (0.01), ^{89}Y (0.01), ^{90}Zr (0.01), ^{118}Sn (0.01), ^{140}Ce (0.01).
Figure 11	R2_07-KEC-20i_16NOV15 (Actually 21Ai)	6.5 J/cm^2	10 Hz	12 µm square	8 µm/s	^{27}Al (0.01), ^{43}Ca (0.01), ^{51}V (0.03), ^{57}Fe (0.01), ^{89}Y (0.03), ^{90}Zr (0.01), ^{118}Sn (0.01), ^{140}Ce (0.01).
Figure 8	R1_07-KEC-22A_16NOV15	5.5 J/cm^2	10 Hz	24 µm square	36 µm/s	^{43}Ca (0.01), ^{51}V (0.02), ^{55}Mn (0.01), ^{140}Ce (0.01), ^{89}Y (0.02), ^{27}Al (0.005), ^{95}Mo (0.02), ^{238}U (0.02), ^{32}S (0.005).
Figure 5	R2b_07-KEC-20i_16NOV15	5.5 J/cm^2	10 Hz	24 µm square	36 µm/s	^{43}Ca (0.01), ^{51}V (0.02), ^{55}Mn (0.01), ^{140}Ce (0.01), ^{89}Y (0.02), ^{27}Al (0.01), ^{95}Mo (0.02), ^{238}U (0.02).
Figure 4 + 7	R1_07-KEC-395i_18NOV15 R3_07-KEC-20i_18NOV15	5.5 J/cm^2	10 Hz	24 µm square	36 µm/s	^{43}Ca (0.01), ^{51}V (0.02), ^{55}Mn (0.01), ^{140}Ce (0.01), ^{89}Y (0.02), ^{27}Al (0.01), ^{95}Mo (0.02), ^{238}U (0.02).
Figure 6, 12,13 + 14	R1b_CIB_19NOV15 R2_CIB_19NOV15 R3_CIB_19NOV15 R2_07-KEC-395i_19NOV15	5.5 J/cm^2	10 Hz	24 µm square	36 µm/s	^{43}Ca (0.01), ^{51}V (0.02), ^{55}Mn (0.01), ^{140}Ce (0.01), ^{89}Y (0.02), ^{27}Al (0.01), ^{95}Mo (0.02), ^{238}U (0.02).

Figure 2	REE_Lines2_18NOV15	5.5 J/cm^2	10 Hz	180 µm circle	20 µm/s	^{24}Mg (0.01), ^{27}Al (0.005), ^{43}Ca (0.01), ^{51}V (0.02), ^{55}Mn (0.01), ^{86}Sr (0.005), ^{89}Y (0.02), ^{139}La (0.01), ^{140}Ce (0.01), ^{141}Pr (0.01), ^{146}Nd (0.01), ^{147}Sm (0.01), ^{153}Eu (0.01), ^{157}Gd (0.01), ^{159}Tb (0.01), ^{163}Dy (0.01), ^{165}Ho (0.01), ^{166}Er (0.01), ^{169}Tm (0.01), ^{172}Yb (0.01), ^{175}Lu (0.01), ^{232}Th (0.01), ^{238}U (0.02).
Figure 2	REE2_06Jan16* REE3_06Jan16*	2.5 J/cm^2	10 Hz	150 µm circle	20 µm/s	^{24}Mg (0.01), ^{27}Al (0.005), ^{43}Ca (0.01), ^{51}V (0.02), ^{55}Mn (0.01), ^{86}Sr (0.005), ^{89}Y (0.02), ^{139}La (0.01), ^{140}Ce (0.01), ^{141}Pr (0.01), ^{146}Nd (0.01), ^{147}Sm (0.01), ^{153}Eu (0.01), ^{157}Gd (0.01), ^{159}Tb (0.01), ^{163}Dy (0.01), ^{165}Ho (0.01), ^{166}Er (0.01), ^{169}Tm (0.01), ^{172}Yb (0.01), ^{175}Lu (0.01), ^{232}Th (0.01), ^{238}U (0.02).
Figure 9	R2_07-KEC-22A_06Jan16*	2.5 J/cm^2	10 Hz	35 µm square	50 µm/s	^{27}Al (0.01), ^{43}Ca (0.01), ^{51}V (0.02), ^{55}Mn (0.01), ^{57}Fe (0.01), ^{66}Zn (0.01), ^{87}Sr (0.015), ^{88}Sr (0.01), ^{89}Y (0.02), ^{90}Zr (0.01), ^{140}Ce (0.01), ^{238}U (0.02).
Figure 18	R1_SG1_06Jan16*	2.5 J/cm^2	10 Hz	85 µm circle	40 µm/s	^{27}Al (0.01), ^{43}Ca (0.01), ^{51}V (0.02), ^{55}Mn (0.01), ^{57}Fe (0.01), ^{66}Zn (0.01), ^{87}Sr (0.015), ^{88}Sr (0.01), ^{89}Y (0.02), ^{90}Zr (0.01), ^{140}Ce (0.01), ^{238}U (0.02).

*Analysed after laser cavity refurbishment.

the resulting map. Individual isotope dwell times were chosen according to their general abundance and their concentration in the analysed material, which was checked with a preliminary evaluation of the signal recorded before experimental setup. Limits of detection (calculated following Longerich et al., 1996) in most cases were below 5 ppm, and typically below 1 ppm. Data reduction and production of trace element distribution maps was undertaken with the software Iolite v2.5 (http://www.iolite.org.au; Hellstrom et al., 2008; Woodhead et al., 2008; Paton et al., 2011). The laser log file was used to synchronise the ICP-MS data and record the x–y information. After importing the combined data into Iolite, baseline 'integrations' were defined and subtracted from reference material and sample integrations using the most appropriate spline type. Once integrations and spline types were defined, the data were reduced with the 'Trace_Elements Data Reduction Scheme' supplied with Iolite. Data reduction was carried out using semi-quantitative mode, following which trace element distribution maps were built with the module 'CellSpace' (Paul et al., 2012). In addition, REE+Y data were obtained for typical carbonate facies to establish a marine origin and the absence of diagenetic alteration (see Kamber et al., 2014 for methods and a review).

Prior to LA-ICP-MS analysis the samples were studied by Scanning Electron Microscopy (SEM), using the facilities at the Centre for Microscopy and Analysis, Trinity College Dublin. The thin sections were coated with carbon and SEM images were taken on a Tescan MIRA XMU FE-SEM (field emission scanning electron microscope) operating under high vacuum conditions. Secondary Electron images (SE images) were taken at 5 kV accelerating voltage to show surface morphology. Backscattered electron images (BSE images) were taken at 15 kV to yield compositional information. Major element spot chemistry was determined by EDS (Oxford Instruments XMax 150 mm^2).

4. Results

As outlined in the introduction, the principle aim of this study was to test whether the petrographically visible polymud fabrics (Neuweiler et al., 2009) and previously unreported spongiform structures in the Little Dal Group are observable in the carbonate chemistry. The results reported here are semiquantative, 2D visualisations of relative abundances of a selection of vital metals within these

structures (Figures 3 – 17). In addition, both a Cretaceous and Silurian sponge sample were also mapped (Figures 11 – 17), and their chemistry was compared with that of the Little Dal Group spongiform structures. Prior to LA-ICP-MS mapping the various sample's surface topography and composition were analysed with a SEM analysis (Figure 1), and a marine origin with an open ocean signal was established for all the analysed samples via their shale normalised REE+Y patterns (Figure 2). All samples display the familiar features of marine carbonate (see Kamber et al., 2014 for a full review of REE+Y systematics).

4.1. Little Dal Group Samples

4.1.1. Little Dal Group Polymuds

Figures 3 to 5 are a set of 2D chemical maps of a number of Little Dal Grouppolymud fabrics, similar to those reported in Neuweiler et al. (2009). Four LA-ICP-MS maps were produced of three distinct areas of polymud, and in each case the polymud sample's surface topography was inspected by SEM. Importantly back scattered electron imaging revealed a complete absence of any apparent difference in composition related to the polymud (Figure 1a). However, the much more sensitive LA-ICP-MS mapping revealed several associations of vital trace and major elements within the various void filling internal sediments of the polymud fabrics.

Initially both Ca and Mg were analysed (Figure 3b). Calcium shows no variation. This confirmed that all materials are calcite with no significant variation in Ca content. However, the Mg maps show variability of several thousand ppm, the distribution of which does not correspond to the petrographically identified features (Figure 3a). This was ascertained for all the other Little Dal Group samples, and thereafter Mg was no longer analysed (Figures 4 - 10). By contrast, both Fe and Mn reveal structures that are not evident in the Ca or Mg distributions (Figure 3c). The structure of the Fe distribution in particular is clearly not random, and indeed far more complex and well defined than the structure that is evident petrographically in the polymud fabric. Other elements that show comparable distributions to Fe and Mn, albeit to a lesser extent, are Ce and Zn (Figure 3c). We note that these elements have similar redox potentials. Conversely, Zr, V, and Y all appear to be enriched in areas of low Fe concentrations (Figure 3d), and so a reasonably coherent picture emerges of two distinct groups of elements, each group showing distributions inverse

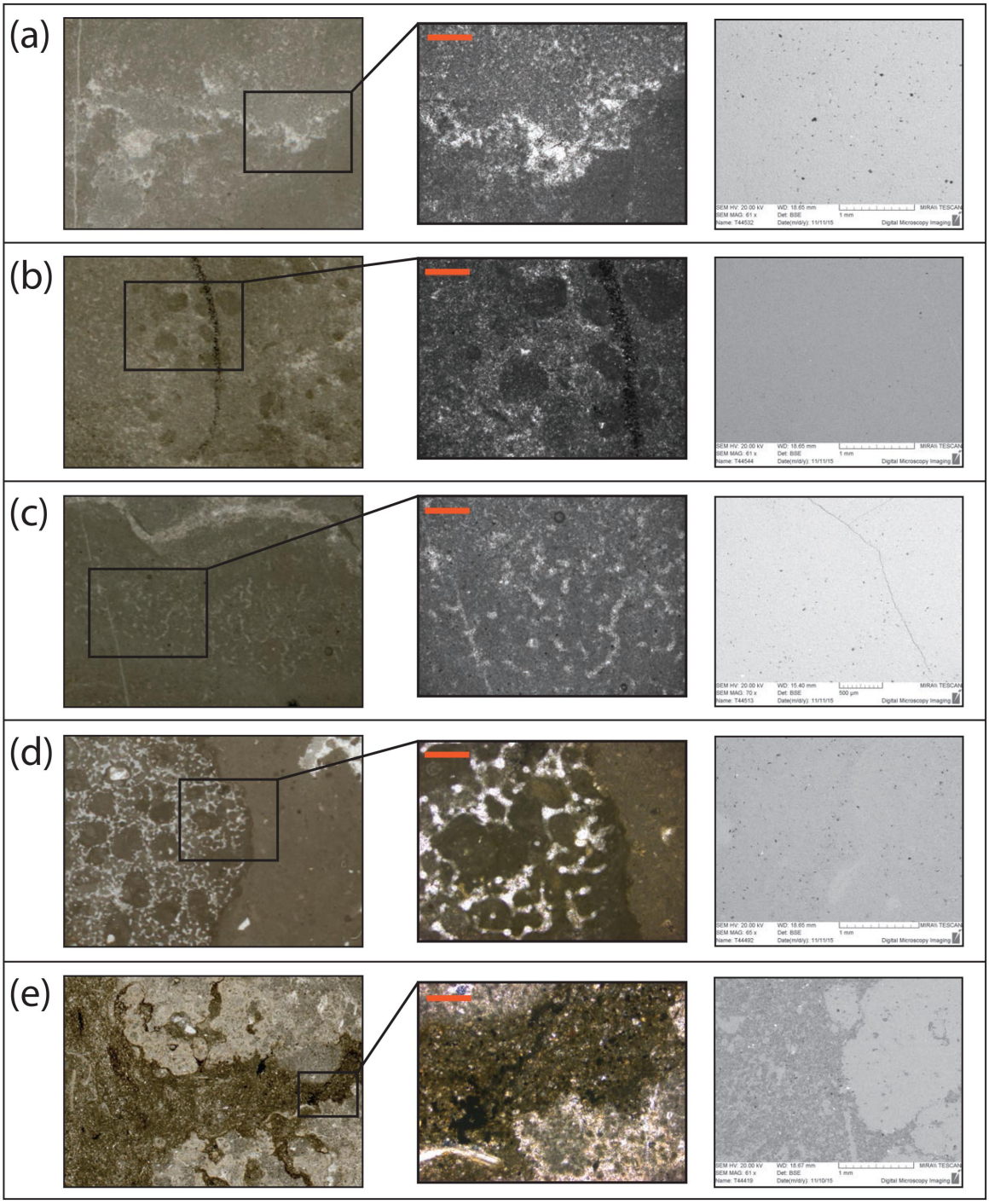


Figure 1: Scanned images, petrographic transmitted light images and SEM back scattered electron images of the Little Dal Group samples (Panels a-c), the cretaceous sponge sample (Pannel d), and the Silurian sponge sample (Pannel e). In each case a high resolution thin section scan of the sample is given for greater petrographic context. Also shown is a petrographic transmitted light image showing greater detail, with a scale bar representing 200 µm, along with a SEM BSE image of that area. Pannel (a) depicts the Little Dal Group polymud analysed in Figure 3 and Figure 4. Pannel b depicts the Little Dal Group spongiform structure analysed in Figure 6. Pannel (c) depicts the Little Dal Group spongiform microstructure analysed in Figures 9-10. Pannel (d) depicts the Cretaceous sponge sample that is analysed in Figure 11, and Pannel (e) depicts the Silurian sponge sample that is analysed in Figure 14

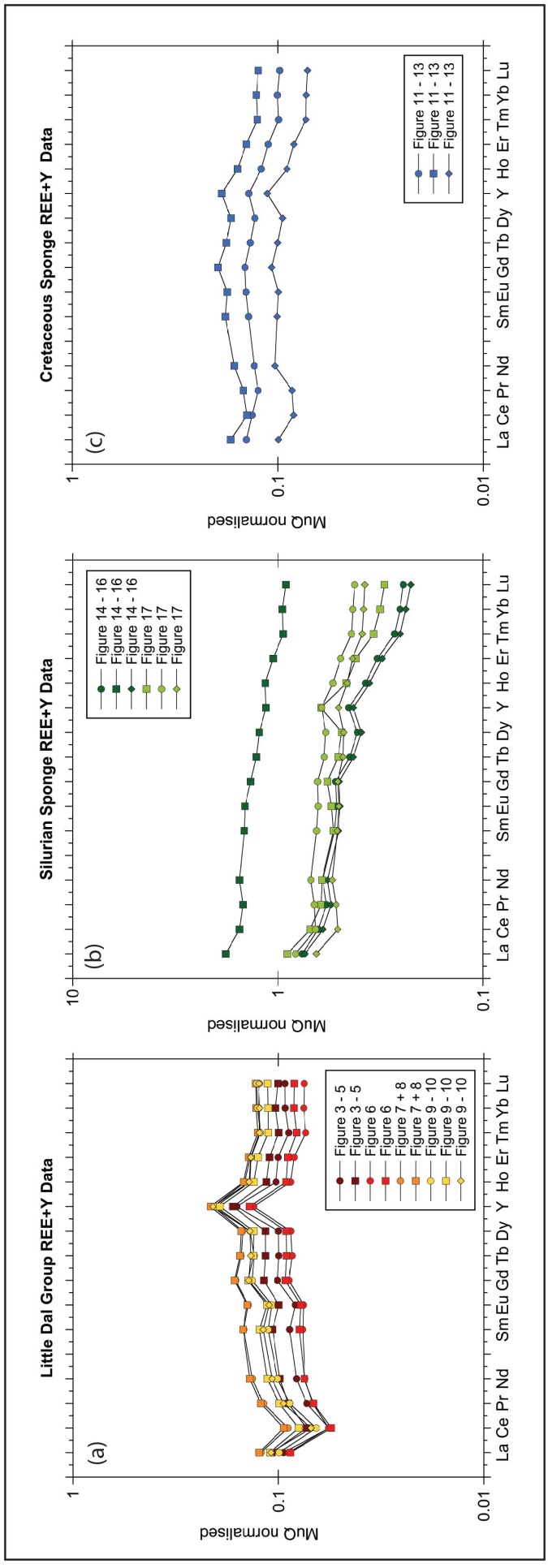


Figure 2: REE+Y data for the Little Dal Group (Panel a), the cretaceous sponge sample (Pannel b), and the silurian sponge sample (Pannel c).

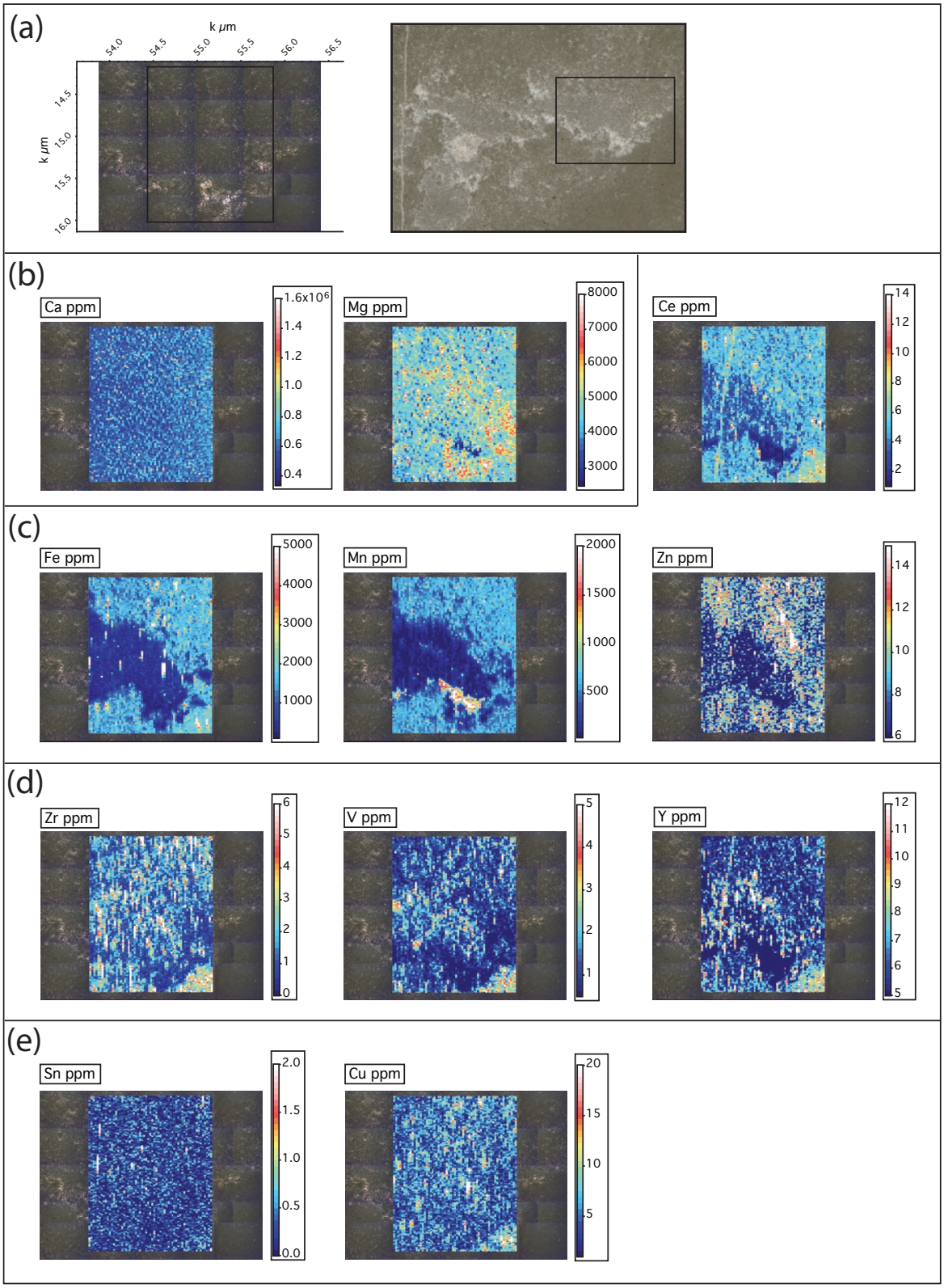


Figure 3: 2D chemical visualisations of a Little Dal Group polymud fabric. Panel (a) shows the base map for the subsequent 2D chemical maps (b-e) along with a high-resolution thin section scan for context. The base map is composed of a mosaic of transmitted light petrographic images, its axes are given in k µm (or µm) for scale, and the mapped area is outlined by a black rectangle for context. A larger portion of a high-resolution thin section scan, with the base map area outlined in order to give greater petrographic context is also shown in panel (a). Panel (a) in Figures 4-17 follow a similar format to that which is described here. Panels (b-e) show 2D chemical maps with the analysed element indicated on the top left of each map, and scale bar indicating semiquantitative concentration levels in ppm on the right hand side of each map.

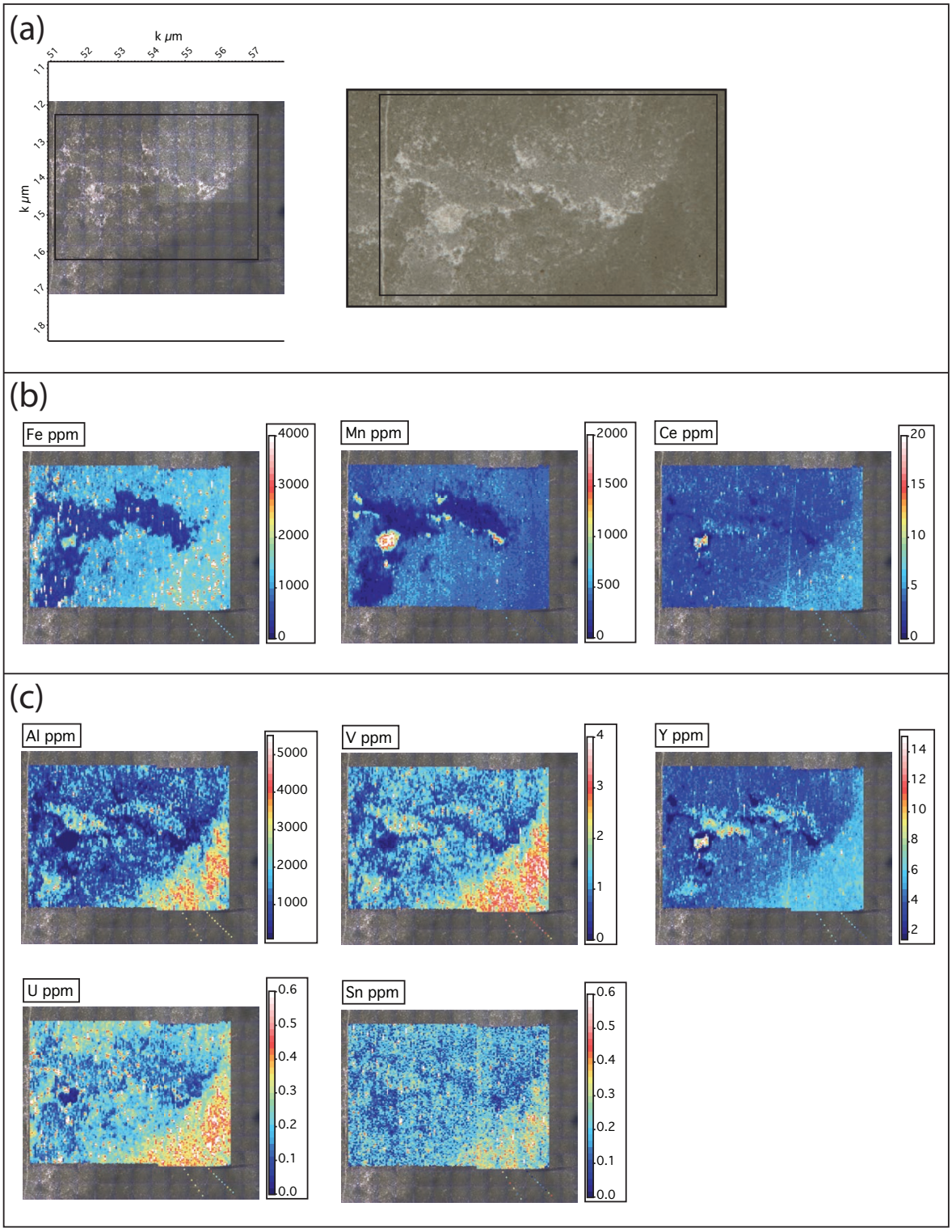


Figure 4: 2D chemical visualisations of a Little Dal Group polymud fabric. The area mapped here covers the entirety of the polymud fabric that was partially mapped in Figure 3. Panel (a) shows the base map for the subsequent 2D chemical maps (b-c) along with a high-resolution thin section scan for context. Panels (b-c) show 2D chemical maps with the analysed element indicated on the top left of each map, and scale bar indicating semiquantitative concentration levels in ppm on the right hand side of each map.

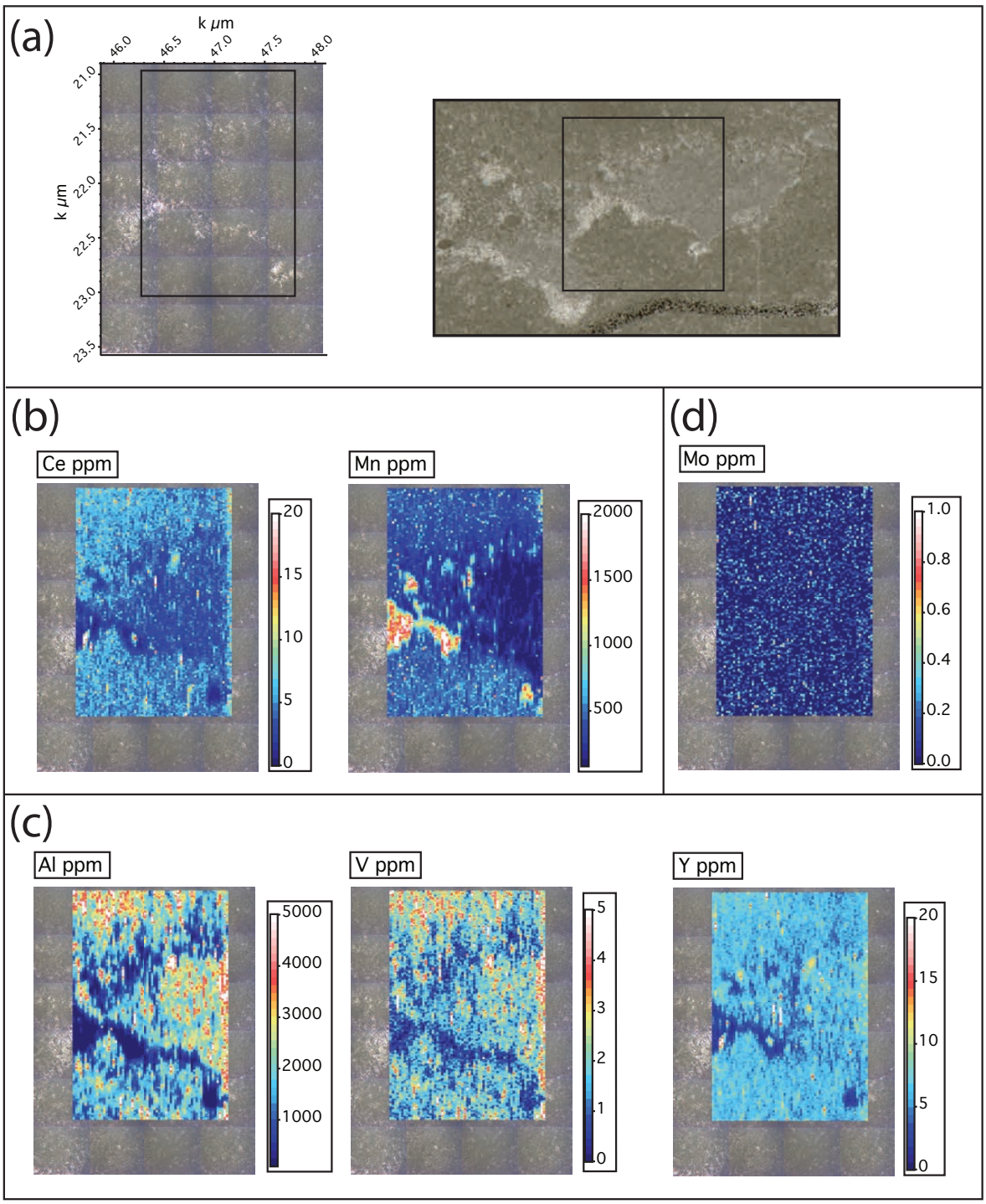


Figure 5: 2D chemical visualisations of a Little Dal Group polymud fabric. Panel (a) shows the base map for the subsequent 2D chemical maps (b-d) along with a high-resolution thin section scan for context. Panels (b-d) show 2D chemical maps with the analysed element indicated on the top left of each map, and scale bar indicating semiquantitative concentration levels in ppm on the right hand side of each map.

of one another (Figure 3c and Figure 3d). In addition, the potentially vital elements Sn and Cu were mapped, but they did not reveal any apparent structure (Figure 3e).

Having established on the initial map that Fe, Mn, V, Ce, and Y were particularly useful elements for illuminating the structure of the polymud fabric, the focus of subsequent experiments on Little Dal Group polymuds was on these analytes. On this basis, a larger map of ca. 4 x 6 mm (Figure 4a) was produced to cover the entirety of the polymud analysed in figure 3, along with some clear primary banding in the sample, visible in the bottom right corner of the mapped area. Again the distribution of Mn, and to a lesser extent Ce, is very similar to that of Fe, aside from incidences when Fe concentrations are in excess of 2,000ppm (Figure 4b). In this experiment, the redox sensitive element U, along with the detrital sediment indicator Al, were also included in the analyte list (Figure 4c). Aluminium, V, U, and to a lesser extent Y and Sn, all show similar distributions (Figure 4c). Their spatial arrangement is not random, rather these elements show very similar distributions to those in figure 3c, namely Zr, V, and Y. Again a picture of two distinct groups of elements emerges; group 1 elements (Figure 4b: Fe, Mn, and Ce) all show similar trends while group 2 elements (Figure 4c: V, Y, Al, U, and Sn) all show similar trends, broadly inversely related to those of group 1. A separate area of polymud on the same sample was analysed to test whether these trends are coherent (Figure 5a). In this case Fe was not analysed, however Mn and Ce (Figure 5b) both follow similar distributions to those of group 1 elements (Fe, Mn, Zn Ce) in both figure 3 and figure 4. Accordingly Al, V and Y (Figure 5c) all followed similar distributions to those of group 2 elements (Al, V, U Y, Zr and Sn) in both figure 3 and figure 4. In addition, the redox sensitive element Mo was mapped, but did not reveal any apparent structure (Figure 5d).

4.1.2. Little Dal Group Spongiforms

Figures 6 to 8 illustrate 2D chemical maps of a number of Little Dal Group carbonate-hosted spongiform structures. These may depict a sponge body fossil with a mm scale canal network but this possibility will only be discussed in the following section. Figures 9 to 10 illustrate 2D chemical maps of a common Little Dal Group carbonate-hosted spongiform microstructure. In each case, the spongiform's surface topography was analysed with the SEM, and once again back scattered electron imaging revealed an absence of any apparent composition related to the spongiform

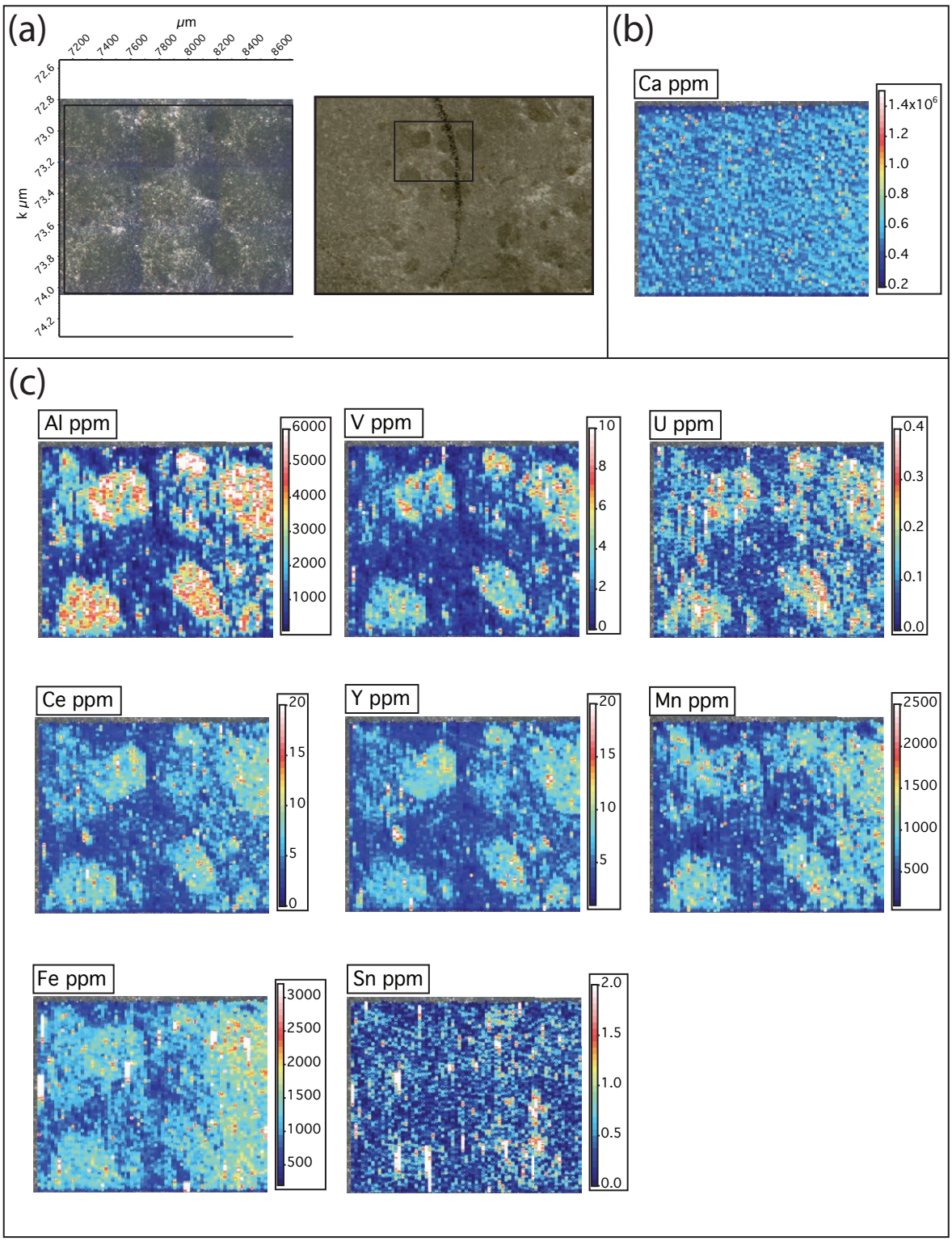


Figure 6: 2D chemical visualisations of a Little Dal Group spongiform structure. Panel (a) shows the base map for the subsequent 2D chemical maps (b-c) along with a high-resolution thin section scan for context. Panels (b-c) show 2D chemical maps with the analysed element indicated on the top left of each map, and scale bar indicating semiquantitative concentration levels in ppm on the right hand side of each map.

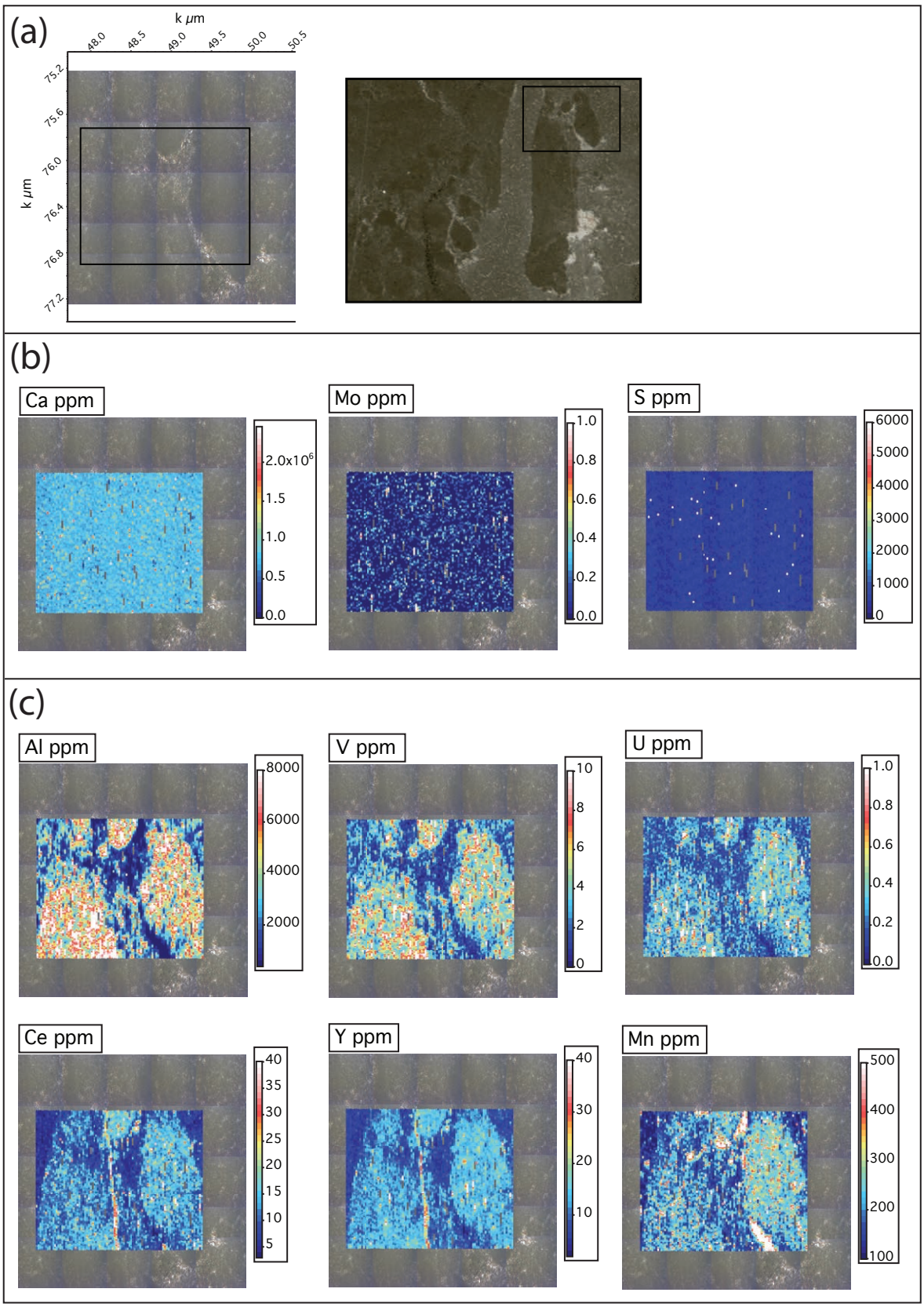


Figure 7: 2D chemical visualisations of a Little Dal Group spongiform structure. Panel (a) shows the base map for the subsequent 2D chemical maps (b-c) along with a high-resolution thin section scan for context. Panels (b-c) show 2D chemical maps with the analysed element indicated on the top left of each map, and scale bar indicating semiquantitative concentration levels in ppm on the right hand side of each map.

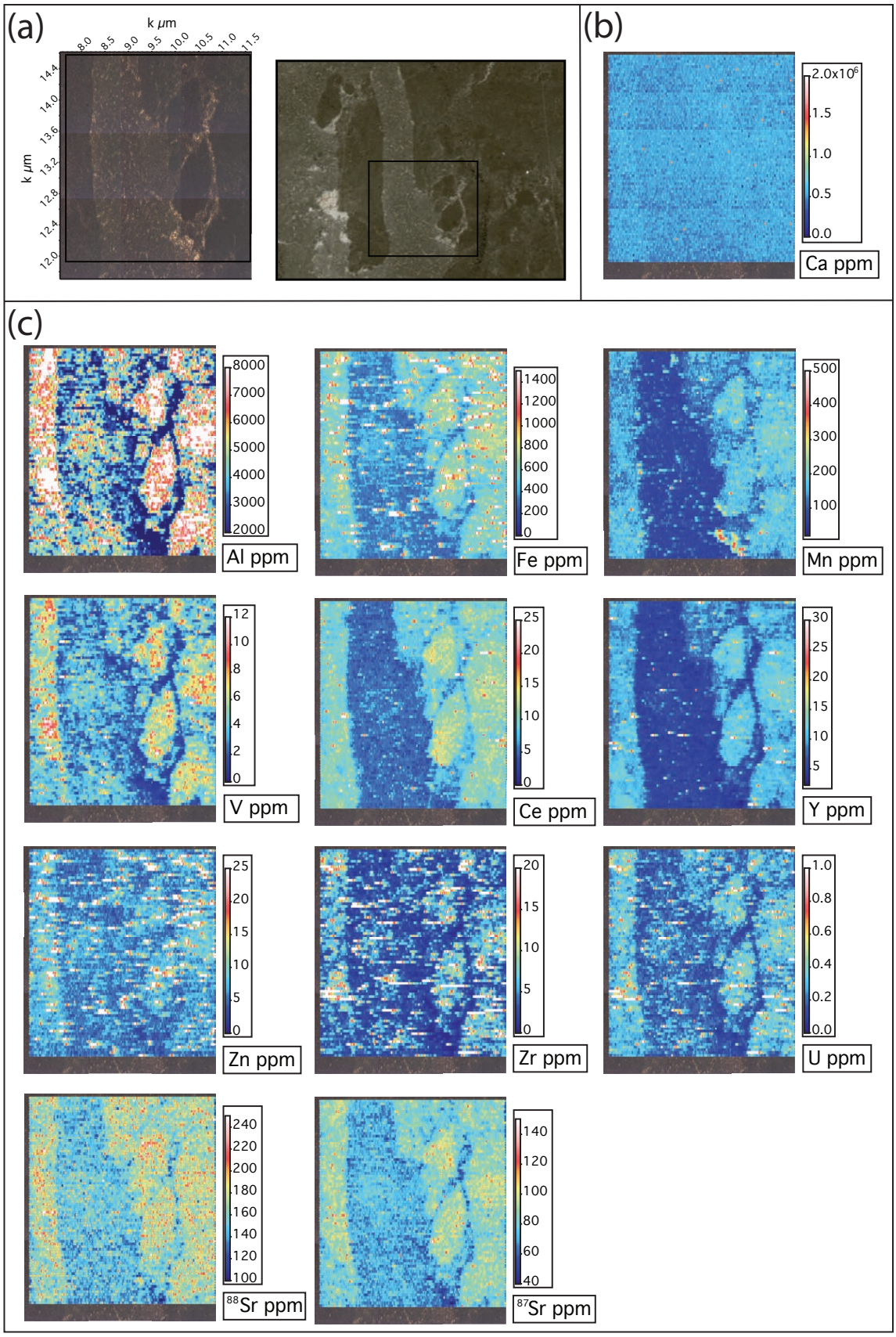


Figure 8: 2D chemical visualisations of a Little Dal Group spongiform structure. Panel (a) shows the base map for the subsequent 2D chemical maps (b-c) along with a high-resolution thin section scan for context. Panels (b-c) show 2D chemical maps with the analysed element, and isotope where applicable, indicated on the bottom right of each map, and scale bar indicating semiquantitative concentration levels in ppm on the right hand side of each map.

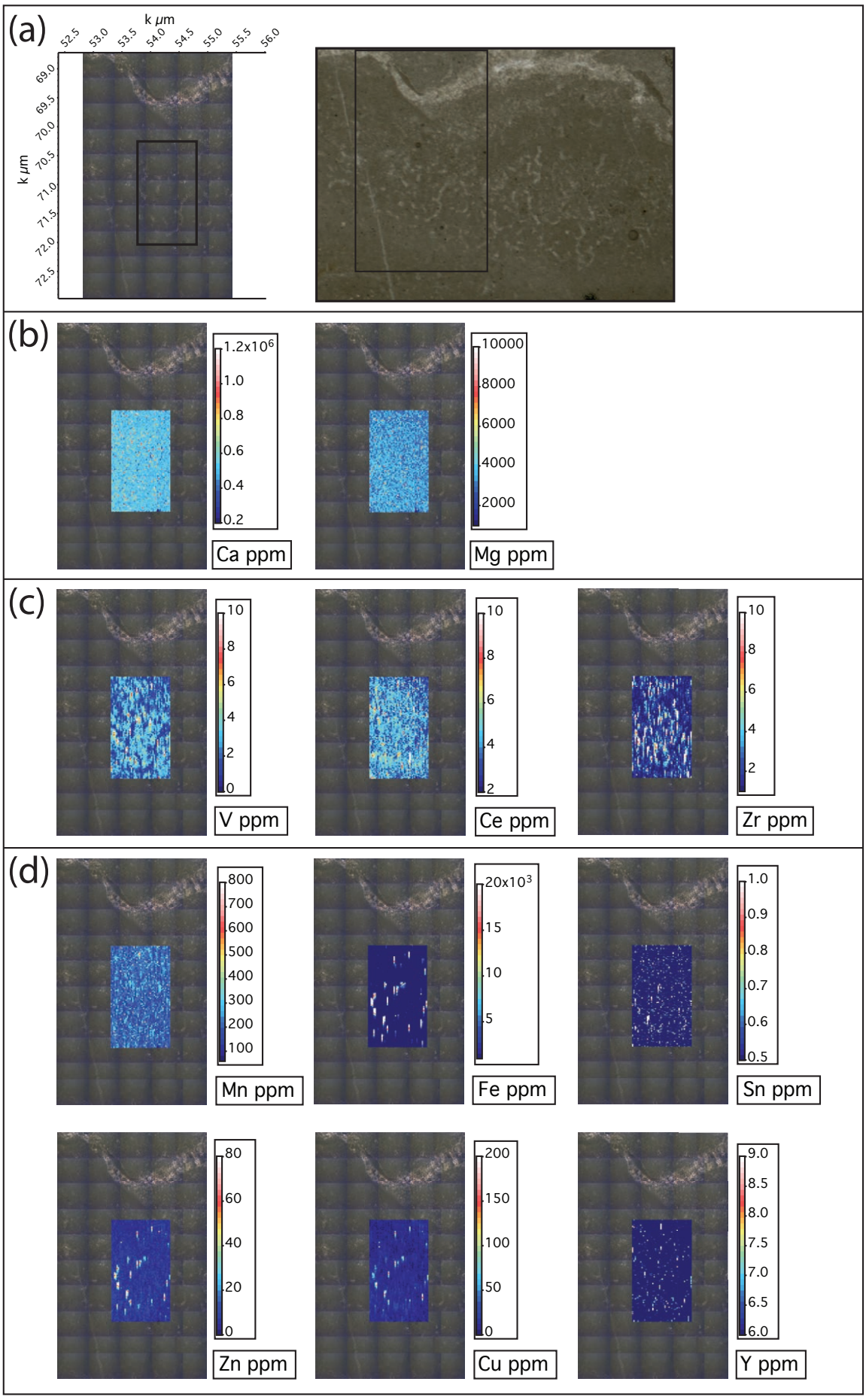

(a)
k µm
52.5
53.0
53.5
54.0
54.5
55.0
55.5
56.0
k µm
69.0
69.5
70.0
70.5
71.0
71.5
72.0
72.5
(b)
1.2x10^6
1.0
0.8
0.6
0.4
0.2
Ca ppm
10000
8000
6000
4000
2000
Mg ppm
(c)
10
8
6
4
2
0
V ppm
10
8
6
4
2
Ce ppm
10
8
6
4
2
Zr ppm
(d)
800
700
600
500
400
300
200
100
Mn ppm
20x10^3
15
10
5
Fe ppm
1.0
0.9
0.8
0.7
0.6
0.5
Sn ppm
80
60
40
20
0
Zn ppm
200
150
100
50
0
Cu ppm
9.0
8.5
8.0
7.5
7.0
6.5
6.0
Y ppm

Figure 9: 2D chemical visualisations of a Little Dal Group spongiform microstructure. Panel (a) shows the base map for the subsequent 2D chemical maps (b-d) along with a high-resolution thin section scan for context. Panels (b-c) show 2D chemical maps with the analysed element indicated on the bottom right of each map, and scale bar indicating semiquantitative concentration levels in ppm on the right hand side of each map.

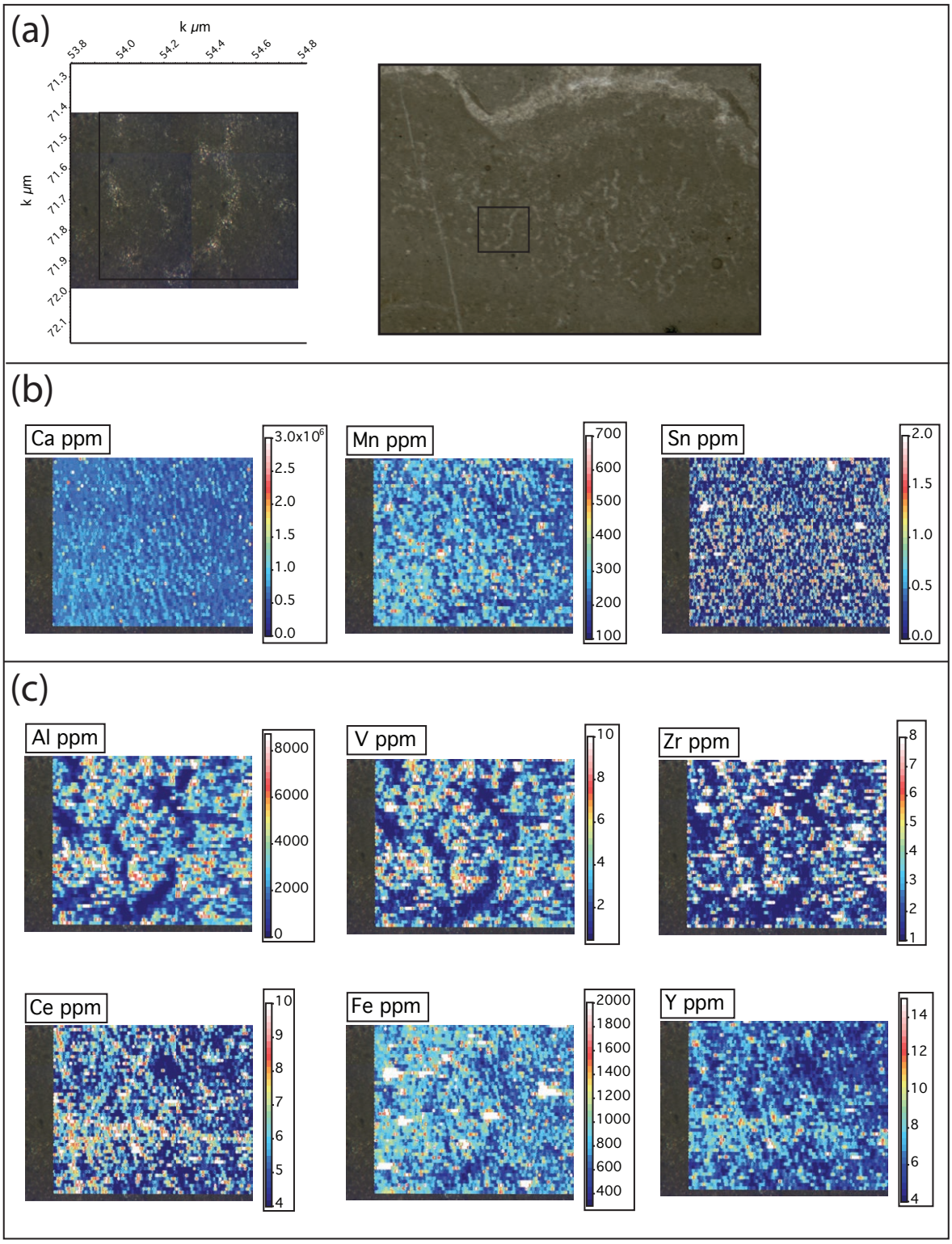


Figure 10: 2D chemical visualisations of a Little Dal Group spongiform microstructure. Because of the limitations of the maps produced in Figure 9, a smaller portion of the spongiform microstructure mapped in Figure 9 was reanalysed at a higher resolution here. Panel (a) shows the base map for the subsequent 2D chemical maps (b-c) along with a high-resolution thin section scan for context. Panels (b-c) show 2D chemical maps with the analysed element indicated on the top left of each map, and scale bar indicating semiquantitative concentration levels in ppm on the right hand side of each map.

surface (Figure 1b and Figure 1c). However, the much more sensitive LA-ICP-MS mapping reveals clear structures matching exactly the distributions of oval canals and surrounding 'framework'. In all cases there is an enrichment of the analysed elements within the canals and a striking depletion in the 'framework'. By contrast, the spongiform structures show a complete lack of variability in their Ca distributions (Figures 6b, 7b and 8b) showing that the structure is not built from different types of Ca- or Mg-carbonate. In all cases the structure is mapped very accurately by the Al, V, U, Ce, Y and Mn distribution (Figures 6c, 7c and 8c), with Fe and Sn showing additional structure in figure 6c, and Fe, Zn, Zr and Sr showing additional structure in figure 8c.

Figure 9 was obtained with a 24 μm spot size and the resulting maps are not as crisp as those of larger areas analysed with the same spot size. Regardless, the microstructure of 'canals' and 'framework' is still visible in the distribution of V, Ce and Zr (Figure 9c). Recognising the limitations of the spatial resolution, a smaller area (the bottom right of Figure 9) was re-analysed with a smaller spot size of 12 μm. This yielded a crisper resolution in which the spongiform structure was clearly resolved with maps of Al, V, Ce, Y, Mn, Fe and Zr (Figure 10c). Again the same pattern of elemental enrichment (in canals) and depletion (framework) was encountered as in the larger scale maps.

4.2. Cretaceous Sponge

Figures 11 to 13 illustrate 2D chemical maps of Cretaceous calcified sponges with automicritic crusts. Figure 11 depicts a sponge body fossil with a well-preserved canal network, while figures 12 and 13 depict sponge body fossils with more degraded canal networks. In each case the sponge's surface topography was imaged with the SEM, and back scattered electron imaging revealed an absence of any major element variation related to the sponge (Figure 1d). Initially both Ca and Mg were analysed (Figure 11b). Calcium shows no variation. This confirmed that all Cretaceous materials are calcite with no significant variation in Ca content (Figures 11b, 12b and 13b). However, the Mg map shows variability of several thousand ppm, the distribution of which only partly corresponds to the petrographically identified features (Figure 11a). This was ascertained for all the other Cretaceous samples, and thereafter Mg was no longer analysed (Figures 12 and 13). By contrast, LA-ICP-MS

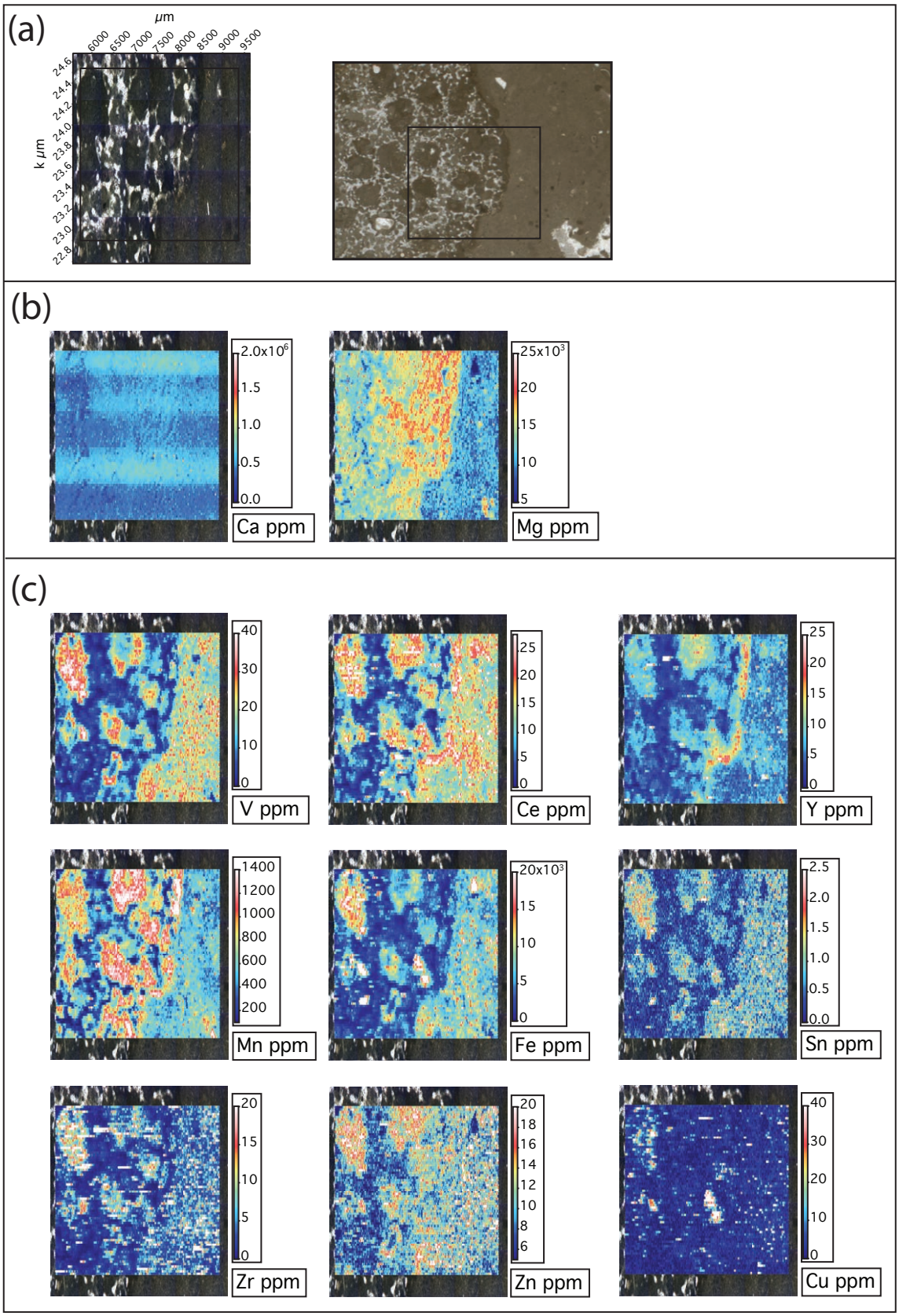


Figure 11: 2D chemical visualisations of a Cretaceous sponge. Panel (a) shows the base map for the subsequent 2D chemical maps (b-c) along with a high-resolution thin section scan for context. The automicritic crust at the rim of the sponge is pointed out by a white arrow on the high-resolution scan in panel (a). Panels (b-c) show 2D chemical maps with the analysed element indicated on the bottom right of each map, and scale bar indicating semiquantitative concentration levels in ppm on the right hand side of each map.

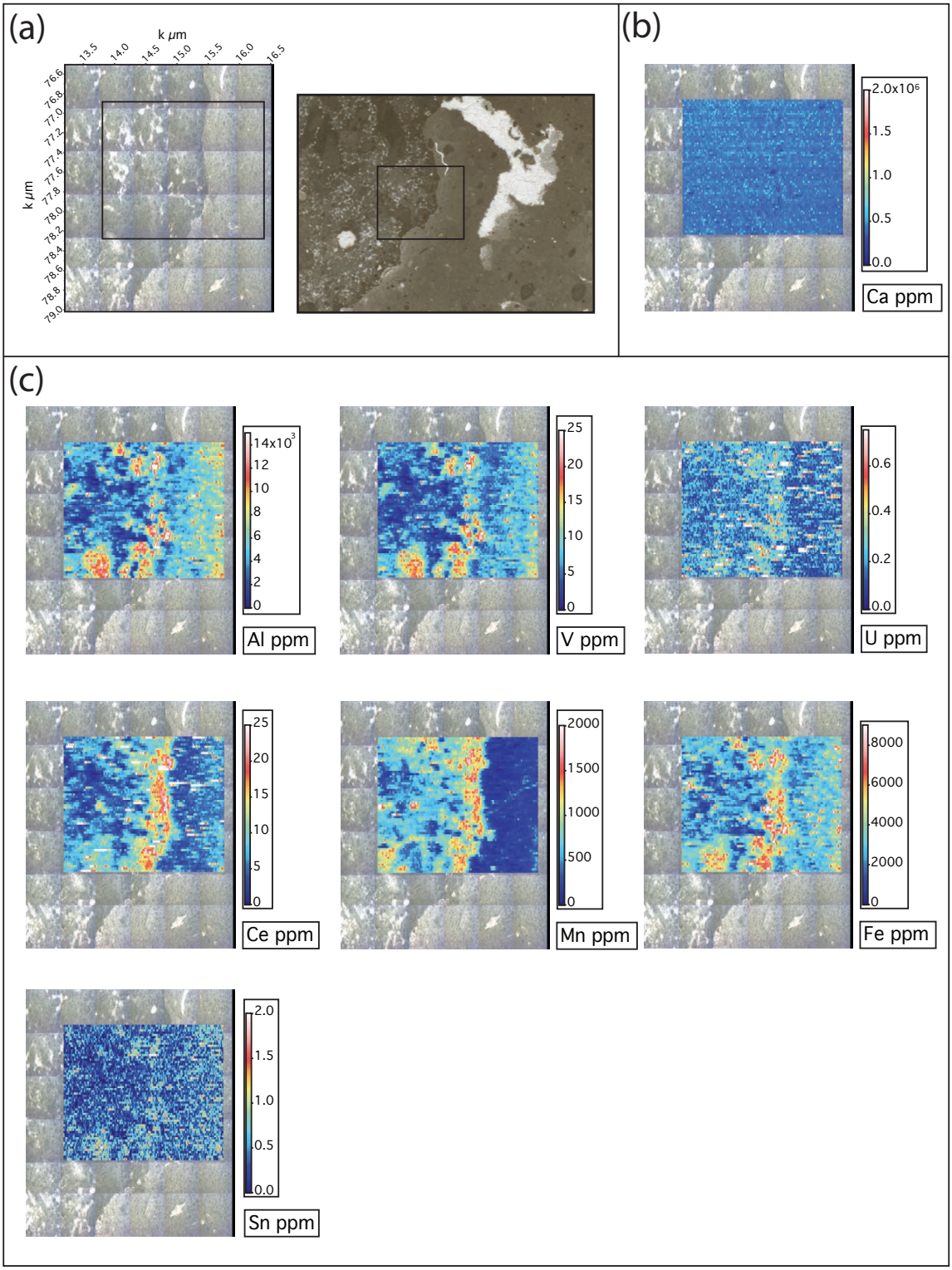


Figure 12: 2D chemical visualisations of a Cretaceous sponge. Panel (a) shows the base map for the subsequent 2D chemical maps (b-c) along with a high-resolution thin section scan for context. The automicritic crust at the rim of the sponge is pointed out by a white arrow on the high-resolution scan in panel (a). Panels (b-c) show 2D chemical maps with the analysed element indicated on the bottom right of each map, and scale bar indicating semiquantitative concentration levels in ppm on the right hand side of each map.

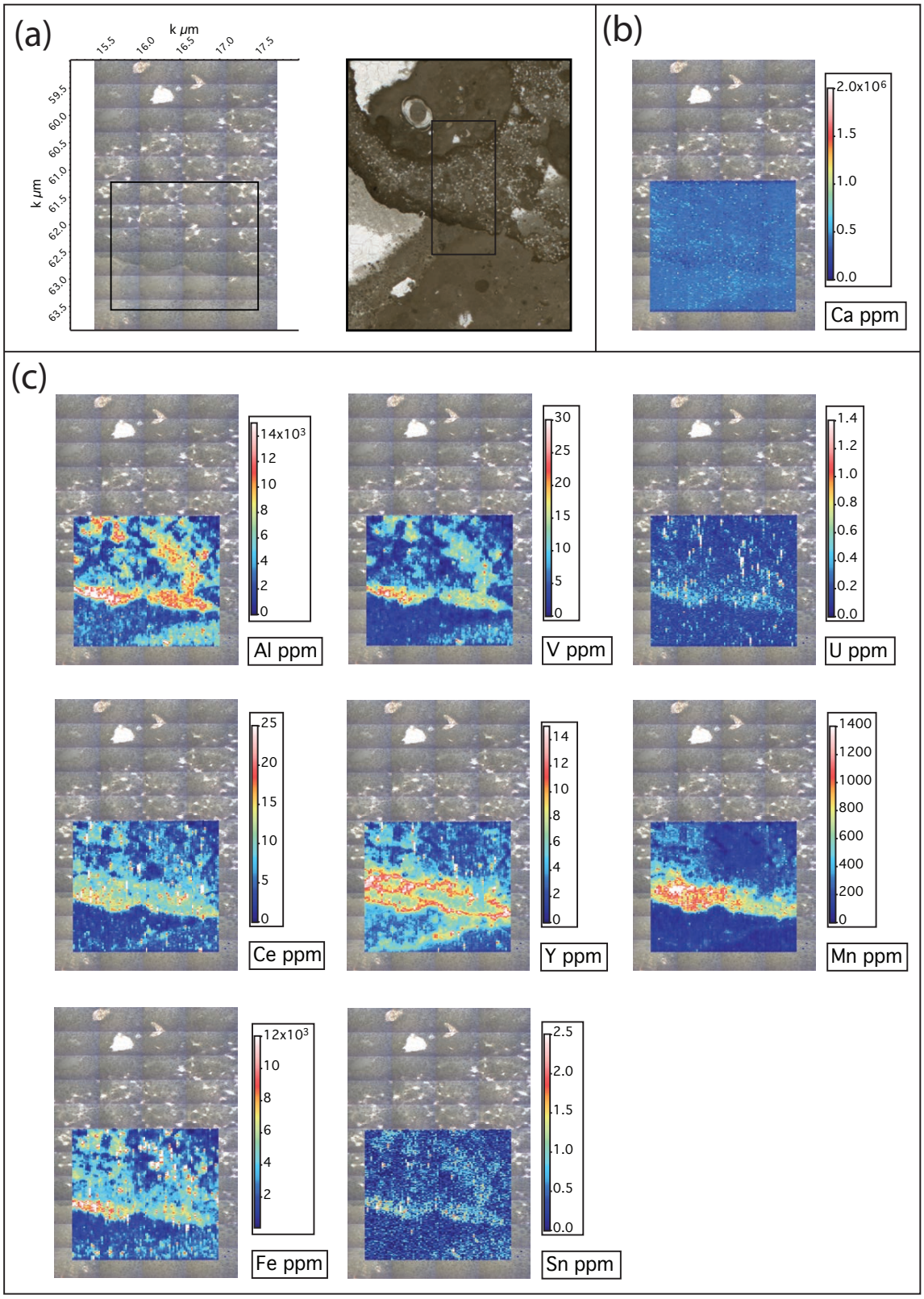


Figure 13: 2D chemical visualisations of a Cretaceous sponge. Panel (a) shows the base map for the subsequent 2D chemical maps (b-c) along with a high-resolution thin section scan for context. The automicritic crust at the rim of the sponge is pointed out by white arrows on the high-resolution scan in panel (a). Panels (b-c) show 2D chemical maps with the analysed element indicated on the bottom right of each map, and scale bar indicating semiquantitative concentration levels in ppm on the right hand side of each map.

mapping reveals a consistent enrichment of the analysed elements within the sediment infilling the sponge canal network and a comparatively strong depletion of these elements in the sponge body fossil itself. The most striking enrichment is in Mn, Fe, V, Ce, and Y (Figure 11c), whereas Sn, Zr, Zn and Cu (Figure 11c) are less clearly elevated in concentration in the sediment infilling the sponge canal network. The carbonate mud surrounding the sponge fossil itself is also enriched (Figure 11c). Aluminium and U were analysed in addition in the experiments that are visualised in figures 12c and 13c, and both were found to follow the established trend of depletion in the sponge body fossil and enrichment in the infilling and surrounding sediment. Furthermore, in each of the mapped Cretaceous sponges there is a striking enrichment of several elements, most notably Ce, Mn and Y (Figures 11c, 12c and 13c), within the automicritic crust at the rim of the sponge preserved at the boundary between the sponge and surrounding infiltrated carbonate sediment (Figures 11a, 12a, and 13a).

4.3. Silurian Sponge

Figures 14 to 17 illustrate 2D visualisations of *Malumispongium*, a Silurian, calcified, siliceous sponge. Figures 14, 15 and 16 represent transects across a calcified sponge canal which has been in filled with sililclastic-bioclastic sediment, while figure 17 represents a detailed map of the boundary between the sponge and the sediment infilling in the canal shown in figure 15. Again, the sponge's surface topography was inspected with the SEM. In this case, back scattered electron imaging revealed a compositional contrast clearly related to the sponge (Figure 1e). The structure visible in BSE is caused by the sediment that had infilled the sponge canal. In this specimen, the infilling sediment is not pure carbonate mud and contains siliclastic detritus that has a different BSE response. It was therefore not surprising that LA-ICP-MS mapping also revealed a clear structure related to the compositional contrast between the calcified sponge and the sediment infilling the sponge canal. In these samples the Ca distribution is not uniform throughout the sponge and the infilling sediment (Figures 14a, 15a, 16a and 17a), unlike in all the other analysed samples (Figures 3 – 13). Instead Ca along with Ce and Y (Figures 14a, 15a and 16a), and Sr and Mn (Figure 17a) are consistently depleted, albeit to varying degrees, in the infilling sediment. Magnesium follows the inverse trend, with all the other analysed elements, i.e. V, Ce, Y, Mn, Fe Sn, Zr, Zn and Cu also enriched in the sediment (Figures 14c, 15c, 16c and

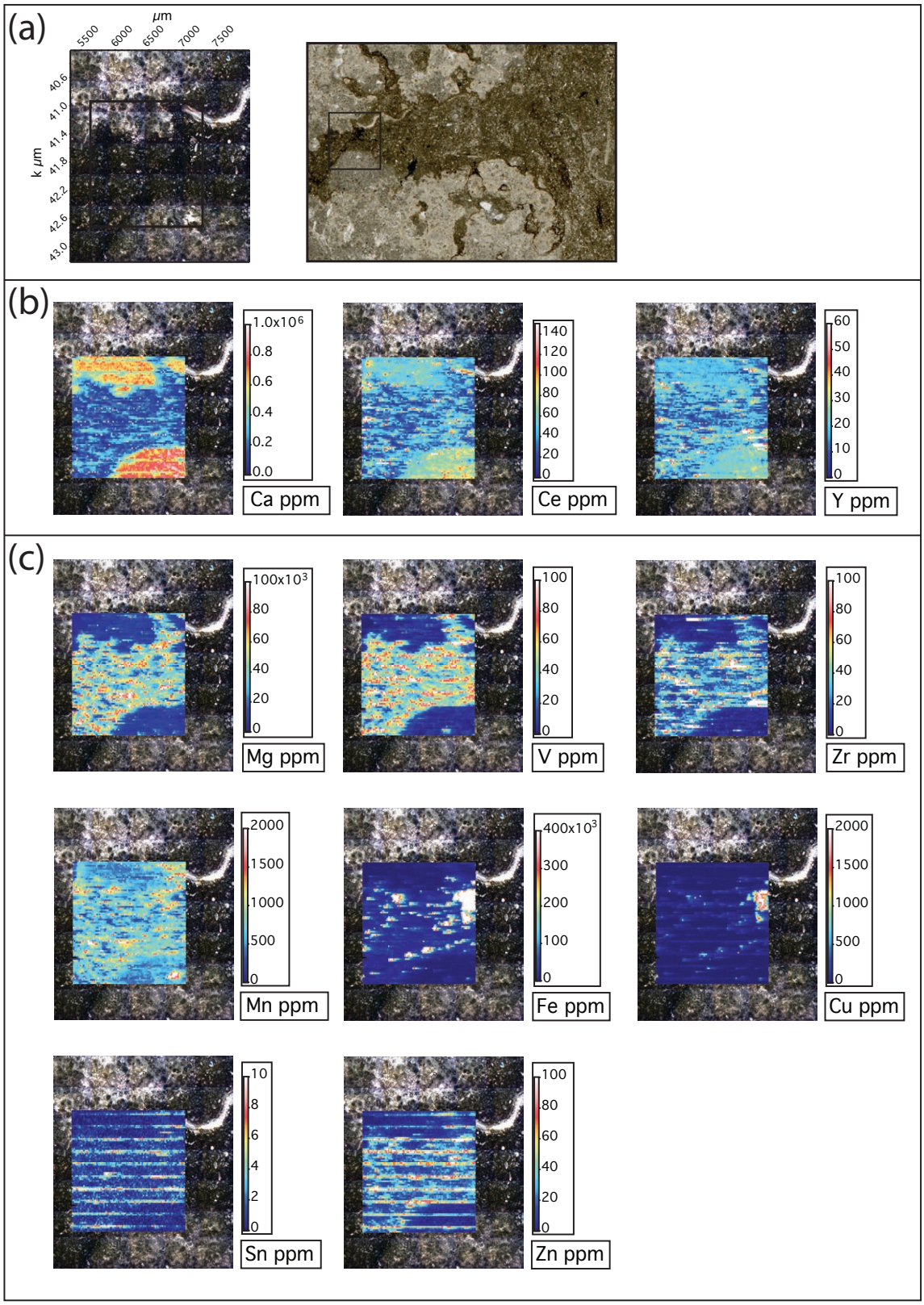


Figure 14: 2D chemical visualisations of a Silurian sponge. Panel (a) shows the base map for the subsequent 2D chemical maps (b-c) along with a high-resolution thin section scan for context. Panels (b-c) show 2D chemical maps with the analysed element indicated on the bottom right of each map, and scale bar indicating semiquantitative concentration levels in ppm on the right hand side of each map. The horizontal lined features particularly visible in maps of Sn and Zn concentrations in panel (c), are artefacts of the LA-ICP-MS analysis.

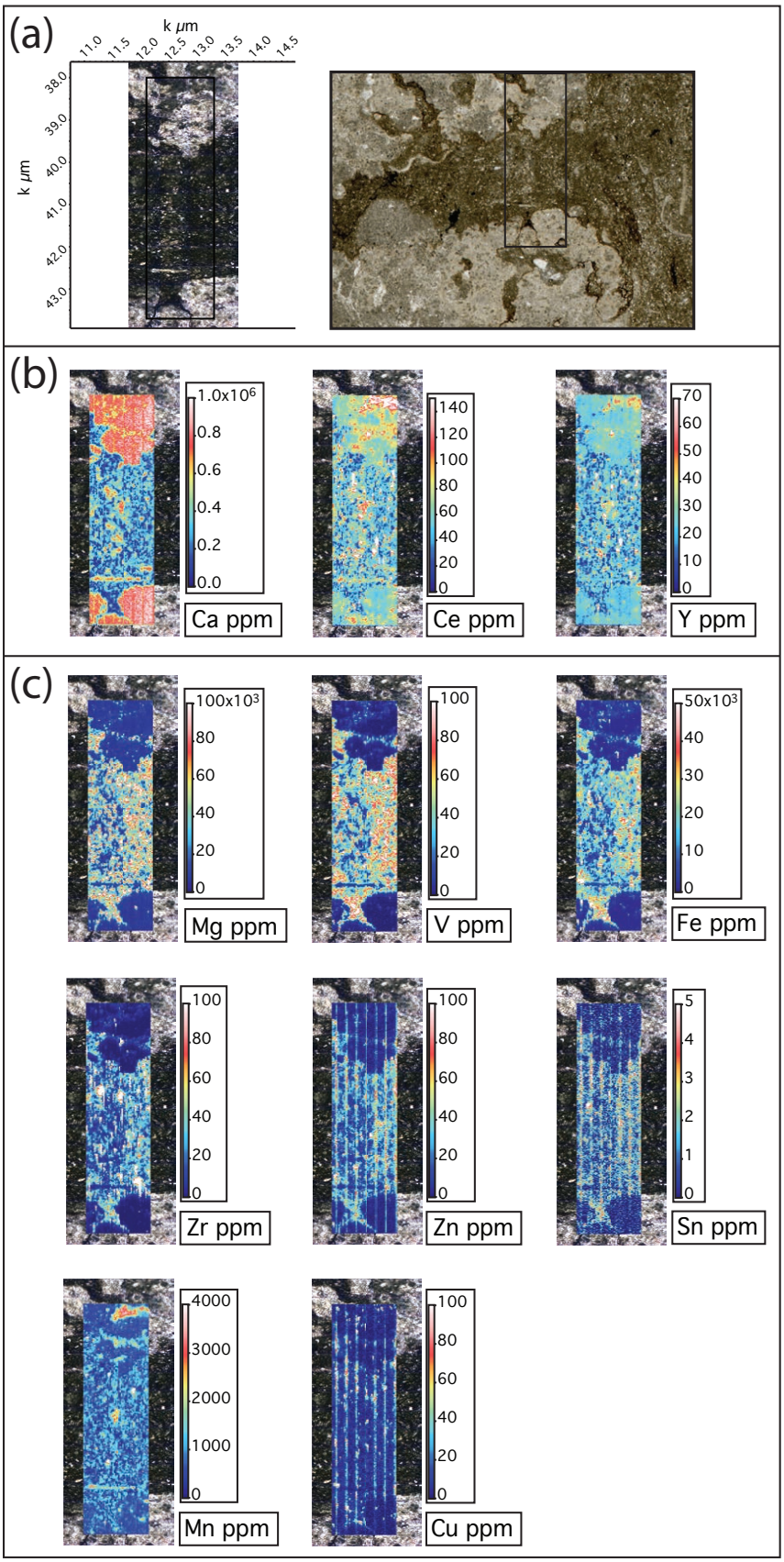


Figure 15: 2D chemical visualisations of a Silurian sponge. Panel (a) shows the base map for the subsequent 2D chemical maps (b-c) along with a high-resolution thin section scan for context. Panels (b-c) show 2D chemical maps with the analysed element indicated on the bottom right of each map, and scale bar indicating semiquantitative concentration levels in ppm on the right hand side of each map. The vertical lined features particularly visible in the maps of Sn, Cu and Zn concentrations in panel (c), are artefacts of the LA-ICP-MS analysis

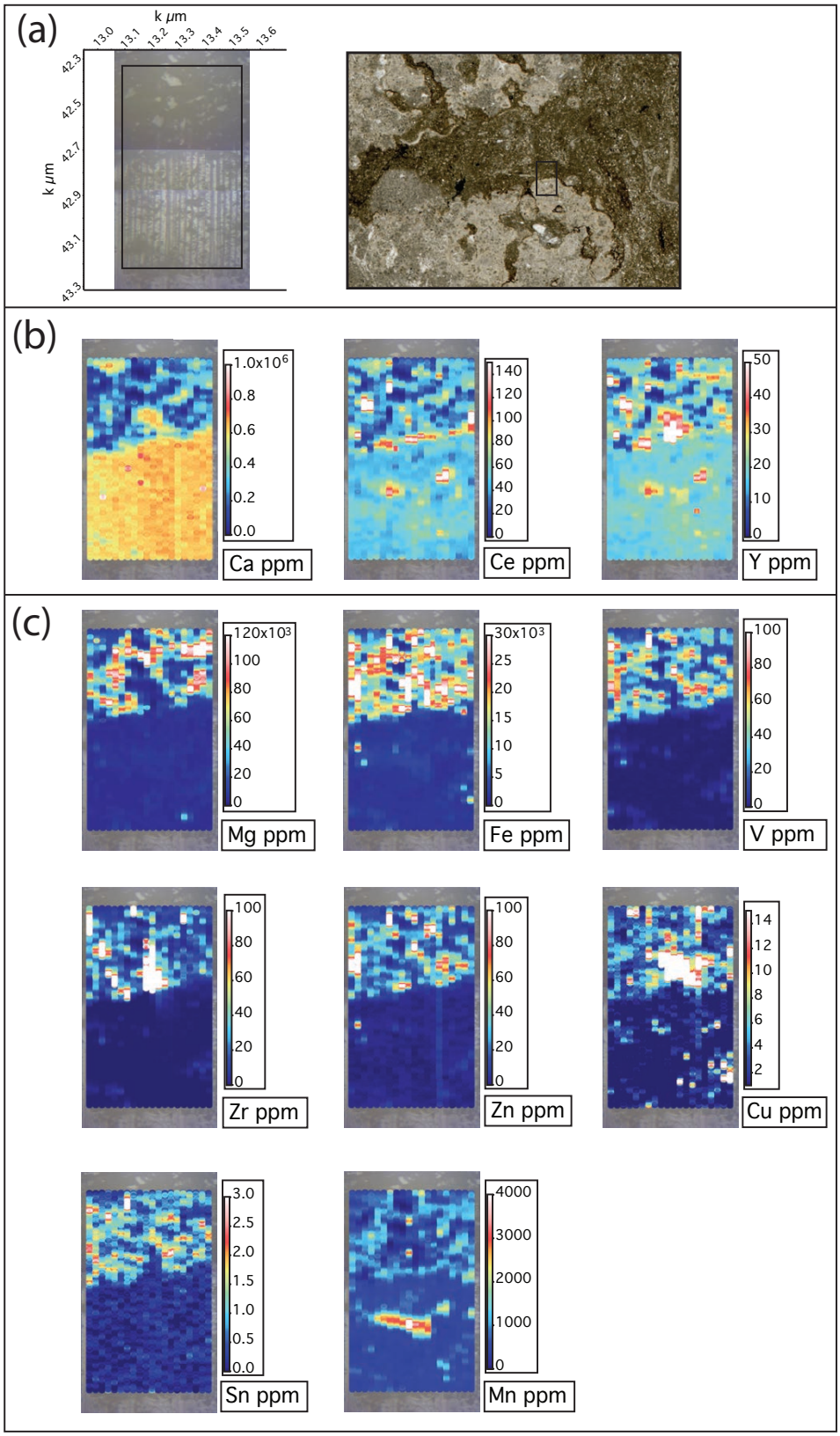


Figure 16: 2D chemical visualisations of a Silurian sponge. The area mapped here represents a higher resolution map of the boundary between the calcified sponge and the sediment infilling the sponge canal that was mapped at a larger scale in Figure 15. Panel (a) shows the base map for the subsequent 2D chemical maps (b-c) along with a high-resolution thin section scan for context. Panels (b-c) show 2D chemical maps with the analysed element indicated on the bottom right of each map, and scale bar indicating semiquantitative concentration levels in ppm on the right hand side of each map. The vertical lined features particularly visible in the maps of Sn, Cu and Zn concentrations in panel (c), are artefacts of the LA-ICP-MS analysis.

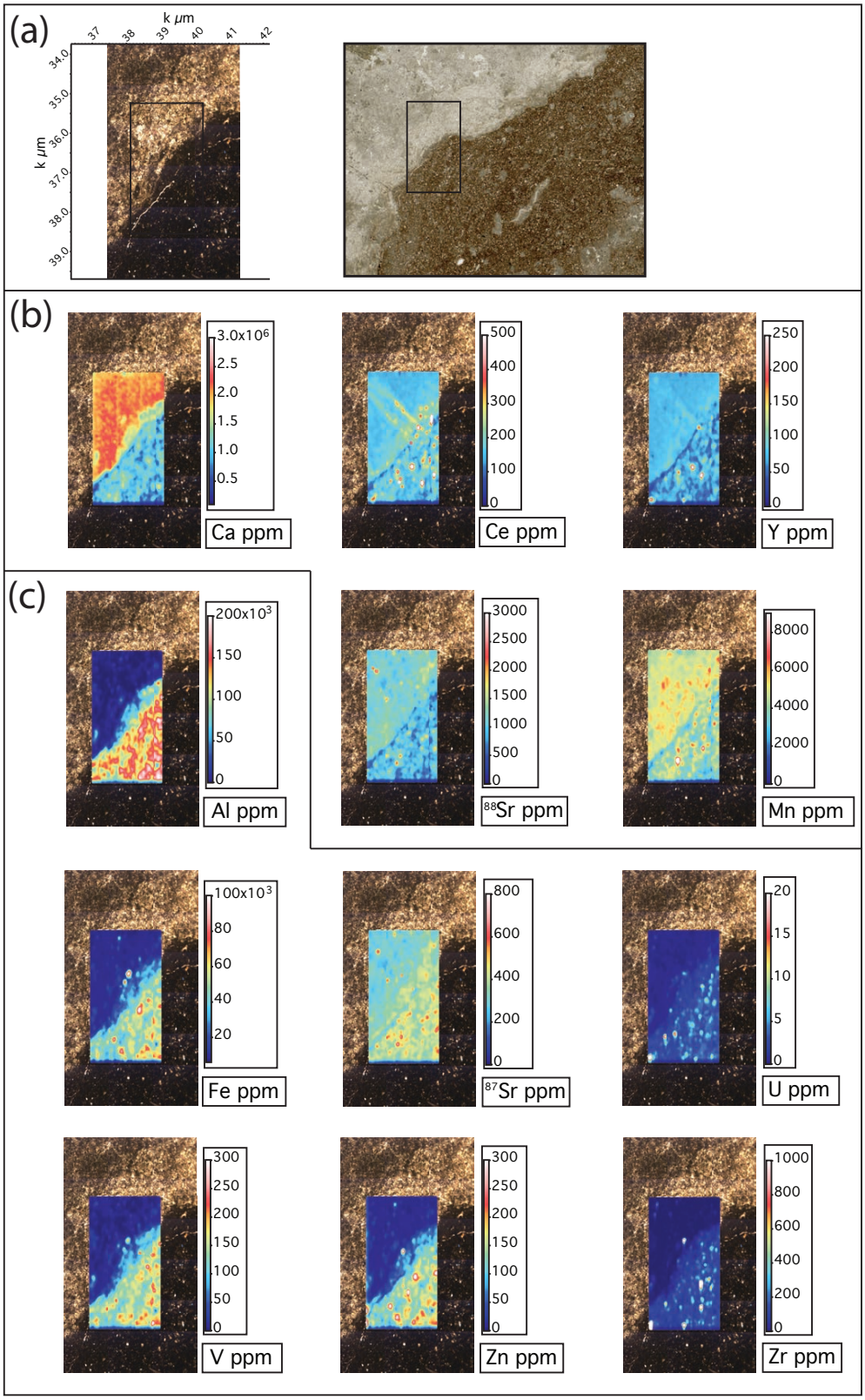


Figure 17: 2D chemical visualisations of a Silurian sponge. The area mapped here is targeted at the accuentuated inner limit between the sponge and the siliclastic sediment infilled osculum. This represents dermal, originally collagen-rich, connective tissue, and is pointed out by a white arrow on the high-resolution scan in Pannel (a). Panel (a) shows the base map for the subsequent 2D chemical maps (b-c) along with a high-resolution thin section scan for context. Panels (b-c) show 2D chemical maps with the analysed element indicated on the bottom right of each map, and scale bar indicating semiquantitative concentration levels in ppm on the right hand side of each map. The vertical lined features particularly visible in the maps of Sn, Cu and Zn concentrations in panel (c), are artefacts of the LA-ICP-MS analysis.

17c). The most important observation from this sample is the consistent depletion of these elements in the sponge body fossil itself (Figures 14c, 15c, 16c and 17c). Figure 17 is a map targeted at the accentuated inner limit between the sponge and the siliclastic sediment infilled osculum, which represents dermal, originally collagen-rich, connective tissue (Figure 17a). A pronounced enrichment of vital elements, as well as Ce, Al and V was found within this dermal connective tissue (Figures 17b and Figure 17c).

5. Discussion

We initially discuss the trace element systematics of the Little Dal Group polymud fabrics as they were the main topic of the study by Neuweiler et al. (2009). Next we elaborate on the first trace element geochemical analysis of spongiform structures in these Neoproterozoic Little Dal Group samples, and their comparison with a Cretaceous and a Silurian sponge. Finally, we address the possible significance of the Little Dal Group spongiform structures.

5.1. Little Dal Group Polymud Fabrics

Prior to the present study, the polymud fabrics have only been identified petrographically in Neoproterozoic material (Neuweiler et al., 2009), and the results reported here are significant in that for the first time, the polymuds could be shown to also have distinctive geochemical character. LA-ICP-MS mapping of the polymuds reveals a structure that is in fact more discrete and pronounced than its petrographic expression. The chemical maps also show more complexities in that several element concentrations revealed irregular secondary areas interpreted as voids, containing internal sediment with distinctive associations between either consistently enriched or depleted trace elements.

One obvious explanation for the polymud structure mapped by the Fe concentration could be the incorporation of an Fe rich detrital sediment. In order to test this proposal, the distribution of Zr (Figure 3d) and Al (Figure 4c), both good indicators of detrital sediment, were investigated. There is clearly no correspondence between Fe (Figures 3c and 4b) and either Zr or Al (Figures 3d and 4c), firmly demonstrating that the Fe distribution is not simply a reflection of the distribution of mud. This suggests that the Fe distribution, and in turn the Mn, Zn and Ce

distributions (Figures 3c, 4b and 5b) reflect different original micro-environments during the life, decay and/or lithification of the organism responsible for the structure.

Very high Fe concentrations, in excess of 3,000 ppm, stand out beyond the general polymud fabric (Figures 3c and 4b). They are caused by analysis of pyrite, or other iron sulphide minerals. However, pyrite-related Fe concentrations are not the dominant feature of the Fe distribution, which confirms that the Fe distributions, and in turn those of Mn, Zn, and Ce, are true distribution patterns and not artefacts of sulphide distribution.

In both maps of the first polymud, a secondary fracture fill is clearly delineated by high Y and Ce concentrations, in excess of 5 ppm (Figures 3 and 4) while the same fracture is not visible in any of the other element maps. Importantly, the distribution patterns of both Y and Ce remain undisturbed in the polymud fabric beside the fracture fill, which suggests that their distribution patterns and in turn the distribution patterns and apparent structure of all the other analysed elements are not related to element re-distribution after diagenesis. A very important observation is that all phases of the polymud fabric have comparatively low REE concentrations. The Ce and Y concentrations in figures 3, 4 and 5, are predominantly below 15 ppm. The very low concentrations mapped by the REE+Y distributions in the Little Dal Group polymud fabrics, argues against a microbial origin of these carbonates because microbial carbonate is consistently enriched in REE (Kamber & Webb, 2007; Kamber et al., 2014).

5.2. Little Dal Group Spongiform Structures vs. Cretaceous and Silurian Sponge Geochemistry

The most important feature of the Little Dal Group carbonate spongiform structures is the consistency of the distribution pattern of depletion within the spongiform 'framework' itself, and enrichment in both the surrounding sediment and the sediment infilling the spongiform canals (Figures 6 – 10). Again, a secondary fracture fill is visible by high concentrations of Y and Ce (Figure 7c), and pyrite can easily be picked out as 'nuggets' of high Fe concentration (Figures 6c, 8c and 9d). However, neither the secondary fracture fill nor the occurrences of pyrite dominate the distribution of these elements, which suggests that their distribution patterns are

related to the formation of the spongiform structure rather than late stage diagenesis or pyrite distribution.

There are many similarities between the major and trace element distribution patterns of the Little Dal Group spongiform structures to those of the Cretaceous sponge. In both cases, Ca has a homogenous distribution across the various components of the spongiform structure (Figures 6b – 13b), while the analysed trace elements are consistently enriched in sediment infilling both the sponge canals and the spongiform canals, while being depleted in the sponge or spongiform 'framework' itself (Figures 6c – 13c). By contrast, the analysed Silurian sponge is different. Namely, the Ca distribution in the Silurian sponge is not uniform, and it is therefore possible to visualise the sponge with BSE (Figure 1e). This is due to the lower Ca concentration of the siliclastic sediment infilling the canals of the Silurian sponge, and is mirrored to a lesser extent by the distributions of both Ce and Y (Figures 14b - 17b). However, aside from the differences in the Ca, Ce and Y distributions, the other analysed elements of the Silurian sponge follow a broadly similar distribution pattern to that of the Cretaceous Sponge and the Little Dal Group spongiform structures.

The primary difference between the major and trace element distributions of the Phanerozoic sponges and the Little Dal Group spongiform structures is that both the Cretaceous and Silurian sponges reveal a clear enrichment of certain elements at the very extremity of the sponge fossil. The automicrite crusts surrounding the edge of the Cretaceous sponge fossil were found to be consistently enriched in Ce, Mn, and Y (Figures 11c, 12c and 13c), while the accentuated inner limit between the sponge and the sediment filled osculum of the Silurian sponge, thought to represent dermal, originally collagen-rich connective tissue, also showed enrichment of Ce, Al, and V (Figure 17b and Figure 17c). However, the Little Dal Group spongiforms revealed no such enrichment (Figures 6 - 10). Nonetheless, there is no obvious extremity of the little Dal spongiform, and should these spongiform structures actually be sponge fossils they are likely representing degraded fragments of very primitive sponges, perhaps similar to Archaeocyaths (Rowland, 2001), preserved in a sponge bearing limestone, rather than sponge body fossils preserved in their entirety.

5.3. Origin and Significance of the Little Dal Group Spongiform Structures

The Little Dal Group spongiform microstructures are notably similar in petrography to Spongiostromidae, first identified in Namurian limestones by Gürich (1907). This form of crust-forming structure resembles stromatoporids, but in detail their structure differs, particularly because of their tendency to degrade (Gürich, 1907). Similar spongiostromate and/or prostromate structures have since been identified in many Phanerozoic strata (e.g. Riding, 1977; Riding, 1991).

More recently it was proposed that spongiform microstructures occurring within Phanerozoic carbonate bioconstructors (Figure 3, Luo & Reitner, 2015) that were previously attributed to stromatolites (i.e. microbial), should be re-attributed to sponges. Furthermore, Luo and Reitner (2015) suggested that these anastomosing filamentous microstructures are in fact comparable to keratose demosponge fossils described by Luo and Reitner (2014).

The Neoproterozoic Little Dal Group spongiform structures have received little attention in the literature, despite their possible significance for the sponge fossil debate (see Table 1). Both the Little Dal Group spongiform structures and microstructures are here shown to persistently exhibit distributions of high trace element concentrations in the canal infill, while the spongiform 'framework' is consistently depleted (Figures 6 - 10). Our present study also shows that neither late stage diagenesis nor pyrite distribution had adversely affected the geochemistry. This consistent pattern of enrichment in the sediment infilling the canals and depletion in the sponge also occurs in Phanerozoic sponges (Figures 11 - 17), and points to a key difference between skeletal carbonates and microbial carbonates in that skeletal carbonates when co-existing with microbial carbonates are always depleted in trace elements. A curious feature of microbial carbonates of all ages is that they consistently exhibit relative enrichment of REE (Kamber & Webb, 2007; Kamber et al., 2014). The reason for this remains to be fully explored, but regardless, both the Little Dal Group spongiform structures and microstructures are here shown to exhibit consistently depleted REE+Y concentrations within the spongiform framework (Figures 6 – 10).

Because keratose demosponges can construct stromatolite-like build-ups that are morphologically similar to microbialites at the level of mega- and microstructures

(Lee et al., 2014; Luo & Reitner, 2015), early metazoans may be preserved in structures similar to microbial products in morphology. Thus, the key question is not whether these structures are biogenic, rather whether they are microbial or skeletal in origin. All of the available evidence is consistent with a skeletal primitive sponge origin of the Neoproterozoic Little Dal Group spongiform structures.

It is premature to propose that the fossil sponge record extends deep into the Cryogenian. However, our study shows that trace element mapping has potential to discriminate between sponge and microbial carbonate. A further impetus to study the Little Dal Group spongiform structures in greater detail still is that their age is compatible with phylogenomic studies and molecular clock estimates that place the origin of the crown metazoan deep within the Cryogenian, (Dunn et al., 2008; Peterson et al., 2008; Sperling et al., 2010; Erwin et al., 2011), in the range of 833-650 Ma (dos Reis et al., 2015).

6. Summary and Conclusions

Polymud fabrics, previously proposed to be the result of sponge taphonomy (Neuweiler et al., 2009) on the basis of petrography, along with previously unreported spongiform structures from the ca. 818 – 723 Ma Little Dal Group were mapped chemically with the LA-ICP-MS method. In terms of major carbonate chemistry, the Little Dal samples are largely composed of calcite, but quite detailed structure is always evident in the distribution of Al, V, Fe, Cu, Zn, Y, Zr, Sn, Ce, and U concentrations. In the Little Dal Group polymuds and spongiforms, pyrite can be easily picked out with high Fe concentrations, however, it is equally clear that pyrite does not dominate the trace metal budget, as several chalcophile elements are in the carbonate phase and not dominated by pyrite (e.g. Cu and Zn are not affected). In addition, late stage fracture fills stand out in these samples through high concentrations of Ce and Y, but left the distribution patterns of the trace and major elements in adjacent carbonate unaffected. Thus, this study confirms that neither late stage diagenesis nor pyrite distribution had adversely affected the preserved geochemistry.

The distribution patterns of major and trace elements in the Little Dal Group polymud fabrics clearly show several irregular secondary structures interpreted as voids, containing internal sediment with distinctive elemental associations, in part

governed by redox behaviour. The compositional maps confirm that the structures are not random artefacts and that trace element geochemistry does map onto petrography. In terms of original significance, more work on both the Little Dal Group polymuds and Phanerozoic polymuds is needed. However, the low concentrations of the REE+Y analysed argues against a microbial origin.

The Little Dal Group spongiform structures and the studied Phanerozoic sponges reveal a clear trend of enrichment of the analysed elements within the spongiform canal network infill and a strong and consistant depletion of these elements in the spongiform 'framework' which could represent a degraded skeleton. The spongiform microstructures in the Little Dal Group follow a similar trend to that of the Little Dal Group spongiform structures and the Phanerozoic sponges, and similar microstructures in Phanerozoic carbonates that were previously attributed to stromatolites but more recently have been re-attributed to sponges (Lou and Reitner 2015). More work is needed both on the Neoproterozoic Little Dal Group spongiform structures and on apparently comparable Phanerozoic spongiostromate and/or prostromate structures. Although the present study did not yield conclusive results regarding Cryogenian sponges, it provides a range of new evidence that is compatible with the idea that the origin of sponges pre-dates the NOE. In addition, the analytical approach proposed here will also lend itself to study of other Neoproterozoic putative sponges (see Table 1).

References

Aitken J (1981) Stratigraphy and sedimentology of the Upper Proterozoic Little Dal Group, Mackenzie Mountains, Northwest Territories. *Proterozoic basins of Canada. Edited by FHA Campbell. Geological Survey of Canada, Paper,* 8, 1-10.

Antcliffe JB (2013) Questioning the evidence of organic compounds called sponge biomarkers. *Palaeontology,* 56, 917-925.

Antcliffe JB, Callow RH, Brasier MD (2014) Giving the early fossil record of sponges a squeeze. *Biological Reviews,* 89, 972-1004.

Ax P (1996) Multicellular Animals: A New Approach to the Phylogenetic Order in NatureSpringer-Verlag. Berlin.

Billings E (1872) Fossils in Huronian rocks. *Canadian Naturalist and Quarterly Journal of Science,* 6, 478.

Bourque P-A, Gignac H (1983) Sponge-constructed stromatactis mud mounds, Silurian of Gaspé, Québec. *Journal of Sedimentary Research,* 53.

Bowring SA, Grotzinger JP, Condon DJ, Ramezani J, Newall MJ, Allen PA (2007) Geochronologic constraints on the chronostratigraphic framework of the Neoproterozoic Huqf Supergroup, Sultanate of Oman. *American Journal of Science,* 307, 1097-1145.

Brain CB, Prave AR, Hoffmann K-H, Fallick AE, Botha A, Herd DA, Sturrock C, Young I, Condon DJ, Allison SG (2012) The first animals: ca. 760-million-year-old sponge-like fossils from Namibia. *South African Journal of Science,* 108, 01-08.

Budd GE (2008) The earliest fossil record of the animals and its significance. *Philosophical Transactions of the Royal Society B: Biological Sciences,* 363, 1425-1434.

Condon D, Zhu M, Bowring S, Wang W, Yang A, Jin Y (2005) U-Pb ages from the neoproterozoic Doushantuo Formation, China. *Science,* 308, 95-98.

Darwin C (1859) On the origins of species by means of natural selection. *London: Murray*, 247.

Desrochers A, Bourque P-A, Neuweiler F (2007) Diagenetic versus biotic accretionary mechanisms of bryozoan–sponge buildups (Lower Silurian, Anticosti Island, Canada). *Journal of Sedimentary Research,* 77, 564-571.

Dos Reis M, Thawornwattana Y, Angelis K, Telford MJ, Donoghue PC, Yang Z (2015) Uncertainty in the Timing of Origin of Animals and the Limits of Precision in Molecular Timescales. *Current Biology,* 25, 2939-2950.

Du W, Wang XL (2012) Hexactinellid sponge spicules in Neoproterozoic dolostone from South China. *Paleontological Research,* 16, 199-207.

Dunn CW, Hejnol A, Matus DQ, Pang K, Browne WE, Smith SA, Seaver E, Rouse GW, Obst M, Edgecombe GD (2008) Broad phylogenomic sampling improves resolution of the animal tree of life. *Nature,* 452, 745-749.

Erwin DH, Laflamme M, Tweedt SM, Sperling EA, Pisani D, Peterson KJ (2011) The Cambrian conundrum: early divergence and later ecological success in the early history of animals. *Science,* 334, 1091-1097.

Fanning CM, Link P (2006) Constraints on the timing of the Sturtian glaciation from southern Australia; ie, for the true Sturtian. In: *Geological Society of America Abstracts with Programs*.

Fanning CM, Link P (2008) Age constraints for the Sturtian glaciation: data from the Adelaide geosyncline, South Australia and Pocatello Formation, Idaho, USA. In: *SELWYN SYMPOSIUM 2008,* pp. 57.

Gao S, Liu X, Yuan H, Hattendorf B, Günther D, Chen L, Hu S (2002) Determination of forty two major and trace elements in USGS and NIST SRM glasses by laser ablation‐inductively coupled plasma‐mass spectrometry. *Geostandards Newsletter,* 26, 181-196.

Glaessner M (1959) Precambrian Coelenterata from Australia, Africa and England.

Gürich G (1907) Versuch einer Neueinteilung der Trilobiten. *Zentralblatt für Mineralogie, Geologie und Paläontologie,* 1907, 129-133.

Halanych KM (2004) The new view of animal phylogeny. *Annual Review of Ecology, Evolution, and Systematics*, 229-256.

Halverson GP, Hoffman PF, Schrag DP, Maloof AC, Rice AHN (2005) Toward a Neoproterozoic composite carbon-isotope record. *Geological Society of America Bulletin,* 117, 1181-1207.

Heaman L, Lecheminant A, Rainbird R (1992) Nature and timing of Franklin igneous events, Canada: implications for a Late Proterozoic mantle plume and the break-up of Laurentia. *Earth and Planetary Science Letters,* 109, 117-131.

Hellstrom J, Paton C, Woodhead J, Hergt J (2008) Iolite: software for spatially resolved LA-(quad and MC) ICPMS analysis. *Mineralogical Association of Canada short course series,* 40, 343-348.

Hoffmann K-H, Condon D, Bowring S, Crowley J (2004) U-Pb zircon date from the Neoproterozoic Ghaub Formation, Namibia: constraints on Marinoan glaciation. *Geology,* 32, 817-820.

Jefferson CW, Parrish RR (1989) Late Proterozoic stratigraphy, U-Pb zircon ages, and rift tectonics, Mackenzie Mountains, northwestern Canada. *Canadian Journal of Earth Sciences,* 26, 1784-1801.

Jochum KP, Weis U, Stoll B, Kuzmin D, Yang Q, Raczek I, Jacob DE, Stracke A, Birbaum K, Frick DA (2011) Determination of reference values for NIST SRM 610–617 glasses following ISO guidelines. *Geostandards and Geoanalytical Research,* 35, 397-429.

Kamber BS, Webb GE (2007) Transition metal abundances in microbial carbonate: a pilot study based on in situ LA-ICP-MS analysis. *Geobiology,* 5, 375-389.

Kamber BS, Webb GE, Gallagher M (2014) The rare earth element signal in Archaean microbial carbonate: information on ocean redox and biogenicity. *Journal of the Geological Society,* 171, 745-763.

Landing E (1994) Precambrian-Cambrian boundary global stratotype ratified and a new perspective of Cambrian time. *Geology,* 22, 179-182.

Lee J-H, Chen J, Choh S-J, Lee D-J, Han Z, Chough SK (2014) Furongian (late Cambrian) sponge–microbial maze-like reefs in the North China Platform. *Palaios,* 29, 27-37.

Lee MS, Soubrier J, Edgecombe GD (2013) Rates of phenotypic and genomic evolution during the Cambrian explosion. *Current Biology,* 23, 1889-1895.

Lees A, Hallet V, Hibo D (1985) Facies variation in Waulsortian buildups, Part 1; a model from Belgium. *Geological Journal,* 20, 133-158.

Lees A, Miller J (1985) Facies variation in Waulsortian buildups. Part 2; Mid‐Dinantian buildups from Europe and North America. *Geological Journal,* 20, 159-180.

Lees A, Miller J (2009) Waulsortian banks. *Carbonate mud-mounds*, 191-271.

Li C-W, Chen J-Y, Hua T-E (1998) Precambrian sponges with cellular structures. *Science,* 279, 879-882.

Longerich HP, Jackson SE, Günther D (1996) Inter-laboratory note. Laser ablation inductively coupled plasma mass spectrometric transient signal data acquisition and analyte concentration calculation. *Journal of Analytical Atomic Spectrometry,* 11, 899-904.

Love GD, Grosjean E, Stalvies C, Fike DA, Grotzinger JP, Bradley AS, Kelly AE, Bhatia M, Meredith W, Snape CE (2009) Fossil steroids record the appearance of Demospongiae during the Cryogenian period. *Nature,* 457, 718-721.

Luo C, Reitner J (2014) First report of fossil “keratose” demosponges in Phanerozoic carbonates: preservation and 3-D reconstruction. *Naturwissenschaften,* 101, 467-477.

Luo C, Reitner J (2015) ‘Stromatolites’ built by sponges and microbes – a new type of Phanerozoic bioconstruction. *Lethaia*, n/a-n/a.

Maloof AC, Porter SM, Moore JL, Dudás FÖ, Bowring SA, Higgins JA, Fike DA, Eddy MP (2010a) The earliest Cambrian record of animals and ocean geochemical change. *Geological Society of America Bulletin,* 122, 1731-1774.

Maloof AC, Rose CV, Beach R, Samuels BM, Calmet CC, Erwin DH, Poirier GR, Yao N, Simons FJ (2010b) Possible animal-body fossils in pre-Marinoan limestones from South Australia. *Nature Geosci,* 3, 653-659.

Muscente A, Michel FM, Dale JG, Xiao S (2015) Assessing the veracity of Precambrian ‘sponge’fossils using in situ nanoscale analytical techniques. *Precambrian Research,* 263, 142-156.

Neuweiler F, D'orazio V, Immenhauser A, Geipel G, Heise K-H, Cocozza C, Miano TM (2003) Fulvic acid–like organic compounds control nucleation of marine calcite under suboxic conditions. *Geology,* 31, 681-684.

Neuweiler F, Daoust I, Bourque P-A, Burdige DJ (2007) Degradative Calcification of a Modern Siliceous Sponge from the Great Bahama Bank, The Bahamas: A Guide for Interpretation of Ancient Sponge-Bearing Limestones. *Journal of Sedimentary Research,* 77, 552-563.

Neuweiler F, Rutsch M, Geipel G, Reimer A, Heise K-H (2000) Soluble humic substances from in situ precipitated microcrystalline calcium carbonate, internal sediment, and spar cement in a Cretaceous carbonate mud-mound. *Geology,* 28, 851-854.

Neuweiler F, Turner EC, Burdige DJ (2009) Early Neoproterozoic origin of the metazoan clade recorded in carbonate rock texture. *Geology,* 37, 475-478.

Paton C, Hellstrom J, Paul B, Woodhead J, Hergt J (2011) Iolite: Freeware for the visualisation and processing of mass spectrometric data. *Journal of Analytical Atomic Spectrometry,* 26, 2508-2518.

Paul B, Paton C, Norris A, Woodhead J, Hellstrom J, Hergt J, Greig A (2012) CellSpace: A module for creating spatially registered laser ablation images within the Iolite freeware environment. *Journal of Analytical Atomic Spectrometry,* 27, 700-706.

Peterson KJ, Cotton JA, Gehling JG, Pisani D (2008) The Ediacaran emergence of bilaterians: congruence between the genetic and the geological fossil records. *Philosophical Transactions of the Royal Society B: Biological Sciences,* 363, 1435-1443.

Planavsky N (2009) Early Neoproterozoic origin of the metazoan clade recorded in carbonate rock texture: COMMENT. *Geology,* 37, e195-e195.

Powell J, Schneider D (2013) *Preliminary Results of Detrital Muscovite 40Ar/39Ar Geochronology from the Eastern Mackenzie Mountains and Mackenzie Plain, Northwest Territories*.

Riding R (1977) Skeletal stromatolites. In: *Fossil Algae*. Springer, pp. 57-60.

Riding R (1991) Cambrian calcareous cyanobacteria and algae. In: *Calcareous algae and stromatolites*. Springer, pp. 305-334.

Rigby JK (1967) Two new early Paleozoic sponges and the sponge-like organism, Gaspespongia basalis Parks, from the Gaspe Peninsula, Quebec. *Journal of Paleontology*, 766-775.

Rowland SM (2001) Archaeocyaths—a history of phylogenetic interpretation. *Journal Information,* 75.

Siegl A, Kamke J, Hochmuth T, Piel J, Richter M, Liang C, Dandekar T, Hentschel U (2011) Single-cell genomics reveals the lifestyle of Poribacteria, a candidate

phylum symbiotically associated with marine sponges. *The ISME journal,* 5, 61-70.

Sperling E, Robinson J, Pisani D, Peterson K (2010) Where's the glass? Biomarkers, molecular clocks, and microRNAs suggest a 200‐Myr missing Precambrian fossil record of siliceous sponge spicules. *Geobiology,* 8, 24-36.

Srivastava M, Simakov O, Chapman J, Fahey B, Gauthier ME, Mitros T, Richards GS, Conaco C, Dacre M, Hellsten U (2010) The Amphimedon queenslandica genome and the evolution of animal complexity. *Nature,* 466, 720-726.

Turner EC, James NP, Narbonne GM (1997) Growth dynamics of neoproterozoic calcimicrobial reefs, Mackenzie Mountains, Northwest Canada. *Journal of Sedimentary Research,* 67, 437-450.

Turner EC, James NP, Narbonne GM (2000) Taphonomic control on microstructure in Early Neoproterozoic reefal stromatolites and thrombolites. *Palaios,* 15, 87-111.

Ubide T, Mckenna CA, Chew DM, Kamber BS (2015) High-resolution LA-ICP-MS trace element mapping of igneous minerals: In search of magma histories. *Chemical Geology,* 409, 157-168.

Wallace M, Woon E (2008) Selwyn Symposium, Vol. *Abstract 91 of Neoproterozoic Climates Origin of Early Life*, 17-21.

Woodhead J, Hellstrom J, Paton C, Hergt J, Greig A, Maas R (2008) A guide to depth profiling and imaging applications of LA–ICP–MS. *Laser Ablation ICP–MS in the Earth Sciences: Current Practices and Outstanding Issues,* 40.

Wörheide G, Dohrmann M, Erpenbeck D, Larroux C, Maldonado M, Voigt O, Borchiellini C, Lavrov D (2012) 1 Deep Phylogeny and Evolution of Sponges (Phylum Porifera). *Advances in marine biology,* 61, 1.

Xiao S, Zhang Y, Knoll AH (1998) Three-dimensional preservation of algae and animal embryos in a Neoproterozoic phosphorite. *Nature,* 391, 553-558.

Yin Z, Zhu M, Davidson EH, Bottjer DJ, Zhao F, Tafforeau P (2015) Sponge grade body fossil with cellular resolution dating 60 Myr before the Cambrian. *Proceedings of the National Academy of Sciences,* 112, E1453-E1460.

Chapter 6: Synthesis

Molecular oxygen has played a crucial role in shaping our planetary environment and the oxygenation of the Earth's surface fundamentally altered global biogeochemical cycles. Its build-up ultimately paved the way for the rise of complex animals at the beginning of the Cambrian. The Earth's surface oxygenation was apparently achieved in two broad steps; the 'Great Oxidation Event' or GOE at ca. 2.3 Ga (e.g. Holland, 1999; Farquhar et al., 2000), and the 'Neoproterozoic Oxidation Event' or NOE almost two billion years later (e.g. Och & Shields-Zhou, 2012). However, reconstruction of the detailed redox-evolution of the Earth's surface environment remains one of the greatest scientific challenges in the geosciences. For example, it is difficult to distinguish atmospheric from oceanic oxidation, and global from local (or even pore water) redox changes.

Despite these challenges, a firm observation is that both postulated oxidation events were apparently accompanied by global glaciations; the Huronian glaciation extending from ca. 2.4 to 2.2 Ga (Melezhik, 2006), and the Neoproterozoic global 'icehouses', expressed in the Sturtian (ca. 720 – 660 Ma) and the Marinoan (ca. 650 – 635 Ma) glaciations (Fairchild & Kennedy, 2007). However, the causality between the apparent step increases in oxygen concentrations, and these two global glaciation events remains unclear. Marine sedimentary rocks hold great potential for the reconstruction of pre-Cambrian atmospheric and oceanic redox evolution. However, most of the currently available information has been derived from deep-water sedimentary rocks (e.g. Bekker et al., 2004; Large et al., 2014). This thesis has advanced discussion of the detailed redox evolution of the atmosphere, via geochemical analysis of *shallow*-marine microbial carbonates, spanning from Palaeoarchaean (c.a. 3.45 Ga) to Cambrian in age. The resulting data and analysis have revealed new and important insights into the Earth's redox evolution in terms of the shallow-marine environment. The main contributions and conclusions of the thesis relevant to the GOE can be summarised as three main findings:

- Finding 1: The Archaean ocean was poorly mixed with respect to sulphate, having generally very low seawater sulphate concentrations

and a very short sulphate residence time (e.g. Canfield, 2004). Thus, modern oceanic sulphur systematics provide limited insight into the Archaean sulphur cycle, and mass independently fractionated (MIF) S-isotope data should not be modelled using the modern S-cycle as an analogue. Instead, it is proposed in this thesis that the 20th century atmospheric lead event provides a better analogue in that similar to industrial lead, the main oceanic input of Archaean sulphur was through atmospheric rain down, with individual giant point sources capable of temporally dominating atmospheric input. Thus, MIF-S signals in preserved pre-GOE sediments are not all global phenomena, instead likely representing fallout from local volcanic eruptions that could imprint recycled MIF-S signals into pyrite of restricted basins. By this process isotopic attenuation of the atmospheric signal is subdued, preventing the formation of an averaged global open ocean sulphur pool. The large range in Neoarchaean $\Delta^{33}S$ may thus record very localised S-isotope signals. The subsequent reduction in $\Delta^{33}S$ range from 2.5 Ga (Figure 1), some 150 Ma before evidence for the GOE, most likely represents a major change in magmatic evolution that occurred at 2.5 Ga (Keller & Schoene, 2012). The increased release of SO_2 into the atmosphere via more effective subduction and/or additional mantle plume events would have overwhelmed the input of MIF-S to the ocean, thereby beginning to attenuate the global MIF S-isotope signals from 2.50 to 2.35 Ga.

- Finding 2: A petrographic survey of microbial-carbonate-hosted-pyrite revealed a first-order difference in preservation of early diagenetic pyrite. Pre-GOE microbial carbonates were shown to be much richer in pyrite and contain grains of greater morphological variability. The disparity in pyrite abundance and morphology is mirrored by the qualitative degree of preservation of reduced carbon (largely as kerogen). The preservation of both delicate pyrite morphologies outlined by reduced carbon and abundant early diagenetic pyrite in Neoarchaean microbial carbonate argues against the presence of

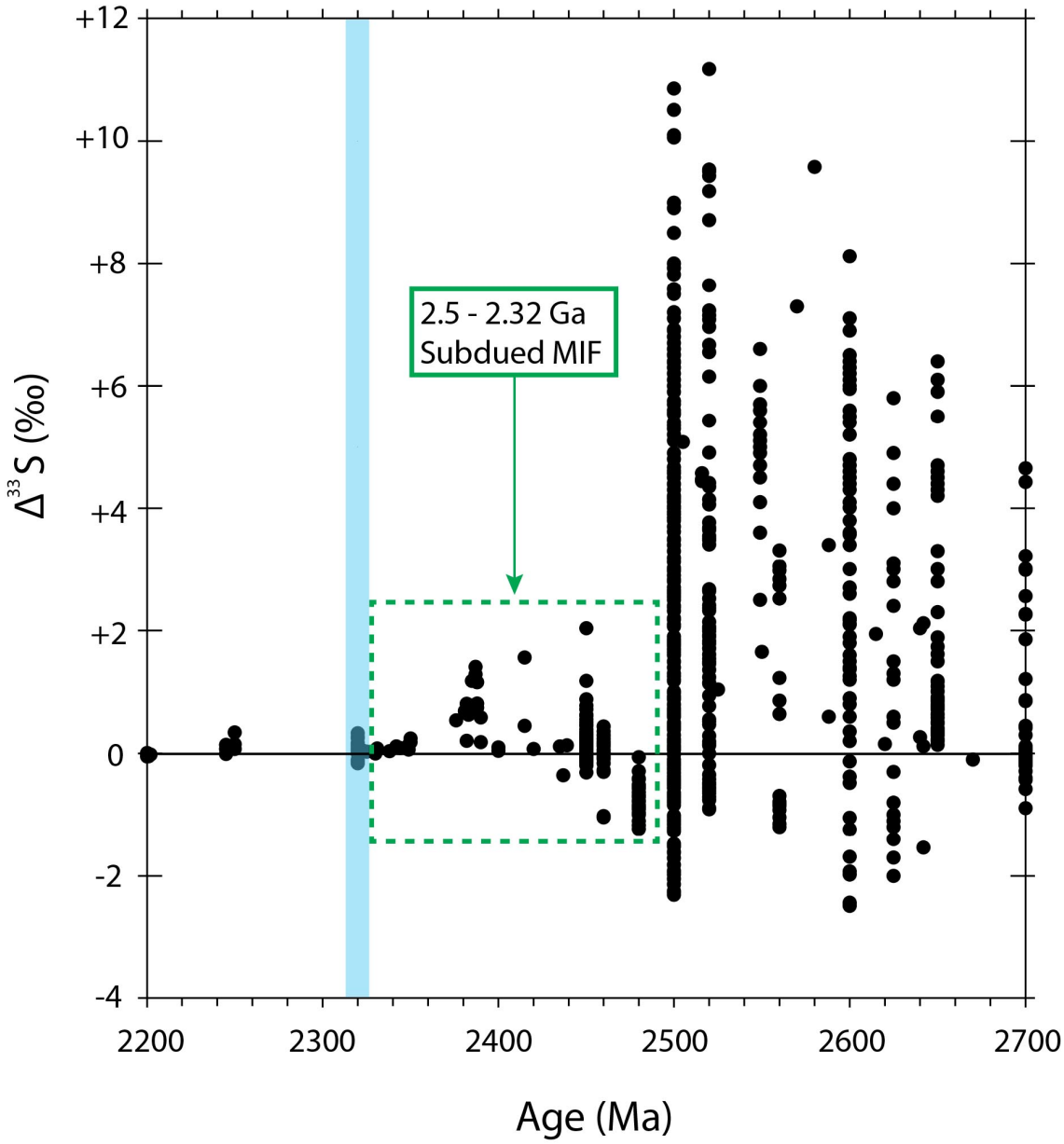


Figure 1: $\Delta^{33}S$ vs. Age plot of previously published MIF-S data from 2700 – 2200 Ma. Data are from references as compiled in Chapter 4, Figure 3. The GOE is depicted by a pale blue bar at 2320 Ma and the subdued MIF from 2500 to 2320 Ma is highlighted by a green dashed box.

appreciable free oxygen in the shallow marine environment at that time, and instead suggests that the Neoarchaean microbial electron tower worked differently (Froelich et al., 1979). The apparent inconsistency with evidence for whiffs of free oxygen in the pre-GOE surface environment (e.g. Anbar et al., 2007) could be the result of other electron donors driving redox reactions, not necessarily free O_2 (e.g. Avrahamov et al., 2014).

- Finding 3: Post-GOE oxidative weathering of landmasses greatly affected the flux of transition metals to the ocean. This evolution appears to be reflected in the composition of pyrite, with younger, post-GOE microbial-carbonate-hosted sulphides exhibiting much greater chemical variation and substitution than the pre-GOE microbial-carbonate-hosted sulphides. The validity of claims for temporal increases or decreases in terrestrial fluxes of certain metals has remained untested as far as the shallow-marine environment is concerned. This thesis presents the first systematic study of trace metal inventories of the shallow marine environment via analysis of microbial-carbonate-hosted pyrite. The new pyrite trace metal data confirm that there was a change in the supply of metal nutrients into the Palaeoproterozoic ocean. The carbonate-hosted pyrites confirm the higher Ni concentration of the Neoarchaean ocean, and record a post-Palaeoproterozoic drop in As concentration, a Zn enrichment in the Mesoproterozoic and Neoproterozoic ocean, and an increased delivery of Co to the Palaeoproterozoic ocean. These temporal trends were not caused by the post-GOE weathering of terrestrial sulphides, because detrital sulphides are still present in the post-GOE Huronian sandstones (e.g. Papineau et al., 2007) and many trace metals do not actually preferentially reside in typical sulphides such as pyrite. Instead these temporal trends were dominantly caused by changes in the make-up of the exposed land surface (e.g. Condie, 1993; Kamber, 2010) and/or by different tectonic regimes (e.g. Shirey & Richardson, 2011) and thus different erosion and weathering rates.

In light of the new findings from the shallow marine sedimentary environment reported in this thesis, it seems logical to propose that the disappearance of MIF S-isotopes exactly coinciding with the Huronian global glaciation reflects the initial build-up of free oxygen (and ozone) in the atmosphere. It can then be hypothesised that this change in atmospheric chemistry resulted in a reorganisation of the greenhouse structure of the atmosphere, initially causing an icehouse. Thus, the GOE is not likely an expression of biological evolution, for example it does not signify the first appearance of photosynthesis (Grassineau et al., 2001), but a response to the global geological functioning of our planet. However, the role of the resulting change in availability of micro-nutrients across the Archaean-Proterozoic boundary remains to be understood.

With regard to the causality of the Neoproterozoic global glaciations and the origin of metazoans, the currently available evidence (e.g. dos Reis et al., 2015; Yin et al., 2015) suggests that metazoans pre-date both the NOE and the Neoproterozoic glaciations. The Neoproterozoic global glaciations are currently attributed to a tectonic context, with a preponderance of landmasses in the middle and low latitudes setting the stage for snowball events (Kirschvink, 1992; Hoffman & Schrag, 2002). However, the breakup of the supercontinent Rodinia started some 70 Ma before the Sturtian glaciation (Figure 2 Mills & Canfield, 2014). In addition, the pre-Sturtian oxygen levels in the atmosphere are very poorly constrained (e.g. Planavsky et al., 2014; Zhang et al., 2016), as is the free oxygen increase through the end-Cryogenian and the Ediacaran (e.g. Lyons et al., 2014). Work carried out as part of this thesis suggests that metazoans could indeed have appeared in the deep Cryogenian, and that they may have contributed to the ventilation of the ocean in the NOE. Thus a possibility arises that the Neoproterozoic glaciations could have been caused by the rise of metazoans rather than the other way round.

It is perhaps not surprising that a thesis concerning itself with such a broad topic as the billion-year history of atmospheric oxygenation has found as many if not more new questions as answers. In terms of future research arising from this work, there is clear evidence that in situ analytical techniques are permitting us to study the sparsely preserved sedimentary record in a more meaningful way. Regardless whether it be S-isotopes, rare earth elements or vital elements, the insight gained over the last decade has revealed that Precambrian shallow-water carbonates hold key information about the global surface evolution. For example, a few mm-sized pyrite grains from within one thin section of a shaly limestone, contain nearly the entire $\Delta^{33}S$ range (9.5 ‰) recorded in all studied Archaean samples. Similarly, in situ analysis of Neoarchaean microbial carbonates can identify individual sediment-input events, which would go undetected in bulk sample analysis and would compromise interpretation. Finally, the ability to visualise in 2D the distribution of not only major elements but now also trace elements over petrographic fabrics is offering real prospect for deciphering the cryptic history of microbial and metazoan evolution.

References

Anbar AD, Duan Y, Lyons TW, Arnold GL, Kendall B, Creaser RA, Kaufman AJ, Gordon GW, Scott C, Garvin J (2007) A whiff of oxygen before the great oxidation event? *Science,* 317, 1903-1906.

Avrahamov N, Antler G, Yechieli Y, Gavrieli I, Joye SB, Saxton M, Turchyn AV, Sivan O (2014) Anaerobic oxidation of methane by sulfate in hypersaline groundwater of the Dead Sea aquifer. *Geobiology,* 12, 511-528.

Bekker A, Holland H, Wang P-L, Rumble D, Stein H, Hannah J, Coetzee L, Beukes N (2004) Dating the rise of atmospheric oxygen. *Nature,* 427, 117-120.

Canfield DE (2004) The evolution of the Earth surface sulfur reservoir. *American Journal of Science,* 304, 839-861.

Condie KC (1993) Chemical composition and evolution of the upper continental crust: contrasting results from surface samples and shales. *Chemical Geology,* 104, 1-37.

Dos Reis M, Thawornwattana Y, Angelis K, Telford MJ, Donoghue PC, Yang Z (2015) Uncertainty in the Timing of Origin of Animals and the Limits of Precision in Molecular Timescales. *Current Biology,* 25, 2939-2950.

Fairchild IJ, Kennedy MJ (2007) Neoproterozoic glaciation in the Earth System. *Journal of the Geological Society,* 164, 895-921.

Farquhar J, Bao H, Thiemens M (2000) Atmospheric influence of Earth's earliest sulfur cycle. *Science,* 289, 756-758.

Froelich PN, Klinkhammer GP, Bender ML, Luedtke NA, Heath GR, Cullen D, Dauphin P, Hammond D, Hartman B, Maynard V (1979) Early oxidation of organic matter in pelagic sediments of the eastern

equatorial Atlantic: suboxic diagenesis. *Geochimica et Cosmochimica Acta,* 43, 1075-1090.

Grassineau N, Nisbet E, Bickle M, Fowler C, Lowry D, Mattey D, Abell P, Martin A (2001) Antiquity of the biological sulphur cycle: evidence from sulphur and carbon isotopes in 2700 million–year–old rocks of the Belingwe Belt, Zimbabwe. *Proceedings of the Royal Society of London. Series B: Biological Sciences,* 268, 113-119.

Hoffman PF, Schrag DP (2002) The snowball Earth hypothesis: testing the limits of global change. *Terra nova,* 14, 129-155.

Holland HD (1999) When did the Earth's atmosphere become oxic? A reply. *Geochem. News,* 100, 20-22.

Kamber BS (2010) Archean mafic–ultramafic volcanic landmasses and their effect on ocean–atmosphere chemistry. *Chemical Geology,* 274, 19-28.

Keller CB, Schoene B (2012) Statistical geochemistry reveals disruption in secular lithospheric evolution about 2.5 [thinsp] Gyr ago. *Nature,* 485, 490-493.

Kirschvink JL (1992) Late Proterozoic low-latitude global glaciation: the snowball Earth.

Large RR, Halpin JA, Danyushevsky LV, Maslennikov VV, Bull SW, Long JA, Gregory DD, Lounejeva E, Lyons TW, Sack PJ (2014) Trace element content of sedimentary pyrite as a new proxy for deep-time ocean–atmosphere evolution. *Earth and Planetary Science Letters,* 389, 209-220.

Lyons TW, Reinhard CT, Planavsky NJ (2014) The rise of oxygen in Earth/'s early ocean and atmosphere. *Nature,* 506, 307-315.

Melezhik VA (2006) Multiple causes of Earth's earliest global glaciation. *Terra Nova,* 18, 130-137.

Mills DB, Canfield DE (2014) Oxygen and animal evolution: Did a rise of atmospheric oxygen "trigger" the origin of animals? *BioEssays,* 36, 1145-1155.

Och LM, Shields-Zhou GA (2012) The Neoproterozoic oxygenation event: environmental perturbations and biogeochemical cycling. *Earth-Science Reviews,* 110, 26-57.

Papineau D, Mojzsis SJ, Schmitt AK (2007) Multiple sulfur isotopes from Paleoproterozoic Huronian interglacial sediments and the rise of atmospheric oxygen. *Earth and Planetary Science Letters,* 255, 188-212.

Planavsky NJ, Reinhard CT, Wang X, Thomson D, Mcgoldrick P, Rainbird RH, Johnson T, Fischer WW, Lyons TW (2014) Low Mid-Proterozoic atmospheric oxygen levels and the delayed rise of animals. *science,* 346, 635-638.

Shirey SB, Richardson SH (2011) Start of the Wilson cycle at 3 Ga shown by diamonds from subcontinental mantle. *Science,* 333, 434-436.

Yin Z, Zhu M, Davidson EH, Bottjer DJ, Zhao F, Tafforeau P (2015) Sponge grade body fossil with cellular resolution dating 60 Myr before the Cambrian. *Proceedings of the National Academy of Sciences,* 112, E1453-E1460.

Zhang S, Wang X, Wang H, Bjerrum CJ, Hammarlund EU, Costa MM, Connelly JN, Zhang B, Su J, Canfield DE (2016) Sufficient oxygen for animal respiration 1,400 million years ago. *Proceedings of the National Academy of Sciences*, 201523449.